# Dynamics of water and ions in montmorillonite clays by microscopic simulation and quasi-elastic neutron scattering

Natalie Malikova

## To cite this version:

Natalie Malikova. Dynamics of water and ions in montmorillonite clays by microscopic simulation and quasi-elastic neutron scattering. Fluid Dynamics [physics.flu-dyn]. Université Pierre et Marie Curie - Paris VI, 2005. English. NNT : . tel-00226343

HAL Id: tel-00226343
https://theses.hal.science/tel-00226343

Submitted on 30 Jan 2008

THESE de DOCTORAT de l'UNIVERSITE PARIS VI
PIERRE ET MARIE CURIE

Spécialité :

Matière Condensée, Chimie et Organisation

présentée par

Natalie MALIKOVA

pour obtenir le grade de

DOCTEUR de l'UNIVERSITE PARIS 6

Sujet de la thèse :

# Dynamique de l'eau et des ions dans des argiles de type montmorillonite par simulation microscopique et diffusion quasi-élastique des neutrons

soutenue le *16 Septembre 2005*

devant le jury composé de :

M. LEVITZ Pierre ........................................ *Rapporteur*

M. VITART Xavier ........................................ *Rapporteur*

M. SMIT Berend ........................................ *Examinateur*

M. HANSEN Jean-Pierre ................................ *Examinateur*

M. LONGEVILLE Stéphane .......................... *Examinateur*

M. TURQ Pierre ........................................ *Examinateur*

M. FUCHS Alain ........................................ *Invité*

M. GIFFAUT Eric ........................................ *Invité*

# Remerciements, Acknowledgments, Poděkování

À Pierre Turq, pour sa direction avisée, le support apporté à mon travail ainsi que sa chaleur et son amitié, Emmanuelle Dubois, pour les innombrables discussions scientifiques que j'ai beaucoup appreciées et pendant lesquelles j'ai tant appris, Virginie Marry pour ses apports précieux concernant l'ensemble de mes travaux, Anthony Cadéne pour ses contributions expérimentales très importantes, Christian Simon, Jean-François Dufrêche, Serge Durand-Vidal, Benjamin Rotenberg, Marie Jardat et Guillaume Mériguet pour leurs nombreuses remarques perspicaces et leur aide immediate, Brigitte Carrez et Lise Michelot pour leurs gentillesse et efficacité, et enfin tous les autres membres du LI2C pour leur accueil ;

À Stéphane Longeville, Jean-Marc Zanotti du LLB pour leur patience pendant nos discussions interminables sur la diffusion des neutrons ;

À Eric Ferrage, Bruno Lanson, Laurent Michot pour leur regard experimental ;

À Eric Giffaut, Scott Altmann, Nicolas Michau de l'ANDRA pour leur soutien scientifique et à l'ANDRA pour le support financier ;

À Pierre Levitz et Xavier Vitart pour le temps dévolue à la lecture de mon manuscript et Berend Smit, Jean-Pierre Hansen et Alain Fuchs pour avoir acceptés de faire partie du jury de ma thèse ;

To Paul Cochrane, Giovanni Ciccotti and Frans Trouw, for fruitful technical and scientific discussions;

To Samuel, Vincent, Dorith, Alexander, Immanuel, Imri, Mickaël, Susha, David, Mark, Patrick, Etienne, Bruno, Lucile, Sylviane, Dominique for personal support from close and far away during my three years in Paris;

Všem svým v Čechách a ve Velké Británii;

merci, thank you, děkuji.

# Contents

# List of Figures

# List of Tables

# Chapter 1

# Introduction (version française)

Les minéraux argileux, riches en silicium et en aluminium, sont les produits de décomposition des minéraux formés dans les profondeurs de la croute ou du manteau terrestre. À la surface de la terre, ils entrent en contact avec un environnement acide (le dioxyde de carbone dissout dans l'eau), une atmosphère active et des fluctuations de température. Ce phénomène, appelé érosion, est la principale source de sédiments et de sols à la surface terrestre sur lesquels se base la biosphère. Les argiles, matériaux stratifiés et à grains fins, donc à grandes aires surfaciques qui leur confèrent des propriétés particulières (rétention d'eau, échanges ioniques), ont un rôle crucial comme réservoir de substances organiques et inorganiques et comme "tampon de pH" pour les sols. Les applications nombreuses des argiles incluent la poterie, la fabrication du papier, l'extraction d'impuretés, la décoloration et plus récemment les tamis moléculaires, la catalyse et le stockage des déchets radioactifs [1] [2] [3].

Cette dernière application est la motivation principale de notre étude. Dans le cadre du stockage des déchets radioactifs, les argiles sont envisagées comme constituant des "barrières ouvragées" construites autour des déchets radioactifs de haute activité et à vie longue. Les propriétés des argiles les plus pertinentes dans ce cadre sont leur faible perméabilité à l'eau et leur propriétés de rétention des cations. La barrière doit retenir l'eau qui s'infiltre depuis les roches environnantes et les cations radioactifs comme $Cs^+$ qui proviennent des déchets stockés eux-mêmes.

Ces propriétés de rétention doivent être conservées sur une certaine gamme de température. La chaleur produite par la décomposition des espèces radioactives qui constituent ces déchets soumet la barrière à des températures élevées. Pour la taille et le lieu du site de stockage étudié par l'ANDRA (Agence Nationale pour la gestion des Déchets RAdioactifs) en France, les modèles macroscopiques de l'évolution de la température de la barrière à long terme prévoient une gamme comprise entre 0 °C and 80 °C [4]. Nous relevons ici la température car elle fait l'objet de ce travail mais nous noterons que d'autres exigences strictes existent pour la barrière ouvragée.

Les propriétés de rétention des argiles sont liées à leur structures et aux phénomènes dynamiques qui apparaissent au niveau atomique. La présente étude se focalise précisément sur cette échelle, sur laquelle les propriétes structurelles mais surtout dynamiques des argiles sont analysées par deux approches complémentaires, simulation microscopique et diffusion des neutrons. Ces deux techniques traitent de la dynamique des espèces atomiques et moléculaires aux mêmes échelles de temps et d'espace, pour des durées de quelques centaines de picosecondes et sur des distances de quelques nanomètres, permettant une comparaison directe.

# Chapter 2

# Introduction

Clays minerals, rich in silicon and aluminium, are the breakdown products of minerals formed in greater depths of the Earth's crust or mantel and which, at the Earth's surface, come into contact with an acidic environment (carbon dioxide dissolved in water), active atmosphere and temperature fluctuations. This so-called weathering process is the main source of sediments and soils on the Earth's surface, on which the biosphere heavily relies. Clays, as layered, fine-grained (high surface area) materials with water retention and ionic exchange capacities, have crucial role in nutrient (both organic and inorganic) retention and pH buffering of soil. A vast number of applications of clays has been developed by mankind, beginning with their use in ceramic ware, paper-making, removal of impurities, decolouring and more recently as molecular sieves, in catalysis and in radioactive waste disposal [1] [2] [3].

The last application has been the main motivation for the present study. In the scenario of radioactive waste disposal clay minerals are potential components of an engineered barrier around high-activity radioactive waste. In the barrier, they are to be found in a compacted form and low-hydration states, at least initially. The properties of clays the most pertinent for the role of the barrier are their low permeability to water and high retention capacity of cations. It is the water seeping from the surrounding rock sediments and radioactive cations such as $Cs^+$ originating from the waste that the barrier needs to retain.

These retention properties need to persist over a certain temperature range as heat is produced during the breakdown of radioactive species in the waste and the barrier is thus subjected to elevated temperatures. Macroscopic modelling of the long-term evolution of the clay barrier, for the scale and location of the waste site studied by ANDRA (Agence Nationale pour la gestion des Déchets RAdioactifs) in France, predicts temperatures in the range between 0 °C and 80 °C [4]. Other strict requirements exist for the engineered barrier, we highlight the elevated temperatures as it is a parameter studied here.

The retention properties of clays can be traced down to their structure and dynamic phenomena occurring on the atomic level. It is exactly this scale of investigation that the current study embraces. The structural, but above all dynamic properties of clays are studied here on the microscopic scale using both modelling and experimental approaches, in particular microscopic simulation and neutron scattering. These two techniques deal with dynamics of atomic/molecular species on the same scale of time and space (time up to thousands of ps, distances up to a few nms) and thus a direct comparison can be attempted. This is to be contrasted with abundant macroscopic diffusion studies of clays (tracer experiments) [5] [6], the space- and timescale of which (distances order of meters and time order of hours, days) places it aside the two techniques above and direct comparison with them is impossible.

# Chapter 3

# Clay Minerals

The atomic structure of clay minerals, determined mainly from detailed X-ray studies beginning in mid-20th century [7] [8] and more recently from electron microscopy and solid state NMR [1], has a number of general features that span the entire clay family. At the same time, there exists almost a continuum of possible atomic substitutions within the general structure and results in blurred boundaries in any attempt to classify clays. Occurrence and even purification down to strictly stoichiometric phases in natural clays is next to impossible and most often we deal with mixtures. On the other hand, the almost gradual change in atomic structure and the resulting properties is an excellent framework for scientific purposes where the influence of a single parameter (e.g. clay layer charge density) can be investigated.

This study is concerned with *montmorillonite* clays, members of the *smectite* clay group. In the classification of clays, smectites are 2:1, dioctahedral, swelling clays. The following sections begin with general structural characteristics of clays and gradually zoom onto smectites, highlighting their behaviour under conditions of increased relative humidity and temperature.

## 3.1 Clay layers: atomic structure and appearance of charge

The basic building block of clays is an $SiO_4$ tetrahedron (the corners of the tetrahedron correspond to O atoms, while the center is occupied by an Si atom). These tetrahedra are arranged in a hexagonal pattern through sharing three of the four corners (O atoms) to form a planar structure referred to as a clay *sheet* (see Figure 3.1 Part a). In 2:1

clays (e.g. smectites), as opposed to 1:1 (e.g. kaolinite) and 2:1:1 (e.g. chlorites) clays, two of such *sheets* come together, with the unshared O atoms facing, to form a clay *layer*. In the mid-region of the clay layer, a sheet of octahedra is generated by the two planes of the unshared O atoms and additional hydroxyl groups (OH). The centers of the generated octahedra are occupied by trivalent aluminium or bivalent magnesium ions. While the former occupies only 2/3 of the octahedra formed (dioctahedral 2:1 clays), the latter occupies all of them (trioctahedral 2:1 clays) which leads to certain structural differences. Figure 3.1 Part b depicts the case of dioctahedral clays, in which incomplete occupation of the octahedra leads, through ion repulsion, to large vacant octahedra (white cavities) and smaller occupied octahedra (yellow).

Overall, a 2:1 clay layer is thus composed of two tetrahedral sheets and a central octahedral sheet. These sheets are however fused, in other words they share planes of oxygen atoms on the boundaries between them. For both dioctahedral and trioctahedral clays, the dimensions of unconstrained tetrahedral and octahedral sheets do not match perfectly and within the fused clay layer, both types of sheets are distorted (Figure 3.1 Part c).

The orientation of hydroxyl groups (one of the octahedron apices; in the *xy* projection it appears in the middle of the hexagonal cavity formed by a group of 6 $Si0_4$ units - refer back to Figure 3.1 Part a) is vertical to the layer in trioctahedral clays and almost horizontal in dioctahedral clays, pointing to the closest vacant octahedron (Figure 3.2).

The highly anisotropic clay layers (thickness $\sim$ 1 nm, lateral size order of nm to cm, m) have a strong tendency to stack into clay *particles*. Within a clay particle, adjacent layers are held by the weaker van der Waals forces but above all electrostatic interactions come into play when individual layers possess an overall electrostatic charge. Overall *negative* charge on clay layers arises by means of isomorphic substitutions of the metal cations, both in the tetrahedral and octahedral sheets. The charge is compensated by cationic species (counterions) on the layer surface or between two adjacent layers (interlayer region) (Figure 3.3). The density and location of isomorphic substitutions together with the nature of the counterion are the crucial factors determining the layer stacking within a clay particle and above all the response of the particle to increased humidity (absorption of water into the interlayer accompanied by increase in layer spacing = swelling), mobility and thus potential exchange of the counterion with an external system. In other words, charged clay layers with compensating mobile cations in-between are the key for all the widely-exploited clay properties such as swelling and water/ion retention.

The general molecular formula for dioctahedral clays with substitutions is $\mathrm{Cat}_{x+y}$ $[\mathrm{Si}_{8-x}\mathrm{Al}_x]$ $(\mathrm{Al}_{4-y}\mathrm{Mg}_y)$ $\mathrm{O}_{20}(\mathrm{OH})_4$, where Cat stands for the counterion. The continuum

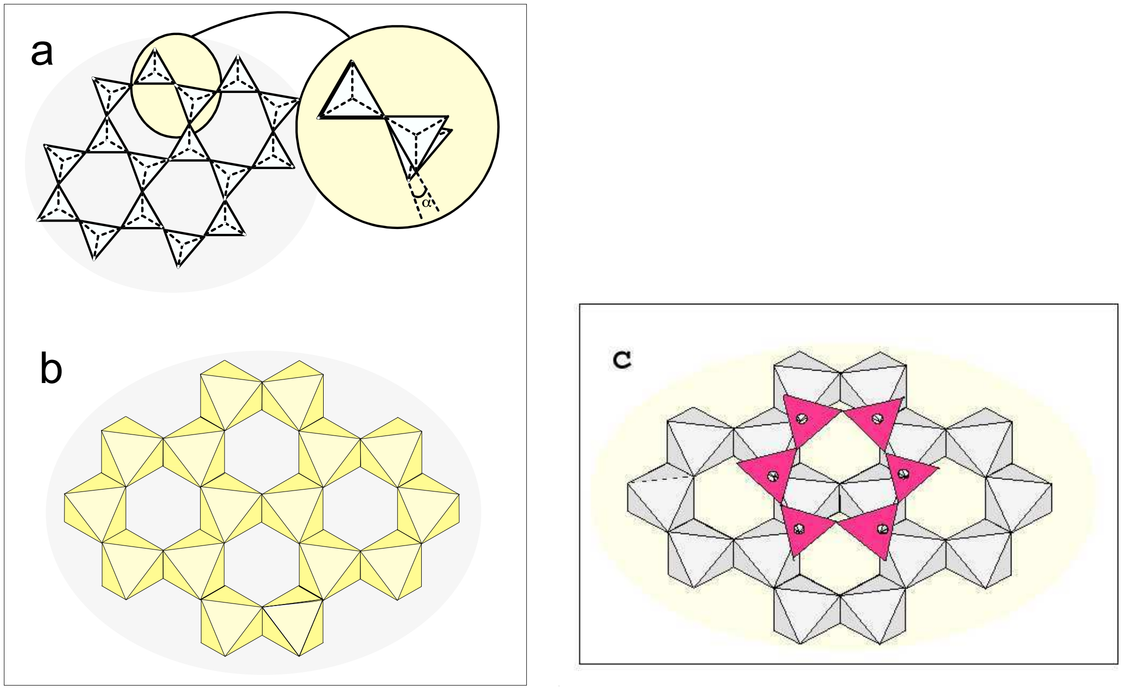

**Figure 3.1: Formation of a clay layer**

**Part a: A tetrahedral sheet formed from a hexagonal arrangement of corner-sharing $\text{Si0}_4$ units (the corners of each tetrahedron correspond to O atoms, while the center is occupied by an Si atom). Part b: Octahedral sheet (case of dioctahedral clays), arises at the interface between two facing tetrahedral sheets. Partial occupancy (2/3) of the centers of octahedra by $\text{Al}^{3+}$ cations leads to the formation of large vacant octahedra (white cavities) and small occupied octahedra (yellow). Part c: Distortion is necessary in the fusion of tetrahedral and octahedral sheets to form a layer. From now on we shall use consistently a reference frame, in which $xy$ is the plane of the clay layers and $z$ is the direction perpendicular to them (figure reproduced from reference [4])**

of naturally-occurring structures with different layer charge (x+y) and resulting properties is classified as shown in Table 3.1.

The first piece of information to notice in Table 3.1 is that swelling and ion exchange properties are delicately linked to the layer charge. For high tetrahedral layer charge in micas, the attraction between layers and abundant counterions is too strong for water to penetrate and the ions to become mobile and exchangeable. For zero-layer charge, there are

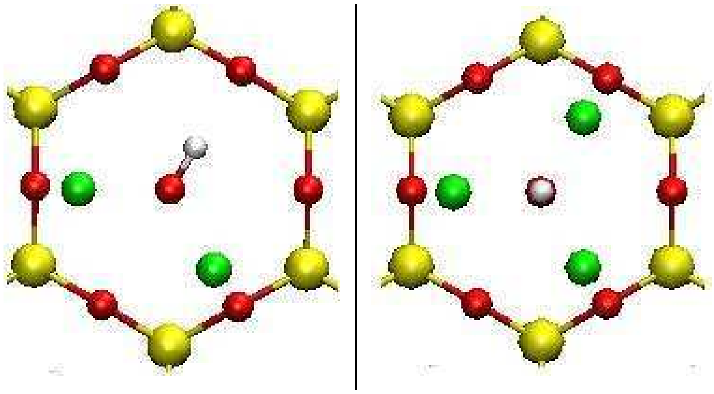

**Figure 3.2: Orientation of structural OH groups.**
**Case of dioctahedral (left) and trioctahedral (right) clays as seen in the $xy$ projection (plane of the clay layers). Yellow: silicon, red: oxygen, green: octahedral cations (e.g. aluminium and magnesium for di- and trioctahedral systems respectively), white: hydrogen. Each silicon (yellow) atom of the hexagonal ring in this representation corresponds to the center of a tetrahedron as depicted in Figure 3.1 Part a, while each oxygen (red) atom in the ring corresponds to the shared corner in Figure 3.1 Part a.**

| Name | Charge[a] | Type of substitution[b] | Natural counterion | Swelling, ion exchange |
|---|---|---|---|---|
| pyrophyllite | 0 | none | none | none |
| smectites | 0.4-1.2 | TET, OCT | $Ca^{2+}$, $Mg^{2+}$, $Na^+$ | ✓ |
| vermiculites | 1.2-1.8 | TET, OCT | $Mg^{2+}$ | ✓ |
| micas | 2.0-4.0 | TET | $K^+$ ($Ca^{2+}$) | none |

**Table 3.1: Classification of dioctahedral 2:1 clays as a function of layer charge.** **[a] Charge in electronic units per $O_{20}(OH)_4$. [b] TET - tetrahedral substitutions, OCT - octahedral substitutions.**

no counterions present, the only forces holding the layers together are of van der Waals type and yet these particles do not absorb water. It is thought to be due to the hydrophobicity of the uncharged layers and their large lateral size compared to their thickness [3]. (The lateral size of clay particles ranges from 0.1 $\mu$ m for smectites up to the macroscopic scale, order of cm for vermiculite and order of m for mica. There is a trend in the formation of laterally larger particles with increasing layer charge [1] [3].)

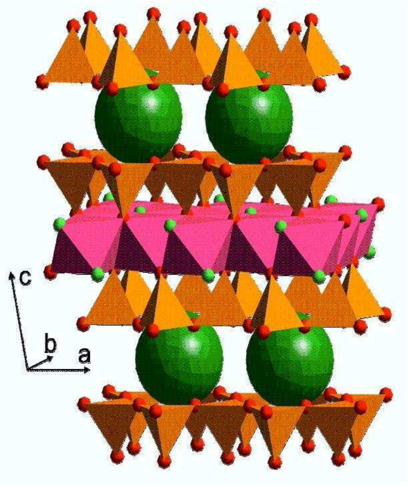

**Figure 3.3: Stacking of clay layers**
**Clay layer: orange - tetrahedral sheets, pink - central octahedral sheet, small red spheres - oxygen atoms, small green spheres - OH groups; large green spheres (not to scale) - compensating counterions in the interlayer. (figure after J.Breu)**

## 3.2 Clay swelling / hydration

Concentrating from now on the group of smectite clays as examples of swelling clays, we shall discuss some further features of clay swelling, which is the pre-requisite for both water-retention and ion-exchange properties of clays.

The swelling characteristics of a clay with a given charge location and density is still strongly dependent on the nature of the counterion. In general three swelling stages are recognized. Swelling begins in a step-wise manner (crystalline swelling, discrete layers of water formed in the interlayer, states referred to as monolayer / monohydrated, bilayer / bihydrated etc., water content of approximately 300 mg of water per 1 g of clay corresponds to the first three water layers), becomes continuous thereafter and in the extreme a colloidal suspension of clay particles ($<$ 10 aligned layers) is formed [8] [9] [10] [11] [12]. The sequence of stable states in the crystalline stage is most sensitive to the balance of ion-water and ion-clay interactions. This line of reasoning rationalizes for example the experimental observation of both monolayer and bilayer states for Na-montmorillonite, and only the monohydrated states in case of Cs-montmorillonite. The mono- to bilayer transition involves the transfer of the ion from the clay surface to the center of the interlayer and the formation of two layers of water to either side of the central ionic plane. With its larger radius, lower charge density and thus a lower hydration enthalpy, this transition is not favourable for the $Cs^+$ ion and the bilayer state is not formed [13] [14].

Crystalline swelling of clays and the structure and dynamics of water and counterions confined between clay layers has been a subject of numerous investigations [15] [16], beginning with experimental techniques such as X-ray diffraction combined with water adsorption gravimetry [10] [11] [12], NMR [17] [18], infra-red spectroscopy [19] [20] and more recently also microscopic simulation [21] [22] [23] [24] [13]. For routine characterisation of the hydration state of a clay sample, the combination of X-ray diffraction and water adsorption gravimetry has been widely used [10] [11] [12]. In principle, X-ray diffraction gives direct access to the layer spacing as a function of relative humidity through the 001 reflection arising from the periodic layer stacking. If coupled with water adsorption gravimetry, the amount of adsorbed water for a given layer spacing can thus be determined (see Figure 3.4).

This approach is however subject to the following complications arising from the nature of real clay systems:

- inhomogeneity in the stacking of the clay layers,
- difficulty of distinguishing water adsorbed on internal (interlayer) and external surfaces of the clay particles, multiple porosities in the system (interlayer, mesopores, macropores etc.. [4] [26])
- appearance of hysteresis in hydration - dehydration cycles, therefore strong dependence of the hydration level on the initial state of the sample [11] [10] [12].

Inhomogeneities in the clay layer ordering in both the $xy$ and the $z$ direction become apparent from X-ray diffractograms themselves. Translational and rotational disorder of layers in the $xy$ plane leads to a turbostratic structure (seen as asymmetric reflections), whereas non-integer spacing between higher-order 00L reflections indicates stacking disorder in the $z$ direction [27] [28] [29] [11]. Further to the disorder in the $z$ direction, this is linked to a phenomenon called *interstratification*, for which we recognize two principal origins [1]. In the first type, adjacent clay layers have different internal structure (such as in a mica-smectite intergrowth) [2]. The difficulty of obtaining pure clay phases from natural samples has already been mentioned. The second type of interstratification is the coexistence of different hydration levels in neighbouring interlayers and thus a mixture of layer spacings. This can occur even within a single clay phase (e.g. montmorillonite) as layer charge can differ locally due to spatial inhomogeneity of isomorphic substitutions. Detailed analysis

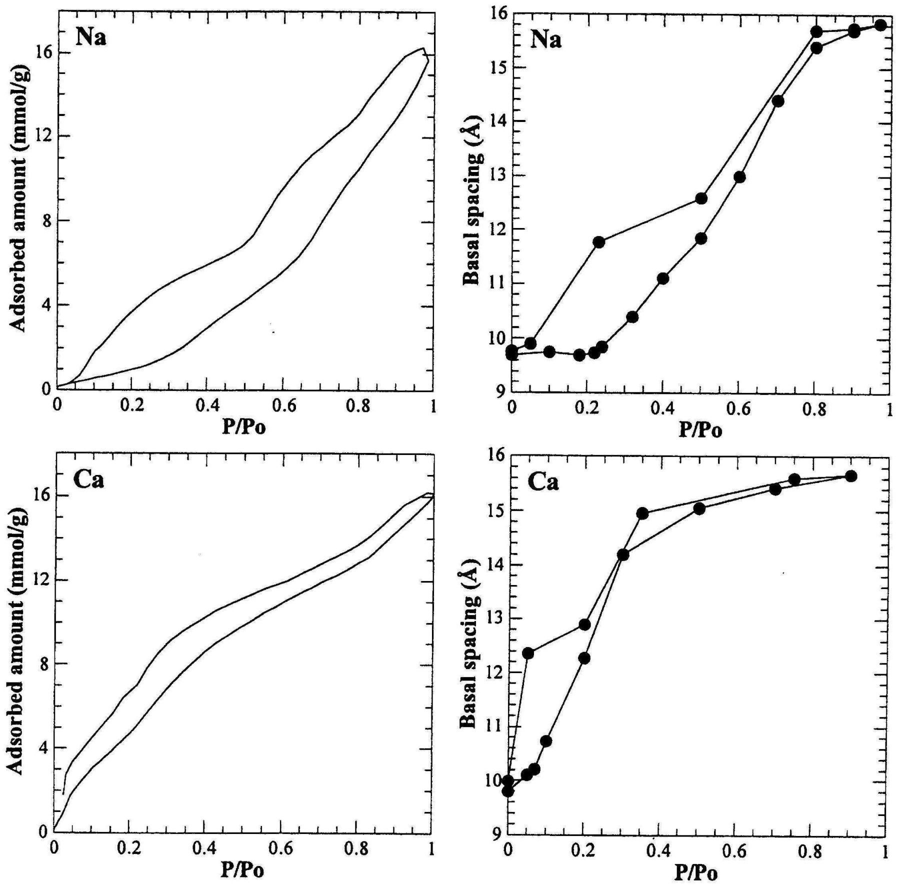

**Figure 3.4: Water adsorption isotherms and concurrent changes in basal spacing (from X-ray diffraction) as a function of relative humidity for Na and Ca montmorillonite.**
**(figure reproduced from ref [25])**

of X-ray diffractograms can then yield the percentage of monolayer, bilayers in the system at a given humidity (Refer to Chapter 8). Interstratification is an important factor in the current study, as the motion of exchangeable cations and interlayer water crucially depends on the total water content and layer spacing. The only way around interstratification seems to be the use of synthetic clays, in the synthesis of which special attention is paid to the homogeneous layer charge [27]. The experimental part of the current study is concerned with natural montmorillonite, where interstratification remains an issue.

Further problem is the presence of water in other than the interlayer porosity. Available estimates of mesoporous water (obtainable only indirectly from for example a combination of water vapour adsorption isotherms and BET nitrogen isotherms) in montmorillonite at 80 % relative humidity give proportions of up to 20 % of total water content [11] [12] [10].

The difficulties, originating in interstratification and presence of water in several porosities in real clay systems, arising during comparison with model clays (used here in microscopic simulation, accounting only for a single type of interlayer), shall become evident.

## 3.3 Clay dehydration on heating

The stability of a clay in a given hydration state depends not only on the surrounding relative humidity but also on temperature and pressure. We shall introduce here the effect of increasing temperature, under constant (atmospheric) pressure and ambient relative humidity ($\sim$ 45 %), which has been studied extensively by thermogravimetry [4] [1] [2] [30] or other methods such as X-ray diffraction [31]. (We note that the combined effect of increased temperature and pressure is very important when studying the stability of hydrated clay deposits in significant depths below the Earth's surface and it has been investigated by both experiment [30] [32] [33] and simulation [34] [35].)

During a single cycle of a thermogravimetric experiment, a clay sample is subjected to a temperature increasing at a constant rate (order of 100°C per hour), and the accompanying changes in its mass are recorded. These experiments are of a *dynamic* nature and care has to be taken with the rate of temperature increase if the purpose is to reach true equilibrium at any given temperature [30] [31]. In general, the following dehydration steps have been observed in the order of increasing temperature (Figure 3.5): desorption of weakly bound molecular water (from external surfaces and macropores between clay particles, at 50-90°C), desorption of strongly bound molecular water (from interlayers, first few hydration shells of counterions, at 100 - 200°C) and dehydroxylation of clay layers (removal of structural OH groups, at temperatures above 550°C). A greater number of dehydration steps in the temperature range of 100 - 200°C is seen for bivalent as compared to monovalent counterions, rationalised on the basis of more numerous hydration shells of the bivalent cations [1]. Overall, the desorption stages of *molecular* water are numerous and not always easily identifiable. Their above assignment to different "families" of molecular water in the system remains rather loose.

For the purposes of this study the main pieces of information are the temperature ranges and duration of heating which result in *reversible* changes in the hydration of the clay sample. Beginning with the high temperature phenomena, the dehydroxylation stage destroys the structure of the clay layers themselves and can in no way be considered

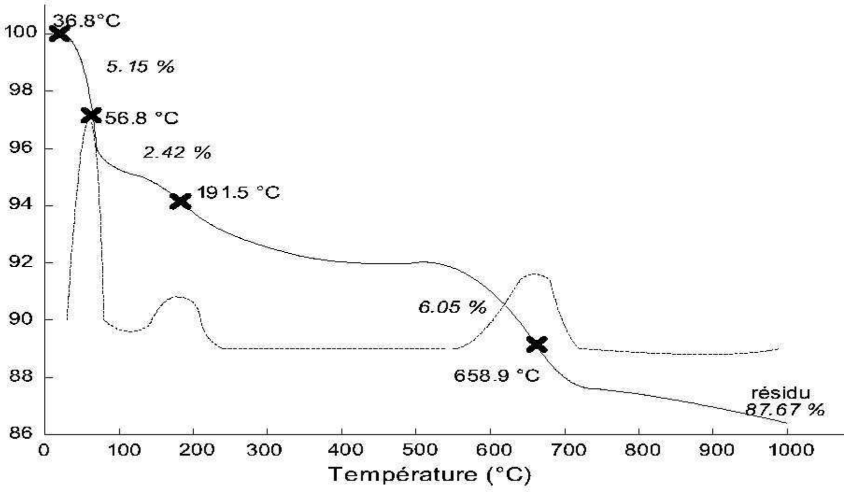

**Figure 3.5: Desorption of water from clay upon heating. Thermogravimetric measurements (direct curve and derivative shown) for a Na-montmorillonite clay. (figure reproduced from reference [4])**

as reversible. Even the removal of the last traces of molecular water in the interlayer, achieved for example by prolonged heating at temperatures higher than 200°C, results in irreversible structural changes in the clay system with at least a partial loss of the rehydration properties [1] [4]. All lower temperature treatments preserving at least the last traces of interlayer water are considered as reversible.

The experimental protocol used in this study for producing dry clay samples involves *constant* temperature heating at approximately 80°C in the presence of a silica gel for a matter of days [36] [4]. The resulting clay samples contain a residual quantity of water, approximately 1 $H_2O$ per interlayer cation [37], and conserve fully their rehydration properties.

# Chapter 4

# Simulation Techniques

In pace with the almost miraculous advances in computing power ever since the Second World War, simulation has been establishing itself in the scientific world as an equal partner to experiment and theory. The interest of *microscopic* simulation is to join the atomic details of a given system (atomic masses, molecular geometry, particle interactions) to the macroscopic properties that are accessible to experimental investigation (the equation of state, transport coefficients, structural order parameters) [38] [39]. The theory of statistical mechanics provides this connection directly only for a handful of idealised systems (e.g. perfect gas, two-dimensional Ising model), whereas in the majority of cases it has to employ approximate schemes. For a given model system, simulation gives essentially exact results and their comparison to the prediction of a theoretical scheme is thus an assessment of the approximation itself. On the other hand simulation-experiment comparison scrutinizes the validity of the model (by definition a simplified version of the real system) used in an attempt to reproduce the behaviour of the real experimental system. If a good model is found, it serves a great deal in explaining the origin of experimentally observed phenomena or can even be employed to predict behaviour of the system under experimentally unattainable conditions. For the latter to be successful, the limits to the validity of the model under extreme conditions have to be well understood.

## 4.1 Constructing model systems

A microscopic picture of a system of N atoms is, under the Born-Oppenheimer approximation, a set of N atomic nuclei in a potential, $V(\mathbf{r})$, arising from the smearing out of the rapid motion of electrons. For a known form of $V(\mathbf{r})$, it is possible to evaluate the potential and kinetic contributions to the overall energy of the system, which depend on nuclear (atomic) positions and nuclear (atomic) momenta respectively. The sum of these two contributions defines the Hamiltonian, which is the key to the time evolution of the system.

The essential input of *classical* microscopic simulations is thus the underlying potential, $V(\mathbf{r})$. Whereas the Monte Carlo technique is based on evaluating the total system energy from $V(\mathbf{r})$ for various atomic configurations, Molecular Dynamics goes further into calculating the force on each atom in the system and then describes the resulting atomic motion. In both cases however, knowledge of $V(\mathbf{r})$ is the starting point [39].

The underlying potential can be expressed as a sum of two-atom (pair), three-atom and higher terms, but often (e.g. for liquids) $V(\mathbf{r})$ is constructed only from the pair contributions. In many such cases *effective* pair potentials are used, which are adjusted to reproduce the experimental data (such as density) for the given system. This is often achieved only for some finite range of experimental conditions such as temperature and pressure.

When simulating a mixture of atomic and molecular species, the atomic detail of molecular species is still preserved. On one level of description, *all* pairs of atoms interact and there is a need for both intermolecular potentials (modelling Van der Waals attraction, steric repulsion etc.) and intramolecular potentials (modelling bond stretching, bending etc.). However in the present study and many other cases, molecular species are considered as rigid bodies, with no internal (vibrational) degrees of freedom. This decoupling of vibrational degrees of freedom on one hand and rotational / translation on the other is possible due the different characteristic times and energies involved and shall be discussed in more detail further on. Therefore, when molecular species are considered as rigid, only intermolecular potentials are necessary and some examples follow immediately [39] [40].

The short-range Van-der-Waals attraction and steric repulsion is commonly characterised by the Lennard-Jones potential of the form

$$V_{ij} = 4\epsilon_{ij}[(\frac{\sigma_{ij}}{r_{ij}})^{12} - (\frac{\sigma_{ij}}{r_{ij}})^{6}] \tag{4.1.1}$$

where $r_{ij}$ is the distance between atoms $i$ and $j$ , $\sigma_{ij}$ and $\epsilon_{ij}$ are empirical parameters for the pair of atoms concerned. This potential form was first used successfully to describe the interaction between argon atoms (atoms $i$ and $j$ of the same kind) [41]. In an extension to systems of more than one atomic type, the above parameters can be expressed as

$$\sigma_{ij} = \frac{\sigma_i + \sigma_j}{2} \tag{4.1.2}$$

$$\epsilon_{ij} = \sqrt{\epsilon_i \epsilon_j} \tag{4.1.3}$$

where $\sigma_i$ and $\epsilon_i$ are characteristic now of a single atomic type (Lorentz-Berthelot rules). In addition to the above, for systems containing atoms with an overall effective charge, the electrostatic interaction is described by the Coulombic potential

$$V_{ij} = \frac{q_i q_j}{4\pi\epsilon_0 r_{ij}} \tag{4.1.4}$$

where $q_i$ and $q_j$ are the effective atomic charges (empirically determined) and $\epsilon_0$ is the permittivity of free space. For the purposes of this study, we shall limit ourselves to the above two potentials and note that an ever-increasing number of other intermolecular and intramolecular potentials exists with a varying degree of complexity but also transferability between systems.

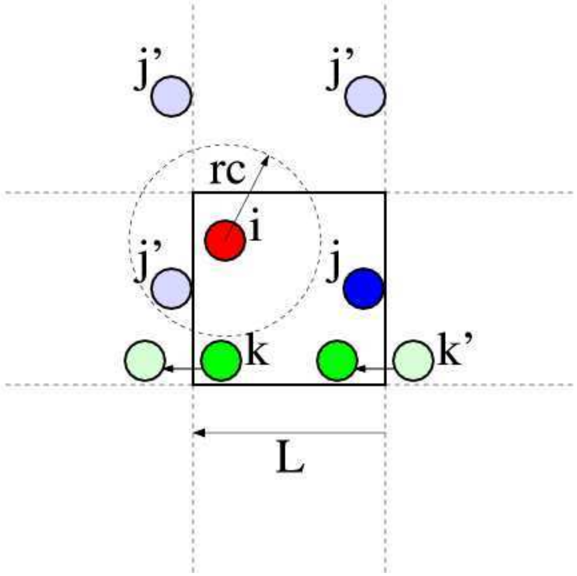

**Figure 4.1: Illustration of periodic boundary conditions and potential cut-off ($rc$) used in simulations.**
**Interaction of atom $i$ with atom $j$ and its periodic images $j'$ is limited to the closest $i$–$j(j')$ pair. Atoms leaving the original simulation box at any step (atom $k$) are replaced by their image entering by construction from the opposite side (atom $k'$).**

The number of atoms in a simulated system ($N$) is highly influenced by the computing power available. Currently, for reasonable simulation times, $N$ can reach up to approximately $10^4$ (for pair potentials it is necessary to evaluate $N(N-1)/2$ atomic pair contributions to the overall energy, so simulation time scales as $N^2$). It is unrealistic to expect such an ensemble of atoms to represent the bulk properties of a solid or liquid due to the high percentage of surface atoms. To overcome this, periodic boundary conditions (usually in all three dimensions) are used to replicate the initial simulation box, in which case a formally infinite system is constructed and the surface disappears [39] [38]. In theory, an atom $i$ in the original box now interacts with an atom $j$ in the original box but also with all its (infinitely many) periodic images (Figure 4.1). Consequently, the evaluation of all $i-j$ contributions to the overall energy is impossible. For the so-called short-range potentials (such as the Lennard-Jones) the $i-j$ contributions are limited to atomic pairs that are separated by less than a cut-off distance, $r_c$. The justification for introducing $r_c$ is as follows. For any pair potential $P(r)$ such that $P(r) \propto r^{-n}$ where $n > 3$, the total potential energy of the $N$ particle system ($U_{pot}$) can be expressed as

$$\begin{aligned}
U_{pot} &= \frac{N\rho}{2}\int_0^{\infty} g(r)P(r)4\pi r^2 dr \\
&= 2\pi N\rho\int_0^{r_c} g(r)P(r)r^2 dr + 2\pi N\rho\int_{r_c}^{\infty} P(r)r^2 dr \\
( & \quad \text{as } g(r)\to 1 \text{ with increasing } r) \\
&= 2\pi N\rho\int_0^{r_c} g(r)P(r)r^2 dr + 2\pi N\rho\int_{r_c}^{\infty} r^{2-n} dr \\
&= 2\pi N\rho\int_0^{r_c} g(r)P(r)r^2 dr + 2\pi N\rho\frac{r_c^{3-n}}{3-n} \qquad (4.1.5)
\end{aligned}$$

where $\rho$ is the density and $g(r)$ is the radial distribution function. (Radial distribution function is a pair distribution function for isotropic and homogeneous systems, it depends only on the separation of two atoms, $r$. It is related to the mean number of particles found in a spherical shell of radius $r$ and thickness $dr$ centered on a reference particle through $n(r)dr = 4\pi r^2\rho g(r)dr$ [42].) The second term in Equation 4.1.5, i.e. the energetic contribution of an atom $i$ at the origin and all atoms $j$ lying beyond a sphere of radius $r_c$ centered on atom $i$, can be made as small as necessary ($3-n$ is negative) by increasing $r_c$ in order to make it negligible in the total potential energy.

It is necessary that the cut-off sphere is completely contained within the original simulation box (for a cubic box of side $L$, $r_c \leq L/2$) [39]. This limits the influence of the artificial periodicity on the resulting properties of the system. As the cut-off radius is determined by the form of the potential, indirectly so is the size of the simulation box. Under the above condition for $r_c$, for any $i-j$ atomic pair there is *at most* one version of atom $j$ (the original or one of its periodic images) in the sphere of radius $r_c$ centered on atom $i$ (Figure 4.1). Thus for each of the original N atoms there are *at most* N-1 pair contributions to be evaluated, as in the case of a finite system. Also, throughout the simulation, it is only necessary to trace the positions of N atoms in the original box (Figure 4.1).

For slow-decaying, long-range potentials (such as the Coulombic) the reasoning of cut-off radius does not apply as the integral in Equation 4.1.5 diverges and other techniques have been developed to deal with them. For the long-range interactions it is impossible to erase the effect of the artificial periodicity of the system. Indeed some methods used to evaluate long-range interactions *rely* on it. The method of Ewald summation evaluating the total electrostatic energy is an example and it uses the representation of the periodic system in the reciprocal space [38] [39]. In this method each point charge is surrounded by a Gaussian charge distribution of the opposite sign (with a characteristic width of $1/\alpha$, where $\alpha$ itself is an adjustable parameter), which results in a collection of *screened* charges, the interaction of which can be effectively treated as short-range and is evaluated in the real space. An additional collection of "cancelling" Gaussian charge distributions then needs to be considered to return the overall situation to the case of point charges. In case of the "cancelling" distribution of charges, the electrostatic energy is evaluated in the reciprocal space and for this calculation the maximal reciprocal space vectors in all three dimensions form another set of adjustable parameters ($\mathbf{k_{x,y,z}}$). An important correction term to be subtracted from the overall electrostatic energy is the self-interaction term of the "cancelling" charge distribution, which is inherently included in the reciprocal space calculation. Further details of the now standard Ewald summation method are to be found in refs [39] [40].

### 4.1.1 Model clay system

For the modelling of hydrated clay systems, an atomic model for the interlayer water molecules, counterions and clay layers is necessary. Construction of models for the $H_2O$ molecule is a vast field in itself. Currently the most successful rigid water models are considered to be from the SPC and the TIP family [43]. The "extended" SPC model (SPC/E), including the self-polarisation energy correction, is used here (O-H bond 1.0 Å, angle H-O-H 109.47 °, charges -0.848 e and +0.424 e for oxygen and hydrogen atoms respectively). It was seen initially to be an improvement to the SPC model in terms of the diffusion coefficient of bulk water at ambient temperature [44] and later it was shown to work well for both structural and dynamic properties of bulk water over a wide range of temperatures and pressures [45].

The construction of model clays systems departed from the known atomic positions within clay layers as determined by X-ray crystallography. The rigid clay model used here is based on the studies of Skipper et al, in which initially the interaction between a water molecule (model MCY) approaching a clay surface (imitated by a network of MCY water molecules arranged in hexagonal patterns) was parametrised for a Matsuoka potential (consisting of exponential terms modelling the London (dispersion) forces and short-range repulsions and a Coulombic term) [46] [47]. Great degree of similarity was therefore implied in the nature of uppermost oxygen atoms of the clay layers and oxygen atoms of free water molecules, while the structural hydroxyl group was represented by "half" of a water molecule. This model reproduced successfully the adsorption energy of water in talc (no charge on clay layers). To obtain a charged clay surface, the charges of octahedral / tetrahedral cations (all clay layer atoms are considered as point charges) were modified without the change of their remaining potential parameters. This study was further extended to use different functional forms of the short-rage potentials (e.g. Lennard-Jones potential) and other models of water, such as the TIP4P model [48] or the SPC/E model [49]. The latter of these is used here. Each atom type in the simulation cell is thus characterised by two Lennard-Jones parameters ($\sigma_i$,$\epsilon_i$) and charge ($q_i$) as listed in Table 4.1. The interaction potential between a pair of atoms is therefore

$$V_{ij} = \frac{q_i q_j}{4\pi\epsilon_0 r_{ij}} + 4\epsilon_{ij}[(\frac{\sigma_{ij}}{r_{ij}})^{12} - (\frac{\sigma_{ij}}{r_{ij}})^6] \qquad (4.1.6)$$

and pair parameters $\sigma_{ij}$ ,$\epsilon_{ij}$ , for $i \neq j$, are obtained from the Lorentz-Berthelot rules.

The model clay under investigation is a montmorillonite type clay with a unit cell of $Cat_{0.75}$ $[Si_8]$ $(Al_{3.25}Mg_{0.75})$ $O_{20}$ $(OH)_4$, where Cat stands for cation in the interlayer. Thus isomorphic substitutions in the clay giving rise to an overall charge on the clay layers are in the octahedral sheet only. As mentioned before substituted atoms differ only in charge, not in the Lennard-Jones parameters (see Table 4.1).

Simulation box for Monte Carlo and Molecular Dynamics simulations contained two layers of clay (area 20.72 Å × 17.94 Å , thickness 6.54 Å), each consisting of 8 of the above unit cells and its charge being balanced by 6 cations in the interlayer (see Figure 4.2). Due to the finite size of the simulation box, rare substitutions present in a real montmorillonite system are not taken into account in the model. The unit cell composition and simulation box size is tuned so that an integer number of counterions is present in the box.

Interlayer cations considered in this study are $Na^+$ and $Cs^+$, the former in both mono- and bihydrated state, the latter in monohydrated state only (bihydrated Cs-montmorillonite is not observed experimentally - refer back to Section 3.2). Based on a previous study [13],

| Molecule | Atom | $q_i$ (e) | $\sigma_i$ (Å) | $\epsilon_i$ (kcal/mol) |
|---|---|---|---|---|
| Clay | Al | 3.0 | 0.0 | 0.0 |
| | Mg (substituting Al) | 2.0 | 0.0 | 0.0 |
| | Si | 1.2 | 1.84 | 3.153 |
| | O (of OH group) | -1.0 | 3.166 | 0.156 |
| | O (octahedral) | -1.424 | 3.166 | 0.156 |
| | O (tetrahedral) | -0.8 | 3.166 | 0.156 |
| | H | 0.424 | 0.0 | 0.0 |
| Water (SPC/E model) | O | -0.848 | 3.166 | 0.156 |
| | H | 0.424 | 0.0 | 0.0 |
| Interlayer counterions | Na | 1.0 | 2.587 | 0.1 |
| | Cs | 1.0 | 3.83 | 0.1 |

**Table 4.1: Atomic parameters for effective pair potentials in the model clay system.**
**Parameters taken from ref [49] and [50].**

we define the mono- and bihydrated state as corresponding to 6 and 12 water molecules per cation, or 36 or 72 water molecules per interlayer in the simulation box, respectively.

Periodic boundary conditions in all three dimensions are applied throughout the simulations. In energy calculation a spherical cut-off of 8.0 Å is used for the Van-der-Waals interaction and a three-dimensional Ewald sum is applied for the evaluation of electrostatic energy. The optimised Ewald sum parameter $\alpha$ was 0.3 and the maximal reciprocal space integers for each of the three directions were determined according to $n_{x,y,z}^{max} > 3.2L_{x,y,z}/r_{cut}$ with the corresponding maximal reciprocal space wavevectors being $k_{x,y,z}^{max} = 2\pi n_{x,y,z}/L_{x,y,z}$ [40] [51]).

## 4.2 Classical microscopic simulations

The previous section was concerned with the input information of classical microscopic simulations. In summary this is a configuration of $N$ atoms, each of a known mass and characteristic parameters (such as charge, Lennard-Jones parameters), together with a set of (pair) potentials modelling the atomic interactions. Each configuration of these $N$ atoms corresponds *microscopically* to a point in the multi-dimensional phase-space defined by the atomic positions and momenta, $(\mathbf{r}^N, \mathbf{p}^N)$, and *macroscopically* to a set of parameters such

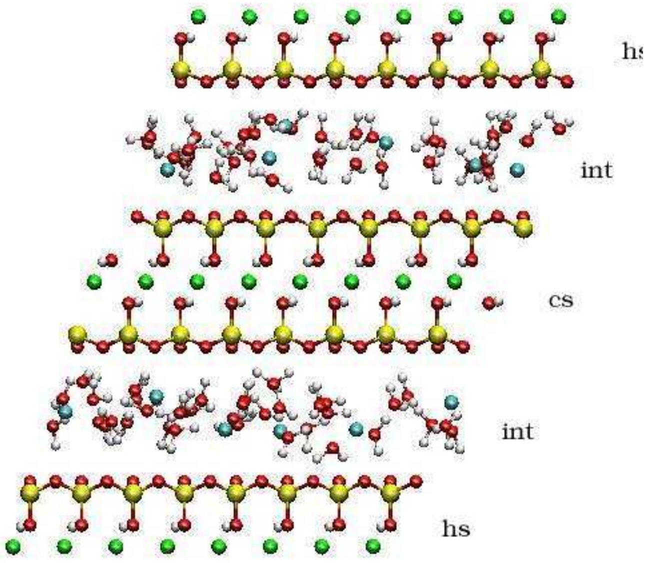

**Figure 4.2: Simulation box for Monte Carlo and Molecular Dynamics simulation.**
**The box consists of two half-layers (hs), central layer (cs) and two interlayers (int) with numbers of ions and water molecules in a predetermined ratio, corresponding to a given hydration state. (green: aluminium atoms, red: oxygen atoms, white: hydrogen atoms, yellow: silicon atoms, blue: counterions, $\mathbf{Na^+}$ or $\mathbf{Cs^+}$)**

as a given temperature and pressure.

The principle of microscopic simulations is to change the atomic configuration and sample the phase-space under the constraint of a particular statistical ensemble (such as $NVE$ corresponding to a constant number of particles, volume and total energy) and provide ensemble averages for the remaining macroscopic quantities. Monte Carlo (MC) and Molecular Dynamics (MD) simulations achieve this in rather different ways. Whereas MC evaluates an ensemble average by stochastic sampling of the phase-space, MD evaluates a time average by tracing, in a deterministic way, the real time evolution of the system. Under the *ergodic* hypothesis, applicable to most commonly studied systems, the ensemble and time average (calculated in the same statistical ensemble) are equivalent. That is why a number of macroscopic equilibrium properties (but not all!) can be evaluated by either of the simulation techniques.

Macroscopic properties can be divided into the following classes, depending on the way they are determined from microscopic quantities.

- Thermodynamic properties calculated directly from the positions and momenta of all atoms in the system (e.g. temperature, pressure) - obtainable both by MC and MD
- Local structural properties calculated from static correlations between particles (e.g. radial distribution functions), density profiles - obtainable both by MC and MD
- Dynamic properties calculated from the *time evolution* of atomic positions and momenta or time-correlation between particles (e.g. diffusion coefficients, viscosity) - obtainable *only* by MD
- Thermodynamic properties related to the volume of phase space available to the system (e.g. entropy, Gibbs free energy), thermodynamic integration necessary - computationally significantly more demanding than the other three classes of properties - obtainable both by MC and MD

The traditional or natural ensembles for MC and MD simulations do not coincide, they are the $NVT$ and $NVE$ ensembles respectively. However, techniques for transforming ensemble averages and fluctuations in different ensembles have been developed [52]. More importantly, extensions of MD and MC simulations to other than their traditional ensembles are now routinely used and some of them shall be discussed in detail further on.

The aim of simulations is after all the imitation of real experimental systems and the most appropriate ensemble would be a constant temperature, constant pressure and constant chemical potential ensemble, a "$\mu PT$" ensemble. In the framework of this study, the $\mu PT$ ensemble corresponds to the conditions of a clay sample in equilibrium with water vapour at a given relative humidity (fixing the chemical potential), a given temperature and pressure (in the simplest of cases, ambient temperature and atmospheric pressure).

In view of the above, the three most widely used statistical ensembles ordered with increasing applicability to real experimental conditions would be: 1) the micro-canonical ($NVE$, constant number of particles $N$, volume $V$ and total energy $E$), 2) canonical ($NVT$, constant number of particles, volume and temperature $T$) and 3) grand canonical ($\mu VT$, constant chemical potential $\mu$, volume and temperature). It is now a routine to run MC and MD simulations also in the $NPT$ ensemble in addition to the above three. The "$\mu PT$"

ensemble itself is inaccessible to simulatios, due to all fixed variables being intensive, *in case of a bulk system.* At present the closest to simulations in the "$\mu PT$" is the Gibbs ensemble technique devised by Panagiotopoulos [53].

We are aware of the first trials of $\mu\sigma_{zz}T$ simulations on clays, where $\sigma_{zz}$ refers to the stress perpendicular to the clay layers [14]. Due to anisotropy of the system, the presence of interacting clay layers and the limit of a few molecules of water inbetween clay layers, the z dimension of the system (layer saparation) and the number of water molecules in the system are no longer stricly extensive variables (and thus their conjugate variables, $\sigma_{zz}$ and $\mu$ respectively, not strictly intensive). Therefore, the above-outlined reasoning for the inaccessibility of a '$\mu PT$' simulation in case of isotropic, bulk systems, does not apply here [38]. In case of clay systems, the $\mu\sigma_{zz}T$ ensemble seems to reflect the best the real experimental conditions. However, all results presented in this study are from simulations in constant $N$ ensembles. In particular, Monte Carlo simulation in the $N\sigma_{zz}T$ and $NVT$ ensembles and Molecular Dynamics simulations in the $NVT$ and $NVE$ ensembles were employed.

### 4.2.1 Monte Carlo simulations

As mentioned previously the Monte Carlo technique samples the multi-dimensional phase-space of a system on N particles in a *stochastic* way in order to obtain an ensemble average of a given quantity. The traditional ensemble of MC is $NVT$, in which the ensemble average of a quantity depending only on particle positions, $A(\mathbf{r}^N)$, is

$$\begin{aligned}\langle A(\mathbf{r}^N)\rangle_{NVT} &= \frac{\int A(\mathbf{r}^N)e^{-(U_p(\mathbf{r}^N)+U_k(\mathbf{p}^N))/(k_bT)}d\mathbf{r}^N d\mathbf{p}^N}{\int e^{-(U_p(\mathbf{r}^N)+U_k(\mathbf{p}^N))/(k_bT)}d\mathbf{r}^N d\mathbf{p}^N} \\ &= \frac{\int A(\mathbf{r}^N)e^{-(U_p(\mathbf{r}^N))/(k_bT)}d\mathbf{r}^N}{\int e^{-(U_p(\mathbf{r}^N))/(k_bT)}d\mathbf{r}^N} \qquad (4.2.1)\end{aligned}$$

where $U_p$ and $U_k$ are the total potential and kinetic energies of the system respectively, $k_b$ is the Boltzmann's constant and $T$ the temperature. In the above equation the integral over particle momenta, which itself can be easily evaluated, has cancelled out and the Boltzmann factor now includes only the total potential energy of the system.

MC generates new configurations "blindly" by random changes to existing configurations. In the $NVT$-MC, these random changes are 1) translation of a free atom 2) overall translation of a rigid molecule 3) rotation of a rigid molecule. By using a so-called *importance sampling*, we achieve that only configurations having a significant contribution to the integrals in Equation 4.2.1 are taken into account, i.e. configurations with high potential energy are rejected.

The weight, $P(m)$, of a configuration $m$ in the above integrals is

$$P(m) = \frac{e^{-U_p(m)/(k_b T)}}{\sum_{\forall\ m} e^{-U_p(m)/(k_b T)}} \tag{4.2.2}$$

It is impractical to consider the weight in this way, as the knowledge of *all* possible configurations is necessary for evaluating the denominator. Instead, at each step of an MC simulation we consider the weight of the newly generated configuration ($m$) *only* with respect to the configuration immediately preceding it ($n$). This scheme constructs series of configurations known as the Markov chains. In order to satisfy the condition that, at any simulation step (or time $t$), the sum of probabilities of all possible configurations is 1, i.e. $\sum_{\forall n} P(n) = 1$, configurations in a Markov chain have to satisfy the condition of *detailed balance*:

$$P(n) W_{n\ \rightarrow\ m} = P(m) W_{m\ \rightarrow\ n} \tag{4.2.3}$$

where $W_{n\ \rightarrow\ m}$ is the transition rate from state $n$ to state $m$. The key to importance sampling is then to find a form of the transition rate satisfying Equations 4.2.2 and 4.2.3. The Metropolis transition rate is the first and still most widely used example [54]. It is implemented as follows.

1. Generate an initial configuration of particles (usually distributed at random or on regular lattice sites)
2. Choose one particle at random, change its position and determine the corresponding change in energy $\Delta U_p(n \rightarrow\ m)$,
3. If $\Delta U_p(n \rightarrow\ m) < 0$, accept configuration $m$ (i.e. count it in the ensemble average) and go to step 2 with $m$ as the starting configuration,
4. If $\Delta U_p(n \rightarrow\ m) > 0$, generate a random number $p$ between 0 and 1,
5. If $p > e^{-\Delta U_p(n \rightarrow\ m)/(k_b T)}$, reject configuration $m$, (i.e. *re-count* configuration $n$ in the ensemble average) and go to step 2 with $n$ as the starting configuration,
6. If $p < e^{-\Delta U_p(n \rightarrow\ m)/(k_b T)}$, accept configuration $m$ (i.e. count it in the ensemble average) and go to step 2 with $m$ as the starting configuration.

The traditional $NVT$ Monte Carlo method has been extended to a variety of other ensembles. We limit ourselves here to mentioning briefly the transition to the $NPT$-MC, a variant of which has been used in the present study ($N\sigma_{zz}T$-MC). In an analogous way to the transition between the more common statistical ensembles (e.g. transition from $NVT$ to $\mu VT$ requiring a large external reservoir of particles, which can be exchanged with the system of interest), a system of volume $V$ is considered as a part (subsystem) of a much larger system (volume $V_0$, with the remaining volume, $V_0 - V$, filled with $M$ ideal gas particles). Volume $V$ is allowed to fluctuate within volume $V_0$. In the limit of $V_0 \to \infty$ and $M \to \infty$, an $NPT$ ensemble for the subsystem is achieved.

In an $NPT$-MC simulation, a change of volume is considered as an additional trial move, in addition to changes in individual particle coordinates, during which *all* particle coordinates are scaled accordingly. Volume change is considered with a probability of $1/N$ to counter-balance the cost of calculating the associated energy difference. The acceptance criterion of the above 6-step scheme is modified in $NPT$-MC to accommodate for the effect of the volume change: $\Delta U_p(n \to\ m)$ now becomes $\Delta U_p(n \to\ m) + P(V_m - V_n) - Nk_bT\ln(V_m/V_n)$ [38].

### Application of Monte Carlo to clay systems

Monte Carlo simulations employed in this study were both in the $N\sigma_{zz}T$, where $\sigma_{zz}$ refers to the stress perpendicular to the clay layers, and $NVT$ ensembles. Beginning with a random distribution of $N$ interlayer species and intentionally large layer spacing, the $N\sigma_{zz}T - MC$ simulation run served to determine the equilibrium spacing for the given interlayer content and temperature. The subsequent $NVT - MC$ run was employed for further equilibration of the interlayer species, while the interlayer spacing as well as the relative horizontal shift of the adjacent clay layers was held fixed. In the $N\sigma_{zz}T - MC$ the following trial moves in the clay system were allowed (refer back to Figure 4.2 for the terminology used):

- vertical displacement of clay half-layers
- horizontal displacement of clay half-layers or central layer
- displacement of the interlayer ions
- displacement of the interlayer water molecules coupled with their re-orientation

For the $NVT - MC$ simulations, only the last two trial moves applied. The probability of carrying out any one of the trial moves at a given MC step is proportional to the inverse of the number of atoms the moves involves. In other words the trial moves concerning clay layers were carried out with a much lower probability [38]. Further technical details of Monte Carlo simulations on clay systems are available in ref [13]. In summary, the above sequence of $N\sigma_{zz}T - MC$ and $NVT - MC$ simulations on clay systems gives access to the following quantities of interest:

- equilibrium clay layer spacing for a give water content
- equilibrium distribution of interlayer atoms
- radial distribution functions: 1) between interlayer atoms only, 2) between interlayer and clay layer atoms

The evolution of these *static* properties shall be investigated in Chapter 5 as a function of temperature. Most importantly however, clay systems equilibrated by MC simulations were used as initial configurations for Molecular Dynamics simulations in order to extract dynamic properties of the system, the main point of interest here.

### 4.2.2 Molecular Dynamics simulations

The basis of Molecular Dynamics (MD) simulations is to trace the real-time evolution of individual atomic positions or atomic trajectories, $\mathbf{r}_i(t)$, in the system. As in the case of Monte Carlo, the only information needed for an MD simulation is an initial configuration of all the atoms in the system and their interacting potentials. The time-evolution of the position of each atom is then governed by the Newton's law of motion

$$\mathbf{F_i}(t) = m\frac{d^2\mathbf{r_i}(t)}{dt^2} = m\ddot{\mathbf{r}}_\mathbf{i}(t) \tag{4.2.4}$$

where $m$ is the mass of the atom and $\mathbf{F_i}(t)$ the overall force on atom $i$ by all other atoms $j$. The force is calculated from the interacting (pair) potential $U_{ij}$ according to $\mathbf{F_i} = \sum_j -\nabla U_{ij}$. Atomic trajectories are thus obtained from the integration of Equation 4.2.4 with respect to time and in a simulation this is done in a discrete way (using a finite timestep $\Delta t$) via an *approximate* integration scheme or algorithm. The most common algorithm, derived from a Taylor expansion of the atomic position around time $t$, is the so-called Verlet algorithm. Its form for the atomic positions is

$$\mathbf{r_i}(t + \Delta t) = 2\mathbf{r_i}(t) - \mathbf{r_i}(t - \Delta t) + \frac{\mathbf{F_i}(t)}{m}(\Delta t)^2 \tag{4.2.5}$$

An analogous algorithm for the atomic velocities $\dot{\mathbf{r}}_\mathbf{i}(t)$ is

$$\dot{\mathbf{r}}_{\mathbf{i}}(t) = \frac{\mathbf{r}_{\mathbf{i}}(t+\Delta t) - \mathbf{r}_{\mathbf{i}}(t-\Delta t)}{2\Delta t} \tag{4.2.6}$$

Thus an MD simulation is a series of calculations, at regular time intervals, of the overall force on each atom, its velocity and consequent propagation of its position.

Rigid bodies in MD simulations require special treatment and in the current MD program they are dealt with by a variant of the so-called SHAKE algorithm [40], which can be summarised in the following steps. For each pair of atoms involved in a bond

- atomic positions are propagated according to the Verlet (or similar) algorithm as if the bond constraint was absent.
- from the change of the bond vector, the magnitude of which is to be conserved, a constraint force is calculated. This force acts on the two atoms in opposite directions along the original bond vector and corrects the bond length.

For rigid bodies with more than two atoms, the above cycle has to be repeated in an iterative way (as adjusting one bond perturbs the neighbouring), until all bond lengths are corrected to within a specified tolerance. Contrary to a free atom, a rigid body has both translational and rotational degrees of freedom. For solving the corresponding equations of motion, a rigid body can be characterised by a center of mass (CoM) and a given orientation. Translational motion of the entire body is then described again by Verlet (or similar) algorithm, involving this time the CoM position and velocity. The case of rotational motion is somewhat more complex but routinely solvable using quaternions [40].

For a system of particles evolving according to Equation 4.2.4, the total energy $E_p + E_k$ is conserved and as such the simulation corresponds to sampling of phase space in the microcanonical ensemble (NVE). In practice, fluctuations or drifts in the total energy are observed, their degree of severity depending on the algorithm used. The criteria for a good algorithm are not straight-forward. While some properties seem necessary for energy-conservation, such as time-reversibility and area preservation (of phase space volumes), they are not sufficient. The Leapfrog algorithm (equivalent to Verlet) implemented in the DLPOLY program used here is both time-reversible, area-preserving and is known to yield sufficiently small drifts or fluctuations in the total energy, while being simple.

As mentioned previously in Section 4.2, the applicability of the microcanonical ensemble for representing real experimental conditions is limited. Two major approaches exist for the extension of MD to the commonly used $NVT$ (canonical) ensemble, known as the Andersen and Nosé-Hoover thermostats. The Andersen thermostat involves a combination of $NVE$-MD and Monte Carlo moves, which at a given time-step instantaneously transfer the system from one constant-energy shell in the phase-space to another. The distribution of the "visited" constant-energy shells is then proportional to the Boltzmann distribution at the desired temperature $T$. In case of the Nosé-Hoover thermostat, overall equations of motion are modified by incorporating degrees of freedom of the thermostat. In an analogous way to $NVE$-MD, a conserved quantity exists for these modified equations of motion.

Whereas both thermostats give static properties of the system that indeed correspond to canonical ensemble averages (in case of the Nosé-Hoover thermostat this is ensured only if the center of mass of the entire system is stationary [38]), in both cases the dynamic properties (time-correlation functions) are *not* independent of the thermostat parameters. The influence of the Nosé-Hoover thermostat is significantly weaker than of the Andersen thermostat, but still it exists. For this reason, the $NVT$-MD is used in many (though not all) cases only for equilibration purposes to a desired temperature and time-correlation functions are collected thereafter from $NVE$-MD particle trajectories. This is the case in the present study. Consequently however, fluctuations of temperature of the order of 3-4 % (about 12 K for room temperature) had to be tolerated for the current system of 220-440 atoms (excluding clay atoms as they are treated as frozen - see later), whereas for the same system size these would be of the order of 0.2-0.3 % in the $NVT$ ensemble. The instantaneous temperature is calculated from atomic velocities (or momenta) according to the equipartition theorem

$$T_{inst} = \frac{\sum_i m_i \dot{r}_i^2(t)}{k_b f} = \frac{2E_k}{k_b f} \tag{4.2.7}$$

where $k_b$ is the Boltzmann's constant and $f$ the number of degrees of freedom of the entire system.

In case of $NPT$-MD, the volume change is considered as a dynamical variable throughout the simulation, in an analogous way to the $NPT$-MC case, where a trial move consisting of a volume change is introduced (see Section 4.2.1). Technically, a conceptually similar modification of the equations of motions is applied to incorporate this volume change as is the case of the degrees of freedom of the Nosé-Hoover thermostat in $NVT$-MD [38].

As summarised in Section 4.2, MD simulations (like MC) give access to thermodynamic properties such as temperature and pressure as well as other *static* properties: local structural information, distribution functions etc. The real strength of MD is the determination of *dynamic* properties, which are completely inaccessible to MC.

We have stayed strictly within the realm of *equilibrium* MD simulations and saw the extensions of the traditional $NVE$-MD to conditions of thermal equilibrium, $NVT$-MD, or both thermal and pressure equilibrium, $NPT$-MD. Yet dynamic properties of a system such as diffusion coefficients and viscosity are all non-equilibrium properties, they characterise the response of the system to *non*-equilibrium conditions such as concentration and pressure gradients. How can we bridge the two ? The connection is provided by the *linear response theory*, according to which the response of a system to a small external perturbation is the same as a spontaneous equilibrium fluctuation [42]. The links between equilibrium particle trajectories (the outcome of MD simulations) and macroscopic dynamic properties of the system come in the form of so-called *Green-Kubo* relations, which equate macroscopic transport coefficients (such as the diffusion coefficient or viscosity) to integrals over various microscopic time-correlation functions [42] [38].

One of the most commonly extracted transport coefficients from equilibrium MD simulations is the diffusion coefficient (D). As we shall use it extensively also in this study, it deserves a more detailed treatment at this stage.

The phenomenon of diffusion is described on the macroscopic scale by [55] [38]

$$D\nabla^2 C(\mathbf{r},t) = \frac{\partial C(\mathbf{r},t)}{\partial t} \tag{4.2.8}$$

where the diffusion coefficient ($D$) appears as the constant of proportionality between the flux of particles, $\partial C(\mathbf{r},t)/\partial t$ and the spatial variation of their concentration, $\nabla^2 C(\mathbf{r},t)$. The solution to the above equation with the boundary condition $C(\mathbf{r},0) = \delta(\mathbf{r})$ is

$$C(\mathbf{r},t) = \frac{1}{(4\pi Dt)^{(d/2)}} e^{-\mathbf{r}^2/4Dt} \tag{4.2.9}$$

where $d$ is the dimensionality of the system. Using the above solution, it was originally shown by Einstein that the diffusion coefficient is related in a simple way to the mean squared displacement (MSD) of the particles, $\langle \mathbf{r}^2(t) \rangle$, as

$$\frac{\partial \langle \mathbf{r}^2(t) \rangle}{\partial t} = 2dD \tag{4.2.10}$$

This equation is the basis of the MSD method for the determination of the diffusion coefficient. In practice, $D$ is determined from the gradient of the linear part of a plot of $\langle r^2(t) \rangle$, versus time. Using the fact that particle velocity is simply the time-derivative of particle position, an equivalent relation between $D$ and the auto-correlation of particle velocity (VACF) can be derived from Equation 4.2.10 when the time-derivative is considered in the limit of $t \to \infty$. It leads to

$$dD = \int_0^\infty dt \langle \mathbf{v}(t)\mathbf{v}(0) \rangle \tag{4.2.11}$$

The above relation is the basis for the VACF method of diffusion coefficient determination, it is a standard example of the Green-Kubo formulae mentioned previously. In practice, the diffusion coefficient is determined from the integral of the velocity auto-correlation function, as the value of this integral stabilizes.

In summary, two equivalent methods are available for the determination of diffusion coefficients from equilibrium particle trajectories, the MSD and the VACF method.

### Application of Molecular Dynamics to clay systems

Molecular Dynamics simulations (DLPOLY code [40]) on clay systems were performed both in the $NVT$ and $NVE$ ensembles. The DLPOLY code implements the Leapfrog algorithm (equivalent to Verlet) for the integration of equations of motion and a variant of the SHAKE algorithm for treating the movement of rigid bodies. Using the equilibrated configuration of both clay layers and interlayer species from MC simulations as the starting point, $NVT$-MD was used for further equilibration of the system at constant temperature, thereafter particle trajectories were collected in the $NVE$ ensemble for the extraction of diffusion coefficients. Both $NVT$-MD and $NVE$-MD were performed with clay layers held as fixed (clay atoms were considered as frozen, at each time-step their positions were used in the calculation of forces exerted on other atoms, however forces on the frozen atoms themselves and their velocities were repeatedly set to zero), while motion of the interlayer species was traced.

The information of interest extracted from MD simulations for the clay systems is

- equilibrium distribution of interlayer atoms (as in MC simulations)
- radial distribution functions: 1) between interlayer atoms only, 2) between interlayer and clay layer atoms (as in MC simulations)
- ”raw” particles trajectories of interlayer species showing preferential sites with respect to the underlying clay layers
- family of time-correlation functions extracted from particle trajectories that are of interest themselves (intermediate scattering functions) or that are used directly for the determination of the macroscopic diffusion coefficient

In Chapter 5, the evolution of particle trajectories and the corresponding diffusion coefficients (determined using both the MSD and VACF method) of interlayer ions and water shall be studied as a function of temperature. Chapter 7 shall deal exclusively with the motion of interlayer water molecules. Their motion shall be characterised not only by macroscopic diffusion coefficients but above all by the corresponding intermediate scattering functions (another example of time-correlation functions - for details of calculation see Section 7.4) as these allow direct comparison to the experimentally measured signals in quasi-elastic neutron scattering experiments.

# Chapter 5

# Case Study 1: Temperature effect in clays by microscopic simulation

## 5.1 Brief review of simulation studies on clay systems

Microscopic simulations of clays have been an active field of research since the late 1980s and began with simulations at ambient temperature and pressure, of clays with various cationic species [21] [48] [23] [13]. The majority of simulation studies on clays concentrates on the static properties such as interlayer spacing as a function of relative humidity and distribution of interlayer species. In some cases dynamical information is extracted and that mostly in the form of overall diffusion coefficients. Bearing in mind that various models of water have been used as well as differing location and abundance of charges on clay layers, the simulated diffusion coefficients ($D_{sim}$) for montmorillonite clays can be summarised as follows (two-dimensional values quoted, see next section for further details): monovalent counterions ($Na^+$, $Cs^+$) in monohydrated systems, $D_{sim}^{ions}$= 0.2-2.5 $\times$ $10^{-10}m^2s^{-1}$, $D_{sim}^{water}$= 1.7-7.0 $\times$ $10^{-10}m^2s^{-1}$, in bihydrated systems, $D_{sim}^{ions}$= 3.7-10 $\times$ $10^{-10}m^2s^{-1}$, $D_{sim}^{water}$= 12-15 $\times$ $10^{-10}m^2s^{-1}$ [13] [56] [57].

Viewing previous publications on microscopic simulation of clay systems, two major approaches are found: simulation in either the $N\sigma_{zz}T$ or the $\mu VT$ ensemble. Considering that the experimental reality for the clay system is best represented in a $\mu\sigma_{zz}T$, by choosing the $N\sigma_{zz}T$ approach we have introduced an additional unrealistic constraint in terms of the fixed number of particles in the system. In the $\mu VT$ ensemble, fixed volume is introduced instead. We do not consider either of the ensembles to be more appropriate in imitating the reality. The $N\sigma_{zz}T$ has been chosen due to its significantly greater technical simplicity. In addition, the temperature range studied has been adapted to correspond to temperatures under which the low-hydration states of montmorillonite can be considered as reasonably stable, i.e. not subject to dehydration (see Section 3.3).

## 5.2 Systems and Conditions of interest

In the domain of microscopic simulations of clays, several studies appeared more recently dealing with non-ambient conditions (increased temperatures and pressures), which are primarily linked to the issue of storage of radioactive waste or bore-hole stability. Attention has been drawn to the particular temperature and pressure to which clay systems are subjected underground. Simultaneous geothermal and geostatic gradients have been considered, in addition to the presence of small organic molecules such as methane, corresponding to the conditions in sedimentary basins up to the depths of a few kilometers [58] [34]. Apart from simulation, X-ray and neutron diffraction studies have given important information on the stable hydration states as well as structure of the pore-fluids under these temperature and pressure gradients [59] [33] [35].

The conditions we present here aim to decouple the effect of pressure and temperature and focus on the latter in the range of approximately 0 °C to 150 °C, under pressure of 1 bar. On a fundamental level, this provides useful information into the temperature effect on a fluid confined in a plane. Also, as mentioned previously, this temperature range was chosen to overlap with the predictions of the long-term temperature evolution of a clay barrier surrounding the site of radioactive waste as considered by ANDRA in France [4]. While the choice of constant (ambient) pressure throughout this study singles out the temperature effect on the clay system, in the underground storage scenario this will not necessarily be the case. In the current absence of detailed pressure data near the waste site (site about 500 m beneath the Earth's surface with clays in a highly compacted form), the present constant-pressure study is therefore to be treated as a first step in the modelling of this system of significant complexity.

In the next sections we present the results of both Monte Carlo and Molecular Dynamics simulations of Na- and Cs-montmorillonites in low hydration states, in particular Na-montmorillonite in both mono- and bihydrated state, Cs-montmorillonite in monohydrated state only. Based on a previous series of simulations, we defined the simulated mono- and bilayer state as corresponding to 6 and 12 water molecules per cation respectively, as these water contents reproduce the experimentally observed (X-ray diffraction) interlayer spacing for the given states [13].

## 5.3 Simulation Details

MC simulations in the $N\sigma_{zz}T$ ensemble, where $\sigma_{zz}$ refers to the stress perpendicular to the clay layers, were employed to equilibrate the system. For a given interlayer cation and hydration state, a series of MC simulations at a fixed value of $\sigma_{zz}$ (1 bar = $10^5$ Pa) and a given temperature from the range 273 K to 420 K (0 °C to 150 °C) was carried out. Information extracted from MC simulations is related to static properties only. We concentrated on the effect of temperature on the interlayer spacing and on the distribution of water and cations in the interlayer.

Further, equilibrated configurations from MC simulations were used as initial configurations in MD runs. After a further equilibration by MD in the $NVT$ ensemble (total simulation length: 50 ps, time step: 0.001 ps, Nosé-Hoover thermostat with time constant 0.5 ps), particle trajectories were collected in the $NVE$ ensemble. Simulations in the $NVE$ ensemble intended for the the determination of diffusion coefficients by the MSD method were 360 ps in length, with $t_{\text{step}}$ = 0.001 ps and time between recorded configurations ($t_{\text{dump}}$) = 0.02 ps. Graphs of MSD versus time gave linear dependence in the region of 50 ps to 150 ps. This is therefore the time domain corresponding to the diffusion coefficients from the current MSD analysis. For the VACF method, the interval between recorded configurations ($t_{\text{dump}}$) is governed by the rate of decay of the velocity autocorrelation function. Here, $t_{\text{dump}}$ had to be decreased to 0.002 ps in order to sample the function sufficiently. Simulations intended for VACF analysis were thus 36 ps in length with $t_{\text{step}}$ = 0.001 ps and $t_{\text{dump}}$ = 0.002 ps. The current VACF analysis gives information about diffusion coefficients on the time scale of less than 20 ps.

Due to the anisotropy of the system, components of the atomic displacements and velocities along the three principal axes in the simulation box ($x$ and $y$ in the plane of the clay layers, $z$ perpendicular to the clay layers) were considered separately. Two-dimensional diffusion coefficients in the plane of the clay layers ($xy$) were calculated as the average of one-dimensional diffusion coefficients in the $x$ and $y$ directions.

## 5.4 Temperature effect on static properties

Interlayer spacing in the temperature range considered shows variation of the order of 0.2-0.3 Å for all three systems studied (Figure 5.1). Density of water phase varies between 0.98-0.99 gcm$^{-3}$ (0 °C) and 0.94-0.95 gcm$^{-3}$ (100 °C) (for reference the density of bulk water varies from 0.999 gcm$^{-3}$ (0 °C) to 0.958 gcm$^{-3}$ (100 °C) [60]). In the calculation of density, the volume available to water molecules in the confined systems was estimated by subtracting the volume occupied by the surface oxygen atoms and the interlayer ions from the total volume of the interlayer. X-ray diffraction study on Na-montmorillonite at temperatures up to 363 K showed only very small changes in the interlayer spacing, in agreement with the data presented here [61].

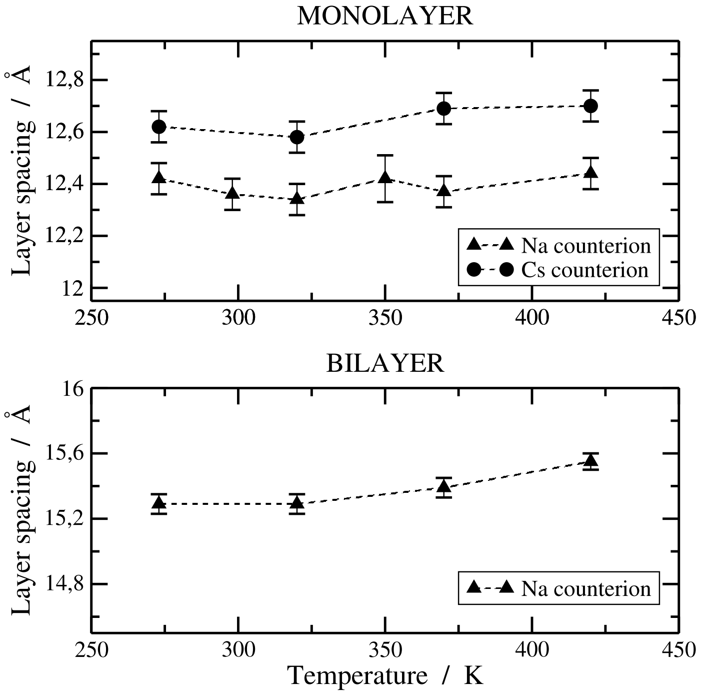

**Figure 5.1: Temperature dependence of interlayer spacing.**

The monohydrate counterion distributions in the interlayer at low temperatures are in agreement with other studies at ambient temperature on a clay with octahedral substitutions only [62] [13]. Two peaks, equidistant from the middle of the interlayer, are observed in case of $Na^+$ (Figure 5.2), a single peak in case of $Cs^+$ (not shown), rationalised previously on the basis of the greater size of $Cs^+$ counterions [51]. For Na-bihydrate, counterion distribution shows a large central peak and side peaks near the clay surface (not shown). Variation in temperature has a small effect on the distribution profiles. Their main features (number and position of peaks) remain the same. The fact that the position of counterions is not strongly influenced by temperature is at first sight surprising. For hydrated systems, ionic profiles in the vicinity of a charged surface depend on the dielectric constant of the solvent, which in turn varies with temperature. However, for the low hydration states studied here, the solvation and ion-clay interactions define predominantly the ionic profiles in these confined systems while the temperature effect is secondary. Smearing in the profiles of the constituent atoms of water as temperature increases is seen, suggesting more disorder in the water phase, as expected.

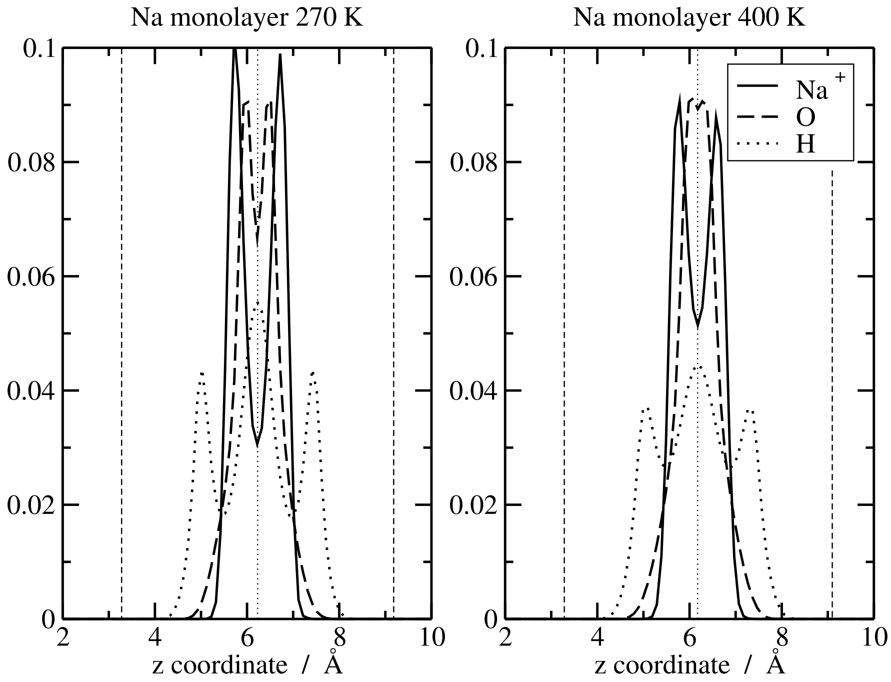

**Figure 5.2: Na monohydrated system, profiles of interlayer atoms ($Na^+$ ion, oxygen atom of water and hydrogen atom of water) along axis perpendicular to clay layers (z axis).**
**Vertical lines indicate position of the topmost oxygen atoms in the clay layers (dashed line) and middle of interlayer (dotted line).**

Orientations of water molecules in the interlayer with respect to the clay layers were found to be strongly biased toward lying in a plane perpendicular to the clay layers with their dipole moment at an angle less than 45 ° from direction parallel to the layers. Evidence for this configuration in case of clays with octahedral substitutions has been provided by IR spectroscopy [15] as well as microscopic simulations [56].

In the following discussion of radial distribution functions ($g_{\mathrm{A-B}}$) we highlight cases where new peaks appear as a function of temperature. Unless stated otherwise, main features of these functions are the same as those reported for the same system at ambient temperatures by Marry et al [13]. The peak positions quoted were reproducible to 0.1 Å. The difficulties of normalisation (assuming isotropic densities) and interpretation of conventional radial distribution functions used in case of inhomogeneous systems have been pointed out previously [63]. In the following section, structural information is based on the analysis of simulation snapshots, which help to partially rationalise the radial distribution functions themselves.

For all systems, no significant shifts in principal peak positions in $g_{\mathrm{Owater-Owater}}$ and $g_{\mathrm{Owater-Hwater}}$ were seen. However, for $\mathrm{Na}^+$ counterion, $g_{\mathrm{Owater-Owater}}$ feature the principal peak at 2.8 Å with a shoulder at 3.2 Å (Figure 5.3). The shoulder is more pronounced in the bihydrated system resolving into a separate peak at 3.2-3.3 Å with additional minimum at 5.5 Å appearing, separating two peaks at 4.9 Å and 6.0 Å (Figure 5.3). The shoulder at 3.2-3.3 Å has been observed previously in some studies at ambient temperature [13] but was not as obvious in others [62] [56].

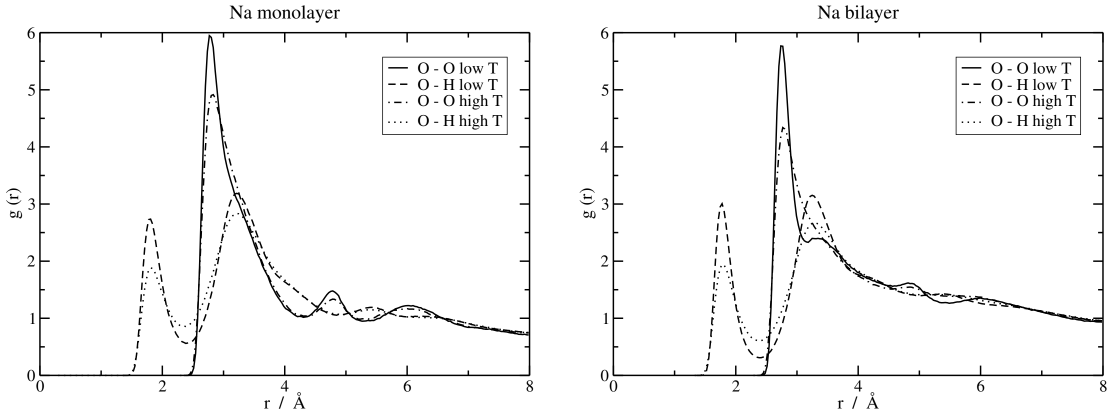

**Figure 5.3: Radial distribution functions between constituent atoms of water for Na-monolayer (left) and Na-bilayer (right).**
**Isotropic density of the atoms involved was assumed in the calculation of the RDF functions. Low temperature corresponds to 270 K, high temperature to 400 K.**

A square model for the first hydration shell of 4 water molecules surrounding the $\mathrm{Na}^+$ ion in the monohydrated system suggests an explanation for the extra features in the $g_{\mathrm{Owater-Owater}}$ in comparison to bulk solution (shoulder at 3.2 Å and extra peak at 4.8 Å) (Figure 5.3 left) [13]. A planar configuration of 4 water molecules in the monohydrated system has already been predicted by simulation [21] [64]. It is essentially the geometrical restriction that disables the formation of a 6-coordinate hydrated ion, even if 6 water molecules per ion are available. Planar 4-coordinate hydrated ions have been observed by Electron Spin resonance for smectites with transition metals such as $Cu^{2+}$ [15]. At first sight, the existence of a 4-coordinate planar complex in case of transition metal ions such as $Cu^{2+}$ is perhaps more obvious than for $Na^+$ ions. However, in case of the $Cu^{2+}$ clay, the 4-coordinate hydrated ion is an intermediate step in the formation of a 6-coordinate hydrated ion when additional layers of water are present between the clay layers [15]. A similar behaviour is therefore considered in the case of $Na^+$.

In case of the bihydrated Na system, octahedral configuration of 6 water molecules around an $Na^+$ ion does not satisfactorily explain the features in $g_{\mathrm{Owater-Owater}}$ (Figure 5.3 bottom). $Na^+$ has a lower hydration energy than the bivalent $Cu^{2+}$ ion [15] and thus a less well-defined octahedron of water molecules is likely. No clear experimental evidence is available for the increased structuring of the water phase in the bihydrated Na-montmorillonite as temperature decreases to around 273 K. Neutron diffraction studies suggest overall that water in this hydration state is rather bulk-like [65], but do not rule out significant perturbation of the hydrogen bonding network [66]. Computer simulations in general suggest greater deviation from the bulk-like structure [56].

In summary, within the static properties of the system, temperature in the given range has a very small effect on the interlayer spacing and the distribution of species in the interlayer. More disorder in the water phase, seen as smearing out of the distribution functions, is observed but number and relative positions of the peaks remain intact. Radial distribution functions confirm that it is only the structure of the water phase and its bonding to the clay surface that change significantly with temperature, however it is recognised that the description in terms of radial distribution functions intended for isotropic systems is not ideal in the case of clays. Even though the SPC/E water model has been validated over the whole temperature range considered (for bulk water), the rigidity of clay layers and water, as well as the classical pair potential pose a limitation to obtaining details of the structural changes occurring in reality. At the same time, the relatively low temperatures studied are unlikely to affect the structure of the clay itself, the clay model used has been subjected in previous simulation studies to temperatures (and pressures) significantly higher than in this work [58] [34].

## 5.5 Temperature effect on dynamic properties

Diffusion coefficients were determined from MD simulations in the $NVE$ ensemble (average of 3 simulations for the MSD analysis and 6 simulations for VACF analysis). In the $NVE$

ensemble, we experienced fluctuations of temperature of approximately 12 K (system size: 220-440 atoms, excluding clay layer atoms as they are considered as frozen - see Section 4.2.2). Problems were encountered with drifts of average temperature in the transition from $NVT$ to $NVE$ simulations. In the following discussion we quote the actual average temperature measured in the $NVE$ ensemble, rather than the equilibration temperature from the initial $NVT$ simulation. For the Na systems, the clay layer arrangement used in the MD simulations was taken from the final arrangement of the MC equilibration without further modification. For the Cs system, a preferential face-to-face arrangement was consistently used ([13]), in order to single out the dependence of diffusion on temperature only.

In MSD analysis mean squared displacement along the $z$ axis tended to a constant and could not be easily fitted to a straight line. In case of VACF, the integral along $z$ yielded values an order of magnitude smaller than in the $x$ and $y$ directions. This shows clearly the confinement of the system in the $z$ direction. Rigorously, for long times, the diffusion coefficient along $z$ should be zero. In both methods, the data for $x$ and $y$ directions were used on their own to determine 2D diffusion coefficients of cations and water molecules (based on data for oxygen atoms) in the $xy$ plane, the plane of the clay layers.

Diffusion coefficients as a function of temperature are summarised in Figures 5.4 to 5.8. Horizontal error bars in Figures 5.4 and 5.6 are shown for a single data set only, but apply equally to the other data sets. Concerning the values for ions, they are based on the trajectories of 12 particles and thus are subject to greater uncertainty than values for water molecules (72 or 144 particles). Especially for low temperatures, MSD curves for ions showed deviations from the expected linear behaviour in the time-range of 50 ps to 150 ps. Trajectories featured in Figure 5.5 to 5.7 correspond to the simulations intended for MSD analysis. Entire trajectories trace the motion of the species over approximately 360 ps with successive readings corresponding to time interval of 0.02 ps. Trajectories presented correspond to the highest and lowest temperatures that were studied for each system. Overall, each system was simulated at at least three different temperatures in the range chosen.

It is understood that the details of the motion of ions and water depend on the chosen model of the clay. At present, the corresponding experimental data (at non-ambient temperature) is not available, however comparison to ambient experimental data is made, where available.

Simulated diffusion coefficients for $Na^+$ and $Cs^+$ ions are of the order of $10^{-10}m^2s^{-1}$ and increase by an order of magnitude over the temperature range studied. A clear difference is observed in the modes of diffusion for the two ions. At both low and high temperature,

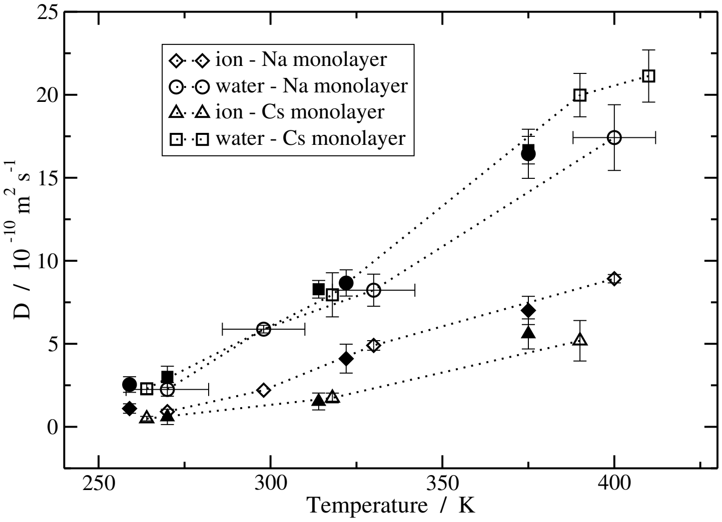

**Figure 5.4: 2D diffusion coefficients for interlayer ions and water in monohydrated systems**
**Long-term diffusion (empty symbols, obtained by MSD) and short-term diffusion (full symbols, obtained by VACF).**

$Cs^+$ ions exhibit a site-to-site jump diffusion, between sites allowing coordination to 3 oxygen atoms from each of the two adjacent clay layers, referred to as the trigonal sites (Figure 5.5 : $xy$ projections). Overall the coordination number of the ions with respect to oxygen atoms of clay only is therefore 6. Together with the oxygen atoms of water, this brings the overall coordination of the $Cs^+$ ions to approximately 12, higher than the bulk value of 9. This applies to the configuration of the clay layers where the number of the 6-coordinate sites with respect to oxygen atoms of clay is maximised as the layers are face-to-face (Figure 5.5, 2nd column). Additional simulations were carried out for a configuration of clay layers closer to the one in Figure 5.5, 3rd column, in which the number of the 6-coordinate sites decreases to a half and the sites are now further apart. Clear preference of $Cs^+$ ions for these sites over simple trigonal sites on one layer only was seen even at high temperatures with a longer residence time in each 6-coordinate site. This is likely to lead to a variation in the overall diffusion coefficient as a function of the clay layer arrangement. No clear site-to-site diffusion is observed for the $Na^+$ ion, which suggests yet again the greater importance of the clay-ion interaction in case of the $Cs^+$ ion, however variation of the diffusion coefficient as a function of the clay layer arrangement has been seen for both systems [13].

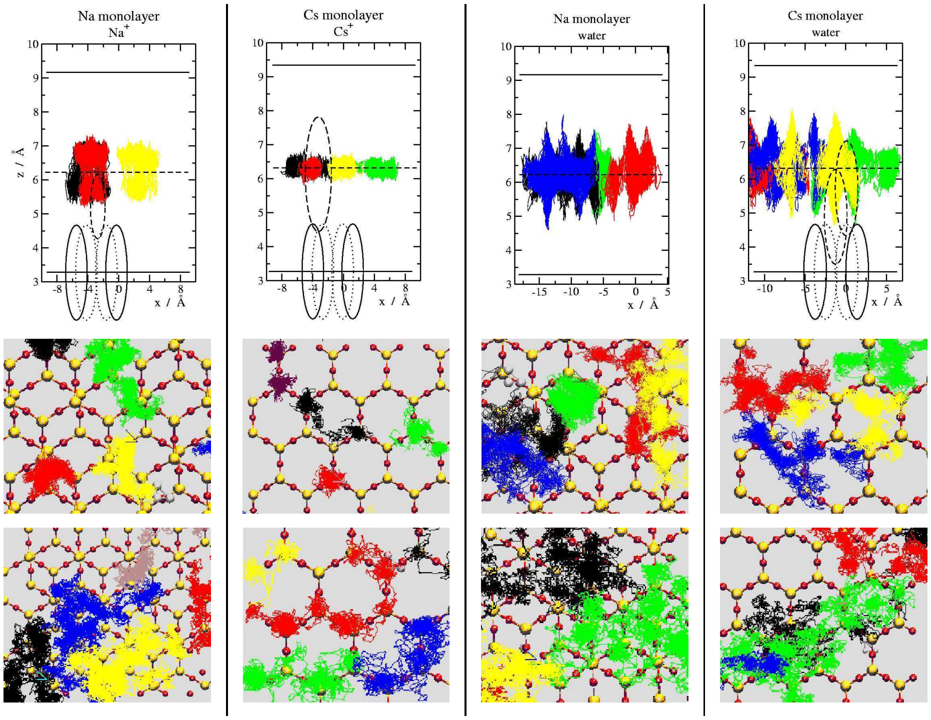

**Figure 5.5: Na and Cs monolayer systems, trajectories of ions and water. Each column corresponds to species indicated. First row: projections *xz* at low temperature; second row: projections *xy* at low temperature; third row: projections *xy* at high temperature. A particular colour corresponds to the same particle in the first and second row, but *not* in the third row. Low temperature stands for 260 K (Cs system) and 270 K (Na system). High temperature stands for 390 K (Cs system) and 400 K (Na system). Ellipses in the graphs of the first row represent oxygen atoms of clay surface and interlayer ions as described in the text. In the second and third row, clay layers on either side of the interlayer are shown (yellow atoms - Si, red atoms - O) together with the trajectories of the interlayer species.**

In the *xz* projections in Figure 5.5 oxygen atoms of the clay layer and the interlayer ions are represented by ellipses based on Pauling radii (1.4 Å for $O^{2-}$, 0.95 Å for $Na^+$ and 1.69 Å for $Cs^+$ ). Full ellipses correspond to two oxygen atoms on opposite sides of a hexagonal cavity, whereas dotted ellipses show oxygen atoms of the same cavity but in a plane further back. If an ion (dashed ellipse) is located in the middle of the cavity, it is in the same $xz$ plane as the front two oxygen atoms (full ellipses). With the help of this scheme, it is clear from the $xz$ projections of the ionic trajectories, that neither of the ions enters significantly into the hexagonal cavity. The $Cs^+$ ion is restricted to the 6-coordinate sites described above while the $Na^+$ ion even if above the hexagonal cavity does not enter. This is due to the presence of its hydration shell as has been observed experimentally by infrared spectroscopy [20].

In the context of other simulation studies, the calculated ionic diffusion coefficients are consistent with ambient temperature simulation of Marry et al [13]. The marginally lower diffusion coefficient in the case of the $Na^+$ ion is within the variation caused by the clay layer arrangement. In this study, the same interaction potentials were used as well as the SPC/E model of water. Chang et al [56] report values for $Na^+$ counterion of the order of $10^{-11}\mathrm{m}^2\mathrm{s}^{-1}$ in simulations with the MCY model of water and clay with both octahedral and tetrahedral substitutions. The preferential sites for the $Cs^+$ ions described here have been observed previously [13] [49]. Evidence from nuclear magnetic resonance suggests more than one type of possible sites for $Cs^+$ ions, reaching 9- to 12-coordinate sites for dehydrated samples [67].

Experimental diffusion coefficients available for cations in clays come mainly from tracer experiments and give values of diffusion coefficients at ambient temperatures of the order of $10^{-16}$ to $10^{-12}$ $\mathrm{m}^2\mathrm{s}^{-1}$. The difficulties encountered in the comparison of tracer experiments and microscopic simulations have been discussed previously [68], the main problem arising from the different timescales involved. Inhomogeneity of the pore size, finite size of clay layers and tortuousity in the real samples has to be taken into account to link the microscopic description to macroscopic observations [69].

The behaviour of the water phase as a function of temperature is similar for the two ions in the monohydrated state. As in the case of the ions the diffusion coefficient increases by an order of magnitude over the temperature range studied (Figure 5.4). From the $xz$ projections in Figure 5.5, it can be seen that water molecules, unlike the ions, enter into the hexagonal cavities of the adjacent clay layers. However, in the plane of the clay layers, the diffusion is rather delocalised as in the case of $Na^+$ ion, though some trajectories show the underlying hexagonal pattern (both Na and Cs system at high temperature - green trajectories).

In light of other studies, diffusion coefficients of water for the monohydrated systems agree well for the case of $Cs^+$ ion with ambient data in ref [13], as comparison is made with the same clay layer arrangement. For the Na system the inferior values reported in the same reference (2.25 to 2.7 $\times$ $10^{-10}\mathrm{m}^2\mathrm{s}^{-1}$ for 2D diffusion) are most probably due to the difference in the clay layer arrangement. Simulated water diffusion coefficients at ambient temperature for Cs-monohydrate by Sutton et al [57] are 17.52 +/- 0.06 × $10^{-10}$m$^2$s$^{-1}$ for a hydration state of 3.5 molecules of water per cation (approximately half a monolayer in our classification), MCY model of water and clay with both octahedral and tetrahedral substitutions. Direct comparison with this system is difficult, the value is nevertheless surprisingly high in light of our results. (We have quoted here the value reported in ref [57] multiplied by a factor of 3/2 to convert from 3D to 2D diffusion coefficient. The 3D diffusion coefficient is an average of all three 1D diffusion coefficients (equation 4.2.10), along the $x$, $y$ and $z$ axes. The 2D diffusion coefficient is an average of only two values, 1D diffusion coefficients along the $x$ and $y$ axes. If the displacement, $\langle r^2(t)\rangle$, along the $z$ axis is zero as in our confined system, the above averages corresponding to 3D and 2D diffusion coefficients differ exactly by a factor of 3/2.)

Data from VACF analysis, based on 36 ps simulations, refer to short-term diffusion, whereas values from MSD analysis (simulation time of 360 ps) to long-term diffusion. Figure 5.4 therefore compares diffusion coefficients obtained for long times (characteristic time 100-150 ps, empty symbols) and short times (characteristic time 5-15 ps, full symbols) for the monohydrated systems. Taking the example of $Cs^+$ ion in Cs-monohydrate, we note that at low temperature, both methods analyse motion within a single bound site, such as the ones shown in the $xy$ projection of the trajectories. In other words the simulation time is comparable to the residence time in a single site. As diffusion coefficients are formally defined in the limit of infinite time, we recognize that in the cases when residence time in a single site is comparable to the simulation time, a long-term tail in the motion of the particles (site-to-site movement) is not seen by the simulations and thus the simulated diffusion coefficient is an underestimate of the value defined formally. Considering the diffusion coefficients from both techniques employed, there is evidence for a slightly slower increase in the diffusion coefficients for the $Cs^+$ ion compared to the $Na^+$ ion as a function of temperature. At the same time, the water phase in the two systems exhibits a very similar behaviour.

Comparing the 2D diffusion coefficients of the ions and water in the Na-bihydrate and bulk system (Figure 5.6), we observe that absolute values of the coefficients are of the same order of magnitude. At the same time, the temperature activation in the clay system is still lower than for the bulk. Quasi-elastic neutron scattering study of water in bihydrated Na-vermiculite [72] has provided evidence for the approach of water diffusion to that of bulk in the bihydrated systems.

For the diffusion of the ion, clear difference is seen from the $xz$ projections of the trajectories as a function of temperature (Figure 5.7). Exchange between sites in the middle of the interlayer and sites closer to the clay layer occur one or two times during

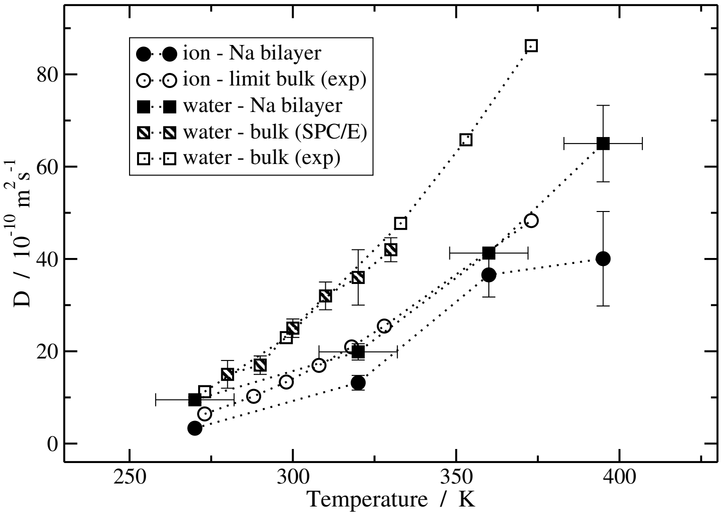

**Figure 5.6: 2D diffusion coefficients for interlayer ions and water in Na-bihydrated system.**
**Comparison to bulk water (both experimental data [70] and data from SPC/E model [71]) and Na$^+$ ion at infinite dilution (experimental data). Data for bulk system are the corresponding 3D values.**

360 ps at low temperature, whereas numerous jumps are observed at high temperatures. As expected, the underlying hexagonal pattern of the layers has minimal influence on the trajectories, as the ions are screened from the clay surface by a layer of water. High degree of delocalisation is seen at high temperatures. Water phase in the bihydrated system is located to the sides of the central plane of the ions. From the *xz* projection, the water phase explores the hexagonal cavities of the underlying clay layers and moves with ease to the opposite side of the interlayer even at low temperature.

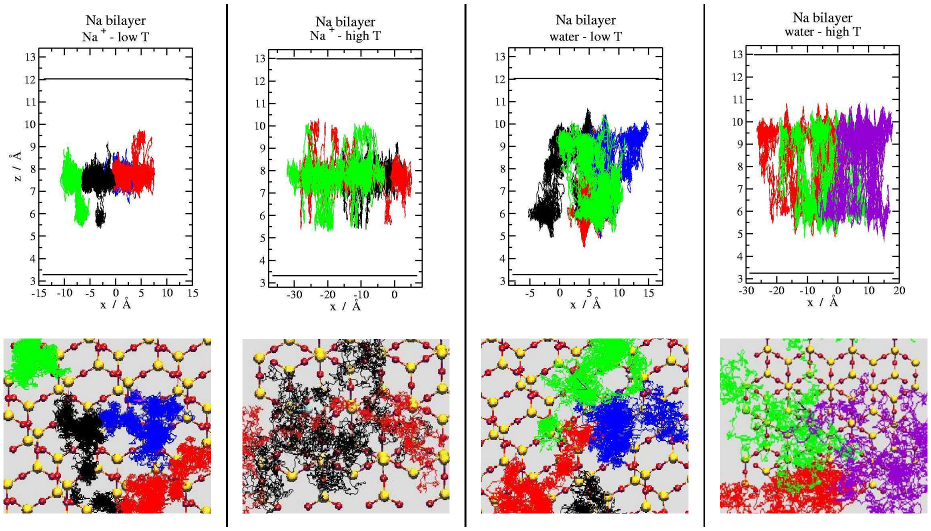

**Figure 5.7: Na bilayer system, trajectories of ions and water.**
**First row: $xz$ projection; second row: $xy$ projection. Each column corresponds to one type of species, from left to right: ions at low temperature, ions at high temperature, water at low temperature, water at high temperature. Low temperature stands for 270 K and high temperature for 400 K. In each column a particular colour corresponds to the same particle in the two projections. Further details as for Figure 5.5**

Figure 5.8 summarises the diffusion of water in the three systems studied and features also experimental data for bulk water as a reference. Arrhenius plot was used to yield approximate energies of activation, which were 12-15 kJmol$^{-1}$ for the monohydrated systems and 14-19 kJmol$^{-1}$ for the Na-bihydrate. These values are of the same order of magnitude as the activation energy for bulk water (18 kJmol$^{-1}$). More detailed comparison with the value for bulk water is difficult as the process of diffusion is very different in the confined systems of clays and the bulk liquid.

In summary, ion diffusion in the Cs system shows clear site-to-site jump diffusion throughout the whole temperature range considered, whereas the Na$^+$ ion does not possess clear preferential sites even at low temperature. The behaviour of the water phase is similar for the two monohydrated systems. The change to the bihydrated Na system is a large step toward bulk behaviour. Diffusion coefficients of the water phase in the bi-hydrated state are of the same order of magnitude as in bulk water, though they increase more slowly as temperature is raised.

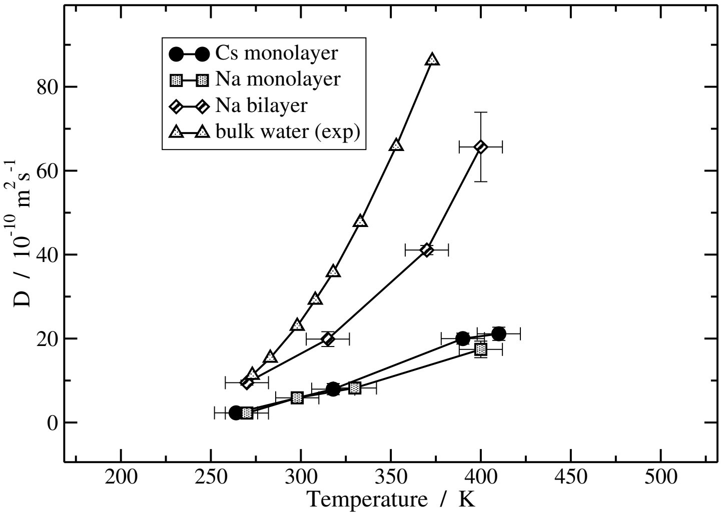

**Figure 5.8: 2D diffusion coefficients of water in the 3 confined systems studied together with experimental data for bulk water (3D values).**

## 5.6 Conclusion

We conclude that temperature variation in the range 0 °C to 150 °C affects mainly the structure of the water phase among the static properties. The $Na^+$ and $Cs^+$ ions show very different modes of diffusion in the monohydrated system. The site-to-site jump diffusion of the $Cs^+$ ion is retained up to high temperatures and contrasts with the absence of clearly defined sites for the $Na^+$ ion even at low temperatures. The fact that the site-to-site jump diffusion of these ions persists up to high temperatures is an important measure, albeit qualitative for the moment, of the affinity of $Cs^+$ ions for the trigonal sites in the model used. More detailed analysis of the residence times of the water molecules in the hydration shells of the respective ions is necessary to answer questions such as whether the $Cs^+$ jumps from one 6-coordinate site to another with a complete or partial loss of its hydration shell. Neither of the ions is seen to enter into the hexagonal cavities. It is generally agreed that in the case of $Na^+$, the presence of a hydration shell increases its effective radius above the dimension of the cavity. Throughout our study we have confirmed that especially for the monohydrated systems the ionic and water diffusion is dependent on the clay layer arrangements to either side of the interlayer and this needs to be decoupled from other parameters such as temperature, as has been attempted here for the Cs system.

The water phase shows very similar dynamics in the two monohydrated systems studied and approaches bulk behaviour in the Na-bihydrate system. On the basis of the results presented, a detailed quantitative comparison of the temperature activation of diffusion for a 2D water phase in the clay and bulk water (3D) is possible.

A hetereionic montmorillonite system (one $Cs^+$ ion per five $Na^+$ ions), has been already studied at ambient temperature [68]. Such a system was supposed to imitate low radionuclide concentration in a clay barrier containing natural $Na^+$ ions. This study concluded that water phase in the system is not perturbed by the presence of the $Cs^+$ ions and behaves as in the pure Na system. As far as the ions were concerned, they retained the characteristics of the homoionic counterparts. It is not unlikely that this trend of independent $Cs^+$ and $Na^+$ diffusion is retained at higher temperatures, each ion continuing to exhibit its characteristic mode of motion.

# Chapter 6

# Experimental Techniques

## 6.1 Neutron scattering

Neutron scattering as a technique for probing atomic and molecular motion is based on the analysis of momentum and energy transfer occurring during a neutron - atomic nucleus interaction. In this interaction the wave-particle duality of the neutron has to be considered. Neutron can be described both as a classical particle with momentum $\mathbf{p} = m\mathbf{v}$, where $m$ is the neutron mass and $\mathbf{v}$ the velocity, as well as a wave with momentum $\mathbf{p} = \hbar\mathbf{k}$ and $|\mathbf{k}| = (2\pi)/\lambda$, where $\lambda$ is the associated wavelength and $\mathbf{k}$ the wavevector of the neutron. For both cases the corresponding neutron energy $E$ is

$$E = \frac{p^2}{2m} = \frac{1}{2}mv^2 = \frac{\hbar^2 k^2}{2m} \tag{6.1.1}$$

There exists both a spatial and energetic (temporal) match between the wavelength and energy of neutrons and the characteristic length- and time-scale of atomic motion in condensed and soft matter. In broad terms, this match is found between cold neutrons (T $\simeq$ 25 K, E $\simeq$ 2 meV) and atomic translational, rotational motion all the way to thermal neutrons (T $\simeq$ 300 K, E $\simeq$ 26 meV) and atomic vibrations [73] [74].

On an interaction with a nucleus, a neutron is scattered *isotropically* and the process can be characterised by a single parameter called the *scattering length.* This parameter can be complex, with the imaginary part representing absorption. For the current purposes we deal only with the real part of the scattering length (here referred to as $b$) and assume that it dominates over the imaginary part and does not vary with the neutron energies considered [75]. The real part of the scattering length varies with the nucleus of every element, but also with the element's isotope and the coupling between the spin states of the nucleus and the incoming neutron. Considering these variations in $b_i$ we define the coherent ($b_{coh}$) and incoherent ($b_{inc}$) scattering length *for each element i* as

$$b_{coh} = \overline{b_i} \tag{6.1.2}$$

$$b_{inc} = \sqrt{\overline{b_i^2} - \overline{b_i}^2} \tag{6.1.3}$$

where the notation $\overline{x}$ denotes the average of quantity $x$. The above two quantities are fundamentally different. Whereas the coherent scattering length describes by itself a system in which all the isotope and spin fluctuations for a single element are smeared out, the incoherent scattering length is composed of exactly these fluctuations. In the absence of theory of nuclear forces, the above scattering lengths remain empirically measured quantities [76] [77].

As shall be shown, all the spatial and temporal information about motion of the scattering atoms is contained in 1) the variation of the scattered neutron intensity as a function of the scattering angle and 2) the variation of the *energy distribution* of scattered neutrons as a function of the scattering angle.

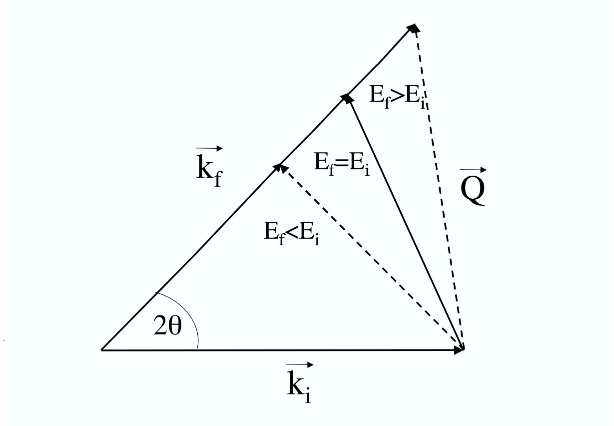

**Figure 6.1: Representation of a neutron scattering process in the reciprocal space.**

**Incident neutron and neutron scattered at an angle $2\theta$ are characterised by the wavevectors $\mathbf{k}_i$ and $\mathbf{k}_f$ respectively. Elastic scattering (green scattering wavevector Q, $|\mathbf{k}_i| = |\mathbf{k}_f|$, zero energy transfer) and quasi-elastic scattering (red scattering wavevectors Q, $|\mathbf{k}_i| \neq |\mathbf{k}_f|$, non-zero energy transfer) is shown.**

Considering incident and scattered neutrons as waves with characteristic wavevectors, neutron scattering process can be represented in the space of these wavevectors (reciprocal space) as shown in Figure 6.1. As seen from this Figure, neutrons scattered at a given angle $2\theta$ result from scattering processes differing in *both* momentum and energy transfers, which are calculated according to

$$\Delta\mathbf{p} = \hbar\mathbf{Q} = \hbar(\mathbf{k_f} - \mathbf{k_i}) \tag{6.1.4}$$

$$\Delta E = \hbar\omega = E_i - E_f = \frac{\hbar^2}{2m}(k_i^2 - k_f^2) \tag{6.1.5}$$

where $E$ and $\mathbf{k}$ are defined as before, subscripts $i$ and $f$ correspond to the initial and final neutron states, $\mathbf{Q}$ is the so-called scattering wavevector and $\omega$ the energy transfer in units of $\mathrm{s}^{-1}$.

The number of neutrons scattered per second into a small solid angle $d\Omega$ in a given direction (defined by two angles with respect to the incident beam direction) with final energies between $E_f$ and $E_f + dE_f$ and normalised by the incident neutron flux is referred to as the *partial differential cross-section*, $(d^2\sigma)/(d\Omega dE_f)$ [77]. Scattering theory, departing from the quantum-mechanical description of the neutron - nucleus interaction leading to energy-momentum transfer, gives the following expression for the above cross-section

$$\frac{d^2\sigma}{d\Omega dE_f} = \frac{k_f}{k_i}\frac{1}{2\pi\hbar N}\sum_{jj'}\overline{b_{j'}b_j}\int_{-\infty}^{+\infty}\langle e^{i\mathbf{Q}\cdot\mathbf{R}_{j'}(t)}e^{-i\mathbf{Q}\cdot\mathbf{R}_j(0)}\rangle e^{-i\omega t}dt \tag{6.1.6}$$

where $N$ is the number of scattering nuclei (scatterers) in the sample, $\mathbf{R}_{j'}(t)$ and $\mathbf{R}_j(0)$ are the positions of the scatterers, $t$ is time and other quantities are defined as before. According to the definition of the coherent and incoherent scattering lengths (Equations 6.1.2 and 6.1.3), the partial differential cross-section can be re-expressed as

$$\begin{aligned}\frac{d^2\sigma}{d\Omega dE_f} &= \frac{k_f}{k_i}\frac{1}{2\pi\hbar N}{b_{coh}}^2\sum_{jj'}\int_{-\infty}^{+\infty}\langle e^{i\mathbf{Q}\cdot\mathbf{R}_{j'}(t)}e^{-i\mathbf{Q}\cdot\mathbf{R}_j(0)}\rangle e^{-i\omega t}dt + \\ &+ \frac{k_f}{k_i}\frac{1}{2\pi\hbar N}{b_{inc}}^2\sum_{j}\int_{-\infty}^{+\infty}\langle e^{i\mathbf{Q}\cdot\mathbf{R}_{j}(t)}e^{-i\mathbf{Q}\cdot\mathbf{R}_j(0)}\rangle e^{-i\omega t}dt\end{aligned} \tag{6.1.7}$$

thus consisting of the coherent scattering arising from pair correlations between positions of nucleus $j$ at time 0 and different nuclei (including nucleus $j$) at time $t$ and incoherent scattering arising from position correlation of the *same* nucleus at different times [77] [76].

The time correlation parts of Equation 6.1.7 are referred to as the *intermediate scattering functions*, $I(\mathbf{Q}, t)$. More precisely

$$I_{coh}(\mathbf{Q}, t) = \frac{1}{N}\sum_{jj'}\langle e^{i\mathbf{Q}\cdot\mathbf{R}_{j'}(t)}e^{-i\mathbf{Q}\cdot\mathbf{R}_{j}(0)}\rangle \tag{6.1.8}$$

$$I_{inc}(\mathbf{Q}, t) = \frac{1}{N}\sum_{j}\langle e^{i\mathbf{Q}\cdot\mathbf{R}_{j}(t)}e^{-i\mathbf{Q}\cdot\mathbf{R}_{j}(0)}\rangle \tag{6.1.9}$$

In Equation 6.1.7 we consider the *temporal* Fourier transform of the intermediate scattering functions called the *scattering functions* or also the *dynamical structure factors*, $S(\mathbf{Q}$,$\omega)$,

$$S(\mathbf{Q}, \omega) = \frac{1}{2\pi}\int_{-\infty}^{+\infty} I(\mathbf{Q}, t)e^{-i\omega t}dt \tag{6.1.10}$$

The partial differential cross-section can thus be re-written as

$$\frac{d^2\sigma}{d\Omega dE_f} = \frac{k_f}{k_i}\frac{1}{\hbar}[{b_{coh}}^2 S_{coh}(\mathbf{Q}, \omega) + {b_{inc}}^2 S_{inc}(\mathbf{Q}, \omega)] \tag{6.1.11}$$

The *spatial* Fourier transform (three-dimensional) of the intermediate scattering functions are the time-dependent pair (self) correlation functions, $G(\mathbf{r}, t)$,

$$G(\mathbf{r}, t) = \frac{1}{(2\pi)^3}\int_{-\infty}^{+\infty} I(\mathbf{Q}, t)e^{-i\mathbf{Q}\cdot\mathbf{r}}d\mathbf{Q} \tag{6.1.12}$$

As shall be seen later, the scattering and intermediate scattering functions are the quantities accessible directly from neutron scattering experiments, whereas the time dependent pair-correlation function is a natural quantity of microscopic simulations, the domain of which is $(\mathbf{r}, t)$. The three quantities contain the same information but present it in real or reciprocal time and space. They are simply linked by forward and inverse Fourier transforms, denoted by FT and FT$^{-1}$ respectively, which can be summarised as follows

$$G(\mathbf{r}, t) \; \frac{\longrightarrow \mathrm{FT}^{-1}(\mathbf{r})}{\longleftarrow \mathrm{FT}(\mathbf{r})} \; I(\mathbf{Q}, t) \; \frac{\longrightarrow \mathrm{FT}(t)}{\longleftarrow \mathrm{FT}^{-1}(t)} \; S(\mathbf{Q}, \omega) \tag{6.1.13}$$

### 6.1.1 Coherent and incoherent scattering

A measurement of scattered neutron intensity at a given scattering angle is *always* a combination of both coherent and incoherent scattering (see Equation 6.1.7).

For static information, the total intensity (integrated over neutron energy transfers) of these two contributions is analysed as a function of the scattering angle. In the case of coherent scattering, which reflects the pair correlation of equivalent scatterers, presence of long range *structural* order in a sample gives rise to a series of sharp (Bragg) peaks. These serve, as in X-ray and light scattering, for structural determination of samples. The total intensity of incoherent neutron scattering contributes to a flat background over the entire range of scattering angles. It contains little structural information, except for the elastic incoherent structure factor, $EISF$ (discussed in detail in Section 7.8).

For dynamic analysis, the vital information is contained in the *distribution of energies* of scattered neutrons at a given scattering angle and *not* in the total integrated intensities. The above applies for neutrons scattered *both coherently and incoherently* and therefore, in theory, dynamic information can be obtained from either of the two contributions. Viewing Equation 6.1.7 it appears that *single* particle motion is somewhat more difficult to obtain from the coherently scattered neutrons (correlations between different particles are also contained), never-the-less the choice remains. For a system of a given atomic composition, it is usually the relative strength of the coherent versus incoherent scattering (one of the two usually dominates) that decides which signal is exploited for dynamic analysis. For some systems relative strengths of the coherent and incoherent signals can be adjusted or even inversed by using suitable isotopes. In most cases it is assumed that isotope substitutions do not change the structural and dynamic properties of a system, the only effect is on the strength of the neutron scattering signals. The most common isotope substitution is between deuterium atoms (relatively low incoherent cross-section) and hydrogen atoms (very large incoherent cross-section).

In the present study, we analyse measurements of the incoherent neutron scattering, which for the system of clays is dominated by the scattering from hydrogen atoms. Where appropriate, we shall discuss briefly the possibilities and attempts to exploit the coherently scattered signal for clay systems.

Final note on coherent versus incoherent scattering concerns the strength of the two signals in the Neutron Spin Echo technique, one of the two quasi-elastic neutron scattering techniques employed here. In NSE, the signal measured at a given scattering angle is not a simple sum of the coherent and incoherent contributions. As shall be explained in detail in Section 6.2, the measured quantity in NSE is the polarisation of the scattered neutron beam, or more precisely the decrease of the beam polarisation on interaction with sample, as compared to an elastically scattered beam. From the quantum-mechanical treatment of the neutron interaction with a nucleus of non-zero spin, it can be shown that the spin vector of the interacting neutron can flip (change of angle by $\pi$). The neutron spin flip is an inevitable accompanying process of the neutron - nucleus interaction. By itself it contains no useful information about the energy transfer that occurs (therefore no information on the atomic dynamics in the sample) and at the same time it decreases the strength of the signal (polarisation) detected, which can be detrimental. In case of hydrogen nuclei (I=1) neutrons scattered coherently undergo no change of spin, however neutrons scattered incoherently undergo a spin flip (reversal of polarisation) with a probability of 2/3. The resulting polarisation, $P(Q)$, from a beam neutrons scattered from hydrogen nuclei is then

$$P(Q) = C(Q)(+1) + \frac{2}{3}I(Q)(-1) + \frac{1}{3}I(Q)(+1) = C(Q) - \frac{1}{3}I(Q) \tag{6.1.14}$$

where $C(Q)$ and $I(Q)$ are the coherent and incoherent intensities at a given $Q$. The spin flip for 2/3 of incoherently scattered neutrons is indicated by polarisation of -1, the other two contributions have polarisation of +1. In summary therefore, relying on incoherent scattering in NSE measurements gives inevitably a rather low signal.

### 6.1.2 Incoherent scattering and atomic motion

Concentrating on the incoherent neutron scattering from now on, we introduce here its interpretation in terms of atomic motion in the sample. While basic concepts are summarised in this section, detailed analysis of the signal measured in neutron scattering experiments is left for Section 6.4.

As can be seen from Equation 6.1.7, the incoherently scattered signal is linked to the time-correlation of position of the *same* atom and as such it probes single particle motion. The interpretation of incoherent neutron scattering is developed further under two principal approximations: 1) decoupling of different modes of atomic / molecular motion as a function of energy transfer (frequency), 2) both momentum and energy transfer fall into the classical approximation, i.e. $\hbar\omega << (1/2)k_bT$ and $(\hbar^2Q^2)/(2m) << (1/2)k_bT$, where $(1/2)k_bT$ is the thermal energy per degree of freedom of the scattering atom [73] [76].

Taking into account the characteristic time-scales of the different modes of motion in condensed and soft matter (translation: $10^{-9} - 10^{-10}$ s, rotation: $10^{-11} - 10^{-12}$ s, vibration: $10^{-14} - 10^{-15}$ s) the mode-decoupling approximation is reasonable. We re-iterate that for dynamic analysis, the vital information is contained in the *distribution of energies* of scattered neutrons at a given scattering angle. In the order of translation, rotation, vibration (order of decreasing time-scale), the modes are responsible for increasingly higher neutron energy transfers. At a given scattering angle, apart from neutron scattered *elastically* (with zero energy transfer), atomic translation and rotation give rise to *quasi-elastic* neutron intensity (neutron having undergone small energy transfers) while vibrational motion is responsible for *inelastic* neutron intensity (neutrons having undergone large energy transfers) [76] [73].

Going back to the expression of the incoherent intermediate scattering function (Equation 6.1.9), the effect of decoupling different modes of atomic motion on the basis of their differing timescale is transcribed into the factorization of this correlation function as shown bellow

$$\begin{aligned} I_{inc}(\mathbf{Q},t) &= \frac{1}{N}\sum_j \langle e^{i\mathbf{Q}\cdot\mathbf{R}_j^{trans}(t)}e^{-i\mathbf{Q}\cdot\mathbf{R}_j^{trans}(0)}\rangle\langle e^{i\mathbf{Q}\cdot\mathbf{R}_j^{rot}(t)}e^{-i\mathbf{Q}\cdot\mathbf{R}_j^{rot}(0)}\rangle\langle e^{i\mathbf{Q}\cdot\mathbf{R}_j^{vib}(t)}e^{-i\mathbf{Q}\cdot\mathbf{R}_j^{vib}(0)}\rangle \\ &= I_{inc}^{trans}(\mathbf{Q},t)\ \ I_{inc}^{rot}(\mathbf{Q},t)\ \ I_{inc}^{vib}(\mathbf{Q},t) \end{aligned} \tag{6.1.15}$$

The analogous expression in the domain of the scattering function, $(\mathbf{Q},\omega)$, is then

$$S_{inc}(\mathbf{Q},\omega) = S_{inc}^{trans}(\mathbf{Q},\omega)\otimes S_{inc}^{rot}(\mathbf{Q},\omega)\otimes S_{inc}^{vib}(\mathbf{Q},\omega) \tag{6.1.16}$$

as the Fourier transform of a product of functions is the *convolution* of Fourier transforms of the individual functions. In this study, we concentrate only on the analysis of the quasi-elastic region. In the quasi-elastic zone the vibrational contribution is a simple Gaussian function of the wavevector $\mathbf{Q}$ [73] [78] and thus

$$I_{inc}^{qel}(\mathbf{Q},t) = I_{trans}(\mathbf{Q},t)I_{rot}(\mathbf{Q},t)e^{-\langle u^2\rangle Q^2/3} \tag{6.1.17}$$

$$S_{inc}^{qel}(\mathbf{Q},\omega) = [S_{trans}(\mathbf{Q},\omega)\otimes S_{rot}(\mathbf{Q},\omega)]e^{-\langle u^2\rangle Q^2/3} \tag{6.1.18}$$

with $\langle u^2\rangle$ being the mean square vibrational amplitude of the atom. The overall $e^{-\langle u^2\rangle Q^2/3}$ term is referred to as the Debye-Waller factor, the exponent is derived from $\langle(\mathbf{Q}\cdot\mathbf{u})^2\rangle = Q^2\langle u^2\rangle\langle\cos^2(\theta)\rangle = 1/3\langle u^2\rangle Q^2$ [78]. In neutron techniques where the measured quantity is $S(\mathbf{Q},\omega)$ or rather $S(Q,\omega)$ (such as time-of-flight), the plot of the logarithm of the total quasi-elastically scattered intensity at a given $Q$ (i.e. $\ln\int_{small\ d\omega} S(Q,\omega)d\omega$) versus $Q^2$ gives a slope of $-\langle u^2\rangle/3$.

On the other hand, the form of the $I_{inc}^{qel}(\mathbf{Q},t)$ and $S_{inc}^{qel}(\mathbf{Q},\omega)$ for translation and rotation is a more complex function of *both* the wavevector and time (or $\omega$). Various models of translation and rotation on the molecular scale exist giving rise to different forms of $I_{inc}^{qel}(\mathbf{Q},t)$ and $S_{inc}^{qel}(\mathbf{Q},\omega)$. Models pertinent to the current study shall be discussed later on. At this stage we summarise that for the analysis of quasi-elastic neutron scattering, a detailed model is necessary for both translational and rotation motion in the system, while the effect of the vibrational motion comes in the form of a Debye-Waller factor scaling the total quasi-elastically scattered intensity at a given $Q$.

Apart from the approximation about decoupling of modes of motion, we have mentioned the so-called classical approximation under which $\hbar\omega << (1/2)k_bT$ and $(\hbar^2Q^2)/(2m) << (1/2)k_bT$. The above implies a uniform population over all energy levels of the scatterer (interacting nucleus/atom), in which case the scattering function can be considered as symmetric, i.e. $S(\mathbf{Q},\omega) = S(-\mathbf{Q},-\omega)$. For low temperatures, when uniform population of all energy levels of the scatterer can no longer be assumed, the probability of neutron energy gain is diminished due to the low occupation of high-energy levels of the scatterer and the symmetry in $\omega$ breaks. In such cases the real scattering function can be approximated by multiplication of the symmetric $S(\mathbf{Q},\omega)$ by the Boltzmann factor, $e^{-\hbar\omega/(2k_bT)}$, to satisfy the microscopic detailed balance condition [76] [73].

### 6.1.3 Temporal and spatial observation domains and scales

The natural spatial *domain* of neutron scattering data is the reciprocal space (characterised by the wavevector $\mathbf{Q}$), while the temporal *domain* can be either real time (Neutron Spin Echo technique) or reciprocal time (Time-of-flight). Within these domains, the spatial and temporal observation *scales* available on a given experimental apparatus are limited by the particular experimental set-up (in case of simulation similar limits exist linked to the size of the simulation box and the simulation length). In general, in order to see any atoms (scatterers) in an investigated system as mobile, *both* of the observation scales of the experimental apparatus (or simulation) have to match the scale of the atomic motion in the system.

At first, taking the example of the intermediate scattering function, $I(Q,t)$, the notion of the wavevector, as a quantity depicting the spatial observation scale, shall be presented in a more visual way. Thereafter, we shall describe the various forms of signal expected depending on the match between the spatial and temporal observation scales and those characteristic to the atomic motion in a sample.

Figure 6.2 features an example of intermediate scattering functions at a series of wavevectors. In all cases a decay of the signal is observed with increasing time, while this decay is faster with increasing wavevector $Q$. Remembering that the intermediate scattering functions are, on the atomic scale, auto-correlation functions of atomic position, their shape can be understood as follows. At a given wavevector $Q$ we observe the position of a particle through an "observation sphere" of radius $2\pi/Q$, which at $t = 0$ is centered on the particle itself (see Figure 6.3). At a later time $t$, we assess whether the particle is still within the observation sphere or not. If the particle is found within the sphere, there is no change to the signal intensity at time $t$, if it is not, the particle makes no longer a contribution to the signal at time *t*.

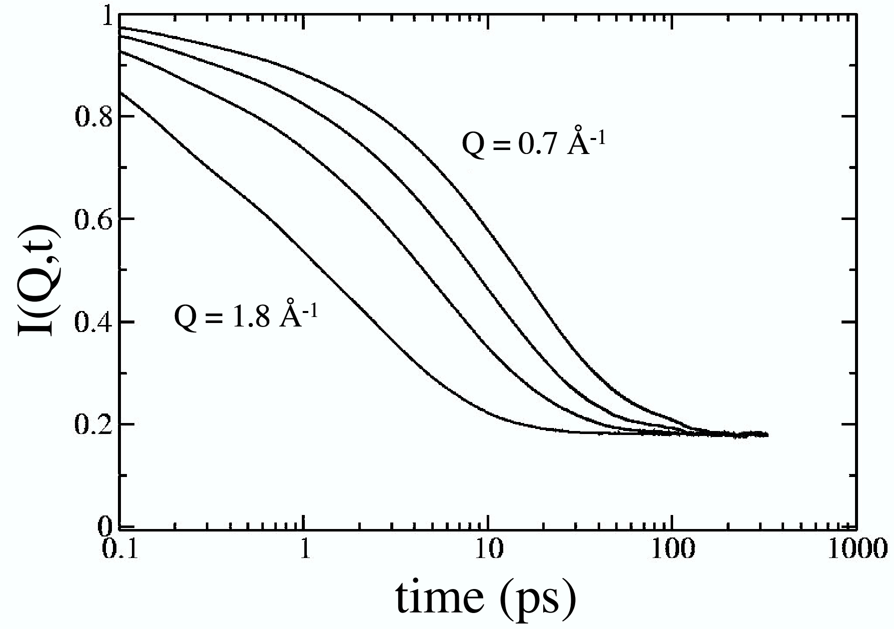

**Figure 6.2: Example of intermediate scattering functions at a series of wavevectors between 0.7 and 1.8 Å$^{-1}$.**
**Examples shown are simulated $I(Q,t)$ signals for the Na-bilayer system.**

Concentrating on the intermediate scattering function at $Q = 0.7$ Å$^{-1}$ in Figure 6.2, it can be concluded that at t=10 ps, 40 % of the particles have left their respective observation spheres, while at t=200 ps this increases to 80 %. For the signal at $Q$ =1.8 Å$^{-1}$ the decay is faster as we now deal with a higher wavevector and thus a smaller observation sphere. Note that in the example shown signals at all wavevectors decay to a constant background of 20 %. This is the signal from particles appearing as stationary on the observation time- and space-scale (these particles remain within their observation spheres throughout the entire time and space range considered). Overall, the signal in Figure 6.2 corresponds to an ensemble of atoms, 80 % of which appear as mobile and 20 % of which appear as

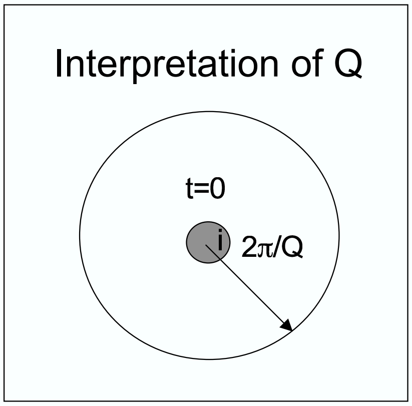

**Figure 6.3: Demonstration of spatial observation scale at a given wavevector $Q$ using the concept of an observation sphere.**
**Position of particle $i$ is inspected as a function of time through an observation sphere of radius $2\pi/Q$ centered on the particle at time $t = 0$.**

immobile, on the timescale of 0.1 - 300 ps for wavevectors 0.7 - 1.8 Å$^{-1}$.

The above example shows two extreme possibilities of moving particles, those seen either as mobile or as immobile on *all* spatial scales (all wavevectors) investigated. Intermediate examples however exist, such as particles undergoing *localised* motion, such as the case of rotation or confined translation (i.e. moving in a pore). Taking the real dimension of the localisation of motion as $M$, these particles will appear as mobile in the high $Q$ region ($Q > 2\pi/M$, small distances) but as $Q$ is decreased towards zero ($Q < 2\pi/M$, large distances) they will appear as immobile as they cannot move over larger distances than the dimension of their confinement/localisation.

In summary, it is crucial to understand that the assessment of mobility or immobility of a particle is always carried out on a given spatial and temporal scale. This is true both for experiment and simulation. For any inter-comparison of dynamic data from different techniques, it is necessary to identify the overlap or mismatch of their accessible observation scales.

Having outlined the general principles of neutron scattering we turn to the description of neutron scattering techniques, real experimental set-ups and data acquisition. The following section outlines the principles of Neutron Spin Echo (NSE) and Time-of-flight (TOF) techniques used in this study. All neutron scattering experiments were carried in Laboratoire Léon Brillouin (LLB) in CEA Saclay, France with access to a 14 MW reactor (Orphée) producing a continuous beam of cold neutrons (maximum of wavelength distribution at 5 Å).

## 6.2 Neutron Spin Echo Technique

The method of Neutron Spin Echo (NSE), developed in the early 1970s by F. Mezei, is based on detecting the change of the intensity of polarisation of a neutron beam on its interaction with sample [79]. This indirect measurement of energy transfers, between atoms in the sample and incoming neutrons, gives the NSE method higher resolution in comparison to other quasi-elastic methods such as backscattering and Time-of-Flight (TOF). In NSE, very small relative changes in neutron energies (or velocities) are converted, after a large number of individual neutron spin precessions, into large changes in the overall polarisation of the neutron beam. Furthermore, the high resolution is achieved without strict requirements on the degree of monochromatisation of the incident neutron beam. This effectively decouples resolution and intensity loss and expands significantly the range of accessible correlation times [79] [80].

The governing principle of the NSE technique is the behaviour of a neutron in a magnetic field [76] [74]. The spin of a neutron exhibits a precession around the direction of a magnetic field *perpendicular* to the direction of its spin. The frequency of this precession is

$$\omega = |\gamma| B \tag{6.2.1}$$

where $\gamma$ is the gyromagnetic ratio of neutron and $B$ the magnitude of the applied magnetic field (Larmor precession). In an NSE experiment (Figure 6.4) a polarised neutron enters a first region of magnetic field ($\mathbf{B}_0$, 1st arm of spectrometer) prior to interaction with sample, thereafter a second region of magnetic field ($\mathbf{B}_1$, 2nd arm of spectrometer) prior to being analysed.

The number of precessions ($N$) carried out in each of the fields depends on the strength of the magnetic field ($B$) and the wavelength of the precessing neutron ($\lambda_0'$), which determines the time spent in the magnetic field ($t$), i.e.

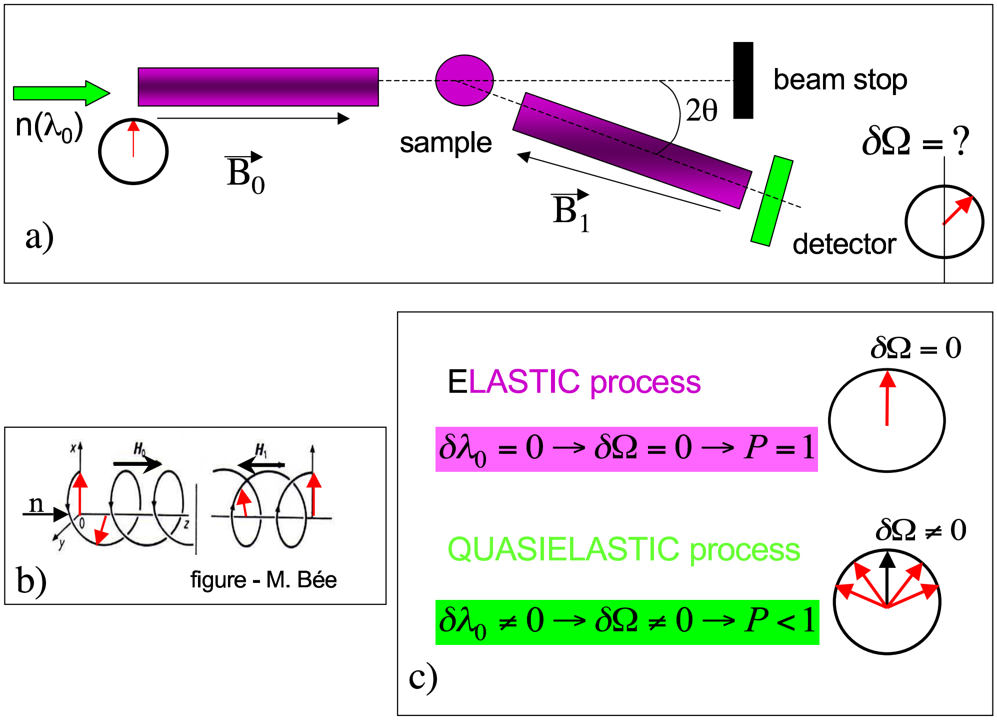

**Figure 6.4: Neutron Spin Echo technique.**
**Part a: The general set-up of an NSE experiment, featuring two spectrometer arms, in front of and behind the sample, under constant magnetic fields $\mathbf{B}_0$ and $\mathbf{B}_1$ respectively. Part b: Precession of neutron spin in two magnetic fields of equal magnitude but opposite direction. Part c: Difference between elastic and quasi-elastic scattering as seen at the detector.**

$$N^{\lambda_0'} = \frac{\omega t}{2\pi} = \frac{|\gamma| B l}{2\pi v} = \frac{|\gamma| B l \lambda_0' m}{2\pi h} \tag{6.2.2}$$

where $t = l/v$, $v = h/(\lambda_0' m)$ (de Broglie relation) have been applied, $l$ being the length of the magnetic region, $m$ neutron mass, $v$ neutron speed and $h$ the Planck's constant. For a distribution of neutron wavelengths, the number of precessions for a neutron of a general wavelength $\lambda_0'$ (as shown above), is simply related to the number of precessions carried out by a neutron corresponding to the *maximum* of the wavelength distribution $(\lambda_0)$;

$$N^{\lambda'_0} = N^{\lambda_0}\frac{\lambda'_0}{\lambda_0} \tag{6.2.3}$$

As a result of the *opposing* directions of the two magnetic fields, precession occurs in opposite senses before and after interaction with the sample. Consider the case when the lengths of the two magnetic regions are the same and $\mathbf{B}_0$ and $\mathbf{B}_1$ are of the same magnitude. The final residual angle (after precession through both arms of the spectrometer) for a neutron of incident wavelength $\lambda'_0$ and final wavelength of $\lambda'_0 + \delta\lambda$, is

$$\begin{aligned}
\delta\Omega &= 2\pi(N_0^{\lambda'_0} - N_1^{\lambda'_0+\delta\lambda}) \\
&= 2\pi(N_0^{\lambda_0}\frac{\lambda'_0}{\lambda_0} - N_1^{\lambda_0}\frac{\lambda'_0+\delta\lambda}{\lambda_0}) \\
&= 2\pi N^{\lambda_0}(\frac{\lambda'_0}{\lambda_0} - \frac{\lambda'_0+\delta\lambda}{\lambda_0}) \\
&= -2\pi N^{\lambda_0}\frac{\delta\lambda}{\lambda_0}
\end{aligned} \tag{6.2.4}$$

as $N_0^{\lambda_0} = N_1^{\lambda_0}$. Note that the above expression is *independent* of $\lambda'_0$, it is only the change in wavelength $\delta\lambda$ that defines the resulting residual angle. The actual measured signal is the projection of the final neutron spin orientation ($p$) along the axis of the initial beam polarisation or

$$p = \cos(\delta\Omega) \tag{6.2.5}$$

which is thus equal to 1 for elastically scattered neutrons ($\delta\lambda = 0$, thus $\delta\Omega = 0$, equal number of precessions in the two arms but in opposite senses) and $< 1$ for inelastically scattered neutrons ($\delta\lambda \neq 0$).

Making the transition from the case of a single neutron to a neutron beam (of a finite wavelength distribution), the signal measured is an ensemble average of the individual neutron residual angles, $\langle\cos(\delta\Omega)\rangle$, referred to a polarisation ($P$). Under 1) the quasi-elastic approximation ($\delta\lambda << \lambda'_0$) and 2) the classical approximation ($k_b T >> \Delta E$, therefore $S(Q,\omega)$ is an even function in $\omega$ and $\int_{-\infty}^{+\infty}\sin(\omega t)S(Q,\omega)d\omega = 0$), it can be expressed as

$$P = \langle\cos(\delta\Omega)\rangle = \frac{\int_{-\infty}^{+\infty}\cos(t_{NSE}\omega)S(Q,\omega)d\omega}{\int_{-\infty}^{+\infty}S(Q,\omega)d\omega} = \frac{I(Q,t_{NSE})}{I(Q,0)} \tag{6.2.6}$$

where $t_{NSE} = (\hbar|\gamma|Bl)/(mv^3)$ is the so-called spin echo time [73] [80].

Measurements at high spin echo times, thus relatively strong static magnetic fields $\mathbf{B}_0$ and $\mathbf{B}_1$ are problematic. A variant of the traditional NSE technique, the Neutron

Resonance Spin Echo (NRSE; developed by R. Gähler and R. Golub in the 1980s) achieves large spin echo times with a system of weak oscillating magnetic fields at the extremities of the two arms of the spectrometer (radio-frequency (RF) coil regions) separated by regions of zero magnetic field (Figure 6.5) [81] [82] [83].

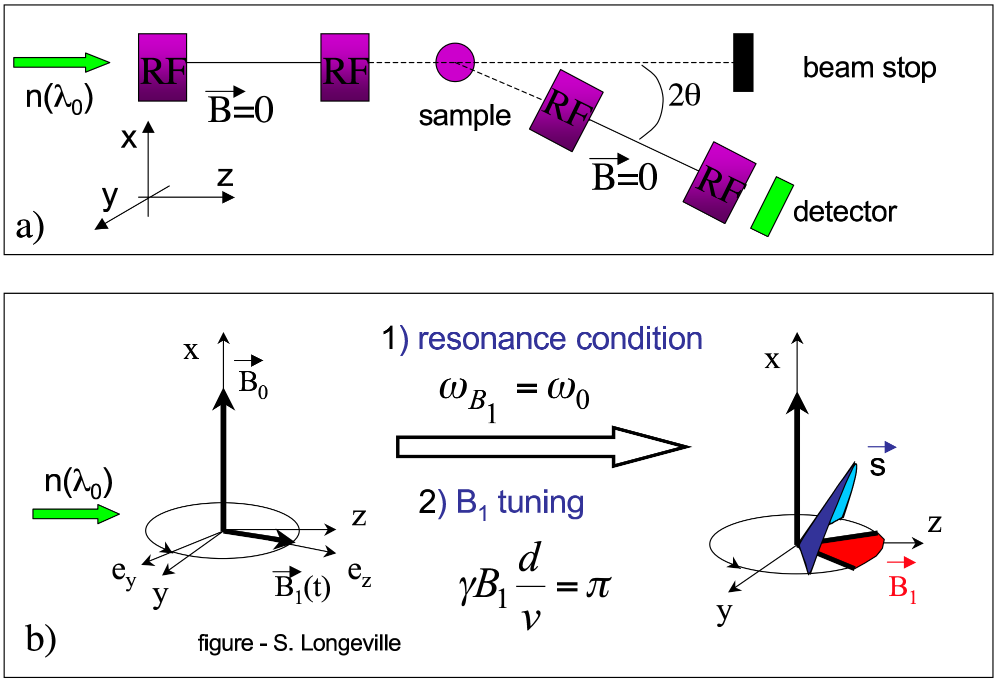

**Figure 6.5: Neutron Resonance Spin Echo technique.**
**Part a: The general set-up of an NRSE experiment. Magnetic fields along the entire lengths of the two spectrometer arms are now replaced by 4 radio-frequency coils regions (RF) at the extremities and zero magnetic field between them. Part b: Tuning of the frequency and magnitude of the oscillating magnetic field, $B_1(t)$, to achieve a spin flip by an angle of $\pi$ in each of the RF regions.**

At each of the four extremities, a static field $\mathbf{B}_0$ along $x$ (along $-x$ in the 2nd arm) and oscillating field $\mathbf{B}_1(t)$ in the $yz$ plane are applied, the latter with finely tuned frequency and magnitude. The $\mathbf{B}_1(t)$ field oscillates in phase in all the 4 RF coil regions and its frequency of oscillation is tuned to the Larmor precession around the $\mathbf{B}_0$ field, i.e.

$$\omega_{B_1} = |\gamma| B_0. \tag{6.2.7}$$

This so-called resonance condition achieves that in the rotating frame of the $\mathbf{B}_1(t)$ field, neutron precesses around $\mathbf{B}_1(t)$ only, i.e. the presence of $\mathbf{B}_0$ is masked. The magnitude of the $\mathbf{B}_1(t)$ field is

$$B_1 = \frac{\pi v}{|\gamma| d} \tag{6.2.8}$$

where $v$ is neutron speed, $d$ width of the RF coil region. Under this condition, neutrons, which are all polarised to arrive with spin in the $yz$ plane into the first RF coil region, precess by an angle of $\pi$ around the $\mathbf{B}_1(t)$ field and thus end up with spins again in the $yz$ plane upon leaving (see Figure 6.5 Part b). As the neutron travels through the central region of the arm (zero magnetic field) with no precession, it finds itself with a phase shift relative to the oscillating field $\mathbf{B}_1(t)$ on its entry (and exit) from the 2nd RF coil region. This phase shift is directly related to the distance between the two RF coil regions ($l$), the width of the RF coil region ($d$) and the neutron speed ($v$). Similarly to the traditional NSE, for an elastically scattered neutron this phase shift is cancelled out in the 2nd arm, whereas a residual phase shift is detected for an inelastically scattered neutron [76]. The main difference between the NSE and NRSE techniques is the way they achieve a controlled precession of the neutron spin. As for the actual measured quantity, this is very similar and for the NRSE techniques can be expressed by Equation 6.2.6 with $t_{NRSE} = (2\omega_{B_1}\hbar(l+d))/(mv^3)$.

In a typical experiment a series of measurements at constant $Q$ (determined by the scattering angle $2\theta$ between the two arms of the spectrometer - see Figure 6.4 Part a) is carried out for different spin echo times, effectively different correlation times. Spin echo time is varied by changing the strengths of $\mathbf{B}_0$ and $\mathbf{B}_1$ in NSE and by changing $\omega_{B_1}$ (and thus the strength of $\mathbf{B}_0$ to satisfy the resonance condition in Equation 6.2.7) in NRSE. For a given value of $Q$, the set of measurements at different spin echo times is to be normalised by the polarisation at zero spin echo time and corrected for the resolution of the apparatus. The latter is determined from measurements on a quartz sample (coherent scatterer) and usually a single set of polarisation measurements at one wavevector (in our case $Q$=1.4 Å$^{-1}$) is sufficient. In the $(Q, t)$ domain the correction of measured data by the resolution of the apparatus is a simple division. The intermediate scattering function $I(Q,t)$ is thus obtained from the raw data according to

$$I(Q,t) = \frac{P(Q,t)}{P(Q,t=0)} \frac{P_{res}(Q,t=0)}{P_{res}(Q,t)} \tag{6.2.9}$$

where the subscript $res$ indicates the resolution measurements. In summary, the quantity obtained from both NSE and NRSE is the intermediate scattering function $I(Q,t)$, the Fourier transform of the scattering function $S(Q,\omega)$.

## 6.3 Time-of-flight Technique

Time-of-flight (TOF) is a classical technique in quasi-elastic neutron scattering, which measures, in a more direct way than NSE, energy transfers occurring on interaction of a neutron with a sample. We concentrate here on the direct geometry TOF, in which a *pulse* of a monochromatic neutrons interacts with the sample and the energy (velocity) of scattered neutrons is deduced from their 'time-of-flight' ($t_{TOF}$) over a known distance [76] [73].

For the TOF spectrometer used, the incoming continuous neutron beam (consisting of a Maxwellian distribution of neutron wavelengths peaked at 5 Å) is chopped up into short pulses of monochromatic neutrons with a set of 6 choppers (rotating discs with a slit). The choppers ensure the selection of neutrons of the desired wavelength as well as preventing the overlap of consecutive pulses [80] [76].

The incident neutron wavelength and the degree of monochromaticity determines the smallest energy transfer detectable, in other words the resolution. Resolution increases with the wavelength of the incident neutrons (the arrival of longer wavelength, lower energy neutrons is dispersed more clearly as a function of time at the detector) and with increasing monochromaticity of the incident beam. Therefore, achieving high resolution with the use of a highly monochromatic beam at a wavelength much higher than the maximum of the Maxwellian distribution of incoming wavelengths is hindered by the serious decrease in the incident neutron flux. This coupling between resolution and flux is one of the major limitations of the TOF technique and one that is not present, to first order, in NSE [80]. At the same time, simultaneous measurements at a wide range of scattering angles is a key to rapid data acquisition in the TOF technique compared to NSE.

Raw measurements in TOF are simply counts of neutrons as a function of arrival time at detectors, placed across a wide range of angles $2\theta$ from the direction of the incident neutron beam (see Figure 6.6). Neutrons arriving at a detector as a function of real time, differ

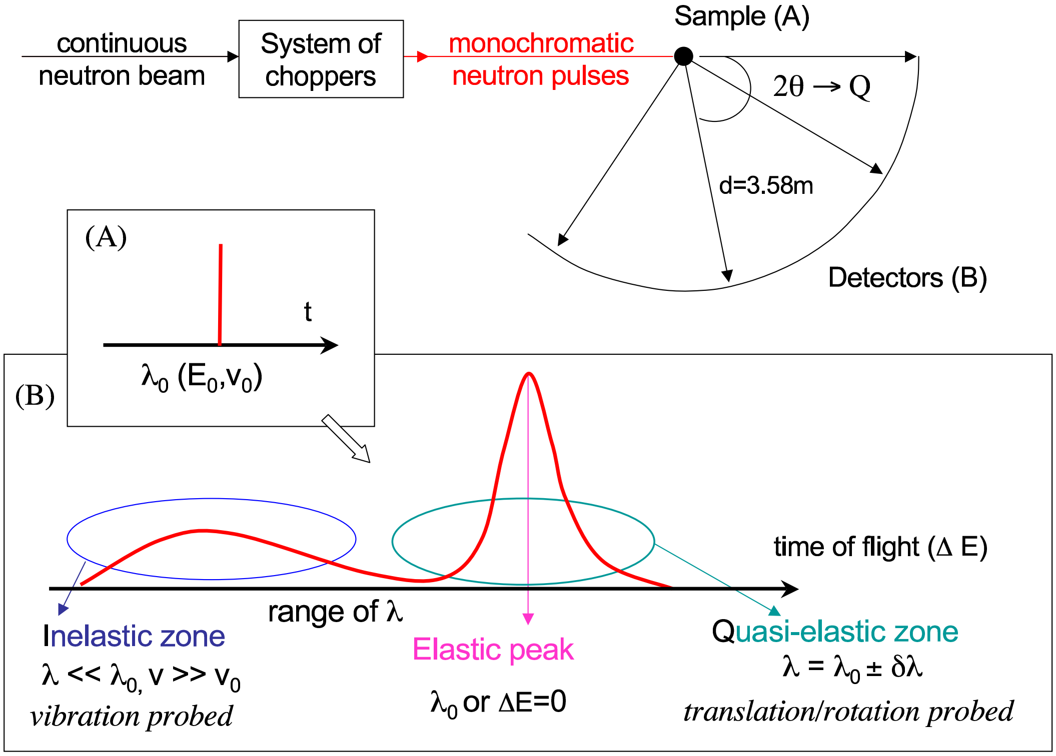

**Figure 6.6: Time-of-flight technique.**
**Monochromatic neutron pulses are produced from the incoming continuous neutron beam and arrive at the sample (A). Scattered neutrons are detected simultaneously at a wide range of scattering angles $2\theta$. Signal at each of the detectors (B) is a dispersion of neutrons of different wavelengths ($\lambda$) as they arrive as a function of real time (the shortest wavelength, fastest neutrons arriving first, having gained energy on interaction with the sample). With increasing energy transfers different modes of motion are probed from translation to vibrational.**

in *both* energy (see Figure 6.6 inset B) and the scattering vector **Q** (refer back to Figure 6.1) [76] [80]. The raw data in the $(2\theta, t_{TOF})$ domain can be converted into the domain of the scattering function, $(Q, \omega)$. The time $(t_{TOF})$ to energy ($E$ or $\omega$) conversion is non-linear according to $\Delta E = (1/2)m(\Delta v)^2 = (1/2)ml^2[-\Delta t_{TOF}/(t_0^2 + t_0\Delta t_{TOF})]^2$, where $m$

is neutron mass, $l$ distance travelled, $v$ neutron velocity, $t_0$ the time-of-flight of elastically scattered neutrons and $\Delta t_{TOF}$ the time-of-flight *difference* between quasi- and elastically scattered neutrons. Then, combining equations for momentum and energy transfer of the interacting neutron, Equations 6.1.4 and 6.1.5, the following equation relating $Q$, $\omega$ and $2\theta$ is obtained

$$\frac{\hbar^2 Q^2}{2m} = 2E_i - \hbar\omega - 2\cos(2\theta)\sqrt{(E_i)^2 - E_i\hbar\omega} \qquad (6.3.1)$$

Thus the signal collected at a given detector (i.e. scattering angle $2\theta$) corresponds to a non-trivial cut through the $(Q, \omega)$ space (Figure 6.7).

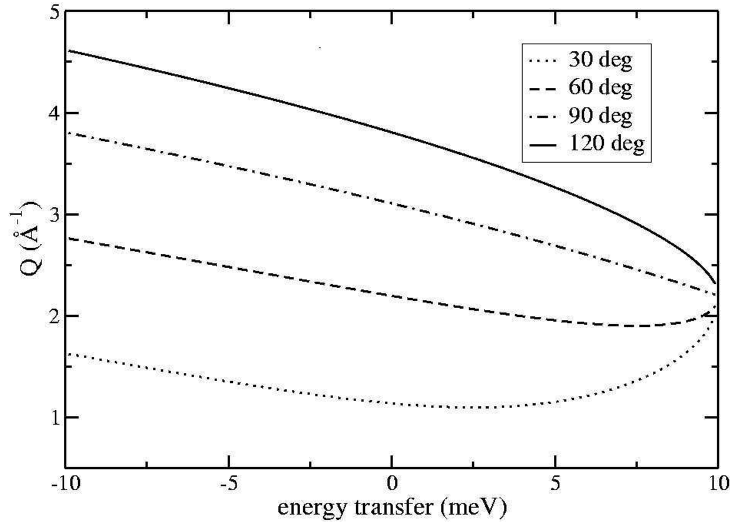

**Figure 6.7: Trajectories through $(Q, \omega)$ space for a detector at a given scattering angle $2\theta$.**

In a rigorous treatment, the scattering function S$(Q, \omega)$ should then be re-constructed from a series of the above cuts. [80] [76] [84]. This rigorous reconstruction has however not been applied in this study.

Resolution measurements for the TOF technique are carried out on a vanadium sample (incoherent scatterer) for all incident neutron wavelengths used. Unlike the simple division of sample measurements by the resolution measurements in the NSE technique, a de-convolution is necessary in the case of TOF as suggested by Equation 6.1.16 for the combination of multiple signals in the $(Q, \omega)$ domain. In practice, a trial model signal is convoluted with the resolution function and compared to the raw experimental data. More details on data analysis are given in the following sections.

## 6.4 Analysis of quasi-elastic scattering - Models of atomic motion

Having outlined the techniques for measuring quasi-elastic scattering we turn back to the detailed interpretation of the measured signal in terms of atomic motion in the sample.

Arriving at Equations 6.1.17 and 6.1.18 for the incoherent quasi-elastic signal, we noted that while the vibrational contribution was a simple Gaussian function of the wavevector, the form of the translational and rotational contributions is complex and a number of dynamic models of these motions on the atomic scale exist. We start here with the simplest models, in particular the isotropic continuous translation diffusion and isotropic rotational diffusion on a sphere.

Any model of long-range translational diffusion has to satisfy the macroscopic diffusion equation (see Equation 6.4.1), which describes the evolution of a system under a concentration gradient. This equation can be re-written microscopically

$$D\nabla^2 G_s(\mathbf{r},t) = \frac{\partial G_s(\mathbf{r},t)}{\partial t} \tag{6.4.1}$$

where $G_s(\mathbf{r},t)$ on one hand can be thought of as the time-dependent self-correlation function, the incoherent (or self) form of Equation 6.1.12, on the other hand it stands for a probability density function, giving the probability of finding an atom, that was at the origin at time 0, at position $\mathbf{r}$ at a later time $t$ [73] [85]. It can be shown that a Gaussian form of $G_s(\mathbf{r},t)$

$$G_s(\mathbf{r},t) = \frac{1}{(4\pi Dt)^{(3/2)}} e^{-\mathbf{r}^2/4Dt} \tag{6.4.2}$$

satisfies the diffusion equation. Through Fourier transformation, dropping the vectorial form of the wavevector, it corresponds to the following exponential and Lorentzian forms for the scattering functions in the $(Q,t)$ and $(Q,\omega)$ domains

$$I^{trans}(Q,t) = e^{-D_t Q^2 t} \tag{6.4.3}$$

$$S^{trans}(Q,\omega) = \frac{1}{\pi} \frac{D_t Q^2}{(D_t Q^2)^2 + \omega^2} \tag{6.4.4}$$

where $D_t$ is the translational diffusion coefficient. In the terminology of Lorentzian functions the $D_t Q^2$ term is the so-called half-width half-maximum (HWHM) of this bell-shaped function. (From now on we shall use the notation of $L(\omega, D_t Q^2)$ for a Lorentzian in $\omega$ with

HWHM of $D_tQ^2$.) Note the Q-dependence of the exponential decay constant in the first equation and thus also of the HWHM of the Lorentzian that follows.

The model of isotropic rotational motion on a sphere was developed by Sears, who considered reorientations of atoms in a molecule by small random angle changes [73]. The corresponding intermediate scattering function is

$$I^{rot}(Q,t) = \sum_{l=0}^{\infty}(2l+1)j_l^2(QR)e^{-l(l+1)D_rt} \tag{6.4.5}$$

where $R$ is the mod of the position vector of the atom from the molecular center of mass, $j_l$ are spherical Bessel functions and $D_r$ is the rotational diffusion coefficient. The above expression is an infinite sum of exponentials, as opposed to the single exponential term in the case of translation. The intensity of each term is governed by the Bessel function of the appropriate order, while the sum of the intensities is 1 according to the following general property of spherical Bessel-functions ([86])

$$\sum_{l=0}^{\infty}(2l+1)j_l^2(x) = 1 \tag{6.4.6}$$

For the range of wavevectors used in most quasi-elastic studies ($Q <$ 2-3 $\text{Å}^{-1}$), the intensity of the higher-order terms is very low and in practice therefore, the infinite series in Equation 6.4.5 is usually truncated after the first two terms. In order to comply with the normalisation of the total intensity, the intensity of the second term is adjusted accordingly to yield

$$\begin{aligned} I^{rot}(Q,t) &= j_0^2(QR)\delta(\omega) + (1 - j_0^2(QR))e^{-2D_rt} && (6.4.7) \\ &= \frac{\sin^2(QR)}{(QR)^2}\delta(\omega) + (1 - \frac{\sin^2(QR)}{(QR)^2})e^{-2D_rt} && (6.4.8) \end{aligned}$$

Performing the Fourier transform of Equation 6.4.7 we arrive at

$$S^{rot}(Q,\omega) = j_0^2(QR)\delta(\omega) + (1 - j_0^2(QR))L(\omega, 2D_r) \tag{6.4.9}$$

In the $(Q,\omega)$ domain the signal is now a delta function at the origin (arising from the Fourier transform of the time-independent zeroth order term in the intermediate scattering function) and a Lorentzian. Note that in the case of rotation the wavevector influences only the intensity of the exponential or Lorentzian term, not their characteristic shape (exponent in $I(Q,t)$ and HWHM of $S(Q,\omega)$ are independent of $Q$).

According to Equations 6.1.17 and 6.1.18 it is now necessary to combine the above translational and rotational scattering functions to form the overall quasi-elastic signal. Taking only the first two terms of the rotational intermediate scattering function as outlined above, the overall intermediate scattering function is then

$$\begin{aligned} I(Q,t) &= e^{-\langle u^2\rangle Q^2/3}[Ae^{-D_tQ^2t}(j_0^2(QR)+(1-j_0^2(QR))e^{-2D_rt})+B] \\ &= e^{-\langle u^2\rangle Q^2/3}[Aj_0^2(QR)e^{-D_tQ^2t}+A(1-j_0^2(QR))e^{-(D_tQ^2+2D_r)t}+B] \end{aligned} \quad (6.4.10)$$

where $A$ and $B$ are respectively the intensities from the diffusing and non-diffusing scatterers (corresponding in our system to constituent hydrogen atoms of interlayer water and structural hydrogen atoms of clay layers respectively as discussed in Section 6.1.3). Note that in a more rigorous treatment the Debye-Waller terms for the diffusing and non-diffusing scatterers should be considered separately. The corresponding scattering function in the $(Q,\omega)$ domain is then

$$S(Q,\omega)=e^{-\langle u^2\rangle Q^2/3}[Aj_0^2(QR)L(\omega,D_tQ^2)+A(1-j_0^2(QR))[L(\omega,D_tQ^2)\otimes L(\omega,2D_r)]+B\delta(\omega)] \quad (6.4.11)$$

where we recognize the elastic peak, $B\delta(\omega)$, and the quasi-elastic zone modelled by a single translational Lorentzian and a convolution of translational and rotational Lorentzians.

Equations 6.4.10 and 6.4.11 are the starting point for modelling the quasi-elastic signal in the $(Q,t)$ and $(Q,\omega)$ domains respectively. In practice the NSE signals are normalised (division by $I(Q,t=0)$) which results in the cancellation of the time- or $\omega$-independent Debye-Waller term. In case of TOF, no such normalisation is applied, the intensities extracted from the fit of the raw data to the above model contain the Debye-Waller factor. As the intensities are later used only in their ratios (e.g. Elastic incoherent sctructure factor - see Section 7.8), the Debye-Waller factor is effectively cancelled out at a later stage. More importantly the expressions in Equations 6.4.10 and 6.4.11 can be further simplified by considering the relative intensities of the individual terms and identification of the dominating terms as a function of the wavevector. Figure 6.8 indicates that at low values of $Q$ (two cases are demonstrated for R=1 Å and R=0.5 Å), the simple translational term dominates over the combined trans-rotational term. This approximation is used very often in the low $Q$ region (below approximately 1 $\text{Å}^{-1}$), for which the combined trans-rotational terms are neglected. In the high $Q$ region however, both terms need to be considered.

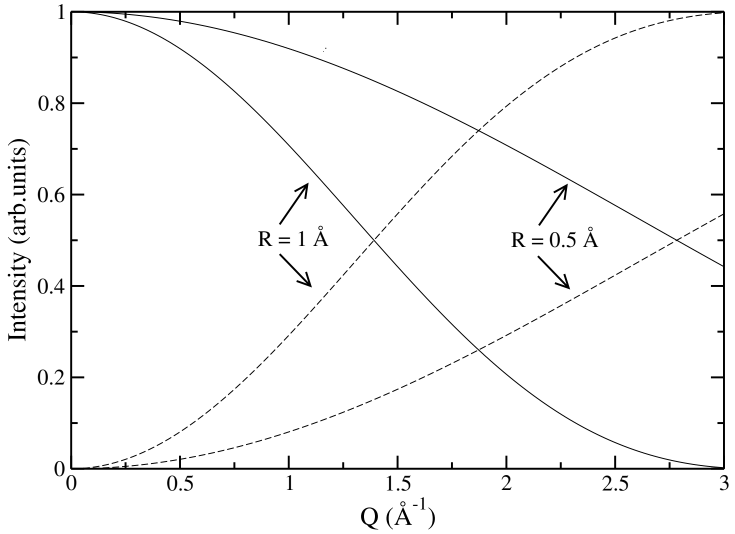

**Figure 6.8: Relative intensities of translational and trans-rotational terms in the low *Q* region.**
**Two cases for different R are shown. Full lines: intensity of translational term, dashed lines: intensity of trans-rotational term.**

The above two models for translation and rotation are the simplest cases and they have served to demonstrate the generalities of the modelling of the quasi-elastic signals. In the following sections, along with the data analysis for the clay systems, we shall develop the models further to suit better the needs of the particular system.

# Chapter 7

# Case Study 2: Dynamics of water in clays, simulation - experiment comparison

## 7.1 Brief review of neutron scattering studies on clay systems

The first quasi-elastic neutron scattering studies on clays, more specifically time-of-flight studies, date back to the beginning of 1980s, therefore earlier than the first simulations on clays. Whereas microscopic simulation gives now access to dynamics of both water and ionic species in the clay system, neutron scattering studies have been limited to the investigation of dynamics of water, relying on the dominating incoherent signal of its constituent hydrogen atoms. Attempts to exploit the coherent signal, in the Neutron Spin Echo technique, and provide information on the dynamics of cations have been for the moment unsuccessful in our own trials and elsewhere [72].

The early TOF studies on clays consider both monovalent and bivalent counterions in low hydration states. Across the various studies, for montmorillonite systems with monovalent counterions, the measured diffusion coefficient of water varies between 0.5 - 4 $\times$ $10^{-10}\mathrm{m}^2\mathrm{s}^{-1}$ for samples at relative humidity (relative humidity is the ratio of the partial pressure of water and the water vapour pressure at a particular temperature) around 40 % and reach up to 10 $\times$ $10^{-10}\mathrm{m}^2\mathrm{s}^{-1}$ at relative humidity around 80 % (loosely corresponding to a monolayer and a bilayer respectively). This range becomes larger when measurements on different types of clay and/or bivalent cations are included. However, overall these early studies do not feature, at ambient temperature and first two hydration states, values of diffusion coefficients higher than half of the bulk value for water ($\mathrm{D}_{exp}^{bulkwater} = 23 \times 10^{-10}\mathrm{m}^2\mathrm{s}^{-1}$ or $2.3 \times 10^{-5}\mathrm{cm}^2\mathrm{s}^{-1}$). This is true for three types of clay studied (hectorite, montmorillonite, vermiculite) and both mono and bivalent counterions [87] [88] [89] [90].

In the recent years, a combination of the TOF and NSE technique has been employed to study water in clay systems [91] [72]. We note that the diffusion coefficients arising from the data in refs [91] [72] have been recently revised [92]. The corrected values are $26.4 \times 10^{-10}\mathrm{m}^2\mathrm{s}^{-1}$ for the TOF technique and $1.7 \times 10^{-10}\mathrm{m}^2\mathrm{s}^{-1}$ for NSE [92]. These studies therefore show rather surprising results. Not only is there a difference of a factor of 15 between the diffusion coefficients determined by the two techniques now available (as the authors note themselves [72]), also the TOF data gives higher values than seen in the early studies, values approaching bulk water behaviour [92] [93].

In summary, comparing (three-dimensional) diffusion coefficients of water in montmorillonite clays with monovalent counterions, determined by microscopic simulation and neutron scattering, the observed ranges agree within a factor of 2 for the monohydrated systems ($\mathrm{D}_{sim}^{water}$= 1.1-4.7 $\times 10^{-10}\mathrm{m}^2\mathrm{s}^{-1}$, $\mathrm{D}_{exp}^{water}$= 0.5 - 4 $\times 10^{-10}\mathrm{m}^2\mathrm{s}^{-1}$) and are even closer for the bihydrated systems ($\mathrm{D}_{sim}^{water}$= 8-10 $\times 10^{-10}\mathrm{m}^2\mathrm{s}^{-1}$, $\mathrm{D}_{exp}^{water}$= $10 \times 10^{-10}\mathrm{m}^2\mathrm{s}^{-1}$). Only the recent measurements of TOF [91] on bihydrated vermiculite do not fall within the range specified above ($26.4 \times 10^{-10}\mathrm{m}^2\mathrm{s}^{-1}$) and keeping in mind the diffusion coefficient of bulk water itself they seem rather questionable.

In the following sections, we analyse and compare in detail the results of Neutron Spin Echo, Time-of-flight and microscopic simulation regarding the dynamics of water in Na-monohydrated, Na-bihydrated and Cs-monohydrated montmorillonite. The comparison is made not only on the level of diffusion coefficients but other, more direct and detailed approaches are attempted.

## 7.2 Simulated and experimental data - levels of comparison

Simulated and experimental dynamical information can be presented on several levels as depicted in Figure 7.1. In case of microscopic simulations, the raw data comes in the form of particle trajectories, therefore a representation of the particle motion in real time and space, domain $(\mathbf{r}, t)$. On the other hand, the experimentally observed quantities in neutron scattering are either in the domain of reciprocal space and real time (intermediate scattering functions, $I(\mathbf{Q}, t)$) or reciprocal time and reciprocal space (scattering functions,

$S(\mathbf{Q}, \omega)$). As mentioned in Section 6.1, the scattering functions are simply a different form of representation of the particle motion and the link between them and the real time and space information is the Fourier transformation in time or space (see Equation 6.1.13).

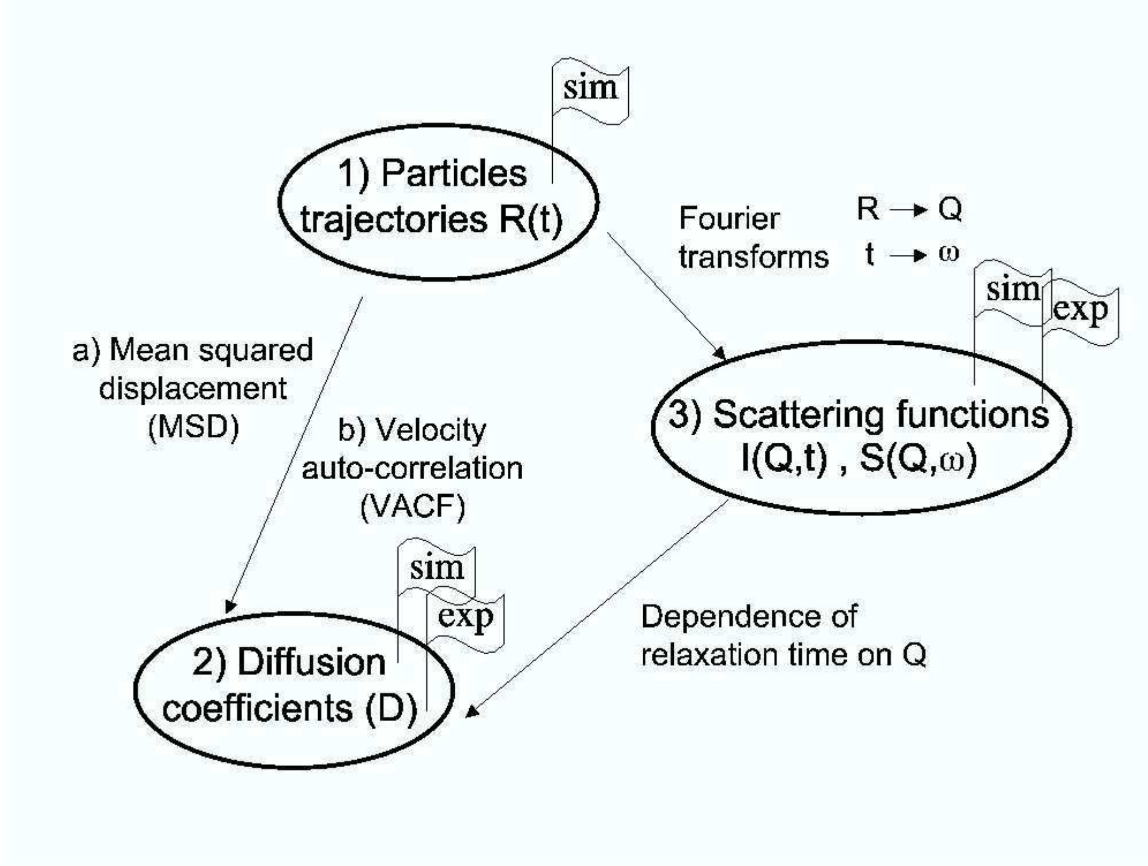

**Figure 7.1: Overview of dynamical data available from simulation and neutron scattering experiments.**

For one level of experiment-simulation comparison, simulated particle trajectories can be used to calculate the corresponding scattering functions (both in the $(\mathbf{Q}, t)$ and $(\mathbf{Q}, \omega)$ domain) and direct comparison with the experimentally observed scattering functions can be made. On the other level, we may wish to characterise the particle motion using a macroscopic property such as the diffusion coefficient. Direct path exists between the raw simulated particle trajectories and this macroscopic property, it entails the calculation of the mean velocity auto-correlation function or the mean-squared displacement of particles in the simulation (see Section 4.2.2). Determination of the diffusion coefficient from neutron scattering data necessitates the interpretation of the experimental scattering functions using the analytical models of particle motion introduced in Section 6.4. Simulated scattering functions can undergo exactly the same treatment (fitting procedure) as the experimental counterparts and thus a second, indirect method for the determination of the diffusion coefficient from simulation is available.

In this study we shall present both the direct comparison of experimental and simulated data on the level of the intermediate scattering function as well as the more indirect comparison on the level of diffusion coefficients.

## 7.3 Experimental details

### 7.3.1 Sample preparation

The clay samples for neutron scattering experiments were prepared according to the following protocol[1].

Natural sodium montmorillonite was obtained by purification and homoionisation of commercial bentonite MX-80. Bentonite (40g) dispersed in de-ionized water ($1\mathrm{dm}^3$) was centrifuged (approx. 20000 g for 30 min) and the top part of sediment re-dispersed in de-ionized water (pH=5, 80°C) by stirring (12 hours, 2 times) to obtain a particular size fraction ($< 2\ \mu$m) of montmorillonite clay particles. This fraction was dispersed in 0.1M NaCl or CsCl solution by stirring (12 hours), repeatedly washed (de-ionized water) until complete removal of $\mathrm{Cl}^-$ ions ($\mathrm{AgNO_3}$ test), dried (heating at 80°C in the presence of a silica gel for a matter of days), crushed and resulting powder stored under dried atmosphere. As determined by Guillaume et al [36], the resulting material is $\mathrm{Cat_{0.76}\ [Si_{7.96}Al_{0.04}]\ (Al_{3.1}Mg_{0.56}Fe^{III}_{0.18}Fe^{II}_{0.16})\ O_{20}(OH)_4}$, where Cat stands for the interlayer counterion, $\mathrm{Na}^+$ or $\mathrm{Cs}^+$ in this case. Dried purified samples (at least 3 days under dry atmosphere) were then equilibrated (3 weeks) at the desired relative humidity (43 %, 95 % and 85-95 % for Na-monolayer, Cs-monolayer and Na-bilayer respectively) at 25 +/- 2°C. The water intake was monitored by mass measurements. The drying of the purified sample before equilibration at a given relative humidity is a crucial step in the sample preparation, due to observed hysteresis in the swelling of clays (causes the appearance of different hydration states at a given relative humidity depending on the initial state). Refer to Section 3.2 for more details on hysteresis, but also on the phenomenon of interstratification (coexistence of different hydration states at a given relative humidity), common in natural clay samples.

---

[1] The samples were prepared by Virginie Marry and Anthony Cadéne

### 7.3.2 Details of experimental set-up

Neutron Spin Echo (NSE) and time-of-flight (TOF) experiments were carried out on the MUSES and MIBEMOL spectrometers in LLB, Saclay, France. NSE measurements (using cold neutrons with incident wavelength ($\lambda_0$) of 5 Å and $\Delta\lambda_0/\lambda_0$ of 0.10 - 0.15) were performed under ambient pressure on 2 mm thick samples. Sample cells were filled under controlled relative humidity and no water loss from the full sample cell was confirmed by weighing throughout the experiment. The montmorillonite samples were fully hydrogenated and thus, to a good approximation, the incoherent scattering signal from the H atoms in the sample was monitored. Polarisation of the scattered neutron beam was measured at carefully chosen Q values, between 0.5 Å$^{-1}$ and 1.8 Å$^{-1}$, in zones of no coherent contribution from the clay structure. As mentioned previously, deuteration of the clay samples in order to exploit the stronger coherent signal (see Section 6.1.1), resulted in a dramatic decrease in the polarisation, most probably due to incomplete exchange of H atoms by D atoms, and deuterated samples were thus not analysed further. By combination of both the NSE and NRSE techniques, correlation times 1 - 86 ps (NSE) and 86 ps - 1 ns (NRSE) were accessible.

Time-of-flight measurements, also of the incoherent signal from the hydrogenated montmorillonite sample (1.5 mm sample thickness) were carried out under reduced pressure (He 200 mbar) at incident neutron wavelength of 9 Å (Q range: 0.21 - 1.30 Å$^{-1}$). This incident neutron wavelength gives resolution of 14 $\mu$eV (HWHM).

## 7.4 Simulation details

Monte Carlo simulations were used to determine the equilibrium layer spacing for a given composition of the interlayer (see Section 4.2.1). Thereafter Molecular Dynamics simulations ($NVE$ ensemble, $t_{step}$ = 0.001ps) traced the motion of the interlayer cations and water, while the clay layers themselves were fixed at the equilibrated positions. Coordinates of all mobile atoms were recorded every 0.02 ps throughout simulations of 655 ps in total length. Trajectories of the constituent hydrogen atoms of interlayer water (not oxygen atoms) were analysed to determine diffusion coefficients using the mean squared displacement (MSD) method (see Section 4.2.2). Due to anisotropy of the system each principal direction was analysed separately. Simulated diffusion coefficients are given as the two-dimensional diffusion coefficients in the $xy$ plane, the plane of clay layers. They were calculated as an average of the one-dimensional diffusion coefficients in the $x$ and $y$ directions. The diffusion coefficient along the $z$ axis, i.e. perpendicular to clay sheets, was zero.

In addition, the incoherent intermediate scattering function, $I_{inc}(Q,t)$, was calculated on the basis of the motion of hydrogen atoms according to the formula

$$I_{inc}(Q,t) = \frac{1}{N_H} \sum_{\forall H} \overline{\langle exp[-i\mathbf{Q} \cdot \mathbf{R}_H(0)] exp[i\mathbf{Q} \cdot \mathbf{R}_H(t)] \rangle}^{Q} \qquad (7.4.1)$$

At every value of $Q$, for each H atom separately, the average of the correlation functions was carried out over 10 Q vectors having the same modulus and being isotropically distributed in space (notation $\overline{\langle ... \rangle}^{Q}$).

## 7.5 Simulated and experimental water content

For the low hydration states of clays studied, the dynamics is likely to be very sensitive to the exact water content in the sample and for any meaningful comparison of the dynamics extracted from the simulation and experiment, the water contents in the simulated and experimental samples should be close. Based on a previous series of simulations [13], we defined the simulated mono- and bilayer state as corresponding to 6 and 12 water molecules per cation respectively, as these water contents reproduce the experimentally observed (X-ray diffraction) interlayer spacing for the given states. Several problems however arise in estimating the water content of the experimental samples and there are two ways in which this was attempted. Firstly, the water content was determined from the difference of mass between the dry and hydrated clay samples. The standard protocol used here for drying clay samples does not result in the complete removal of interlayer water. Approximately one molecule per interlayer cation is still supposed to be present in the resulting dry sample [37]. Adding this uncertainty in the initial water content to the problem of hysteresis in clay hydration and the fact that no two natural clay samples behave exactly in the same way due to structural inhomogeneities, water content estimation by mass measurements has to be interpreted with some care. In case of montmorillonite clays (containing immobile structural H atoms), the water content can also be determined from the limiting value of experimentally measured $I(Q,t)$ at large $t$ (NSE technique). As the content of immobile structural H atoms, giving rise to a constant background in the $I(Q,t)$, is known, it provides means for calculating from the otherwise normalised signal the absolute numbers of the remaining mobile H atoms in the system. However, this second method relies on the observation of a clear plateau in the measured $I(Q,t)$ and as problems with the NRSE technique were experienced in our trials, this was not always achieved. Table 7.1

summarises the water contents for the three samples studied using the above two methods and features for comparison the simulated water content.

| SYSTEM | Water content ($H_2O$ / $Cat^+$) | | |
|---|---|---|---|
| | Exp - from mass | Exp - from $I(Q,t)$ | Simulation |
| Na-bilayer | 9.3 - 11.3 (85 % RH )<br>12.5 - 14.5 (95 % RH ) | 9.3 - 12 (85 % RH )<br>12 - 15 (95 % RH ) | 12 |
| Na-monolayer | 3.0 - 5.0 | 6.1 - 10.5 | 6 |
| Cs-monolayer | 8.0 - 10.0 | 6.1 - 10.5 | 6 |

Table 7.1: Experimental and simulated interlayer water content

In case of the Na-bilayer, the simulated water content (12 $H_2O$ / $Cat^+$) seems to be in-between the contents of the two slightly different experimental samples used. The two experimental methods for water content estimation agree reasonably well with each other. Otherwise, the simulated water content agrees well with detailed analysis of X-ray diffractograms for a Na-montmorillonite phase with interlayer spacing of 15.52 Å corresponding to a bihydrate (see Chapter 8), though note that not exactly the same sample preparation was used in this and the X-ray diffraction study (for the latter relative humidity of 80 % was used). This is a recurrent problem in clay studies, which calls for the unification of the drying and hydration procedures if any meaningful comparison of different techniques is to be attempted.

For the monohydrated systems, a wide range of possible water contents exists when the long-time plateau of the $I(Q,t)$ signals from NSE is considered (10.6 - 6.1 $H_2O$ / $Cat^+$). This was due to problems with the NRSE measurements at high correlation times. Longer correlation times are needed for the clear identification of a long-time plateau in the monolayer systems than in the Na-bilayer, as the decay of the signal is slower (slower dynamics in the monolayer states). Taking into account also the results of mass measurements, the water content in the monolayer systems is most probably towards the lower end of the above range in case of $Na^+$ counterion, but somewhat higher for the $Cs^+$ counterion. The data are clearly less satisfactory than for the Na-bilayer system.

The phenomenon of interstratification during clay hydration was introduced already in Section 3.2. With increasing degree of interstratification the applicability of the simulated system with identical water contents in each interlayer becomes obviously more questionable. It is likely that samples with higher water content will be affected more by interstratification due to more possibilities of water redistribution among individual interlayers.

## 7.6 Dynamics: Comparison of scattering functions

Figures 7.2 and 7.3 compare directly the simulated and experimental (NSE) intermediate scattering functions for the three systems studied, in each case for three Q values as indicated. Simulation predicts decreasing relaxation times (faster dynamics) in the order Cs-monolayer, Na-monolayer, Na-bilayer. In NSE itself the difference between the two monolayers is not clear, but clearly faster dynamics is seen for the Na-bilayer. The agreement between the two methods for a given system is visibly better in case of the monolayers. Never-the-less, even for these systems the simulation results are shifted slightly towards lower relaxation times (faster dynamics). This difference seems accentuated in the bilayer state (difference reaching a factor of approximately 2 between the experimental and relaxation times).

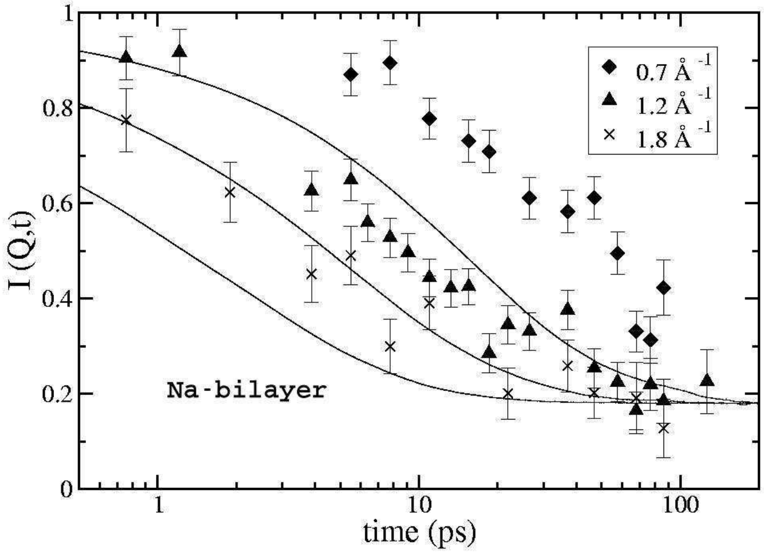

**Figure 7.2: Intermediate scattering functions, $I(Q,t)$, from simulation and Neutron Spin Echo experiments for Na-bilayer system. (Data for sample equilibrated at 85 % relative humidity are presented.)**

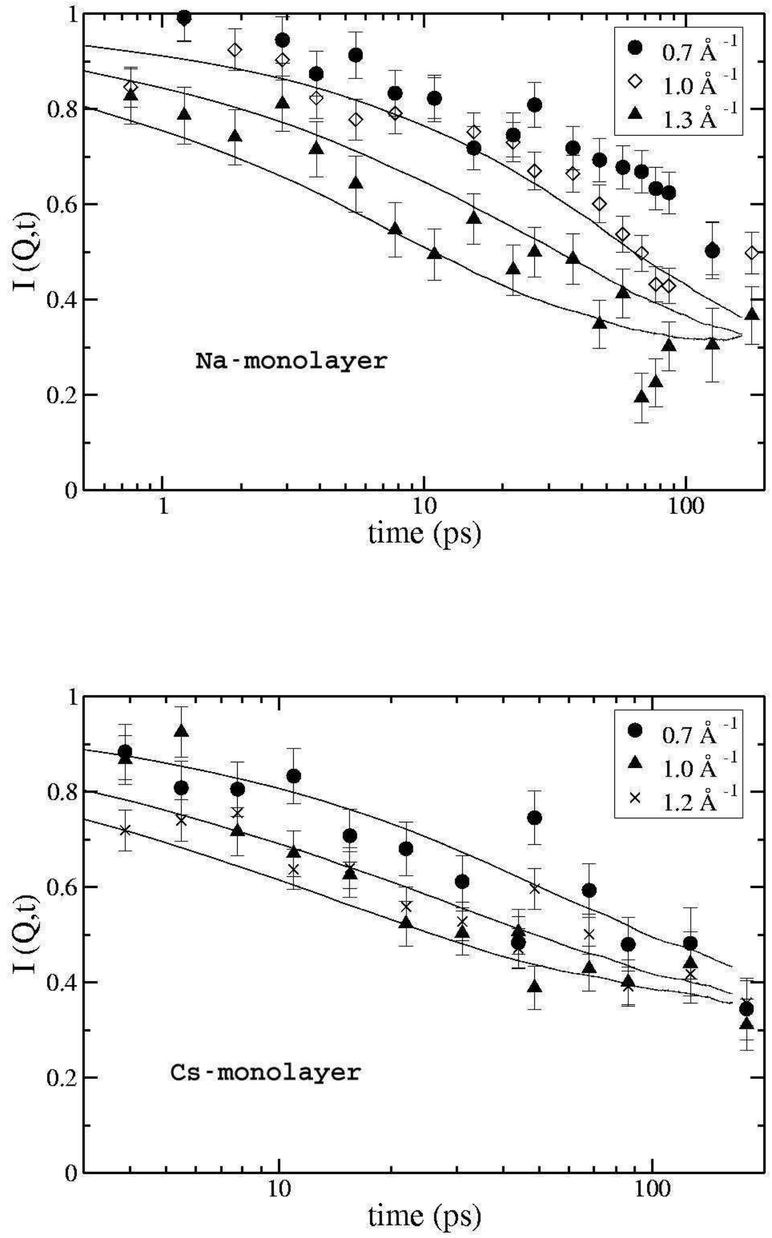

**Figure 7.3: Intermediate scattering functions, $I(Q,t)$, from simulation and Neutron Spin Echo experiments for Na and Cs monolayer systems.**

For the Na-bilayer, which exhibits faster dynamics in the simulation than NSE, the simulated water content (12 $H_2O$ / $Cat^+$) is a slight overestimation of the experimental water content for the sample at 85 % relative humidity as seen from Table 7.1. The agreement with simulation is better when the results of the sample prepared at 95 % relative humidity are used (see later Figure 7.5).

Direct comparison of the above two techniques (NSE and simulation) with the corresponding TOF data is more problematic. As mentioned previously, raw TOF data are in the $(Q, \omega)$ rather than the $(Q, t)$ domain and the effect of the resolution function cannot be eliminated easily as in the case of NSE (overall signal is a convolution of the resolution function and sample signal). Figure 7.4 gives an example of the raw TOF data for a low and high value of $Q$. In general the wider the quasi-elastic broadening observed (as compared to the width of the resolution function), the faster the dynamics probed. As in the case of the NSE technique, the TOF raw data suggests only a marginal difference between the two monolayer systems while it shows clearly faster dynamics in the Na-bilayer.

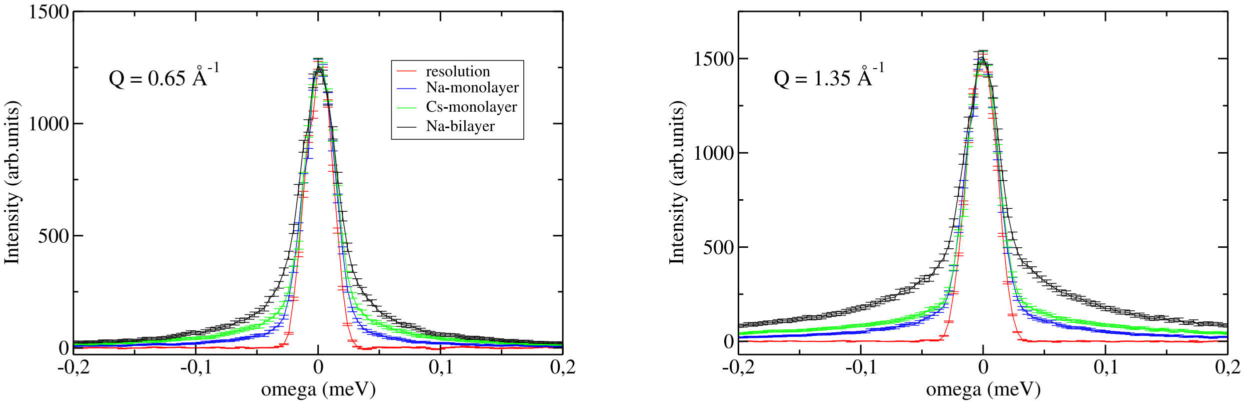

**Figure 7.4: Examples of raw TOF data (in $(Q, \omega)$ domain) for all three systems studied together with the TOF resolution function**

Returning to the issue of direct comparison of NSE, TOF and simulation data, two possibilities exist. (For the sake of simplicity, in the next paragraphs we abbreviate *sample* and *res* to $C$ and $R$ respectively and denote $I(Q, t)$ and $S(Q, \omega)$ as $I$ and $S$ only.) On one hand, the comparison can be done in the $(Q, \omega)$ domain into which the simulated and treated NSE data (treatment according to Equation 6.2.9) are transformed and modified by the TOF resolution function (to obtain $S_R^{TOF} \otimes S_C^{sim,NSE}$) for direct comparison with the raw TOF sample data (path A):

1. $FT^{-1}(t)[S_R^{TOF}] = I_R^{TOF}$
2. $y = \tilde{I}_C^{sim,NSE}\tilde{I}_R^{TOF}$
3. $FT(t)[y] = S_R^{TOF} \otimes S_C^{sim,NSE}$

where superscript $\tilde{}$ refers to the normalised intermediate scattering function, e.g. $\tilde{I}_R^{TOF} = (I_R^{TOF})/(I_R^{TOF}|_{t=0})$. On the other hand, the comparison can be made in the $(Q,t)$ domain, into which the TOF data is transformed with the decoupling of the TOF resolution function and the sample-only signal (to obtain $\tilde{I}_C^{TOF}$) for the comparison with treated NSE data and simulated data [94] [95] (path B):

1. $FT^{-1}(t)[S_R^{TOF}] = I_R^{TOF}$
2. $y = FT^{-1}(t)[S_R^{TOF} \otimes S_C^{TOF}] = I_R^{TOF} I_C^{TOF}$
3. $\tilde{I}_C^{TOF} = \tilde{y}/\tilde{I}_R^{TOF}$

Both of the above transformation paths have weak points. The former path, taking the simulated and already treated NSE data and convoluting them with the TOF resolution function, amounts to a further degradation of the signals themselves. The latter path suffers from deformations during the inverse Fourier transforms of the raw sample data (step B.2) due to the proximity of cut-off of the measured positive energy transfers to the elastic peak (becomes more serious with increasing $Q$ due to increasing broadening of the quasi-elastic signal) as well as uncertainty in the normalisation factors (values at $t = 0$) of the resulting $I(Q,t)$ signals [95]. A further criticism regarding the second path is sometimes raised. It is based on the fact that in reality the TOF resolution function changes its form (shape) as a function of energy transfers and thus the raw TOF sample signal is not a simple convolution (in the mathematical meaning of the term) with the resolution function. As a result, the division step in the $(Q,t)$ domain (step B.3) is not strictly correct for decoupling of the resolution and the sample-only signal.

Overall, it is not obvious which of the above transformation paths is preferable to allow the direct comparison between NSE/simulation and TOF data. We present here the second path for the Na-bilayer system for a wavevector of 1.0 Å$^{-1}$. It was necessary to extrapolate the raw TOF $S(Q,\omega)$ signal into large positive energy transfers (symmetric extrapolation around $\omega = 0$) prior to the inverse Fourier transformation (step B.2) in order to eliminate "ringing" phenomena in the resulting $Q,t$ signal [96]. (Note that $S(Q,\omega)$ symmetric in $\omega$ is justifiable only in the classical approximation - refer to Section 6.1.2). The final $\tilde{I}_C^{TOF}(Q,t)$

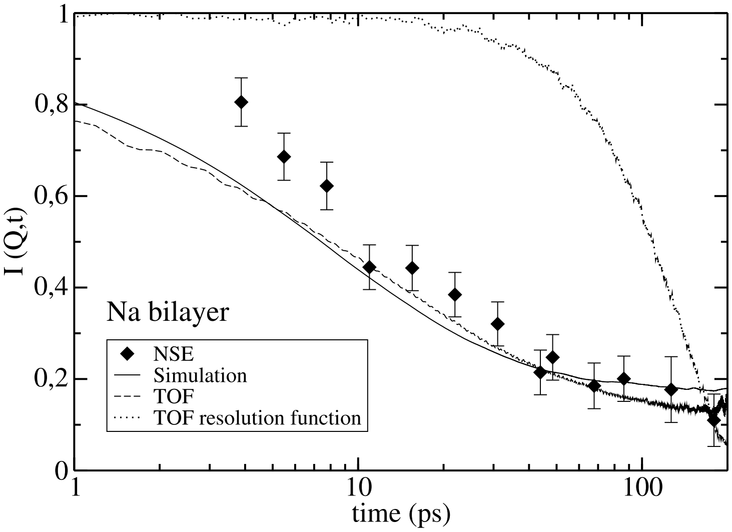

**Figure 7.5: Direct comparison of TOF, NSE and simulation data in the $(Q, t)$ domain.**
**Example shown is of the Na bilayer system and data at Q $\simeq$ 1.0 Å$^{-1}$**

signal is shown in Figure 7.5 together with the simulated and NSE data as well as the TOF resolution function in the $(Q, t)$ domain.

From this Figure TOF data appear very close to the simulation, while both show faster dynamics than NSE. This shall be confirmed, for the wavevector chosen, in the following section in which all three types of data are analysed in terms of a model of atomic motion and the corresponding relaxation times. We do have some confidence in the above TOF $I(Q, t)$ signal and the fact that in this case we were able to neglect the changes in the TOF resolution function throughout the transformation path. The validity check consisted of re-convoluting the above $\tilde{I}_C^{TOF}(Q, t)$ signal with the TOF resolution function, *while taking into account the changes in the TOF resolution function as a function of energy transfers.* This brought us back to the raw TOF sample signal within good accuracy. At the same time, repeating the same procedure for the monolayer states for various wavevectors was not successful. The above re-convolution did not generate the original signal within reasonable accuracy.

In summary, we have attempted to transform the TOF data into the $(Q, t)$ domain for direct comparison with NSE and simulation data. The transformation path involves some difficult steps including the estimation of normalisation parameters for the resulting $I(Q,t)$ signal [95]. While rather successful for the Na-bilayer state, this was not the case for the monolayer systems. The most probable reason is the very narrow quasi-elastic broadening observed for the monolayer states in comparison to the width of the resolution function itself (see Figure 7.4), which introduces significant errors along the transformation path.

The next sections concentrate on the indirect comparison of the three techniques in terms of relaxation times extracted when specific models of motion are applied to fit the observed data. The information from the TOF resolution function in the $(Q,t)$ domain calculated in this section will be of great use. The narrow quasi-elastic broadening of the signal from the monolayer states will be seen again as a source of uncertainties, this time in the extracted relaxation times. The model fitting procedures in the following sections are of comparable complexity to the transformations presented here, especially for the TOF technique, and it seems logical that both the direct and indirect inter-comparison of the various techniques should be pursued further. The lack of attempts at the direct comparison between the TOF and NSE technique in the literature is somewhat puzzling.

## 7.7 Dynamics: Comparison of relaxation times and diffusion coefficients

### 7.7.1 Isotropic continuous translational diffusion: simplest model for low Q region

Section 6.4 outlined the two basic models of translational and rotational motion on the atomic scale and the corresponding shapes of the scattering functions. More precisely, these models were the isotropic continuous translation and isotropic rotation on a sphere. It was also noted that in the low $Q$ region, the dominating term is the simple translational term (see Figure 6.8). In this section we depart from this simple translational term to model the three sets of data (simulation, NSE and TOF) in their respective spatial / temporal domains up to wavevectors of approximately 1.2 Å$^{-1}$. The high resolution TOF measurements (incident neutron wavelength of 9 Å) allow analysis of the quasi-elastic zone in terms of translational motion without a rotational contribution not *only* due to a very low intensity of the trans-rotational term in the low $Q$ region, but also due to resolution considerations (the trans-rotational contribution in form of a wide Lorentzian is seen as a flat background at high resolution). At the same time, TOF measurements for $Q < 0.65$ Å$^{-1}$ could not be analysed due to decreased total scattered intensity, a consequence of sample orientation with respect to the incoming neutron beam.

According to Equations 6.4.10 and 6.4.11 the simulation / NSE and TOF data at a given $Q$ should be fitted with

$$I(Q,t) = Ae^{-t/\tau} + (1-A) \tag{7.7.1}$$

$$\begin{aligned} S^{raw}(Q,\omega) &= A(S_{res}(Q,\omega) \otimes [\frac{1}{\pi}\frac{1/\tau}{(1/\tau)^2+\omega^2}]) + (1-A)S_{res}(Q,\omega) \\ &= A(S_{res}(Q,\omega) \otimes [L(\omega,1/\tau]) + (1-A)S_{res}(Q,\omega) \end{aligned} \tag{7.7.2}$$

where A and $\tau$ are the fit parameters, the latter being the relaxation time (appears in units of time or energy). Note that for the TOF data (Equation 7.7.2), the resolution function still appears explicitly in the equation, the overall raw signal is a convolution of the "true" sample signal and the resolution function. In case of the NSE data (Equation 7.7.1), the resolution function simply multiplies the sample signal and thus after a division (see Equation 6.2.9) we can deal directly with the "true" sample signal.

In real systems however almost always we find deviations from the above exponential and Lorentzian behaviour of the scattering functions. This applies for both experiment and simulation and is linked to the presence of several families of diffusing species with slightly different diffusion coefficients ($D_t$), presence of interface and thus breaking down of the isotropic nature of diffusion etc. A more general model for the low $Q$ region is used extensively instead of the above. It allows for a range of relaxation times in the sample and comes in the form of a stretched exponential

$$I(Q,t) = A\exp[-(t/\tau)^{\beta}] + (1-A), \text{with } 0 < \beta \leq 1 \tag{7.7.3}$$

with both $\beta$ and $\tau$ now as the fit parameters. Decreasing $\beta$ usually indicates a wider distribution of relaxation times. Diffusion coefficient is then extracted from *average* relaxation times $\langle\tau\rangle$ as a function of $Q^2$. The average relaxation time at each $Q$ is

$$\langle\tau\rangle = \frac{\tau}{\beta}\,\Gamma(\frac{1}{\beta}) \tag{7.7.4}$$

where $\Gamma$ indicates the Gamma function, which has a known analytical form. An analytical expression for the analogous stretched Lorentzian does not exist, the modelled signal is generated and modified by the resolution function in the $(Q,t)$ domain, the result is then Fourier transformed numerically into the $(Q,\omega)$ domain for comparison with the raw TOF sample data.

For the clay systems studied here, we applied Equation 7.7.3 to the simulation and NSE data (fitting range approximately 1 - 300 ps for the two techniques) , as simple exponential behaviour was clearly seen not to be obeyed. In case of the TOF data, the data modelling is more complex involving the convolution with the resolution function and initially only the simple Lorentzian in modelling of the TOF data was applied (fitting range -0.2 meV to 0.2 meV, due to cut-off in the positive energy transfers). Later trials with a stretched Lorentzian produced very little difference to the average relaxation times as a function of $Q$. An example of the raw experimental data with the corresponding fits is shown in the case of Na-bilayer in Figure 7.6 for both NSE and TOF techniques.

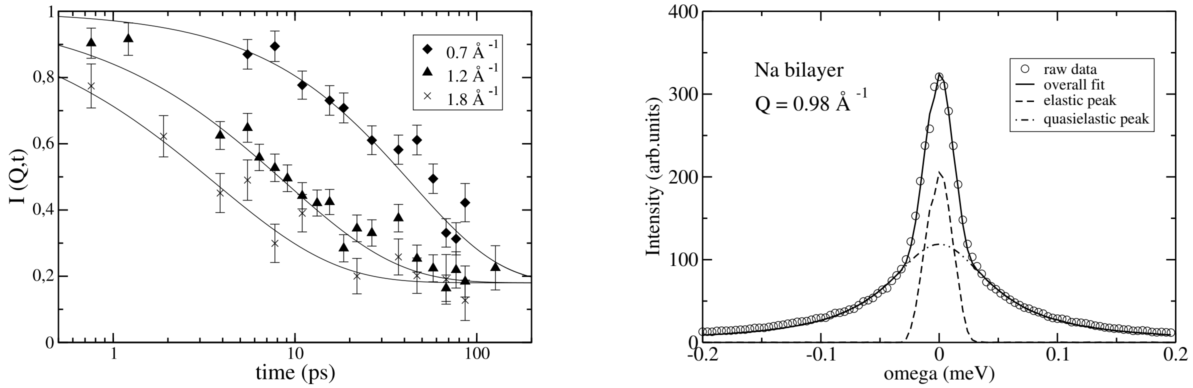

**Figure 7.6: Examples of experimental data together with stretched exponential (Lorentzian) fits for the NSE and TOF techniques.**

After the extraction of characteristic relaxation times as a function of $Q$ from the above model functions, we analysed the limiting slope as $Q \rightarrow 0$ in the plot of $1/\tau$ (or $1/\langle\tau\rangle$) versus $Q^2$ which is equal to the translational diffusion coefficient. (According to the continuous isotropic translational diffusion model $1/\tau = D_t Q^2$ and thus the slope should be the same across the entire range of $Q$. In reality this is not always seen and levelling off of the curve at high $Q$ is seen as a signature of jump rather than continuous diffusion. This breakdown of the continuous diffusion model at high $Q$ is discussed in the next section.) The plots of $1/\tau$ (or $1/\langle\tau\rangle$) versus $Q^2$ corresponding to the three systems studied are summarised in Figures 7.7 and 7.8.

Table 7.2 summarises the *approximate* diffusion coefficients determined from the limiting slopes (as $Q \rightarrow 0$) of data sets in the above Figures. In addition Table 7.2 contains

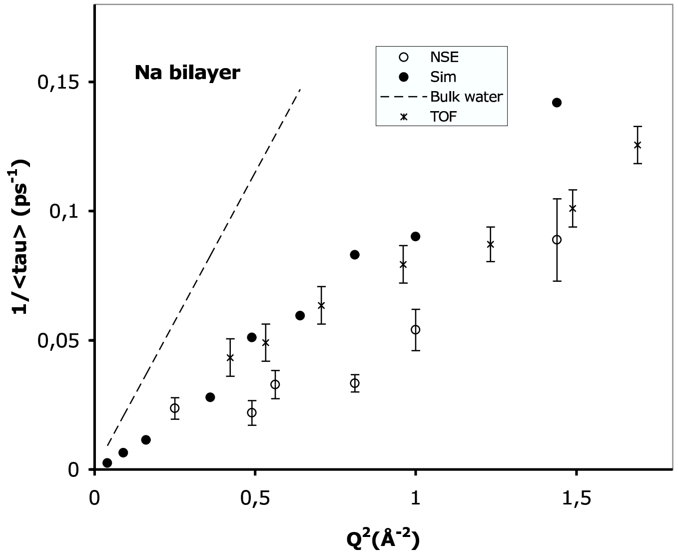

**Figure 7.7: Plot of $1/\langle\tau\rangle$ versus $Q^2$ in the low $Q$ range for Na-bilayer system The inverse relaxation time is extracted from modelling the experimental data with a single translational term without rotational contribution.**

three-dimensional simulated diffusion coefficients determined by the MSD method - refer back to Sections 7.2 and 5.5 for the MSD method and conversion between two- and three-dimensional diffusion coefficients.

| SYSTEM | (D) × $10^{-10}$ m$^2$ s$^{-1}$ | | | |
|---|---|---|---|---|
| | Sim | Sim (from MSD) | NSE | TOF |
| Na-bilayer | 10.0 | 8.1 ± 0.3 | 5.0 | 10.0 |
| Na-monolayer | 2.5 | 3.8 ± 0.2 | 2.5 | 8.0 |
| Cs-monolayer | 1.5 | 2.8 ± 0.3 | 1.5 | 11.0 |

**Table 7.2: Approximate diffusion coefficients (D) for the three clay systems studied
Determination from the limiting slopes (as $Q \to 0$) of inverse relaxation times $(1/\tau)$ plotted versus $Q^2$ as well as three-dimensional simulated diffusion coefficients from the MSD method in case of simulation.**

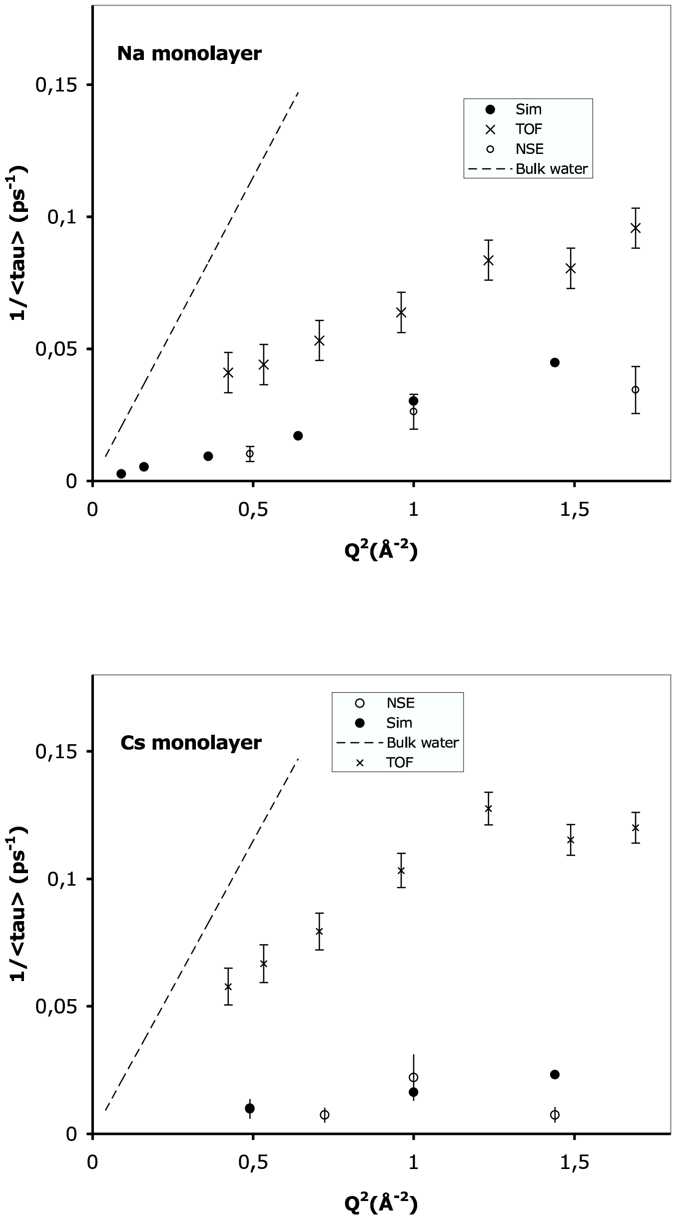

**Figure 7.8: Plot of $1/\langle\tau\rangle$ versus $Q^2$ in the low $Q$ range for Na and Cs monolayer systems**
**Details as for Figure 7.7**

The significance of relaxation times featured in Figures 7.7 and 7.8 has to be interpreted with some care. As individual data points arise from fitting of experimental and simulated data with *stretched* exponentials (or their equivalent in the $(Q, \omega)$ domain), the signals are characterised by *average* relaxation time, in which a number of dynamical phenomena are most certainly mixed (with increasing $Q$, $\beta$ exponents decreased down to 0.5 indicating a severe departure from a mono-exponential behaviour). Further, the difficulty in extracting diffusion coefficients from these representation is clear. Primarily it is the lack of necessary points at small $Q$ values for the two experimental techniques and deviations from linear trend for the data points present. Keeping all the above limitations in mind but also the fact that direct comparison at least between the NSE and simulation without any fitting procedure is also available from Section 7.6, the following can be drawn from the data. We turn first to the comparison between the direct and indirect methods of extracting diffusion coefficient from simulation and later on comment upon the relaxation times determined from experiment and simulation.

We have been somewhat uncertain regarding the exact values that should be used in the comparison between the direct and indirect paths of determining the diffusion coefficient from simulation. It seems most correct to compare the indirectly determined value (from Q-dependence of relaxation times of simulated intermediate scattering functions) to the three- rather than two-dimensional value from the MSD method. As the fitting of the simulated intermediate scattering functions used in this section uses an isotropic model of translational diffusion, isotropic analysis should also be applied in the MSD method to extract a three-dimensional diffusion coefficient. Remembering that the *same* particle trajectories are at the beginning of each of the paths, the differences between the two diffusion coefficients can be viewed as an indication mainly of the errors that are introduced during the fitting procedure of the simulated intermediate scattering functions and distortions that arise when the motion is characterised using the average relaxation times from stretched exponentials.

Regarding the simulation-experiment comparison, in the bilayer state the TOF and simulation shows somewhat faster dynamics than NSE itself, as was already seen from the direct comparison. On the other hand for the monolayer systems a very different picture arises, with NSE and simulation being in very good agreement (consistent with direct comparison) while TOF measurements indicate considerably faster dynamics in both monolayer states. While the TOF data for the bilayer state is consistent with diffusion coefficients from previous TOF studies, this is not the case for the monolayer data, the current TOF data show significantly faster dynamics [89] [90] [87]. At this point it is very instructive to mention again the range of correlation times available by the three techniques. While simulation and NSE can probe correlation times up to approximately

300ps, for the TOF technique the cut-off comes much before, around 70-100ps. Figure 7.9 features the TOF resolution function in the $(Q,t)$ domain for the apparatus used and compares it to the decay of the signal (NSE) in the three systems studied.

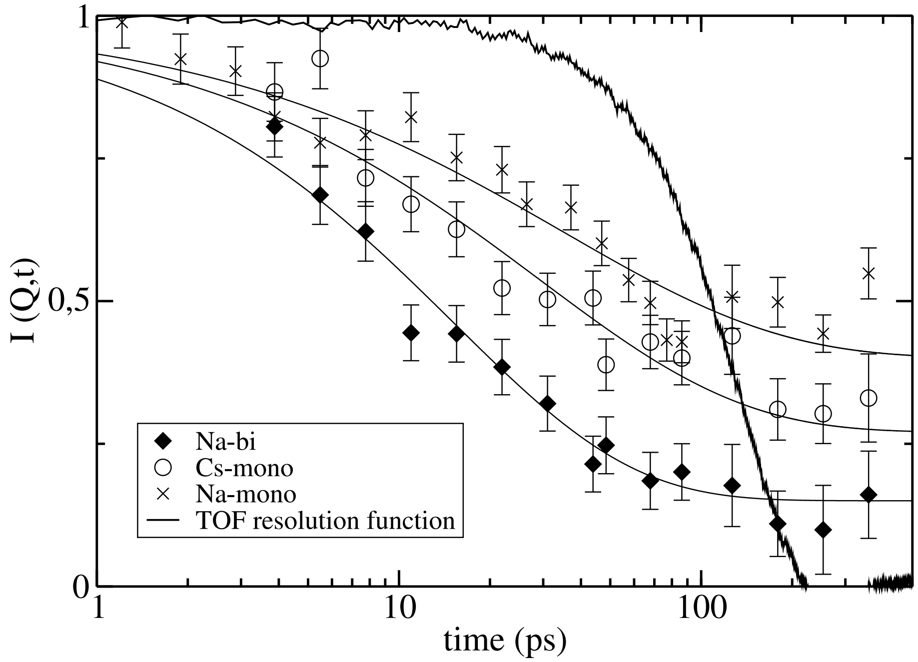

**Figure 7.9: Decay of the TOF resolution function in the $(Q,t)$ domain compared to the NSE data for the three systems studied.**
**NSE data for all three systems correspond to Q = 1.0 Å$^{-1}$**

As can be seen for the $Q$ value shown, the TOF technique probes into sufficiently high correlation times to see the decay of all the mobile H atoms in the Na-bilayer system, but the case is marginal for the Na-monolayer and Cs-monolayer system. A proportion of the slow moving H atoms (relaxation times beyond 70-100ps) in the latter two systems will be seen as immobile by the TOF technique. Thus they contribute to elastically scattered intensity and are excluded from the dynamical analysis shifting the overall relaxation times to lower values, i.e. faster dynamics. In addition, the effect of this low TOF resolution cut-off is more pronounced with decreasing $Q$, slower decay of the signal, and thus affects the most the low $Q$ region from which the overall diffusion coefficient is extracted. Note that the extracted average relaxation times for the Cs-monolayer systems are most certainly an underestimate as the raw TOF data (see Figures 7.4) shows clearly slower dynamics in Cs-monolayer than Na-bilayer and this is contradicted by the average relaxation times from the model fitting.

In summary, the agreement between the NSE and simulated data for the monohydrated systems is very good, as was already indicated by the direct comparison of $I(Q,t)$ signals. The faster dynamics indicated by TOF is most probably a consequence of insufficiently long correlation times probed. The quasi-elastic broadening of the monolayer systems was very narrow in comparison to the width of the TOF resolution function, which reformulates the problem: the TOF technique cannot distinguish in the monolayer states the immobile and slowly moving H atoms in the system, it overestimated the intensity of the elastic scattering and thus underestimates the resulting relaxation times.

Following the reasoning of accessible correlation times for the three techniques, for the Na-bilayer system we would expect a very good agreement between NSE, simulation *and* TOF as the times probed by TOF are now sufficiently long for the relaxation of all the mobile H atoms in the interlayer (refer back to Figure 7.9). Figure 7.7 is then perhaps a slight disappointment, as the NSE data show slightly slower dynamics than the other two techniques (TOF and simulation), which agree rather well. As the Na-bilayer system has the highest water content out of the three samples, interstratification is more of an issue than in the monolayer states and could be responsible for some of the observed differences between simulation and NSE, which agreed very well for the monolayer states. If this is true, how then do we account for the differences between the two *experimental* data sets ? At the same time, the difference is of a factor of 2 at most in the inverse TOF and NSE relaxation times for the Na-bilayer and considering the complexity of the two experimental techniques but also of the clay system itself, the data could be just as well treated as being in good agreement. The crucial test would be comparing TOF and NSE measurements from the same, *physically* the same, clay sample to avoid any potential difference in hydration states.

### 7.7.2 Continuous versus jump diffusion

The model of continuous isotropic translation predicts a constant slope of the plot of $1/\tau$ versus $Q^2$ equal to $\mathrm{D}_t$. As seen from Figures 7.7 and 7.8, some indication of levelling off of the TOF data towards the high-$Q$ end is suggested, especially for the Na-bilayer and Cs monolayer systems. This behaviour has been repeatedly seen by TOF for several systems and is commonly interpreted by a jump rather than continuous translation model [76].

Making the transition from a continuous diffusion to a diffusion by jumps between sites of mean three-dimensional separation $\langle r^2 \rangle$ (various distributions of site separations can be applied, here we refer to the commonly used Gaussian distribution) and residence time $\tau_{res}$ in each site, the HWHM or $1/\tau$ of the Lorentzian modelling the scattering function in the $(Q, \omega)$ domain changes from $\mathrm{D}_t Q^2$ to

$$\mathrm{HWHM}(Q) = \frac{1}{\tau_{res}}[1 - e^{-Q^2 \langle r^2 \rangle / 6}] \tag{7.7.5}$$

In the limit of small $Q$, $\mathrm{HWHM}(Q) = Q^2 \langle r^2 \rangle / (\tau_{res} 6)$ , which can be identified again as $\mathrm{D}_t Q^2$ with $\mathrm{D}_t = \langle r^2 \rangle / (\tau_{res} 6)$ as in the description of diffusion by random walk [55]. So in this limit the continuous and jump diffusion models are identical. In the limit of high $Q$, $\mathrm{HWHM}(Q) = 1/\tau_{res}$. In other words the inverse residence time is the high $Q$ asymptotic limit in the plots of HWHM or $(1/\tau)$ versus $Q^2$.

In TOF studies on clays, evidence of a plateau at high $Q$ is commonly seen and the data are thus analysed using the above jump-diffusion model with the Gaussian distribution of jump lengths [90] [89] [87]. This analysis gives access to the diffusion coefficients of water, residence time and mean-squared jump lengths between sites. Appearance of the plateau was seen when raw TOF data were analysed using two Lorentzians representing translational and rotational motion as well as using a more simplistic approach with a single Lorentzian for translational motion. Data in a recent NSE study on clays were also interpreted using a jump-diffusion model, however, in this technique the evidence for a plateau was much weaker due to a lack of points and significant error bars in the high-Q region [72].

From the data presented here, it is rather difficult to conclude whether jump diffusion is the better description of water diffusion in clays as compared to continuous diffusion. The only technique that suggests any jump-diffusion is the TOF. No plateau is seen towards the high end of the $Q$ range considered in the simulation and NSE data. The difference has been sometimes attributed to the incorrect comparison of relaxation times from stretched exponentials on one hand (NSE, simulation here) and a HWHM of a simple Lorentzian on the other (TOF) [97] [98]. This is unlikely to be the only reason, our own attempt at analyzing the TOF data using a stretched Lorentzian has produced only small change to the overall shape of the TOF curve.

For a convincing argument in favour of either the jump or the continuous diffusion, reliable data for high $Q$ values are necessary as this is the regime in which the two models diverge. Data sets (simulation, NSE and TOF) in Figures 7.7 and 7.8 stop at a wavevector of about 1.2 Å$^{-1}$ as beyond this limit the simple translational model is likely to be insufficient due to rotational coupling (refer back to Section 6.4). If we continue, while keeping

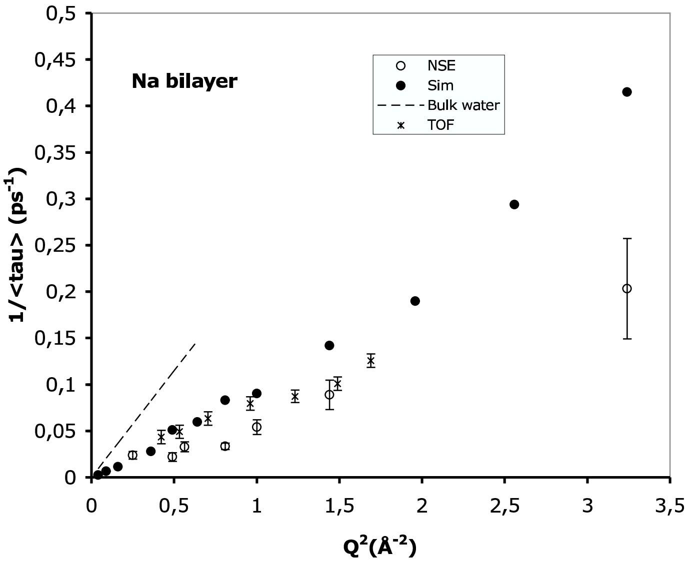

**Figure 7.10: Plot of $1/\langle\tau\rangle$ versus $Q^2$ for Na-bilayer system over a large range of $Q$.**
**The inverse relaxation time is extracted from modelling the experimental data with a single translational term.**

in mind the limitation, with the same treatment into the high $Q$ values, the situation becomes as shown in Figure 7.10. In the simulated data set the gradient increases in the high-$Q$ region, but the experimental sets lack the necessary points to indicate the presence or absence of a plateau.

The same linear dependence without the appearance of a plateau has been reported in other modelling studies on neighbouring clays [97] [99] which used the simple translational model function at high $Q$. Even in cases when the rotational contribution is properly taken into account, an agreement between simulated and experimental TOF data (showing a plateau) is not obvious in the high $Q$ region, as shown in a detailed study on polymer solutions [100]. For bulk water itself, the situation is not entirely clarified. While a plateau at high $Q$ values has been observed for water in many quasi-elastic neutron scattering studies, especially for water under super-cooled [101] [102] or confined [103] [104] conditions, simulation data do not reproduce this behaviour [105] [98]. At the same time, slightly different descriptions emerge regarding jump diffusion of water (surface water on zirconium oxide [106]), introducing fixed jump-lengths and thus a slight maximum in the inverse relaxation time versus $Q^2$ curve, before a plateau is reached. In summary, at this stage we cannot present a convincing argument for or against either of the jump and continuous water diffusion in clay systems, especially not on the basis of analysis which neglects rotational contribution to the scattering functions, as is the case here.

### 7.7.3 Bounded translational diffusion: towards more complex a model in the low Q region:

Considering the particular geometry of the interlayer in the low hydrated clay systems, which can be considered as space confined between two parallel planes, the applicability of the isotropic translational diffusion model used in Section 7.7.1 is in the least questionable. This applies especially in the low $Q$ region, where the spatial scale of observation $(2\pi/Q)$ is larger than the separation of the confining clay layers. We thus consider here a anisotropic diffusion between two planes and the resulting forms of the scattering functions.

It has been shown analytically that for a geometry of two-parallel plates separated by distance $M$ in the $z$ direction, the scattering function $S(Q,\omega)$ is of the form

$$S(Q,\omega) = \sum_{n=0}^{\infty} A_n(Q_\perp M) L_n(\omega, D_\| Q_\|^2 + \frac{n^2\pi^2 D_\perp^2}{M^2})] \tag{7.7.6}$$

where $L_n(\omega)$ are Lorentzians of the shown HWHM, subscripts $\perp$ and $\|$ denote the projections perpendicular and parallel to the clay layers (refer to Figure 7.11 for the description of the system in terms of these projections) and the intensities $A_n(Q_\perp M)$ are of a known analytical form [107] [108] [109]. In the limit of $M \longrightarrow 0$ and thus $D_\perp \longrightarrow 0$, Equation 7.7.6 simplifies to the case of a two-dimensional diffusion

$$S_{2d}(Q,\omega) = L(\omega, D_\| Q_\|^2) = L(\omega, D_\| Q^2 \sin(\theta)^2) \tag{7.7.7}$$

where the angle $\theta$ is as defined in Figure 7.11. In the limit of $M \longrightarrow \infty$, Equation 7.7.6 comes again to the case of unbounded isotropic diffusion with $S(Q,\omega) = L(\omega, DQ^2)$. In the case of clay systems we are clearly in the regime of small $M$. As we saw in the simulation study, the diffusion coefficient in the direction perpendicular to the clay layers is zero and as a result, we could reasonably consider the water diffusion in clays as a two-dimensional diffusion.

Note that Equation 7.7.7 contains the angle $\theta$ as an additional variable, in other words the signal measured now depends on the orientation of the clay layers in the system with respect to the scattering wavevector (the direction of the incident neutron beam). Measuring the

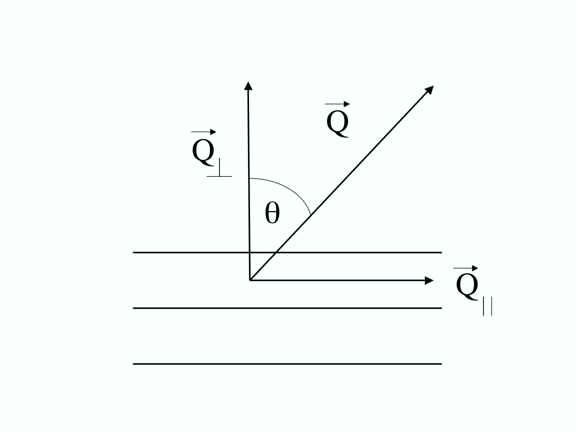

**Figure 7.11: Description of the clay system in terms of projections of wavevectors parallel and perpendicular to the clay layers.**

signal from a powder sample of clay particles, with random orientations of the clay layers with respect to the incident neutron beam, we have to consider the powder average of Equation 7.7.7, in other terms

$$\langle S_{2d}(Q,\omega)\rangle_\theta = \int_0^\pi L(\omega, D_\| Q^2 \sin(\theta)^2)\frac{1}{2}\sin\theta d\theta \tag{7.7.8}$$

The corresponding expression in the $(Q,t)$ domain is

$$\langle I_{2d}(Q,t)\rangle_\theta = \int_0^\pi e^{-D_\| Q^2 \sin(\theta)^2 t}\frac{1}{2}\sin\theta d\theta \tag{7.7.9}$$

The issue of the powder average from a two-dimensional diffusion has been treated in detail most recently by Lechner et al, who has considered the differences in the S$(Q,\omega)$ signals from three-dimensional and powder-average two dimensional diffusion [110]. It was pointed out that the principal feature of the powder averaged two-dimensional diffusion is a logarithmic singularity at zero energy transfers ($\omega = 0$) or in other words divergence of the elastic scattering intensity. This originates from the situations when the scattering wavevector is perpendicular to the plane of the clay layers. As in this direction the motion is restricted or localised due to the confinement, the neutron is scattered elastically. (Remembering the discussion in Section 6.1.3, we re-iterate that this appearance of elastic intensity in case of confined translational motion is a similar concept to the appearance of elastic intensity when rotational motion is considered, another example of localised motion.) In practice the elastic intensity in case of powder averaged two-dimensional diffusion does not diverge due to finite resolution of the apparatus, but its significant increase is expected as compared to the three dimensional diffusion. However, as noted by Lechner et al, the difference in the quasi-elastic region between the two modes of diffusion is minimal. (In case of systems, for which the more likely mode of motion is a question to be answered, it is suggested that the most appropriate way of *distinguishing* the two modes is the consideration of the elastic scattering intensity at constant $Q$ as a function of increasing resolution [110]. Other studies have considered the overall form of the scattering function, modelled it with various two- and three-dimensional diffusion models while searching simply for the best fit to the experimental data amongst all the models [106]. The differences between the quality of the various fits are however never spectacular.)

In the case of low hydrated clay powder samples, we could simply assume that powder averaged two-dimensional diffusion is the mode of diffusion and continue with the appropriate analysis to extract a two-dimensional diffusion coefficient. However, viewing the rather complex forms of Equations 7.7.8 and 7.7.9 as opposed to their three-dimensional counterparts, we should indeed consider whether the precision of the data is sufficient to see a difference of the two modes. If this is not the case, the complex fitting procedure with expression for the powder-averaged two-dimensional diffusion might not be worth the effort. That this is indeed the case for the current NSE experimental data on clays is illustrated in Figure 7.12 for the case of Na-bilayer.

Three theoretical curves are shown corresponding to 1) a simple exponential term, Equation 6.4.3, modelling isotropic translational diffusion with $D_t = 5 \times 10^{-10}$ m$^2$ s$^{-1}$ (value taken from Section 7.7.1), 2) a simple exponential term, analogue of Equation 7.7.7 in the $(Q,t)$ domain, modelling 2D diffusion with $D_\parallel = 7.5 \times 10^{-10}$ m$^2$ s$^{-1}$ (3/2 value of the three-dimensional value was taken - see Section 5.5), this would correspond to the signal detected for $Q$ vectors in the plane of a two-dimensional diffusion and 3) more complex expression, Equation 7.7.9 modelling powder (isotropic) average of the two-dimensional diffusion, as the signal from a powder clay sample. As can be seen from Figure 7.12, the accuracy of the data is sufficient to differentiate the first two cases (simple exponential terms differing by a factor of 3/2 in their relaxation times), however the powder averaging of the two-dimensional diffusion brings the $I(Q,t)$ curve very close to the three-dimensional isotropic case and both curves fall within the experimental error bars. In other words, the accuracy of the NSE data is insufficient to justify the complex two-dimensional analysis. A similar comparison could be made in the $(Q,\omega)$ domain for the case of the raw TOF sample data, but the theoretical curves would have to be convoluted with the TOF resolution function (see Section 7.6). Instead, we attempted directly to model the raw TOF sample data with the $Q,\omega$ analogue of Equation 7.7.9. It proved unsuccessful, we suspect the

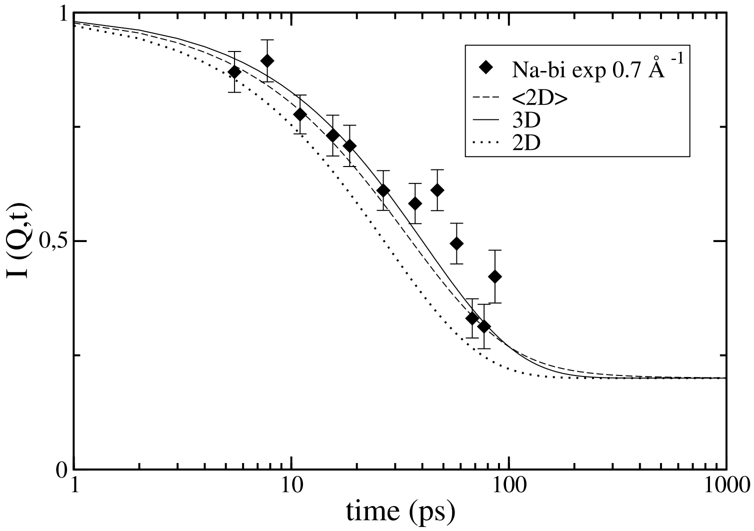

**Figure 7.12: Comparison of NSE data and two- and three-dimensional model of translational diffusion in case of Na bilayer.**
**Curves "3D", "2D" and "⟨ 2D ⟩" correspond respectively to isotropic diffusion, two dimensional diffusion (signal that would be detected for wavevectors in the plane of the diffusion, this does not apply directly to the powder clay samples studied here) and powder averaged two-dimensional diffusion.**

reason is similar as in the NSE case.

## 7.8 Geometry of confinement and elastic incoherent structure factor

In the previous sections we discussed at length the dynamic information extracted from the decay of the intermediate scattering functions or broadening of the scattering functions. We noted that for a given scattering wavevector $Q$, immobile scatterers contribute to a constant background in $I(Q,t)$ and to intensity at zero energy transfers (i.e. elastic peak intensity) in $S(Q,\omega)$. In this section we look in more detail at the percentage of immobile scatterers seen at different values of $Q$ or the Elastic incoherent structure factor, $EISF(Q)$. As shall be seen, this *static* quantity can give information on the geometry of confining media in which scatterers diffuse.

$EISF(Q)$ is formally defined as the limit of the intermediate scattering function $I(Q,t)$ as $t \to \infty$. In practice however, both in neutron scattering and simulation, measurements are carried out over a finite range of relaxation times (limited on one hand by the experimental set-up and on the other by the length of simulation), and thus the experimental / simulated $EISF(Q)$ is never the formally defined quantity but applies to the timescale probed. For the NSE method, $EISF(Q)$ has been taken simply as the long-time value of the intermediate scattering function at a given value of $Q$. The same could be done for the simulated intermediate scattering functions, but in case of simulation $EISF(Q)$ can also be calculated according to

$$EISF(Q)_{sim} = \frac{1}{N_H} \sum_{\forall H} \overline{\langle |exp[-i\mathbf{Q}\cdot\mathbf{R}_H]|^2 \rangle}^{Q} \tag{7.8.1}$$

$\mathbf{Q}$ is the wavevector, $\mathbf{R}_H$ the position of an H atom and notation $\overline{\langle ... \rangle}^{Q}$ corresponds to an average over several $Q$ vectors of the same modulus distributed isotropically or otherwise in space [111]. Note that the above equation gives the same result as taking the actual long-time value of the simulated intermediate scattering function calculated according to Equation 7.4.1. Passing from the $(Q,t)$ to the $(Q,\omega)$ domain of the TOF technique, $EISF(Q)$ is now calculated according to

$$EISF(Q)_{TOF} = \frac{I_{el}}{I_{el} + I_{qel}} \tag{7.8.2}$$

in other words, at a given value of $Q$ it is the ratio of the elastic and total scattered intensities.

Prior to presenting the $EISF(Q)$ data determined by the three techniques for the clay systems studied, it is instructive to consider the expected form of $EISF(Q)$. In general, two families of H atoms (scatterers with dominating incoherent cross-section) are to be distinguished in the clays investigated. These are the structural H atoms (OH groups in clay layers) and constituent H atoms of interlayer water molecules. In order for any of the scatterers to be seen as mobile the spatial and temporal scales of their atomic motion and of the observation have to match as was already discussed in Section 6.1.3. From previous knowledge of the clay systems, the structural H atoms were expected to be seen as immobile on the time-scale of the neutron scattering experiments and the data in the previous sections are consistent with this. In simulation the structural H atoms were immobile by construction (rigid clay layers). Rather straight-forwardly, this family of immobile scatterers contributes to a constant background in the $EISF(Q)$ with height corresponding to the fraction of structural H atoms in the overall H atom content. On the other hand, the $EISF(Q)$ signal from the family of diffusing H atoms in the interlayer is more complex. Concentrating at first on the match of the temporal scales of motion and observation, it was noted in Section 7.6 that while the timescale of all three techniques matched well the relaxation times of interlayer H atoms for the Na-bilayer system at the wavevectors presented (all greater than 0.7 $\text{Å}^{-1}$), this was no longer the case for the monohydrated systems. In particular, the resolution of the TOF technique, presented in the $(Q,t)$ domain, decayed faster than the sample signal itself as determined by the NSE and simulation. As a result, some of the slowly diffusing interlayer H atoms are seen as immobile by the TOF technique and an increase in the $EISF(Q)$ is likely for the monohydrated systems at any value of $Q$ and for the Na-bilayer system perhaps for $Q > 0.7$ $\text{Å}^{-1}$. Further issue is the confinement of the translational motion of H atoms in the interlayer. It was mentioned in section 6.1.3 that scatterers carrying out localised motion such as rotation or confined translation can be seen as immobile when the spatial observation scale $(2\pi/Q)$ is greater than the dimension of the localisation. The case of rotation as three-dimensionally localised motion was analysed in Section 6.4 and was shown to give rise to a specific form of $EISF$ (Bessel function of zeroth order). A very similar treatment would apply to three-dimensionally confined translation, such as translational within a spherical pore [73]. The case of clay systems is however more complex as we deal here with confinement between two planes or confinement in one dimension only. The analytical form of the *one-dimensional* scattering function *in the direction of the confinement*, or $S(Q_\perp M, \omega)$ for the case of two clay layers separated by a distance $M$ is

$$\begin{aligned} S(Q_\perp M,\omega) &= A_0(Q_\perp M)\delta(\omega) + \sum_{n=1}^{\infty} A_n(Q_\perp M) L_n(\omega, \frac{n^2\pi^2 D_\perp^2}{M^2})] \\ &= \frac{2[1-cos(Q_\perp M)]}{(Q_\perp M)^2}\delta(\omega) + \sum_{n=1}^{\infty} A_n(Q_\perp M) L_n(\omega, \frac{n^2\pi^2 D_\perp^2}{M^2})] \qquad (7.8.3) \end{aligned}$$

where the notation of Section 7.7.3 has been adopted, with $Q_\perp$ being a wavevector perpendicular to the clay layers [107] [108]. However, the overall three-dimensional scattering function $S(Q,\omega)$ for $Q$ along any direction in space (with components $Q_\perp$ and $Q_\parallel$) is

$$\begin{aligned} S(Q,\omega) &= \frac{2[1-cos(Q_\perp M)]}{(Q_\perp M)^2} L(\omega, D_\parallel Q_\parallel^2) + \\ &\quad + \sum_{n=1}^{\infty} A_n(Q_\perp M) L_n(\omega, D_\parallel Q_\parallel^2 + \frac{n^2\pi^2 D_\perp^2}{M^2})] \qquad (7.8.4) \end{aligned}$$

therefore a combination of Equation 7.8.3 with Lorentzians of finite widths, representing unbounded diffusion in the direction parallel to clay layers. The function represented by $A_0(Q_\perp L)$ no longer represents the intensity modulation of the elastic peak (in other words $EISF(Q)$), rather it modulates the intensity of the first Lorentzian of Equation 7.8.4 [107]. For oriented clay samples, where it is possible to measure the signal along a $\mathbf{Q}$ perpendicular to the clay layers ($Q_\parallel = 0$ in Equation 7.8.4), an $EISF$ would be still expected in the form of $A_0(Q_\perp M)$. However, for randomly oriented clay samples this is no longer the case as any given wavevector $\mathbf{Q}$ has a non-zero projection in the plane of the clay layers for at least some clay particles in the sample and thus a finite width of the $L(\omega, D_\parallel Q_\parallel^2)$ appears. The form of the resulting $EISF(Q)$ in the randomly oriented case is thus rather complex, possibly a damped version of the $A_0(Q_\perp L)$ function.

In summary we expect a constant background in the $EISF(Q)$ arising from the structural H atoms in clay layers. In addition to that, further increase in $EISF(Q)$ can be either the result of what we refer to as an "apparent" $EISF(Q)$ due to insufficiently large relaxation times probed and thus slowly moving scatterers appearing as immobile or the result of spatial confinement of the motion giving rise to a "true" $EISF(Q)$. As far as experiments are concerned, the form of the "true" $EISF(Q)$ is rather complex due to the random orientation of the clay particles in the sample. In case of simulation, $EISF(Q)$ is at first calculated as for a collection of randomly oriented clay particles to allow comparison with the experimental data, however later the motion of the interlayer H atoms is analysed in its projections parallel and perpendicular to the clay layers and the results compared to the analytical expression of the expected "true" $EISF(Q)$ as shown in Equation 7.8.3 for the one-dimensional confinement. This decoupling of particle motion along chosen directions is possible only for the simulation data and no comparison to experiment can be carried out as oriented experimental samples were not used. As shall be seen the exercise is never-the-less highly instructive for differentiating the temporal and spatial origins of the observed $EISF(Q)$.

Figures 7.13 and 7.14 summarise the experimentally determined $EISF(Q)$ and the simulated counterparts calculated according to Equation 7.8.1 using an average over 10 isotropically distributed wavevectors at each value of $Q$. In each of the figures we indicate, both for simulation and experiment, the expected height of the constant background in $EISF(Q)$ arising from structural OH groups. Note that this is unfortunately not always exactly the same for the simulated and experimental system of a given type. Beginning with the results of the Na-bilayer, the agreement of the three methods is very good in the range shown, down to $Q = 0.7$ Å$^{-1}$ the three sets do not show any increase with respect to the expected constant background. In this system the background is very close for the simulation and experiment (similar water contents). Below $Q = 0.7$ Å$^{-1}$ the simulated data show an upward trend. It is certain that this is at least partially an "apparent" $EISF(Q)$, it was possible to check directly that the simulation length of 655 ps was not sufficient to trace the complete decay of the intermediate scattering functions for the low $Q$ values in this system.

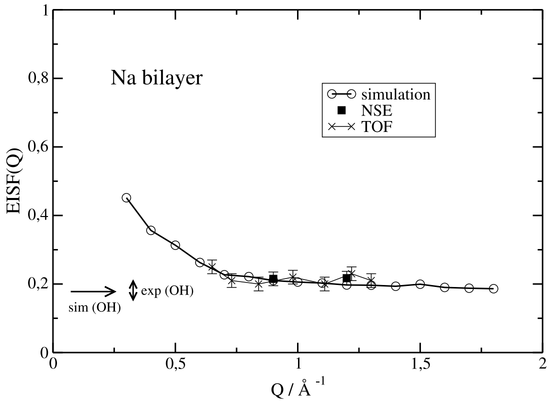

**Figure 7.13: Elastic incoherent structure factor for Na bilayer system determined by NSE, TOF and simulation (isotropic calculation in case of simulation).**

The results for the monolayer states are at first sight much less satisfactory. The levels of the constant background in simulation and experiment are now further apart, but this is partially a consequence of the overall lower water content in the samples and thus the differences between simulated and experimental background levels being accentuated in $EISF(Q)$ as it is a *normalised* quantity. Regarding the simulated data for both monolayer systems, it appears higher than the expected constant background over the entire $Q$ range. Due to slower dynamics than in the Na-bilayer state this could be seen as a more severe form of the "apparent" $EISF(Q)$. (Note that in the fitting procedure of the simulated intermediate scattering functions to extract relaxation times, even if the entire curve could not be generated from the simulated trajectories of 655 ps in length, the theoretical constant background corresponding to structural OH was imposed in the exponential fit and *not* the $EISF(Q)$ values given here. As a result the effect of the simulation length on the extracted relaxation times was much less severe than might be thought viewing the $EISF(Q)$ data here.) Comparing then the two sets of experimental data, we note that in both monolayer systems the TOF set is higher than the NSE counterpart. If we assume that the experimental samples in the two cases had the same water content (though note

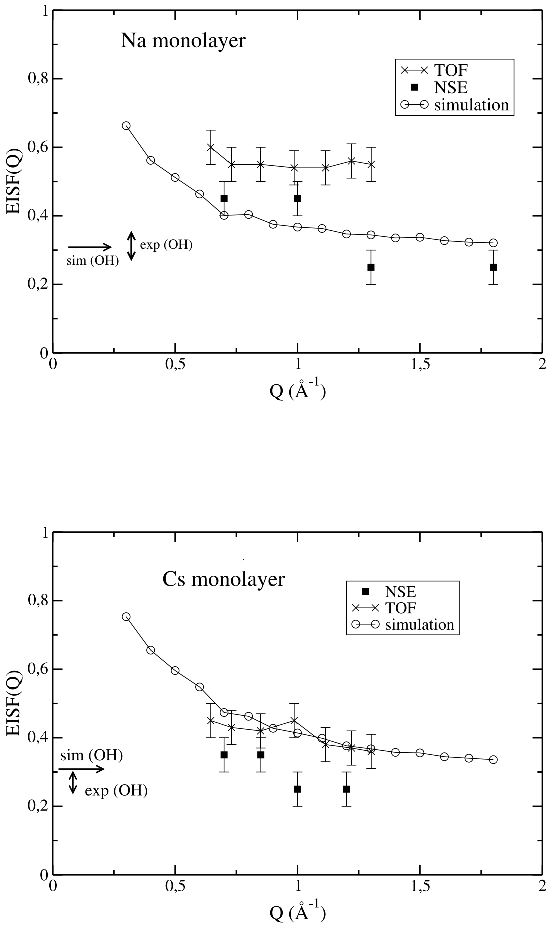

**Figure 7.14: Elastic incoherent structure factor for Na and Cs monolayer systems determined by NSE, TOF and simulation (isotropic calculation in case of simulation).**

that physically different samples were used, some differences are thus inevitable and they shall be accentuated in the normalised $EISF$ signal), this observation is consistent with the conclusion of the previous section: due to very narrow broadening of the quasi-elastic signal with respect to the TOF resolution, TOF overestimates the elastic intensity (and thus $EISF(Q)$) and as a result underestimates the relaxation times (predicts faster dynamics). At the same time, the raw TOF sample data can be fitted, for the monolayer states, with a wide range of ratios for the intensities of the elastic and quasi-elastic peaks as their respective broadenings become almost indistinguishable. The error bars for the

TOF sets in Figure 7.14 are thus very difficult to determine (the effect is smaller on the average relaxation time extracted). Last point is that both experimental sets do indicate an increase in the $EISF(Q)$ signal as $Q$ decreases.

In Figures 7.13 and 7.14 it is very difficult to distinguish the spatial (referred to here as the "true" $EISF(Q)$) and temporal (referred to here as the "apparent" $EISF(Q)$) origins of the observed increase in $EISF(Q)$ towards lower $Q$ values. This is true for both the simulated and experimental data presented. It is only with the aid of simulation, which enables calculating the $EISF(Q)$ restricted to one or two dimensions, that we arrive at decoupling the two contributions. Figures 7.15 and 7.16 summarise simulated $EISF(Q)$ data determined from particle trajectories using the formula 7.8.1, where the average over $Q$ vectors was carried out in three distinct ways: 1) 10 $Q$ vectors distributed in 3D (isotropic), case presented previously, 2) 10 $Q$ vectors distributed in the XY plane, the plane of the clay layers, 3) 1 $Q$ vector in the Z direction, i.e. perpendicular to the clay layers. The isotropic and XY analysis gives apparently similar results, whereas the analysis along Z shows a distinctly different behaviour. Analysing the system in the XY plane, we consider the motion of interlayer H atoms in directions that are not bound, on the other hand analysis along Z gives us the signal for a highly confined motion between the adjacent clay layers. The isotropic case is a combination of these two extremes.

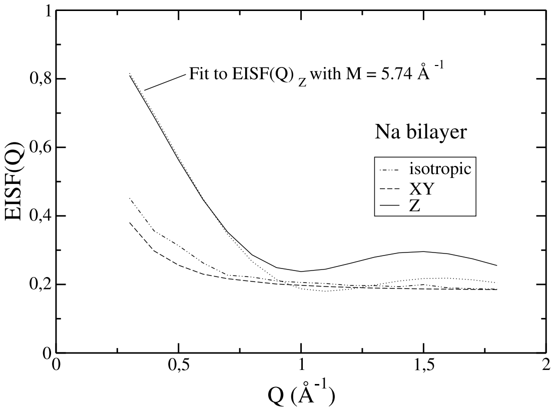

**Figure 7.15: Elastic incoherent structure factor for Na bilayer system determined by simulation for various spatial components of the particle motion. XY corresponds to the plane of clay layers, Z direction is perpendicular to the clay layers.**

Focusing only on the family of mobile interlayer H atoms, i.e. on the variation of the

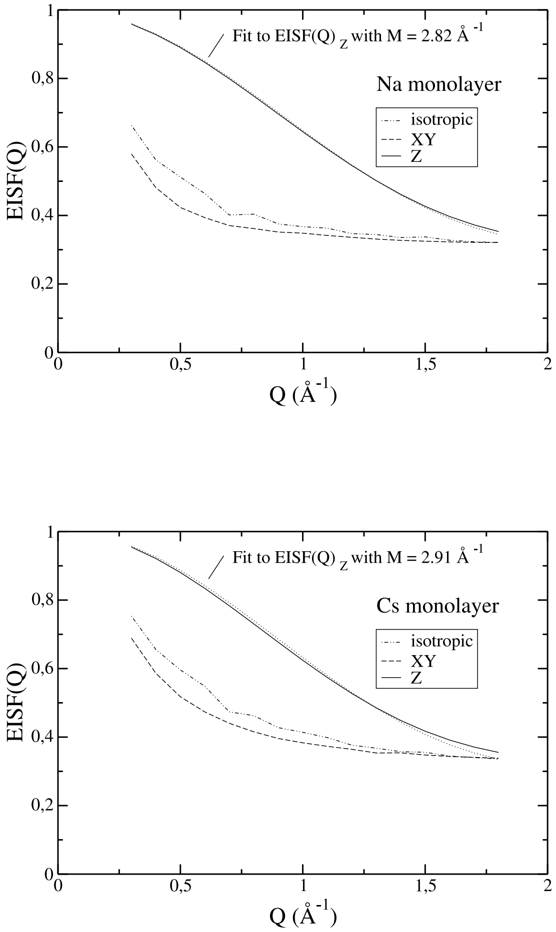

**Figure 7.16: Elastic incoherent structure factor for Na and Cs monolayer systems determined by simulation for various spatial components of the particle motion.**
**XY corresponds to the plane of clay layers, Z direction is perpendicular to the clay layers.**

*EISF* signals *above* the constant background corresponding to structural OH (0.31 and 0.18 for the model mono- and bihydrated systems respectively), the following is seen. For the $EISF(Q_{XY})$ signal, with decreasing $Q$ (increasing distance of correlation) an increase is observed. Knowing that the H atoms are not spatially bound in the XY plane, the increase in stationary H atoms must be an "apparent" EISF resulting from the limited simulation time. This is well demonstrated on Figure 7.17 where the results of three different simulations runs are presented. The transition from 72ps to 360ps to 720ps run is accompanied by a significant decrease in the $EISF(Q_{XY})$ values at low $Q$. In the limit $t_{sim} \rightarrow \infty$, the signal should be the background constant, its level corresponding to the percentage of structural H atoms. Turning to the analysis along the Z direction, the $EISF(Q_Z)$ signal has a very different form. It has already been shown that for the confining geometry between two parallel plates, the resulting *one-dimensional* EISF signal is a Bessel function of the zeroth order (refer back to Equation 7.8.3). Fitting the $EISF(Q_Z)$ data for the three systems studied (arising from simulation of 720 ps for the bilayer system and 360 ps for the monolayer systems) with this theoretically predicted form, we arrive at realistic plate (clay layer) separation of 5.74 Å, 2.79 Å and 2.83 Å for Na-bi, Na-mono and Cs-monolayer respectively. These distances correspond very well to the vertical space that H atoms explore during the simulation, as can be seen directly from individual particle trajectories (refer back to Figures 5.5 and 5.7). The evolution $EISF(Q_Z)$ as a function of simulation length can be seen in Figure 7.17. Under a certain critical length (for the bilayer system it was 720 ps) the $EISF(Q_Z)$ does not resemble a Bessel function as the time is insufficient for the H atoms to explore fully the space available in the Z direction (the signal is yet again a superposition of true and apparent EISF). As the length of the simulation increases the form of $EISF(Q_Z)$ decreases to the appropriate Bessel function, (form of the true EISF signal for this geometry of confinement). Further increase in the simulation length would result in no additional change, the Bessel function form is the limiting form for the $EISF(Q_Z)$. Note that for the monolayer systems, simulation length of 360 ps was sufficient to recover the appropriate Bessel function form. We note that in the high-$Q$ region the simulated EISF signal is not seen to descend to the Bessel Function form (unlike the low-$Q$ region). This is unlikely to be improved by longer simulation times, it is a phenomenon at high $Q$, therefore on a small spatial scale. It is likely that in this high-$Q$ region, $EISF(Q)$ signal from the *rotational* motion of the hydrogen atoms, the other form of *localised* motion in the system, has non-negligible contribution. This might be highlighted by decoupling the translation (CoM motion of the overall water molecule) and rotational motion of the constituent H atoms. This is easily done in simulation and we are currently carrying out the first trials for the clay systems studied here.

It can be finally appreciated that the simulated isotropic $EISF(Q)$ for clays (one-dimensionally confined systems) is a complex mixture of the true and apparent EISF signal and its detailed interpretation is almost impossible. This is of course also the case for the experimentally determined $EISF(Q)$ from powder clay samples.

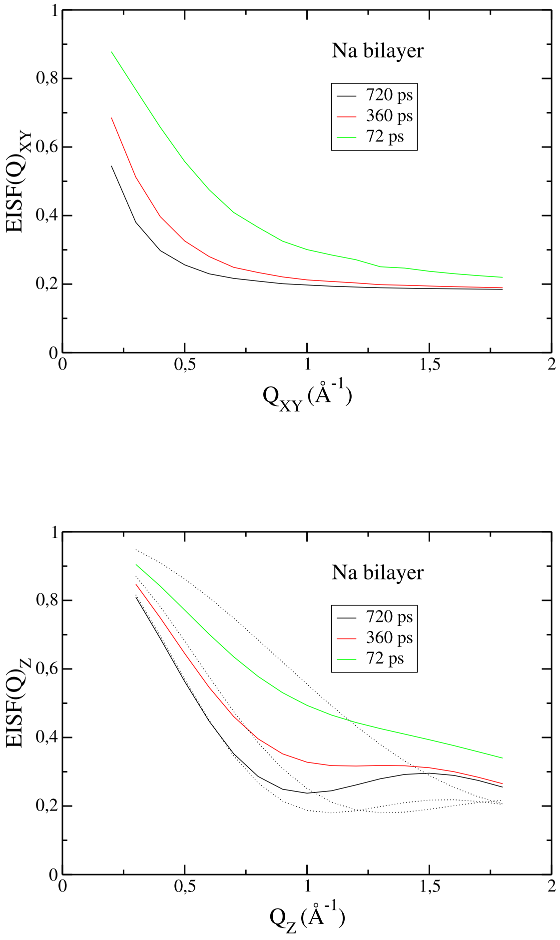

**Figure 7.17: Influence of simulation time on the observed EISF signal both in the plane of the clay sheets (XY) and the direction perpendicular to them (Z) The dotted lines in the bottom figure trace the best fits of a Bessel function form to the three EISF signals. The simulated EISF is clearly far from a Bessel function form for short simulations and approaches it as simulation time increases.**

## 7.9 Conclusion

Regarding the dynamics of water in Na- and Cs- monohydrated montmorillonite samples, the simulation and NSE results show a very good agreement, both giving diffusion coefficients of the order of 1-3 × $10^{-10}\mathrm{m}^2\mathrm{s}^{-1}$. The TOF technique has been seen to significantly underestimate water relaxation times (therefore overestimate water dynamics, by a factor of up to 3 and 7 in the two systems respectively), primarily due to insufficiently long correlation times probed.

In case of the Na-bihydrated system, the TOF results are in a closer agreement with the other two techniques (techniques differ by a factor of 2 at most, both simulation and TOF yield diffusion coefficient of approximately $10 \times 10^{-10}\mathrm{m}^2\mathrm{s}^{-1}$, while the NSE data gives approximately $5 \times 10^{-10}\mathrm{m}^2\mathrm{s}^{-1}$). Water dynamics in this system is faster than in the monohydrated counterparts and the cutoff of measurable correlation times in TOF poses no longer a severe problem. At the same time, the close agreement between NSE and simulation seen in the monohydrated systems is lost in the Na-bilayer case. The phenomenon of interstratification of the real clay system, likely to be more important a factor in this most hydrated sample, can account for some differences between the simulated and NSE relaxation times. In case of the natural Na-bilayer montmorillonite clay presented here, the 001 peak (as seen by neutron diffraction) was significantly broadened (HWHM 1 Å), pointing to the above phenomenon. At the same time, it is after all possible that simulation no longer reproduces the correct dynamics in the bilayer system due to inappropriate potentials used.

In terms of real experimental systems, low hydration states might appear as an advantage as we avoid several water environments in the sample (interstratification of interlayers, water in larger porosities) rendering the model clay system with a single type of interlayer more applicable. At the same time, for monohydrated systems inevitably weaker signals are obtained, simply due to an overall lower water content, and the slow dynamics might fall out of the commonly used range of correlation times, as seen in the case of the TOF spectrometer used here. Note that only a *combination* of the three different techniques used here allowed the identification of this type of mismatch.

Apart from the study of relaxation times, attention has been paid to the incoherent structure factor ($EISF$), giving in theory information on the geometry of confinement of the diffusing species. Due to the one-dimensional nature of confinement in clays and the use of powder clay samples, the analysis of experimentally observed $EISF$ is not straightforward. Simulation has played a key role in understanding the various contributions to $EISF$ in clay systems and in clearly distinguishing the *spatial* and *temporal* origins of this quantity, inherently present both in experiment and simulation.

At this stage, we look towards other clay systems, in one aspect or another simplified versions of montmorillonite. In overcoming the problem of interstratification, a promising candidate is a synthetic hectorite clay, which is prepared under carefully controlled conditions resulting in a homogeneous charge distribution on the clay layers [27]. As already observed by neutron diffraction, the hectorite system exhibits a very sharp transition from monohydrated to bihydrated interlayers as relative humidity is increased (i.e. very narrow humidity range of co-existence) and very thin diffraction peaks at each stage indicating a much narrower distribution of interlayer spacings for each state. Figure 7.18 summarises the inverse average relaxation times versus $Q^2$ for a Na-bihydrated hectorite sample, showing an excellent agreement between the TOF and NSE data in the low $Q$ region. The corresponding simulation data for the hectorite system is being currently generated.

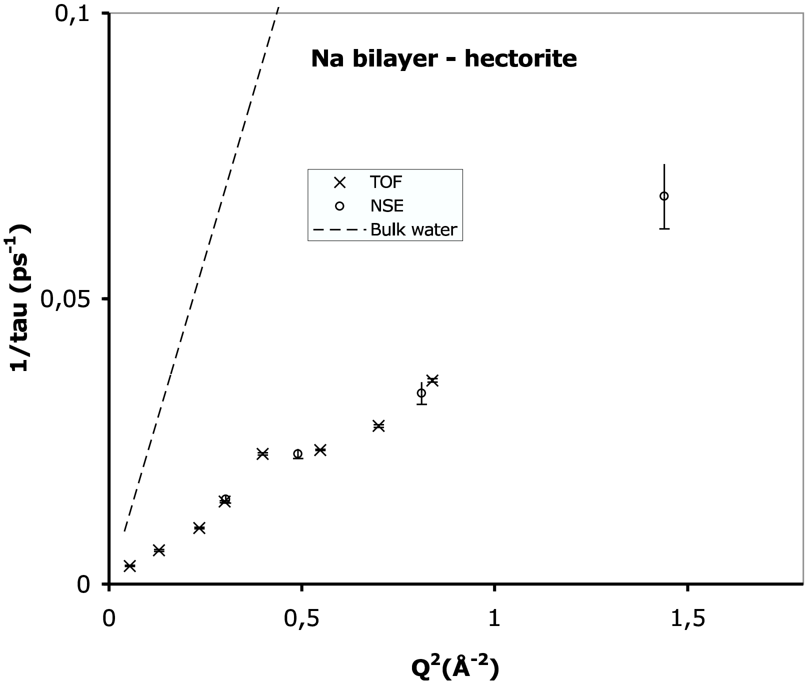

**Figure 7.18: Plot of $1/\langle\tau\rangle$ versus $Q^2$ in the low $Q$ range for Na-bihydrated hectorite system, NSE and TOF data only.**
**The inverse relaxation time is extracted from modelling the experimental data with a single translational term without rotational contribution.**

Another complication of montmorillonite systems is the small size of their particles. Apart from favouring the formation of large-scale porosities (mesopores, macropores), preferential orientations of the sample with respect to the neutron beam are almost impossible to achieve. Vermiculite clays, mentioned several times already, form particles on the scale of millimeters and have already been exploited to study anisotropy of diffusion in clays as preferential orientations of the clay particles are easily achieved [72] [91]. The use of oriented vermiculite samples and data collection at a range of resolutions as suggested by Lechner et al [110] could provide a highly convincing set of experimental data supporting the two-dimensional nature of water diffusion in clays.

# Chapter 8

# Further Topics

## 8.1 Combining X-ray powder diffraction and microscopic simulation

Static information from Monte Carlo simulations, more precisely the distribution of interlayer atoms, aided here in the modelling of the 00L reflections of high resolution X-ray diffractograms in case of bihydrated sodium montmorillonite.

On the basis of X-ray diffractograms, a new configuration was proposed for the interlayer structure in bihydrated sodium montmorillonite with cations located in the mid-plane of the interlayer and $H_2O$ molecules scattered around two main positions with Gaussian-shaped distributions. Previous models used only planes of water molecules in the interlayer with some positional disorder resulting from thermal motion. The new interlayer configuration generates an X-ray pattern that is significantly closer to the experimentally observed data and its credibility is further supported by Monte Carlo simulation. The water content associated with the proposed configuration matches closely the amount of interlayer water determined independently from water vapour adsorption/desorption isotherm experiments.

For further details see published article of Eric Ferrage et al in the annex.

# Chapter 9

# General Conclusion

Montmorillonite clays in low hydration states, with $Na^+$ and $Cs^+$ compensating counterions, have been investigated here by a combination of modelling/simulation and experimental techniques to obtain information on the local structure and dynamics of the interlayer species (water and counterions). The atomic scale phenomena in the interlayer of clays are a key for understanding the macroscopically observed water and ionic retention capacity of these systems.

At the same time as exploiting the predictive power of simulation studies, it is necessary to assess the applicability of the model to real systems. Both of these paths are explored here. At first the predictions of simulation into dynamics of water and ions in clays at elevated temperatures are presented (within the temperature range pertinent for the radioactive waste disposal scenario). These results show a marked difference between the modes of diffusion of the $Na^+$ et $Cs^+$ counterions which persists over the entire temperature range. In terms of water dynamics, a significant step towards bulk water behaviour is seen on transition from the monolayer to bilayer states. The second major part of the study is the detailed comparison between simulation and quasi-elastic neutron scattering regarding ambient temperature water dynamics. Overall, the two approaches are found to be in good agreement with each other. Albeit a minor part of the research work presented here, the comparison between simulation and high resolution X-ray diffraction studies concerned with details of water distribution in the interlayer is another successful attempt to bridge the domains of simulation and experiment.

Only from the comparison between various techniques, is it possible to appreciate the limitations of any one of them. This was clearly shown here in the case of the time-of-flight neutron scattering technique when studying water dynamics in the monohydrated systems. At the same time questions have arisen from the simulation - experiment comparison about the applicability of the model clay system itself. In view of interstratification in the real clay samples or water in other than the interlayer porosity, the model systems accounting only for a single type of interlayer seem too simplistic. The strength of the mutual assessment of different techniques when applied to study the same phenomenon is perhaps the most important message resulting from this study.

The realm of microscopic simulation of clays is moving towards non-rigid models for clay layers as well as water molecules [112]. Other aspects, such as clay edge effects, might require a transition entirely away from classical microscopic towards *ab-initio* descriptions [113]. In the comparison between simulation and neutron scattering regarding diffusion in clays, the issue is at present more the simplification of the experimental system, rather than adding complexity to the model itself (example is the synthetic hectorite clay briefly presented here). Further unresolved topics regarding dynamics of the interlayers species by neutron scattering include clear demonstration of the anisotropy of water diffusion as well as any kind of information on the cationic diffusion itself.

While being initiated by the potential application of clays as constituents of the engineered barrier around radioactive waste, this atomic-scale study cannot provide direct answers regarding the long-term properties of the barrier itself. Rather, it should be viewed as an essential link in a chain of approaches at different scales, which all have to be combined in order to arrive at an in-depth understanding of the processes involved. Within the framework of research into radioactive waste disposal, transport of water and ions in clays has been studied extensively both on the microscopic (atomic) and macroscopic scales (tracer experiments [5] [6] [4]) and at present the appropriate model-experiment comparison is available only for each of these observation scales separately. The great challenge that remains is to establish the connection between these two limits of description of the system.

# Chapter 10

# Conclusion Générale

Les argiles de type montmorillonite dans des états de faible hydratation et avec des cations compensateurs $Na^+$ et $Cs^+$ ont été étudiées ici par un ensemble de modélisation/simulation et de techniques expérimentales afin d'obtenir les informations sur la structure locale et la dynamique des espèces interfoliaires (eau et cations). Les phénomènes à l'échelle atomique dans l'espace interfoliaire sont à l'origine des propriétés de rétention de ces systèmes observées à l'échelle macroscopique.

Simultanément à l'exploitation des puissances prédictives de la simulation, il est nécesasaire de s'assurer de l'applicabilité du modèle aux systèmes réels. Ces deux voies sont explorées ici. Premièrement, les prédictions de la simulation sur la dynamique de l'eau et des ions interfoliaires aux températures élevées sont présentées dans la gamme des températures pertinentes pour le scénario du stockage des déchets radioactifs. Ces résultats montrent une différence notable entre les modes de diffusion des deux cations compensateurs, $Na^+$ et $Cs^+$, qui persiste sur toute la gamme de températures considérées. Pour la diffusion de l'eau, un pas significatif vers le comportement de l'eau "bulk" est observé dans la transition entre l'état mono- et bihydraté. La deuxième partie principale de ce travail concerne la comparaison détaillée des simulations avec la diffusion quasi-élastique des neutrons, ceci dans le cadre de la diffusion de l'eau à température ambiante. Les deux approches sont globalement en très bon accord. Finalement, nous présentons une comparaison entre la simulation et les études de diffraction de rayons X à haute résolution qui concerne la distribution détaillée de l'eau interfoliaire. Même si ce n'est qu'une partie annexe de la recherche présentée dans ce manuscript, elle jette à nouveau et avec succès un pont entre les disciplines de la simulation et de l'expérience.

Il n'est possible d'appréhender les limites des différentes techniques qu'en les comparant les unes aux autres. Cela a été clairement démontré ici dans le cadre de la diffusion des neutrons par la technique de temps de vol pour la dynamique de l'eau dans les systèmes mono-hydratés. Par ailleurs, la comparaison des simulations et des expériences a soulevé la question de la pertinence du modéle d'argile utilisé en simulation. En effet, le système modèle qui ne prend en compte qu'un seul type d'espace interfoliaire parait trop simplifié, notamment en raison de l'interstratification dans les échantillons d'argiles réels et de la présence d'eau hors des porosités interfoliaires. Le message le plus important qui frappe à l'issue de ce travail est probablement la force de l'utilisation de différentes techniques lorsqu'elles sont appliquées à l'étude d'un même phénomène.

Le domaine de la simulation microscopique des argiles évolue vers les modèles de feuillets d'argiles et de molécules d'eau non rigides [112]. D'autres aspects, comme les effets de bords des argiles, peuvent necessiter une transition de la description classique vers les approches *ab-initio* [113]. Dans la comparaison des données dynamiques entre la simulation et la diffusion des neutrons, les avancées actuelles se basent plutôt sur la simplification des systèmes expérimentaux que sur l'augmentation de la complexité des systèmes modèles. Le système de l'hectorite synthétique introduit ici en est un très bon exemple. Une démonstration claire de l'anisotropie de la diffusion de l'eau ainsi que toute information sur la diffusion des cations sont d'autres sujets non résolus concernant la dynamique des espèces interfoliaires par diffusion des neutrons.

Bien qu'initié par les applications potentielles des argiles comme constituants des barrières ouvragées autour des déchets radioactifs, cette étude à l'échelle atomique n'a pas vocation à donner de réponse directe sur le comportement à long terme de la barrière elle même. C'est dans un ensemble plus vaste combinant des approches à toutes les échelles, dont la présente étude forme un maillon essentiel, que ce comportement pourra être appréhendé. Dans le cadre de ces recherches sur le stockage des déchets radioactifs, le transport de l'eau et des ions dans les argiles a été très largement étudié, aussi bien à l'échelle microscopique (niveau atomique) qu'à l'échelle macroscopique (expériences avec traceurs [5] [6] [4]). Aujourd'hui, une comparaison convenable entre modèles et expériences n'existe que pour chacune de ces échelles d'observations prise séparément. Le défi majeur à ce jour est d'établir un lien entre les deux limites extrêmes de description du transport dans les argiles.

# Bibliography

[1] L. Fowden, R. M. Barrer, P. B. Tinker - editors. *Clay Minerals: Their structure, behaviour and use;* Royal Society - London, 1984.

[2] B. Velde. *Introduction to clay minerals;* Chapman and Hall, 1992.

[3] R.F. Giese, C.J. van Oss. In *Surfactant science series*, Vol. 105; Marcel Dekker, 2002.

[4] ANDRA. *Referentiel Materiaux, Tome 2 : Les Materiaux argileux;* Rapport C.RP.AMAT.01.060, 2001.

[5] M. Molera, T. Eriksen. *Radio. Acta* **2004**, *90*, 753–760.

[6] C. Daqing, T. Eriksen. *Radio. Acta* **1998**, *82*, 287–292.

[7] R. W. G. Wyckoff. In *Crystal Structures*, Vol. 4; John Wiley and Sons, 1968.

[8] K. Norrish. *Disc. Faraday Soc.* **1954**, *18*, 120–134.

[9] L.L. Schramm, J.C.T. Kwak. *Clays and Clay Minerals* **1982**, *30*, 40–48.

[10] I. Bérend, J.M. Cases, M. Francois, J.P. Uriot, L.J. Michot, A. Masion, F. Thomas. *Clays and Clay Minerals* **1995**, *43*, 324–336.

[11] J.M. Cases, I. Bérend, M. Francois, J.P. Uriot, F. Thomas, J. E. Poirier. *Langmuir* **1992**, *8*, 2730–2739.

[12] J.M. Cases, I. Bérend, M. Francois, J.P. Uriot, L.J. Michot, F. Thomas. *Clays and Clay Minerals* **1997**, *45*, 8–22.

[13] V. Marry, P. Turq. *J.Chem.Phys.* **2002**, *117*, 3454–3463.

[14] E.J.M. Hensen, B. Smit. *J.Phys.Chem. B* **2002**, *106*, 12664–12667.

[15] G. Sposito, R. Prost. *Chemical Reviews* **1982**, *82*, 553–573.

[16] R. Calvet. *Ann. Agron.* **1973**, *24*, 77.

[17] J. Fripiat, J. Cases, M. Francois, M. Letellier. *J. Coll. Inter. Sci.* **1982**, *89*(2), 378–400.

[18] A. Delville, M. Letellier. *Langmuir* **1995**, *11*, 1361–1367.

[19] H. Suquet, R. Prost, H. Pezerat. *Clay Miner.* **1977**, *12*, 113.

[20] G. Sposito, R. Prost, J.P. Gaultier. *Clays and Clay Minerals* **1983**, *31*, 9–16.

[21] A. Delville. *Langmuir* **1992**, *8*, 1796–1805.

[22] E.S. Boek, P.V. Coveney, N.T. Skipper. *Langmuir* **1995**, *11*, 4629–4631.

[23] F.C. Chang, N.T. Skipper, G. Sposito. *Langmuir* **1997**, *13*, 2074–2082.

[24] M. Chávez-Páez, L. dePablo, J.J. dePablo. *J.Chem.Phys.* **2001**, *114*(24), 10948–10953.

[25] L. J. Michot F. Villiéras, M. François, I. Bihannic, M. Pelletier, J.-M. Cases. *C. R. Geoscience* **2002**, *334*, 611–631.

[26] K. Faisandier, C.H. Pons, D. Tchoubar, F. Thomas. *Clays and Clay Minerals* **1998**, *46*, 636–648.

[27] J. Breu, W. Seidl, A. Stoll. *Z. Anorg. Allg. Chem.* **2003**, *629*, 503–515.

[28] C. E. Weaver. *Am. Mineralogist* **1956**, *41*, 202–221.

[29] A. Viani, A. F. Gualtieri, G. Artioli. *Amer. Mineralogist* **2002**, *87*, 966–975.

[30] A.F. Koster van Groos, S. Guggenheim. *American Mineralogist* **1984**, *69*, 872–879.

[31] H. J. Bray, S. T. Redfern, S. M. Clark. *Miner. Mag.* **1998**, *62(5)*, 647–656.

[32] A. F. Koster van Groos, S. Guggenheim. *Am. Miner.* **1987**, *72*, 292–298.

[33] T.-C. Wu,W. A. Bassett, W.-L. Huang, S. Guggenheim, A. F. Koster van Groos. *Am. Miner.* **1997**, *82*, 69–78.

[34] J.O. Titiloye, N.T. Skipper. *Mol. Phys.* **2001**, *99*, 899–906.

[35] A. V. de Siqueira, C. Lobban, N. T. Skipper, G. D. Williams, A. K. Soper, R. Done, J. W. Dreyer, R. J. Humphreys, J. A. R. Bones . *J. Phys.: Condens. Matter* **1999**, *11*, 9179–9188.

[36] D. Guillaume, A. Neaman, M. Cathelineau, R. Mosser-Ruck, C. Peiffert, M. Abdelmoula, J. Dubessy, F. Villieras, A. Baronnet, N. Michau. *Clay Minerals* **2003**, *38(3)*, 281–302.

[37] I. Bérend. *Les Mechanismes d'hydratation de montmorillonites homoioniques pour des pressions relatives inferieures a 0.95;* These de doctorat, Institut National Polytechnique de Lorraine, 1991.

[38] D. Frenkel, B. Smit. *Understanding Molecular Simulations, From Algorithms to Applications;* Academic Press, 2002.

[39] M.P. Allen, D.J.Tidelsley. *Computer simulation of Liquids;* Oxford Science Publications, 2002.

[40] W. Smith, T. Forester. *The DLPOLY2 user manual;* Daresbury Laboratory, Warrington, England, 2001.

[41] A. Rahman. *Phys. Rev.* **1964**, *136*(2A), A405 – A411.

[42] J. P. Hansen, I. R. McDonald. *Theory of simple liquids;* Academic Press, 1986.

[43] B. Guillot. *J. Mol. Liq.* **2002**, *101*, 219–260.

[44] H.J.C. Berendsen, J.R. Grigera, T.P. Straatsma. *J.Phys.Chem.* **1987**, *91*, 6269–6271.

[45] J. Brodholt, B. Wood. *Journal of Geophysical Research* **1993**, *98*, 519–536.

[46] N.T. Skipper, K. Refson, J.D.C. McConnell. *Clay Minerals* **1989**, *24*, 411–425.

[47] N.T. Skipper, K. Refson, J.D.C. McConnell. *J. Chem. Phys.* **1991**, *94*(11), 7434–7445.

[48] E.S. Boek, P.V. Coveney, N.T. Skipper. *J.Am.Chem.Soc.* **1995**, *117*, 12608–12617.

[49] D. Smith. *Langmuir* **1998**, *14*, 5959–5967.

[50] S. Koneshan, J. C. Rasaiah, R. M. Lynden-Bell, S. H. Lee. *J. Phys. Chem. B* **1998**, *102*(21), 4193–4204.

[51] V. Marry. *Modelisation Microscopique de la strucutre et de la dynamique de l'eau et des ions dans les argiles de stockage de type montmorillonite;* These de doctorat, Universite Pierre et Marie Curie, 2002.

[52] J. L. Lebowitz, J. K. Percus, L. Verlet. *Phys. Rev.* **1967**, *153*, 250–254.

[53] A. Z. Panagiotopoulos. *Mol. Phys.* **1987**, *61*, 813–826.

[54] N. Metropolis, A. W. Rosenbluth, M. N. Rosenbluth, A. N. Teller, E. Teller. *J. Chem. Phys.* **1953**, *21*, 125–130.

[55] R. J. Hunter. *Foundatios of Colloid Science;* Oxford Univeristy Press, 2001.

[56] F.C. Chang, N.T. Skipper, G. Sposito. *Langmuir* **1995**, *11*, 2734–2741.

[57] R. Sutton, G. Sposito. *Journal of Colloid and Interface Science* **2001**, *237*, 174–184.

[58] A.V.C. de Siqueira, N.T. Skipper, P.V. Coveney, E.S. Boek. *Mol. Phys.* **1997**, *92*, 1–6.

[59] W.-L. Huang, W. A. Bassett, T.-C. Wu. *Am. Miner.* **1994**, *79*, 683–691.

[60] L. Harr, J. S. Gallagher, G. S. Kell. *NBS/NRC Steam Tables;* Hemisphere Publishing, 1984.

[61] K. Kawamura, Y. Ichikawa, M. Nakano, K. Kitayama, H. Kawamura. *Engineering Geology* **1999**, *54*, 75–79.

[62] N.T. Skipper, G. Sposito, F.C. Chang. *Clays and Clay Minerals* **1995**, *43*, 294–303.

[63] S.-H. Park, G. Sposito. *J. Phys. Chem. B* **2000**, *104*, 4642–4648.

[64] A. Delville, S. Sokolowski. *J.Phys.Chem.* **1993**, *97*, 6261–6271.

[65] R.K. Hawkins, P.A. Egelstaff. *Clays and Clay Minerals* **1980**, *28*, 19–28.

[66] D.H. Powell, K. Tongkhao, S.J. Kennedy, P.G. Slade. *Clays and Clay Minerals* **1997**, *45*, 290–294.

[67] C.A. Weiss, R.J. Kirkpatrick, S.P. Altaner. *Am. Mineralogist* **1990**, *75*, 970–982.

[68] V. Marry, P. Turq. *J.Phys.Chem. B* **2003**, *107*, 1832–1839.

[69] H. Kato, M. Muroi, N. Yamada, H. Ishida, H. Sato. *Scientific basis for nuclear waste management*, Vol. 18; Materials Research Society, Pennsylvania, 1995.

[70] M. Holz, S.R. Heil, A. Sacco. *Phys.Chem.Chem.Phys.* **2000**, *2*, 4740–4742.

[71] M. IN HET Panhuis, C.H. Patterson, R.M. Lynden-Bell. *Molecular Physics* **1998**, *94*, 963–972.

[72] J. Swenson, R. Bergman, S. Longeville. *J. Chem. Phys.* **2001**, *115*, 11299–11305.

[73] M. Bée. *Quasi-elastic neutron scattering; Principles and Applications in Solid State Chemistry, Biology and Material Science;* Adam Hilger, 1988.

[74] F. Mezei. In *Lecture Notes in Physics*, Vol. 128; Springer Verlag, 1980.

[75] W. Marshall, S. W. Lovesey. *Theory of thermal neutron scattering;* Clarendon Press, 1971.

[76] M. Bée - editor. In *J. de Physique IV - Proceedings*, Vol. 10; EDP Sciences, 2000.

[77] G. L. Squires. *Introduction to the theory of Thermal Neutron Scattering;* Dover Publications, 1996.

[78] C. Kittel. *Introduction to Solid State Physics;* John Wiley and Sons, 1996.

[79] F. Mezei. *Z. Physik* **1972**, *255*, 146–160.

[80] A.-J. Dianoux, G. Lander - editors. *Neutron Data Booklet (2nd edition);* Old City Publishing, 2003.

[81] R. Gãhler, R. Golub. *Z. Phys. B - Cond. Mat.* **1987**, *65*, 269–273.

[82] R. Golub, R. Gãhler. *Physics Letters A* **1987**, *123*, 43–48.

[83] R. Gãhler, R. Golub. *J. Phys France* **1988**, *49*, 1195–1202.

[84] J. G. Powles. *Mol. Phys.* **1973**, *26*(6), 1225–1350.

[85] T. Springer - editor. In *Springer Tracts in Modern Physics*, Vol. 64; Springer-Verlag, 1972.

[86] M. Abramowitz, I. A. Stegun. *Handbook of mathematical functions;* Dover publications, 1972.

[87] D.J. Cebula, R.K. Thomas, J.W. White. *Clays and Clay Minerals* **1981**, *29*, 241–248.

[88] C. Poinsignon, J. Estrade-Szwarckopf, J. Conard, A.J. Dianoux. *Proc. Int. Clay Conf., Denver 1985* **1987**, pages 284–291.

[89] J.J. Tuck, P.L. Hall, M.H.B. Hayes, D.K. Ross, J.B. Hayter. *J.Chem.Soc., Faraday Trans. 1* **1985**, *81*, 833–846.

[90] J.J. Tuck, P.L. Hall, M.H.B. Hayes, D.K. Ross, C. Poinsignon. *J.Chem.Soc., Faraday Trans. 1* **1984**, *80*, 309–324.

[91] J. Swenson, R. Bergman, W.S. Howells. *J. Chem. Phys.* **2000**, *113*, 2873–2879.

[92] E. Mamontov. *J. Chem. Phys.* **2004**, *121*, 9193–9194.

[93] J. Swenson, R. Bergman, W.S. Howells, S. Longeville. *J. Chem. Phys.* **2004**, *121*, 9195.

[94] W. S. Howells. *Physica B* **1996**, *226*, 778–81.

[95] F. Trouw, D. Bedrov, O. Borodin, G. D. Smith. *Chem. Phys.* **2000**, *261*, 137–148.

[96] W. H. Press, B. P. Flannery, S. A. Teukolsky, W. T. Vetterling. *Numerical Recipes, The Art of Scientific Computing;* Cambridge University Press, 1986.

[97] M. Arab, D. Bourgeard, K. S. Smirnov. *Phys. Chem. Chem. Phys.* **2003**, *5*, 4699–4707.

[98] S.-H. Chen, P. Gallo, F. Sciortino, P. Tartaglia. *Phys. Rev. E* **1997**, *56*(4), 4231–4243.

[99] M. Arab, D. Bourgeard, K. S. Smirnov. *Phys. Chem. Chem. Phys.* **2004**, *6*, 2446–2453.

[100] O. Borodin, F. Trouw, D. Bedrov, G. D. Smith. *J. Phys. Chem. B* **2002**, *106*(20), 5184–5193.

[101] J. Teixeira, M.-C. Bellissent-Funel, S.-H. Chen, A. J. Dianoux. *J. de Phys.* **1984**, *C7*, 65–71.

[102] M.-C. Bellissent-Funel, J. Teixeira. *J. Mol. Struc.* **1991**, *250*, 213–230.

[103] M.-C. Bellissent-Funel, K. F. Bradley, S. H. Chen, J. Lal, J. Teixeira. *Physica A* **1993**, *201*, 277–285.

[104] J. Teixeira, J.-M. Zanotti, M.-C. Bellissent-Funel, S. H. Chen. *Physica B* **1997**, *234-236*, 370–374.

[105] J. J. Ullo. *Phys. Rev. A* **1987**, *36*(2), 816–826.

[106] E. Mamontov. *J. Chem. Phys.* **2004**, *121*(18), 9087–9097.

[107] P.L. Hall, D.K. Ross. *Mol. Phys.* **1978**, *36*, 1549–1554.

[108] P.L. Hall, D.K. Ross. *Mol. Phys.* **1981**, *42*, 673–682.

[109] A. J. Dianoux, F. Volino, H. Hervet. *Mol.Phys.* **1975**, *30*, 1181–1194.

[110] R. E. Lechner. *Solid State Ionics* **1995**, *77*, 280–286.

[111] G. R. Kneller, V. Keiner, M. Kneller, M. Schiler. *nMOLDYN: A Program Package for a Neutron Scattering Oriented Analysis of Molecular Dynamics Simulations;* 1996.

[112] R. T. Cygan, J.-J. Liang, A. G. Kalinichev. *J.Phys.Chem B* **2004**, *108*, 1255–1266.

[113] B. R. Bickmore, K. M. Rosso, K. L. Nagy, R. T. Cygan, C. J. Tadanier. *Clays and Clay. Min.* **2003**, *51*(4), 359–371.

# Annex

Published manuscripts

MOLECULAR PHYSICS, 20 SEPTEMBER 2004, VOL. 102, NO. 18, 1965–1977

# Temperature effect in a montmorillonite clay at low hydration—microscopic simulation

N. MALIKOVA[1,2], V. MARRY[1], J.-F. DUFRÊCHE[1], C. SIMON[1], P. TURQ[1]* and E. GIFFAUT[2]

[1]Laboratoire Liquides Ioniques et Interfaces Chargées, boite postale 51, Université P. et M. Curie, 4 place
Jussieu, F-75252 Paris Cedex 05, France

[2]ANDRA, Parc de la Croix Blanche, 1/7 rue Jean Monnet, F-92298 Châtenay-Malabry Cedex, France

(*Received 19 May 2004; revised version accepted 9 July 2004*)

The effect of temperature in the range 0–150°C was studied for homo-ionic montmorillonite clays with $Na^+$ and $Cs^+$ compensating ions in low hydration states. Monte Carlo and molecular dynamics simulations were employed to provide both static and dynamic information concerning the interlayer ions and water molecules, and emphasis was laid on the temperature activation of the diffusion coefficients. Principal structural changes were limited to the interlayer water phase. In the monohydrated systems, neither of the cations was seen to enter into the hexagonal cavities of the clay. $Cs^+$ exhibited clear site-to-site diffusion between sites allowing coordination to six oxygen atoms of the clay sheets, this behaviour persisting to high temperatures. Preferential sites for the $Na^+$ counterion were much less well-defined, even at low temperatures. The behaviour of the water phase in the monohydrated states was similar for the two ions. A rapid approach to bulk dynamics was seen in the transition from monohydrated to bihydrated Na-montmorillonite. A detailed quantitative comparison of the temperature activation of diffusion for a two-dimensional water phase and three-dimensional bulk water is presented for the first time.

## 1. Introduction

Subject to intense research in the domain of microscopic simulation since the late 1980s, clay materials, in their compacted form, are candidates for one of the constituents of engineered barriers around underground storage sites for high-activity radioactive waste [1]. The properties of clays most pertinent for their role as a barrier are their low permeability to water and high retention capacity for cations. In the scenario of the radioactive waste site, it is water seeping from the surrounding rock sediments and radioactive cations such as $Cs^+$ originating from the waste that need to be retained by the engineered barrier.

The above properties of clays can be traced to their microscopic structure. On this scale, clays consists of fused layers of oxides of $Al^{3+}$ or $Mg^{2+}$ in an octahedral configuration and oxides of $Si^{4+}$ in a tetrahedral configuration. The covalent bonding within a single sheet contrasts with the relatively weak interactions between individual sheets. By substituting $Al^{3+}$, $Mg^{2+}$ or $Si^{4+}$ by lower valence cations, the clay sheets acquire a negative charge, which is then compensated by cationic species entering between the sheets into the so-called interlayer. Under increased humidity the system is capable of absorbing water, and, on the microscopic scale, hydration of the cationic species in the interlayer occurs [2]. The extent of this so-called swelling critically depends on the balance between the clay–cation and water–cation interaction [3, 4]. In turn, the degree of hydration dramatically influences the dynamics of both the cationic species and the water phase in the interlayer [5]. This is true especially for clays with a low water content, when discrete layers of water are formed around the ions in the interlayer (approximately 300 mg of water per 1 g of clay, corresponding to the first three water layers). This is the region of the so-called crystalline swelling [6]. Extreme clay hydration produces a colloidal dispersion of clay particles in water, each particle consisting of a few aligned clay sheets (less than 10 sheets) [7].

Studies of the dynamics of cationic species and water in clays are complex due to the multi-scale structure of the system [8]. On the mesoscopic scale, aggregates of aligned clay sheets form particles of the order of 10 to 1000 nm in size, depending on the type of clay. The dynamics of water and cationic species is therefore not confined only to the nanopores of the system, the interlayer spacing, but also to mesopores and

---

*Author for correspondence. e-mail: pt@ccr.jussieu.fr

*Molecular Physics* ISSN 0026–8976 print/ISSN 1362–3028 online
http://www.tandf.co.uk/journals
DOI: 10.1080/00268970412331290995

macropores between the clay particles and their aggregates [9]. However, with respect to the clay barriers surrounding radioactive waste, the clay material is in a compressed form and in the condition of low hydration. Compression of the clay material leads to a significant reduction in its macroporosity [9]. We are therefore dealing with a system, the properties of which are primarily influenced by the behaviour of water and positively charged species in the interlayer and mesopores. Microscopic simulations have been a valuable tool for zooming into the lowest scale of the clay structure and providing both static and dynamic information on the interlayer species.

Aside from microscopic simulations at ambient temperature and pressure of clays with various cationic species [10–13], attention has been drawn to the particular temperature and pressure to which clay systems are subjected underground. Simultaneous geothermal and geostatic gradients have been considered previously, in addition to the presence of small organic molecules such as methane, corresponding to the conditions in sedimentary basins up to a depth of a few kilometers [14, 15]. Apart from simulation, X-ray and neutron diffraction studies have provided important information on the stable hydration states as well as the structure of the pore fluids under these temperature and pressure gradients [16–18]. The conditions presented in this paper aim to decouple the effect of pressure and temperature and focus on the latter in the range of approximately 0 to 150°C, under a pressure of 1 bar. Here, the waste is considered to be deposited at about 500 m below the Earth's surface and the temperature to which the surrounding clay barrier is subjected is determined by long-term heating of the barrier by the waste itself, as radioactive decay takes place. The temperature range determined by macroscopic simulations for the case of vitrified radioactive waste is 0–90°C [9]. While the choice of a constant (ambient) pressure throughout our study singles out the temperature effect on the clay system, in the underground storage scenario this will not necessarily be the case. In the current absence of detailed pressure data near the waste site, the present constant-pressure study is therefore to be treated as a first step in the modelling of this system of significant complexity.

In this article we present the results of both Monte Carlo and molecular dynamics simulations of Na- and Cs-montmorillonite systems in low hydration states. After viewing the changes in the distribution of cations and water molecules in the interlayer as a function of temperature, we concentrate on the dynamical properties of the interlayer species with increasing temperature and make a comparison with bulk water.

## 2. Models and simulation techniques

The model clay under investigation was a montmorillonite-type clay with a unit cell of $Cat_{0.75}[Si_8](Al_{3.25}Mg_{0.75})O_{20}(OH)_4$, where Cat is the cation in the interlayer. Thus substitutions in the clay were in the octahedral layer only. This composition is an approximation of the montmorillonite extracted from MX80, which is a material systematically studied in connection with the issue of nuclear waste [1]. Interlayer cations considered were $Na^+$ and $Cs^+$, the former in both the mono- and bihydrated state, the latter in the monohydrated state only, as bihydrated Cs-montmorillonite is not observed experimentally [4]. Based on our previous study [19], we defined the mono- and bihydrated state as corresponding to six and 12 water molecules per cation, respectively (also referred to as monolayer and bilayer). As we are studying the behaviour of clay systems with constant water content as a function of temperature, a question automatically arises concerning the temperature range in which these particular degrees of hydration remain largely intact. On heating, the first dehydration phase of Na-montmorillonite has been observed at 140°C, followed by a second step at 210°C [20]. Other sources present the first dehydration phase at a temperature as low as 57°C, corresponding to weakly bound water on external surfaces and macropores, with a second phase at approximately 190°C [9]. On the basis of a more recent detailed X-ray diffraction study into the kinetics of clay dehydration [21], the monohydrated states can indeed be treated as stable in the temperature range considered, whereas the case of the bihydrated state is marginal towards the higher end of our temperature range.

Both Monte Carlo (MC) and molecular dynamics (MD) simulations were used to study the above system. Information extracted from MC simulations is related to equilibrium properties. We investigated the effect of temperature on the sheet spacing and on the distributions of interlayer species in the interlayer for a given hydration state. More importantly, equilibrated configurations from MC simulations were used in MD simulations to determine the diffusion coefficients of the interlayer species and provide their trajectories.

The simulation box for both MC and MD simulations contained two sheets of clay (area $20.72\,Å \times 17.94\,Å$, thickness $6.54\,Å$), each consisting of eight unit cells and its charge being balanced by six cations in the interlayer. Each interlayer contained 36 or 72 water molecules for the mono- and bihydrated state, respectively. The clay sheets were considered as rigid. The model of water used was the rigid SPC/E model (O–H bond $1.0\,Å$, angle H–O–H $109.47°$, charges $-0.848e$ and $+0.424e$ for oxygen and hydrogen atoms, respectively), as the main interest of the study was the dynamics of the gallery species [22]. The validity of this model over the whole temperature range studied has been confirmed [23]. Interaction potentials used were the Lennard–Jones 6–12 and Coulombic potential. Each atom in the simulation cell was thus characterized by two Van der Waals parameters ($\sigma_i$, $\epsilon_i$) and charge ($q_i$). The interaction potential between a pair of atoms was therefore

$$V_{ij} = \frac{q_i q_j}{4\epsilon_0 r_{ij}} + 4\epsilon_{ij}\left[\left(\frac{\sigma_{ij}}{r_{ij}}\right)^{12} - \left(\frac{\sigma_{ij}}{r_{ij}}\right)^{6}\right]. \quad (1)$$

Atomic charges and parameters $\sigma$ and $\epsilon$ were taken from Smith [24]. The pair of parameters $\sigma_{ij}$, $\epsilon_{ij}$, for $i \neq j$, were obtained from the Lorentz–Berthelot rules. Periodic boundary conditions in all three dimensions were applied throughout the simulations.

MC simulations in the $N\sigma_{zz}T$ ensemble, where $\sigma_{zz}$ refers to the stress perpendicular to the clay sheets, were employed to equilibrate the system. For a given interlayer cation and hydration state, a series of MC simulations at a fixed value of $\sigma_{zz}$ ($1\,\text{bar} = 10^5\,\text{Pa}$) and a given temperature from the range 273–420 K ($0-150°\text{C}$) was carried out. Technical details of MC simulations of clay systems have been published previously [19]. Briefly, they allow displacements of individual interlayer species as well as movements (horizontal and vertical) for the entire clay sheets. In the evaluation of the energy, a spherical cut-off of 8.0 Å was used for the Lennard–Jones 6–12 potential. Coulombic interactions were dealt with by a 3D Ewald summation.

Viewing previous publications on the microscopic simulation of clay systems, two general approaches are found: simulation in either the $N\sigma_{zz}T$ or the $\mu VT$, grand-canonical, ensembles. The experimental reality corresponds to the '$\mu PT$' ensemble, which is, however, inaccessible to simulations, due to all fixed variables being intensive, in the case of a bulk system. By choosing the $N\sigma_{zz}T$ approach, we have introduced an additional unrealistic constraint in terms of the fixed number of particles in the system, whereas in the $\mu VT$ approach, a fixed volume would have been introduced. We do not consider either of the ensembles to be more appropriate in imitating reality. The $N\sigma_{zz}T$ approach was chosen due to its significantly greater technical simplicity, but also the temperature range studied has been adapted to correspond to temperatures under which the low-hydration states of montmorillonite remain intact, as mentioned above.

In addition to the above discussion, we appreciate that the anisotropy of the clay system allows simulation in the $\mu\sigma_{zz}T$ ensemble. With the volume change being restricted to the $z$ dimension and with the presence of the interacting clay sheets, the volume ($z$ dimension) and number of water molecules in the system are no longer extensive variables. The same reasoning as for the inaccessibility of a '$\mu PT$' simulation in the case of an isotropic bulk system does not apply here [25]. This ensemble would be a great improvement over the two general approaches used so far in simulating clay systems and is envisaged for future studies.

MD simulations (DLPOLY code [26]) were performed under constant volume, the clay sheets were held fixed and the motion of the interlayer species was traced. The code implements the Verlet algorithm for the integration of the equations of motion, a variant of the SHAKE algorithm for treating the movement of rigid bodies and 3D Ewald summation to evaluate Coulombic interactions. Each system was initially equilibrated for 50 ps in the $NVT$ ensemble (time step ($t_{\text{step}}$) = 0.001 ps, Nosé–Hoover thermostat with time constant 0.5 ps). Thereafter, trajectories of the interlayer species were collected in the $NVE$ ensemble.

Both methods for the evaluation of diffusion coefficients from particle trajectories, the mean squared displacement (MSD) and the auto-correlation of velocity (VACF) methods, are presented. Due to the anisotropy of the system, components of the atomic displacements and velocities along the three principal axes in the simulation box ($x$ and $y$ in the plane of the clay sheets, $z$ perpendicular to the clay sheets) were considered separately in the analysis. In the MSD method, one-dimensional diffusion coefficients are determined from the Einstein relation [25]

$$\lim_{t\to\infty} \frac{\langle r^2(t)\rangle}{t} = 2D, \quad (2)$$

where $r$ is the one-dimensional displacement, $t$ is time and $D$ is the diffusion coefficient. In practice, the diffusion coefficient is determined from the gradient of the linear part of a plot of MSD, $\langle r^2(t)\rangle$, versus time. In the VACF method, we depart from the following one-dimensional equation [25]:

$$D = \int_0^\infty \mathrm{d}t\,\langle v_x(t)v_x(0)\rangle, \quad (3)$$

where $v_x$ is the one-dimensional velocity and $t$ and $D$ are defined as for equation (2). In this case, the diffusion coefficient is determined from the integral of the velocity auto-correlation function, as the value of this integral stabilizes.

Simulations in the $NVE$ ensemble intended for MSD analysis were 360 ps in length, with $t_{\text{step}} = 0.001$ ps and time between recorded configurations ($t_{\text{dump}}$) = 0.02 ps. Graphs of MSD versus time gave a linear dependence in the region of 50–150 ps and this is therefore the time range corresponding to the diffusion coefficients from the MSD analysis. For the VACF method, the interval between recorded configurations ($t_{\mathrm{dump}}$) is governed by the rate of decay of the auto-correlation function. Here, $t_{\mathrm{dump}}$ had to be decreased to 0.002 ps in order to sample the auto-correlation function sufficiently. Simulations intended for VACF analysis were 36 ps in length with $t_{\mathrm{step}} = 0.001$ ps and $t_{\mathrm{dump}} = 0.002$ ps. The VACF analysis therefore gives information concerning the diffusion coefficients on the time scale of less than 20 ps.

## 3. Results and discussion

### 3.1. *Static properties*

The sheet spacing in the temperature range considered shows a variation of the order of 0.2–0.3 Å for all three systems studied (figure 1). The density of the water phase varies between 0.98–0.99 g cm$^{-3}$ (0°C) and 0.94–0.95 g cm$^{-3}$ (100°C) (for reference the density of bulk water varies from 0.999 g cm$^{-3}$ (0°C) to 0.958 g cm$^{-3}$ (100°C) [27]). In the calculation of density, the volume available to water molecules in the confined systems was estimated by subtracting the volume occupied by the surface oxygen atoms and the interlayer ions from the total volume of the interlayer. An X-ray diffraction study of Na-montmorillonite at temperatures up to 363 K showed only very small changes in the sheet spacing, in agreement with the data presented here [28].

The monohydrate counterion distributions in the interlayer at low temperatures are in agreement with other studies at ambient temperature on a clay with octahedral substitution only [19, 29]. Two peaks, equidistant from the middle of the interlayer, are observed in the case of Na$^+$ (figure 2), and a single peak in the case of Cs$^+$ (not shown), rationalized previously on the basis of the greater size of the Cs$^+$ counterion [30]. For Na-bihydrate, the counterion distribution shows a large central peak and side peaks near the clay surface (not shown). Changes in temperature have a small effect on the distribution profiles. Their main features (number and position of peaks) remain unchanged. The fact that the position of the counterions is not strongly influenced by temperature is, at first sight, surprising. For hydrated systems, ionic profiles in the vicinity of a charged surface depend on the dielectric constant of the solvent, which, in turn, varies with temperature. However, for the low hydration states studied here, the solvation and ion–clay interactions predominantly define the ionic profiles in these confined systems, while the temperature effect is secondary. Smearing in the profiles of the constituent atoms of water as the temperature increases is observed, suggesting more disorder in the water phase, as expected.

The orientations of the water molecules in the interlayer with respect to the clay sheets (reference system as in [19]) were found to be strongly biased towards lying in a plane perpendicular to the clay sheets with their dipole moment at an angle of less than 45° from the direction parallel to the sheets. Evidence for this configuration in the case of clays with octahedral substitution has been provided by IR spectroscopy [31] and microscopic simulations [32].

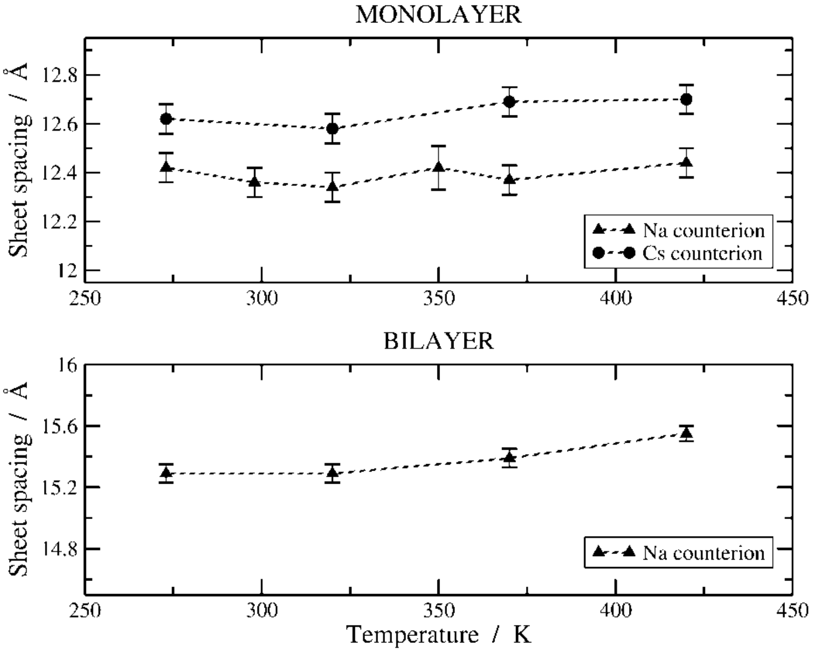

Figure 1. Temperature dependence of the sheet spacing for the three systems studied.

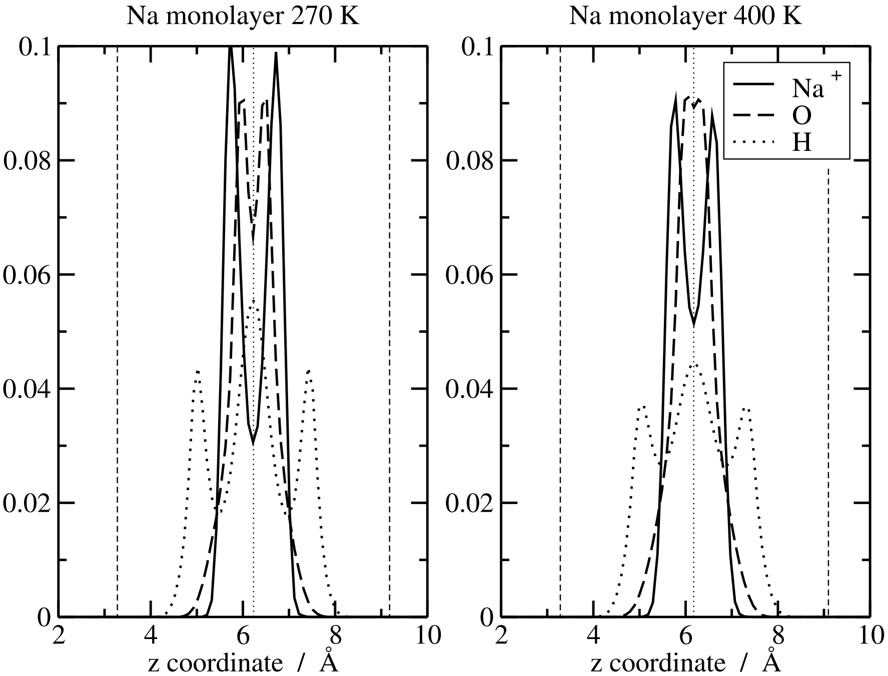

Figure 2. Na-monohydrated system; profiles of interlayer atoms (Na$^+$ ion, the oxygen atom of water and the hydrogen atom of water) along the axis perpendicular to the clay sheets (*z* axis). Vertical lines indicate the position of the topmost oxygen atoms in the clay sheets (dashed line) and the middle of the interlayer (dotted line).

In the following discussion of the radial distribution functions ($g_{\mathrm{A-B}}$) we highlight cases where new peaks appear as a function of temperature. Unless stated otherwise, the main features of these functions are the same as those reported for the same system at ambient temperature by Marry *et al.* [19]. The peak positions quoted were reproducible to 0.1 Å. The difficulties of the normalization (assuming isotropic densities) and interpretation of conventional radial distribution functions used in the case of inhomogeneous systems have recently been highlighted [33]. In the following section, structural information is based on the analysis of simulation snapshots, which help to partially rationalize the radial distribution functions themselves.

For all systems, no significant shifts in the principal peak positions of $g_{\mathrm{Owater–Owater}}$ and $g_{\mathrm{Owater–Hwater}}$ were observed. However, for the Na$^+$ counterion, $g_{\mathrm{Owater–Owater}}$ showed a principal peak at 2.8 Å with a shoulder at 3.2 Å (figure 3). The shoulder is more pronounced in the bihydrated system, resolving into a separate peak at 3.2–3.3 Å with an additional minimum at 5.5 Å, separating two peaks at 4.9 and 6.0 Å (figure 3). The shoulder at 3.2–3.3 Å has previously been observed in some studies at ambient temperature [19], but was not as obvious in others [29, 32].

A square model for the first hydration shell of four water molecules surrounding the Na$^+$ ion in the monohydrated system suggests an explanation for the extra features of $g_{\mathrm{Owater–Owater}}$ compared with the bulk solution (shoulder at 3.2 Å and an extra peak at 4.8 Å) (figure 3, top) [19]. A planar configuration of four water molecules in the monohydrated system has already been predicted by simulation [10, 34]. It is essentially the geometrical restriction that disables the formation of a six-coordinate hydrated ion, even if six water molecules per ion are available. Planar four-coordinate hydrated ions have been observed by electron spin resonance for smectites with transition metals such as Cu$^{2+}$ [31]. At first sight, the existence of a four-coordinate planar complex in the case of transition metal ions such as Cu$^{2+}$ is perhaps more expected than for Na$^+$. However, in the case of Cu$^{2+}$ clay, the four-coordinate hydrated ion is an intermediate step in the formation of a six-coordinate hydrated ion when additional layers of water are present between the clay sheets [31]. Similar behaviour is therefore considered in the case of Na$^+$.

In the case of the bihydrated Na system, an octahedral configuration of six water molecules around a Na$^+$ ion does not satisfactorily explain the features of $g_{\mathrm{Owater–Owater}}$ (figure 3, bottom). Na$^+$ has a lower hydration energy than the bivalent Cu$^{2+}$ ion [31] and thus a less well-defined octahedron of water molecules is likely. No clear experimental evidence is available for the increased structuring of the water phase in bihydrated Na-montmorillonite as the temperature decreases to around 273 K. Neutron diffraction studies

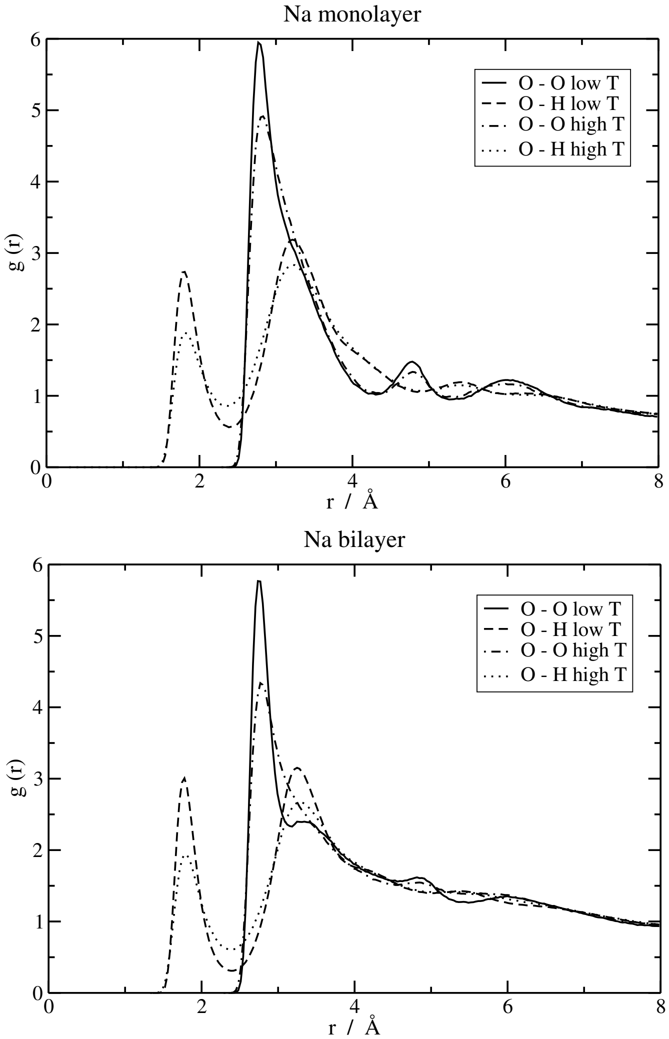

Figure 3. Radial distribution functions between constituent atoms of water for the Na monolayer (top) and the Na bilayer (bottom). The isotropic density of the atoms involved was assumed in the calculation of the RDF functions. Low temperature corresponds to 270 K, high temperature to 400 K.

suggest overall that water in this hydration state is rather bulk-like [35], but do not rule out significant perturbation of the hydrogen-bonding network [36]. Computer simulations, in general, suggest a greater deviation from the bulk-like structure [32].

In summary, within the static properties of the system, temperature in the given range has a very small effect on the sheet spacing and the distribution of species in the interlayer. More disorder in the water phase, observed as a smearing of the distribution functions, is observed, but the number and relative positions of the peaks remain intact. Radial distribution functions confirm that it is only the structure of the water phase and its bonding to the clay surface that change significantly with temperature. However, it is recognized that the description in terms of radial distribution functions intended for isotropic systems is not ideal in the case of clays. Even though the SPC/E water model has been validated over the whole temperature range considered (for bulk water), the rigidity of the clay sheets and water, as well as the classical pair potential, pose a limitation to obtaining details of the structural changes occurring in reality. Also, the relatively low temperatures studied are unlikely to affect the structure of the clay itself. The clay model used here has been subjected in previous simulation studies to temperatures (and pressures) significantly higher than in this work [14, 15].

### 3.2. *Dynamic properties*

Diffusion coefficients were determined from MD simulations in the *NVE* ensemble (average of three simulations for the MSD analysis and six simulations for VACF analysis). *NVE* is the preferred ensemble for the determination of diffusion coefficients as the trajectories of particles are unbiased. In the *NVT* ensemble, bias arises from the coupling of the system to a heat bath and care has to be taken in choosing a sufficiently small coupling constant of the thermostat [25]. In the *NVE* ensemble, we experienced fluctuations in temperature of approximately 12 K (system size 800–1000 atoms). Problems were encountered with drifts of the average temperature in the transition from *NVT* to *NVE* simulations. In the following discussion we quote the actual average temperature measured in the *NVE* ensemble, rather than the equilibration temperature from the initial *NVT* simulation. For the Na systems, the clay sheet arrangement used in the MD simulations was taken from the final arrangement of the MC equilibration without further modification. For the Cs system, a preferential face-to-face arrangement was consistently used [19], in order to single out the dependence of diffusion on temperature only.

In MSD analysis, the mean squared displacement along the $z$ axis tended to a constant and could not easily be fitted to a straight line. In the case of VACF, the integral along $z$ yielded values an order of magnitude smaller than in the $x$ and $y$ directions. This shows clearly the confinement of the system in the $z$ direction. Rigorously, for long times, the diffusion coefficient along $z$ should be zero. In both methods, the data for the $x$ and $y$ directions were used on their own to determine 2D diffusion coefficients of cations and water molecules (based on data for oxygen atoms) in the $XY$ plane, the plane of the clay sheets.

Diffusion coefficients as a function of temperature are summarized in figures 4–8. The horizontal error bars in figures 4 and 6 are shown for a single data set only, but apply equally to the other data sets. The values for ions are based on the trajectories of 12 particles and thus are subject to greater uncertainty than values for water molecules (72 or 144 particles). Especially for low temperatures, MSD curves for ions showed both linear and non-linear behaviour in the time range 50–150 ps. Trajectories featured in figures 5–7 correspond to the simulations intended for MSD analysis. Entire trajectories trace the motion of the species over approximately 360 ps with successive readings corresponding to a time interval of 0.02 ps. The trajectories presented correspond to the highest and lowest temperatures studied for each system. Overall, each system was simulated at least three different temperatures in the range chosen.

The details of the motion of ions and water depend on the chosen clay model. At present, the corresponding experimental data (at non-ambient temperature) are not available, however comparison with ambient experimental data is made, where available, in the following discussion.

Simulated diffusion coefficients for $Na^+$ and $Cs^+$ ions are of the order of $10^{-10}\,m^2\,s^{-1}$ and increase by an order of magnitude over the temperature range studied. A clear difference is observed in the mode of diffusion for the two ions. At both low and high temperature, $Cs^+$ ions exhibit site-to-site jump diffusion between sites, allowing coordination to three oxygen atoms from each of the two adjacent clay sheets, referred to as the

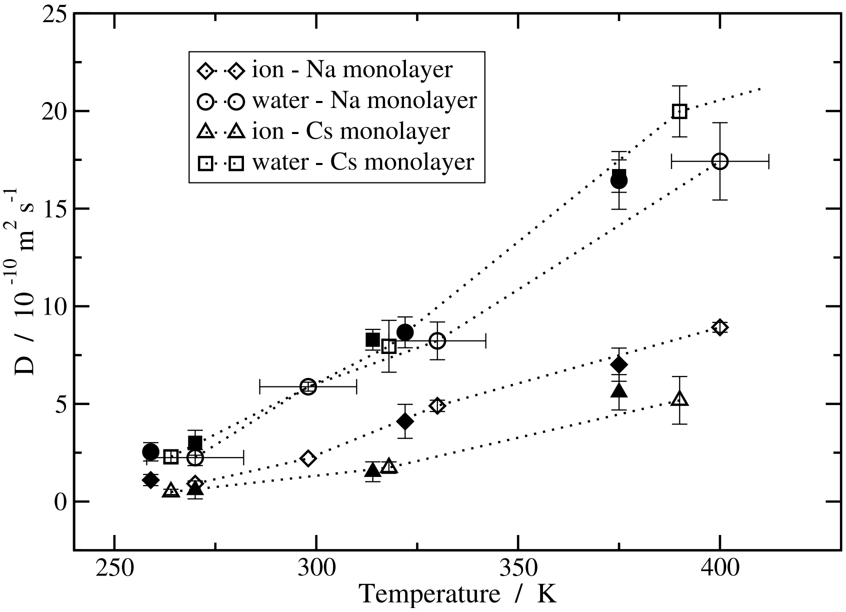

Figure 4. Two-dimensional diffusion coefficients for interlayer ions and water in monohydrated systems; long-term diffusion (empty symbols, obtained by MSD) and short-term diffusion (filled symbols, obtained by VACF).

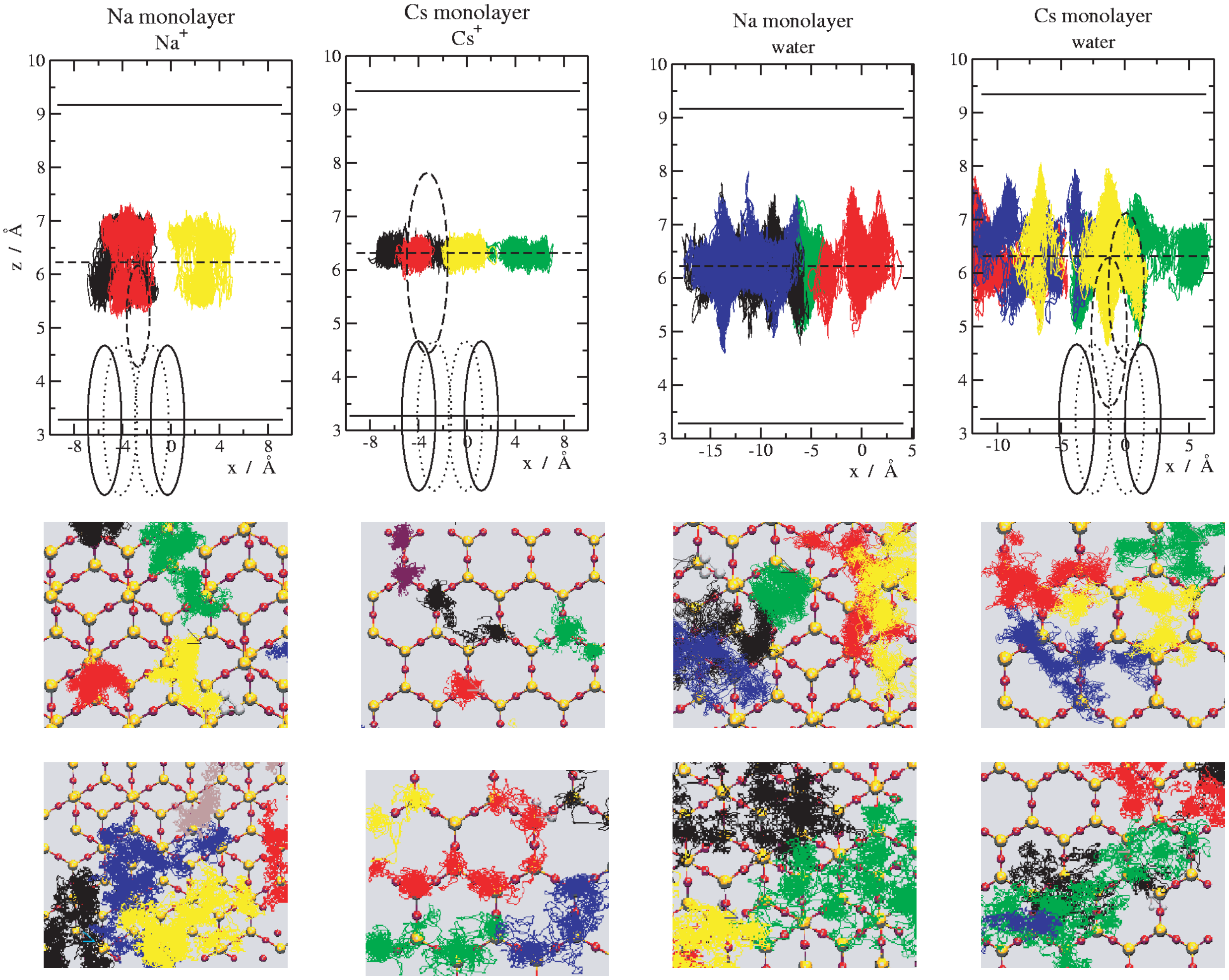

Figure 5. Na and Cs monolayer systems; trajectories of ions and water. Each column corresponds to the species indicated. First row: projections *x*–*z* at low temperature; second row: projections *x*–*y* at low temperature; third row: projections *x*–*y* at high temperature. A particular colour corresponds to the same particle in the first and second rows, but not in the third row. Low temperature indicates 260 K (Cs system) and 270 K (Na system). High temperature indicates 390 K (Cs system) and 400 K (Na system). Ellipses in the graphs of the first row represent oxygen atoms of the clay surface and the interlayer ions as described in the text. Clay sheets on either side of the interlayer are shown in the second and third rows (yellow atoms—Si, red atoms—O) together with the trajectories of the interlayer species.

trigonal sites (figure 5: *x*–*y* projections). Overall, the coordination number of the ions with respect to the oxygen atoms of the clay is therefore only six. Together with the oxygen atoms of water, this brings the overall coordination of the $Cs^+$ ions to approximately 12, higher than the bulk value of nine. This applies to the configuration of the clay sheets, where the number of six-coordinate sites with respect to the oxygen atoms of clay is maximized as the sheets are face-to-face (figure 5, second column). Additional simulations were carried out for a configuration of clay sheets more similar to that in figure 5 (third column), in which the number of six-coordinate sites decreases to a half and the sites are now further apart. A clear preference of $Cs^+$ ions for these sites over the simple trigonal sites on one sheet was only observed at high temperatures with a longer residence time in each six-coordinate site. This is likely to lead to a variation in the overall diffusion coefficient as a function of the clay sheet arrangement. No clear site-to-site diffusion is observed for the $Na^+$ ion, which suggests yet again the greater importance of the clay–ion interaction in the case of the $Cs^+$ ion. However, variation of the diffusion coefficient as a function of the clay sheet arrangement has been observed for both systems [19].

In the *x*–*z* projections of figure 5 the oxygen atoms of the clay sheet and the interlayer ions are represented by ellipses based on Pauling radii (1.4 Å for $O^{2-}$, 0.95 Å for $Na^+$ and 1.69 Å for $Cs^+$). Full ellipses correspond to two oxygen atoms on opposite sides of a hexagonal cavity, whereas dotted ellipses show oxygen atoms of the same cavity, but in a plane further back. If an ion (dashed

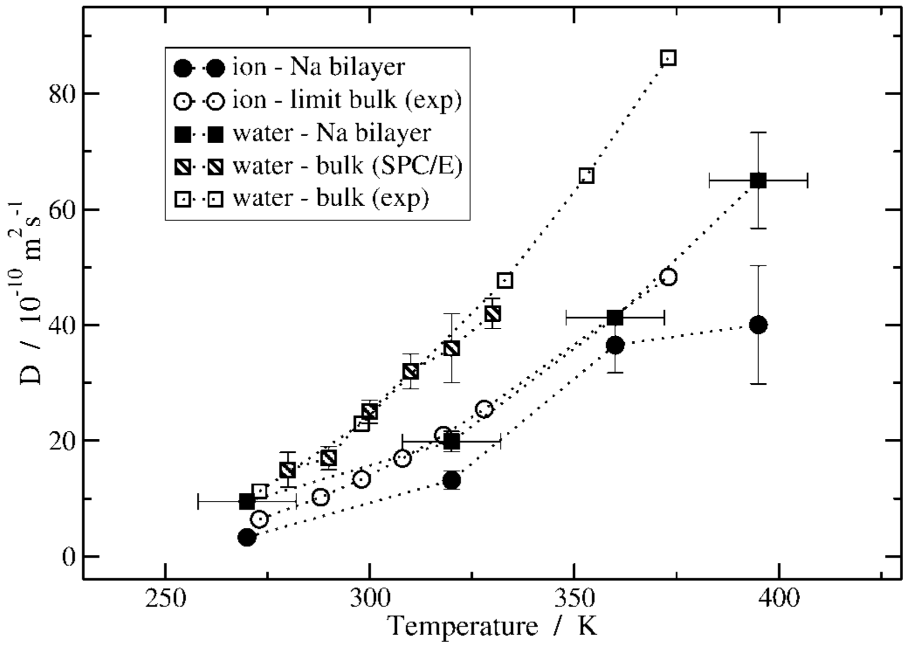

Figure 6. Two-dimensional diffusion coefficients for interlayer ions and water in the bihydrated Na system. Comparison with bulk water (both experimental data [43] and data from the SPC/E model [44]) and the $Na^+$ ion at infinite dilution (experimental data). Data for the bulk system are the corresponding 3D values.

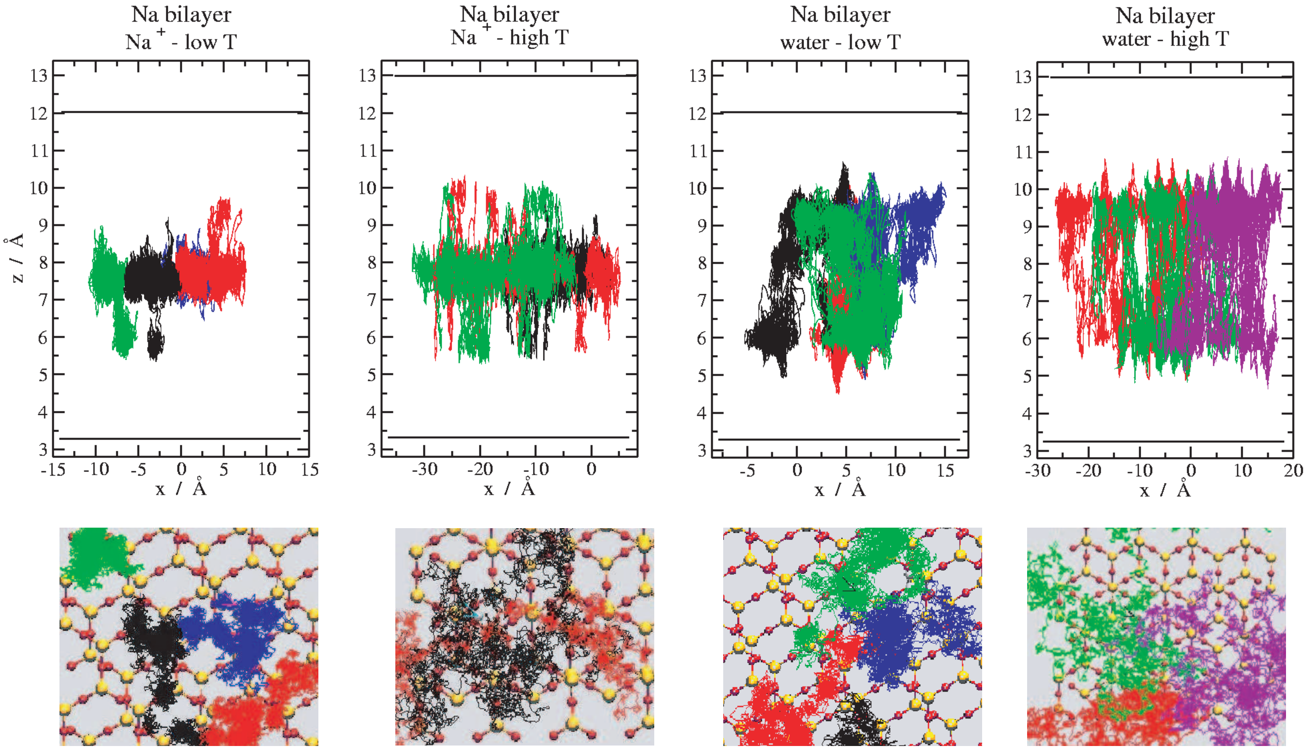

Figure 7. The Na bilayer system; trajectories of ions and water (first row: $x$–$z$ projection; second row: $x$–$y$ projection). Each column corresponds to one species; from left to right: ions at low temperature, ions at high temperature, water at low temperature, water at high temperature. Low temperature indicates 270 K and high temperature 400 K. In each column a particular colour corresponds to the same particle in the two projections. Further details as for figure 5.

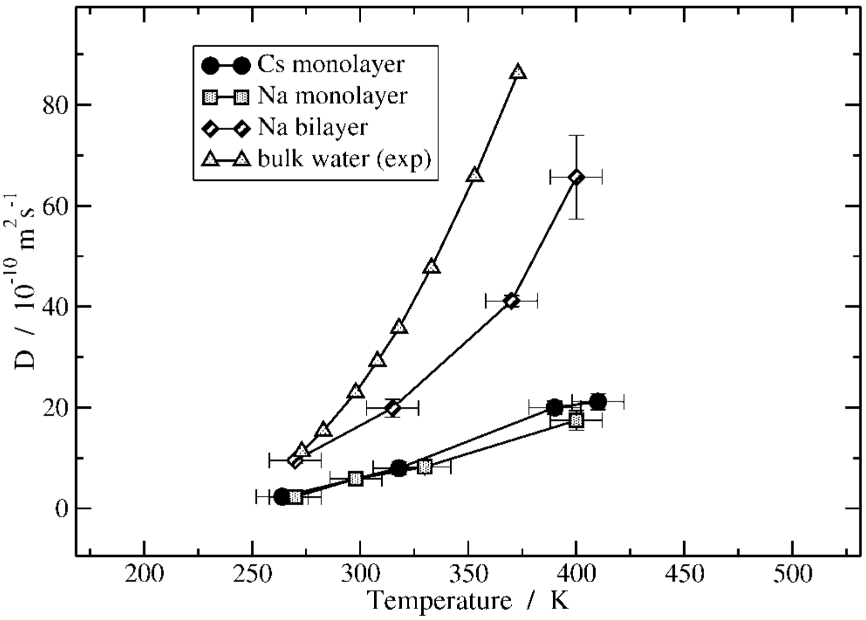

Figure 8. Two-dimensional diffusion coefficients of water in the three confined systems studied, together with the experimental data for bulk water (3D values).

ellipse) is located in the middle of the cavity, it is in the same *xz* plane as the front two oxygen atoms (full ellipses). With the aid of this scheme, it is clear from the *x*–*z* projections of the ionic trajectories that neither of the ions enter significantly into the hexagonal cavity. The $Cs^+$ ion is restricted to the six-coordinate sites described above, whereas the $Na^+$ ion, even if above the hexagonal cavity, does not enter it. This is due to the presence of the hydration shell, as observed experimentally using infrared spectroscopy [37].

In the context of other simulation studies, the calculated ionic diffusion coefficients are consistent with the ambient temperature simulation of Marry *et al.* [19]. The marginally lower diffusion coefficient in the case of the $Na^+$ ion is within the variation caused by the clay sheet arrangement. In this study, the same interaction potentials were used as well as the SPC/E model of water. Chang *et al.* [32] report values for the $Na^+$ counterion of the order of $10^{-11}\,m^2\,s^{-1}$ in simulations with the MCY model of water and clay with both octahedral and tetrahedral substitution. The preferential sites for the $Cs^+$ ions described here have been observed previously [19, 24]. Evidence from nuclear magnetic resonance suggests more than one type of possible site for $Cs^+$ ions, reaching nine- to 12-coordinate sites for dehydrated samples [38].

Experimental diffusion coefficients available for cations in clays come mainly from tracer experiments and give values of diffusion coefficients at ambient temperatures of the order of $10^{-16}$ to $10^{-12}\,m^2\,s^{-1}$. The difficulties encountered in the comparison of tracer experiments and microscopic simulations have been discussed previously [39], the main problem arising from the different timescales involved. Inhomogeneity of the pore size, finite size of the clay sheets and tortuosity in the real samples have to be taken into account to link the microscopic description to macroscopic observations [40]. This link has been achieved in our previous study in the case of $Cs^+$ diffusion in montmorillonite at ambient temperature [39].

The behaviour of the water phase as a function of temperature is similar for the two ions in the monohydrated state. As in the case of the ions the diffusion coefficient increases by an order of magnitude over the temperature range studied (figure 4). From the *x*–*z* projections in figure 5, it can be seen that water molecules, unlike the ions, enter into the hexagonal cavities of the adjacent clay sheets. However, in the plane of the clay sheets, the diffusion is rather delocalized, as in the case of the $Na^+$ ion, although some trajectories show the underlying hexagonal pattern (both the Na and Cs system at high temperature—green trajectories).

In light of other studies, diffusion coefficients of water for the monohydrated systems agree well for the case of the $Cs^+$ ion at ambient temperature in [19], as a comparison can be made with the same clay sheet arrangement. For the Na system the inferior values reported in the same reference ($2.25-2.7 \times 10^{-10}\,m^2\,s^{-1}$ for 2D diffusion) are most probably due to the difference in the clay sheet arrangement. Experimental data for ambient temperatures from neutron scattering studies are available for the Na system only and these are consistent with the data presented here [32]. Inelastic neutron scattering, tracing the movements of hydrogen atoms in the system, allows direct comparison with the simulations as it accesses similar timescales (order of 100 ps). Simulated water diffusion coefficients at ambient temperature for Cs-monohydrate reported by Sutton and Sposito [41] are $17.52 \pm 0.06 \times 10^{-10}\,\mathrm{m^2\,s^{-1}}$ for a hydration state of 3.5 molecules of water per cation (approximately half a monolayer in our classification), the MCY model of water and clay with both octahedral and tetrahedral substitution. Direct comparison with this system is difficult, but the value is nevertheless surprisingly high in light of our results. (We have quoted here the value reported in [41] multiplied by a factor of 3/2 to convert from a 3D to a 2D diffusion coefficient. The 3D diffusion coefficient is an average of all three 1D diffusion coefficients (equation (2)), along the $x$, $y$ and $z$ axes. The 2D diffusion coefficient is an average of only two values, the 1D diffusion coefficients along the $x$ and $y$ axes. If the displacement, $\langle r^2(t)\rangle$, along the $z$ axis is zero as in our confined system, the above averages corresponding to the 3D and 2D diffusion coefficients differ exactly by a factor of 3/2.)

Data from VACF analysis, based on 36 ps simulations, refer to short-term diffusion, whereas values from MSD analysis (simulation time 360 ps) refer to long-term diffusion. Figure 4 therefore compares diffusion coefficients obtained for long times (characteristic time 100–150 ps, empty symbols) and short times (characteristic time 5–15 ps, full symbols) for the monohydrated systems. Taking the example of the $Cs^+$ ion in Cs-monohydrate, we note that, at low temperature, both methods analyze motion within a single bound site, such as those shown in the $x$–$y$ projection of the trajectories. In other words, the simulation time is comparable to the residence time in a single site. As diffusion coefficients are formally defined in the limit of infinite time (equations (2) and (3)), we recognize that, in the cases when the residence time in a single site is comparable to the simulation time, a long-term tail in the motion of the particles (site-to-site movement) is not observed by the simulations and thus the simulated diffusion coefficient is an underestimate of the value defined formally. Considering the diffusion coefficients obtained from both techniques employed, there is evidence for a slightly slower increase in the diffusion coefficients for the $Cs^+$ ion compared with the $Na^+$ ion as a function of temperature. At the same time, the water phase exhibits very similar behaviour in the two systems.

Comparing the 2D diffusion coefficients of the ions and water in the Na-bihydrate and bulk system (figure 6), we observe that the absolute values of the coefficients are of the same order of magnitude. However, the temperature activation in the clay system is still lower than for the bulk. A quasi-elastic neutron scattering study of water in bihydrated Na-vermiculite [42] has provided evidence for the approach of water diffusion to that of the bulk in bihydrated systems.

For the diffusion of the ion, a clear difference is seen from the $x$–$z$ projections of the trajectories as a function of temperature (figure 7). Exchange between sites in the middle of the interlayer and sites closer to the clay sheet occurs one or two times during 360 ps at low temperature, whereas numerous jumps are observed at high temperatures. As expected, the underlying hexagonal pattern of the sheets has a minimal influence on the trajectories, as the ions are screened from the sheet by a layer of water. A high degree of delocalization is observed at high temperatures. The water phase in the bihydrated system is located to the sides of the central plane of the ions. From the $x$–$z$ projection, the water phase explores the hexagonal cavities of the underlying clay sheets and moves with ease to the opposite side of the interlayer even at low temperature.

Figure 8 summarizes the diffusion of water in the three systems studied and also shows experimental data for bulk water as a reference. An Arrhenius plot was used to yield the approximate energies of activation, which were 12–15 $\mathrm{kJ\,mol^{-1}}$ for the monohydrated systems and 14–19 $\mathrm{kJ\,mol^{-1}}$ for the Na-bihydrate. These values are of the same order of magnitude as the activation energy for bulk water (18 $\mathrm{kJ\,mol^{-1}}$). A more detailed comparison with the value for bulk water is difficult, as the process of diffusion is very different in the confined systems of clays and the bulk liquid.

In summary, ion diffusion in the Cs system shows clear site-to-site jump diffusion throughout the whole temperature range considered, whereas the $Na^+$ ion does not exhibit clear preferential sites even at low temperature. The behaviour of the water phase is similar for the two monohydrated systems. The change to the bihydrated Na system is a large step towards bulk behaviour. Diffusion coefficients of the water phase in the bihydrated state are of the same order of magnitude as in bulk water, although they increase more slowly as the temperature rises.

## 4. Conclusion

We conclude that temperature variation in the range $0-150^\circ\mathrm{C}$ mainly affects the structure of the water phase among the static properties. $Na^+$ and $Cs^+$ ions show very different modes of diffusion in the monohydrated system. The site-to-site jump diffusion of the $Cs^+$ ion is retained up to high temperatures and contrasts with the absence of clearly defined sites for the $Na^+$ ion even at low temperatures. The fact that the site-to-site jump diffusion of these ions persists up to high temperatures is an important measure, albeit qualitative for the moment, of the affinity of $Cs^+$ ions for the trigonal sites in the model used. More detailed analysis of the residence times of the water molecules in the hydration shells of the respective ions is necessary to answer questions such as whether the $Cs^+$ jumps from one six-coordinate site to another with a complete or partial loss of its hydration shell. Neither of the ions are seen to enter into the hexagonal cavities. It is generally agreed that, for the case of $Na^+$, the presence of a hydration shell increases its effective radius above the dimensions of the cavity. Throughout this study we have confirmed that, especially for monohydrated systems, ionic and water diffusion is dependent on the clay sheet arrangement on either side of the interlayer and this needs to be decoupled from other parameters such as temperature, as has been attempted here, for the Cs system.

The water phase shows very similar dynamics in the two monohydrated systems studied and approaches bulk behaviour in the Na-bihydrate system. On the basis of the results presented, a detailed quantitative comparison of the temperature activation of diffusion for a 2D water phase in clay and bulk water (3D) is possible for the first time.

A hetero-ionic montmorillonite system (one $Cs^+$ ion per five $Na^+$ ions) has already been studied at ambient temperature in an attempt to model a Na-montmorillonite with a trace of $Cs^+$ [39]. This study concluded that the water phase in the system is not perturbed by the presence of the $Cs^+$ ions and behaves as in the pure Na system. As far as the ions were concerned, they retained the characteristics of their homo-ionic counterparts. It is likely that this trend of independent $Cs^+$ and $Na^+$ diffusion is retained at higher temperatures, each ion continuing to exhibit its characteristic mode of motion.

This research was supported by ANDRA (Agence Nationale pour la Gestion des Déchets Radioactifs).

## References

[1] ANDRA, Referentiel Materiaux, Tome 1: Contexte et Objet, Rapport C.RP.AMAT.01.060, 2001.

[2] Giese, R. F., and van Oss, C. J., 2002, *Colloid and Surface Properties of Clays and Related Minerals*, S.rfactant Science Series, vol. 105 (New York: Marcel Dekker).

[3] Hensen, E. J. M., and Smit, B., 2002, *J. Phys. Chem.* B, **106,** 12664.

[4] Bérend, I., 1991, Les Mechanismes d'hydratation de montmorillonites homoioniques pour des pressions relatives inferieures a 0.95, These de doctorat, Institut National Polytechnique de Lorraine.

[5] Calvet, R., 1973, *Ann. Agron.*, **24,** 77.

[6] Cases, J. M., Bérend, I., Francois, M., Uriot, J. P., Michot, L. J., and Thomas, F., 1997, *Clays clay Miner.*, **45,** 8.

[7] Schramm, L. L., and Kwak, J. C. T., 1982, *Clays clay Miner.*, **30,** 40.

[8] Faisandier, K., Pons, C. H., Tchoubar, D., and Thomas, F., 1998, *Clays clay Miner.*, **46,** 636.

[9] ANDRA, Referentiel Materiaux, Tome 2: Les Materiaux Argileux, Rapport C.RP.AMAT.01.060, 2001.

[10] Delville, A., 1992, *Langmuir*, **8,** 1796.

[11] Boek, E. S., Coveney, P. V., and Skipper, N. T., 1995, *Langmuir*, **11,** 12608.

[12] Chang, F. C., Skipper, N. T., and Sposito, G., 1997, *Langmuir*, **13,** 2074.

[13] Chávez-Páez, M., dePablo, L., and dePablo, J. J., 2001, *J. chem. Phys.*, **114,** 10948.

[14] de Siqueira, A. V. C., Skipper, N. T., Coveney, P. V., and Boek, E. S., 1997, *Molec. Phys.*, **92,** 1.

[15] Titiloye, J. O., and Skipper, N. T., 2001, *Molec. Phys.*, **99,** 899.

[16] Huang, W.-L., Bassett, W. A., and Wu, T.-C., 1994, *Am. Miner.*, **79,** 683.

[17] Wu, T.-C., Bassett, W. A., Huang, W.-L., Guggenheim, S., and Koster van Groos, A. F., 1997, *Am. Miner.*, **82,** 69.

[18] de Siqueira, A. V., Lobban, C., Skipper, N. T., Williams, G. D., Soper, A. K., Done, R., Dreyer, J. W., Humphreys, R. J., and Bones, J. A. R., 1999, *J. Phys.: condens. Matter*, **11,** 9179.

[19] Marry, V., Turq, P., Cartailler, T., and Levesque, D., 2002, *J. chem. Phys.*, **117,** 3454.

[20] Koster van Groos, A. F., and Guggenheim, S., 1984, *Am. Miner.*, **69,** 872.

[21] Bray, H. J., Redfern, S. T., and Clark, S. M., 1998, *Miner. Mag.*, **62,** 647.

[22] Berendsen, H. J. C., Grigera, J. R., and Straatsma, T. P., 1987, *J. phys. Chem.*, **91,** 6269.

[23] Brodholt, J., and Wood, B., 1993, *J. Geophys. Res.*, **98,** 519.

[24] Smith, D., 1998, *Langmuir*, **14,** 5959.

[25] Frenkel, D., and Smit, B., 2002, *Understanding Molecular Simulations, From Algorithms to Applications* (New York: Academic Press).

[26] Smith, W., and Forester, T., 2001, *The DLPOLY2 User Manual* (Warrington, UK: Daresbury Laboratory).

[27] Harr, L., Gallagher, J. S., and Kell, G. S., 1984, *NBS/NRC Steam Tables* (Hemisphere Publishing).

[28] Kawamura, K., Ichikawa, Y., Nakano, M., Kitayama, K., and Kawamura, H., 1999, *Engng Geol.*, **54,** 75.

[29] Skipper, N. T., Sposito, G., and Chang, F. C., 1995, *Clays clay Miner.*, **43,** 294.

[30] Marry, V., 2002, Modelisation microscopique de la strucutre et de la dynamique de l'eau et des ions dans les argiles de stockage de type montmorillonite, These de doctorat, Universite Pierre et Marie Curie.

[31] Sposito, G., and Prost, R., 1982, *Chem. Rev.*, **82,** 553.

[32] Chang, F. C., Skipper, N. T., and Sposito, G., 1995, *Langmuir*, **11,** 2734.

[33] Park, S.-H., and Sposito, G., 2000, *J. phys. Chem.* B, **104,** 4642.

[34] Delville, A., and Sokolowski, S., 1993, *J. phys. Chem.*, **97,** 6261.

[35] Hawkins, R. K., and Egelstaff, P. A., 1980, *Clays clay Miner.*, **28,** 19.

[36] Powell, D. H., Tongkhao, K., Kennedy, S. J., and Slade, P. G., 1997, *Clays clay Miner.*, **45,** 290.

[37] Sposito, G., Prost, R., and Gaultier, J. P., 1983, *Clays clay Miner.*, **31,** 9.

[38] Weiss, C. A., Kirkpatrick, R. J., and Altaner, S. P., 1990, *Am. Miner.*, **75,** 970.

[39] Marry, V., and Turq, P., 2003, *J. phys. Chem.* B, **107,** 1832.

[40] Kato, H., Muroi, M., Yamada, N., Ishida, H., and Sato, H., 1995, *Scientific Nasis for Nuclear Waste Management*, vol. 18 (Pittsburgh, PA: Materials Research Society), p. 277.

[41] Sutton, R., and Sposito, G., 2001, *J. Colloid Interface Sci.*, **237,** 174.

[42] Swenson, J., Bergman, R., and Howells, W. S., 2001, *J. chem. Phys.*, **113,** 2873.

[43] Holz, M., Heil, S. R., and Sacco, A., 2000, *Phys. Chem. chem. Phys.*, **2,** 4740.

[44] In het Panhuis, M., Patterson, C. H., and Lynden-Bell, R. M., 1998, *Molec. Phys.*, **94,** 963.

ELSEVIER

Current Opinion in Colloid and Interface Science 9 (2004) 124–127

Current Opinion in
COLLOID and
INTERFACE SCIENCE

www.elsevier.com/locate/cocis

# Na/Cs montmorillonite: temperature activation of diffusion by simulation

N. Malikova[a,b], V. Marry[a], J.-F. Dufrêche[a], P. Turq[a,]*

[a]*Laboratoire Liquides Ioniques et Interfaces Chargées, boite postale 51, Université P. et M. Curie, 4 place Jussieu, F-75252 Paris Cedex 05, France*
[b]*ANDRA, Parc de la Croix Blanche, 1/7 rue Jean Monnet, F-92298 Châtenay-Malabry Cedex, France*

## Abstract

The effect of temperature in the range of 0–150 °C was studied for homoionic montmorillonite clays with $Na^+$ and $Cs^+$ compensating ions in low hydration states. Both static and dynamic information concerning the interlayer ions and water molecules was obtained by Monte Carlo and molecular dynamics. Principal structural changes were limited to the water phase, marked difference was observed in the modes of diffusion of $Cs^+$ and $Na^+$ ions. $Cs^+$ ion exhibited a clear site-to-site diffusion between sites allowing coordination to six oxygen atoms of the clay sheets, this behaviour persisted to high temperatures. Preferential sites for the $Na^+$ counterion were significantly less well-defined, even at low temperatures. Water phase showed similar behaviour in the Na/Cs-monohydrated systems, a rapid approach to bulk dynamics was seen in the transition from monohydrated to bihydrated Na-montmorillonite.

*Keywords:* Cs/Na montmorillonite; Temperature effect; Low hydration

## 1. Introduction

The potential application of compacted clays as components of engineered barriers around underground storage sites of high-activity radioactive waste has led to intense research of these materials [1]. The most important properties of clays for this barrier are their low permeability to water and high retention capacity of cations, which can be traced down to their microscopic structure. Clays consist of fused layers of octahedra of oxides of $Al^{3+}$ or $Mg^{2+}$ and tetrahedra of $Si^{4+}$. The covalent bonding within a single sheet contrasts with the relatively weak interactions between individual sheets. By substitution of $Al^{3+}$, $Mg^{2+}$ or $Si^{4+}$ with lower valence cations, the clay sheets acquire a negative charge, which is then compensated by cationic species between the sheets (so-called interlayer). With increasing humidity, discrete water layers are formed in the interlayer, with varying water content per layer depending on the charge of the sheets and the nature of the counterion. The dynamics of the interlayer species is critically dependent on the water content in the system. Experimental investigation of dynamics of ions and water in macroscopic clay samples is often complex due to multiple porosities in the system: between clay sheets, clay particles and their aggregates [2]. Microscopic simulations have been a valuable tool in providing both static and dynamic information on the interlayer species by zooming onto the smallest type of porosity. In this paper we addressed the issue of the effect of temperature (0–150 °C) on the behaviour of the interlayer species, while considering two different counterions.

## 2. Models and simulation techniques

The model clay under investigation was a montmorillonite type clay with a unit cell $Cat_{0.75}[Si8](Al_{3.25}Mg_{0.75})O_{20}(OH)_4$ where Cat stands for cation in the interlayer. Interlayer cations considered were $Na^+$ and $Cs^+$, the former in both mono- and bihydrated state, the latter in monohydrated state only as bihydrated Cs-montmorillonite is not observed experimentally. Based on our previous study [3], we defined the mono- and bihydrated state as corresponding to 6 and 12 water molecules per cation, respectively. From dehydration studies the water in the first two layers leaves at temperatures above 150 °C [2] and thus it is meaningful

---

*Corresponding author.
*E-mail address:* pt@ccr.jussieu.fr (P. Turq).

1359-0294/04/$ - see front matter © 2004 Elsevier Ltd. All rights reserved.
doi:10.1016/j.cocis.2004.05.016

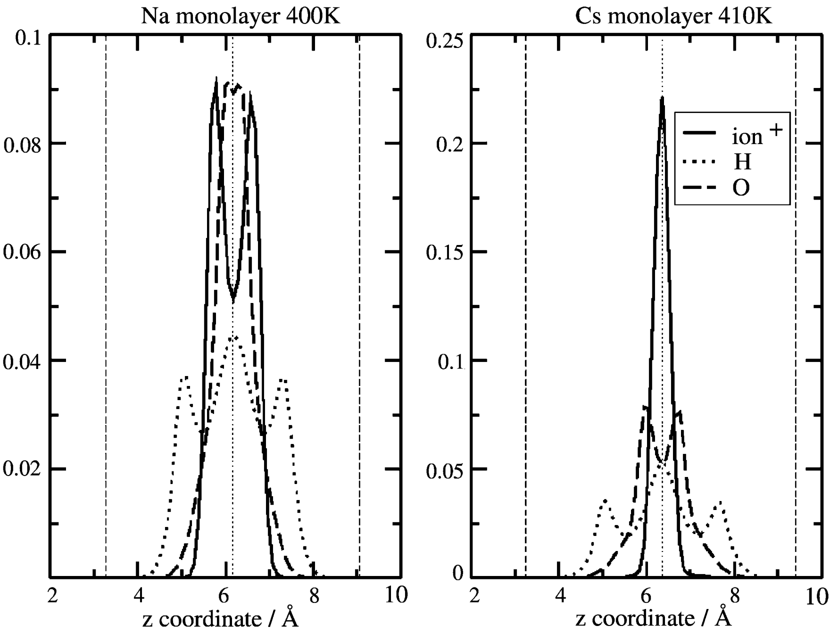

Fig. 1. Monohydrated systems, profiles of interlayer atoms. Vertical lines: surface of clay sheets and middle of interlayer.

to subject the monolayer and bilayer state to the chosen temperature range, without changing the water content of the system. The simulation box contained two sheets of clay (area 20.72×17.94 Å, thickness 6.54 Å), each consisting of eight unit cells. Six balancing counterions were introduced into the interlayer together with 36 or 72 water molecules for monolayer and bilayer, respectively. The clay sheets were considered as rigid. The model of water used was the rigid SPC/E model [4]. The validity of this model over the whole temperature range studied has been confirmed [5]. Interaction potentials used were the Lennard–Jones 6–12 and Coulombic potential as described in Ref. [3], where further technical details are also to be found. Monte Carlo (MC) simulations ($N\sigma_{zz}T$ ensemble, $\sigma_{zz}=1$ bar) were carried out to give equilibrium sheet spacing and distributions of atoms in the interlayer at a given temperature. Starting from equilibrium configurations of MC, molecular dynamics (MD) simulations (*NVE* ensemble, 360 ps, time step = 0.001 ps) followed to determine the diffusion coefficients of interlayer species.

## 3. Results and discussion

Sheet spacing in the temperature range considered shows variation of the order of 0.2–0.3 Å for all three systems studied. The interlayer distributions of counterions and water molecules along axis perpendicular to clay sheets broaden with increasing temperature (Fig. 1) but retain the number and position of peaks characteristic for the given counterion at ambient temperatures [6,3]. The analysis of radial distribution functions showed no changes in the equilibrium distances between the ions and water molecules over the temperature range studied. For the $Na^+$ ion, coordination numbers of water molecules were maintained at four and six for Na mono- and bi- hydrated states, respectively, as seen previously [7]. Radial distribution functions involving oxygen atoms of the clay sheets, features a prominent peak in the case of $Cs^+$ ion, corresponding to $Cs^+$ sites above Si atoms of the clay sheet, with coordination to the nearest three oxygen atoms of the clay, as shall be discussed later. On the basis of the radial distribution function between oxygen atoms of water, additional structuring seems to occur in the water phase of Na

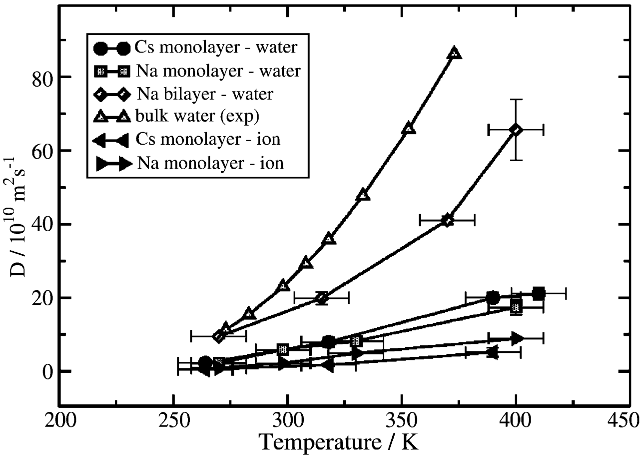

Fig. 2. Two-dimensional diffusion coefficients as a function of temperature for ions and water in Na and Cs montmorillonite.

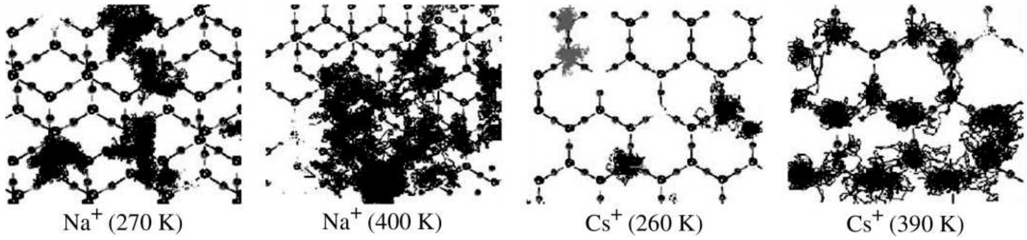

Fig. 3. Trajectories of ions at low and high temperatures. Entire trajectories trace the motion of the species over approximately 360 ps.

montmorillonite as temperature is lowered (appearance of a shoulder at 3.2 Å in addition to the main peak at 2.8 Å).

Data from the mean squared displacement method (MSD) for the determination of diffusion coefficients are presented [8]. Due to the anisotropy of the system, motion in the three principal directions was considered separately. In MSD analysis mean squared displacement along the $z$-axis tended to a constant and could not be easily fitted to a straight line. This shows clearly the confinement of the system in the $z$ direction. The data for $x$ and $y$ directions were used on their own to determine two-dimensional diffusion coefficients of cations and water molecules (based on data for oxygen atoms) in the plane of the clays sheets ($xy$ plane).

Diffusion coefficients of water and ions as a function of temperature are summarized in Fig. 2, while trajectories of $Na^+$ and $Cs^+$ ions in the monohydrated systems only are shown in Fig. 3. Simulated diffusion coefficients for $Na^+$ and $Cs^+$ ions are of the order of $10^{-10}$ $m^2$ $s^{-1}$ and increase by an order of magnitude over the temperature range studied. A clear difference is observed in the modes of diffusion for the two ions. At both low and high temperature, $Cs^+$ ions exhibit a site-to-site jump diffusion, between sites allowing coordination to three oxygen atoms from each of the two adjacent clay sheets, referred to as the trigonal sites. Overall the coordination number of the ions with respect to oxygen atoms of clay only is therefore six. Together with the oxygen atoms of water, this brings the overall coordination of the $Cs^+$ ions to approximately 12, higher than the bulk value of nine. The number of the six-coordinate clay sites explored by the ions throughout 360 ps increases from 1 to 2 at low temperature (264 K) to 5 sites on average at high temperature (390 K). This applies to the configuration of the clay sheets where the number of the six-coordinate sites with respect to oxygen atoms of clay is maximized as the sheets are face-to-face. For other configurations of the clay, clear preference for these six-coordinate sites is also seen. This is likely to lead to a variation in the overall diffusion coefficient as a function of the clay sheet arrangement. No clear site-to-site diffusion is observed for the $Na^+$ ion, which suggests yet again the greater importance of the clay–ion interaction in case of the $Cs^+$ ion, however, variation of the diffusion coefficient as a function of the clay sheet arrangement has been seen for both systems [3]. From $x$–$z$ projections of the ionic trajectories, neither of the ions enters into hexagonal cavities. The $Cs^+$ ion is restricted to the six-coordinate sites described above while the $Na^+$ ion even if above the hexagonal cavity does not enter, due to the presence of its hydration shell [9]. The preferential sites for the $Cs^+$ ions described here have been observed previously [3,10]. Evidence from nuclear magnetic resonance suggests more than one type of possible sites for $Cs^+$ ions, reaching 9- to 12-coordinate sites for dehydrated samples [11].

The behaviour of the water phase as a function of temperature is similar for the two ions in the monohydrated states. Water molecules, unlike the ions, enter into the hexagonal cavities of the adjacent clay sheets. However, in the plane of the clay sheets, the diffusion is rather delocalised as in the case of $Na^+$ ion. For Na-bihydrate, the two-dimensional diffusion coefficients of water are of the same order of magnitude as for bulk water, with a lower temperature activation. Approach to bulk diffusion has been seen by neutron scattering [12]. Arrhenius plot was used to yield approximate energies of activation for the diffusion of water, which were 12–15 kJ $mol^{-1}$ for the monohydrated systems and 14–19 kJ $mol^{-1}$ for the Na-bihydrate. These values are of the same order of magnitude as the activation energy for bulk water (18 kJ $mol^{-1}$).

## Acknowledgments

This research is supported by ANDRA (Agence Nationale pour la Gestion des Déchets Radioactifs).

## References

[1] ANDRA. Referentiel Materiaux, Tome 1: Contexte et objet; Rapport C.RP.AMAT.01.060, 2001.

[2] ANDRA. Referentiel Materiaux, Tome 2: Les Materiaux argileux; Rapport C.RP.AMAT.01.060, 2001.

[3] Marry V, Turq P, Cartailler T, Levesque D. Microscopic simulation of structure and dynamics of water and counterions in a monohydrated montmorillonite. J Chem Phys 2002;117:3454–63.

[4] Berendsen HJC, Grigera JR, Straatsma TP. The missing term in effective pair potentials. J Phys Chem 1987;91:6269–71.

[5] Brodholt J, Wood B. Simulation of the structure and thermodynamic properties of water at high pressures and temperatures. J Geophys Res 1993;98:519–36.

[6] Skipper NT, Sposito G, Chang FC. Monte Carlo simulation of interlayer molecular structure in swelling clay minerals. 2. Monolayer hydrates. Clays Clay Miner 1995;43:294–303.

[7] Delville A. Structure of liquids at solid interface: an application to the swelling of clay by water. Langmuir 1992;8:1796–805.

[8] Frenkel D, Smit B. Understanding molecular simulations, from algorithms to applications. Academic Press, 2002.

[9] Sposito G, Prost R, Gaultier JP. Infrared spectroscopic study of adsorbed water on reduced-charge Na/Li montmorillonites. Clay Clay Miner 1983;31:9–16.

[10] Smith D. Molecular computer simulations of the swelling properties and interlayer structure of cesium montmorillonite. Langmuir 1998;14:5959–67.

[11] Weiss CA, Kirkpatrick RJ, Altaner SP. Variations in interlayer cation sites of clay minerals as studied by 133Cs MAS nuclear magnetic resonance spectroscopy. Am Mineral 1990;75:970–82.

[12] Swenson J, Bergman R, Howells WS. Quasielastic neutron scattering of two-dimensional water in a vermiculite clay. J Chem Phys 2000;113:2873–9.

Available online at www.sciencedirect.com
SCIENCE DIRECT®
ELSEVIER
Chemical Physics 317 (2005) 226–235
Chemical Physics
www.elsevier.com/locate/chemphys

# Diffusion of water in clays – microscopic simulation and neutron scattering

N. Malikova [a,b,*], A. Cadéne [a], V. Marry [a], E. Dubois [a], P. Turq [a,*], J.-M. Zanotti [c], S. Longeville [c]

[a] *Laboratoire Liquides Ioniques et Interfaces Chargées, boite postale 51, Université P. et M. Curie, 4 place Jussieu, F-75252 Paris Cedex 05, France*
[b] *ANDRA, Parc de la Croix Blanche, 1/7 rue Jean Monnet, F-92298 Châtenay-Malabry Cedex, France*
[c] *Laboratoire Léon Brillouin, CEA-CNRS, CEA Saclay, F-91191 Gif-sur-Yvette, France*

Received 30 December 2004; accepted 25 April 2005
Available online 6 June 2005

## Abstract

The dynamics of water in porous charged media (montmorillonite clay) is investigated on the picosecond-timescale by quasi-elastic neutron scattering (time-of-flight (TOF) and neutron spin echo (NSE) techniques) and classical molecular dynamics simulations. Correspondence is discussed not only in terms of integrated quantities such as diffusion coefficients but also more directly on the level of intermediate scattering functions. Both simulated and experimental water diffusion coefficients are of the order of $5–10 \times 10^{-10}$ m$^2$ s$^{-1}$. Closer analysis suggests that, unlike NSE, TOF and simulation underestimate relaxation times in the low-$Q$ region due to insufficiently large correlation times probed. Comparison between experimental and simulated dynamics is rendered difficult by the features of the real montmorillonite clay (interstratification, mesoporous water) omitted in the model. For the de-coupling of phenomena in a real clay, a more complete set of data for the montmorillonite clay (different ions, hydration states) or the use of other, in some respect more homogeneous clays (hectorite, vermiculite) is suggested.

*Keywords:* Montmorillonite clay; Water diffusion; Quasi-elastic neutron scattering; classical molecular dynamics simulations

## 1. Introduction

As constituents of soil, clay minerals are naturally occurring highly abundant materials, the study of which spans over several fields of research, from geology (geological timing, soil weathering and stability) to biochemistry (binding of nutrients and pollutants in soil, catalysis) [1]. More recently, the potential application of clays as components of barriers around underground storage sites of radio-active waste has intensified the study of mobility of water and ionic species in these systems [2]. At the same time these investigations shed light onto more fundamental issues such as dynamics of liquids in confined media and phenomena at a solid/liquid interface.

The crystal structure of clays has been established from X-ray diffraction studies for almost all types of common clays [3]. Individual clay layers consist of fused sheets of octahedra of $Al^{3+}$ or $Mg^{2+}$ oxides and tetrahedra of $Si^{4+}$ oxides. Substitution of $Al^{3+}$, $Mg^{2+}$ or $Si^{4+}$ with lower valence ions results in an overall negative charge on the layers, which is then compensated by cationic species (counterions) between clay layers (interlayers). Under increasing relative humidity the compensating ions become hydrated and the spacing between individual layers increases [1]. While the detailed swelling characteristics of a clay (interlayer spacing as a

---

[*] Corresponding authors. Tel.: +33 1 4427 3108; fax: +33 1 4427 3228.
*E-mail addresses:* malikova@ccr.jussieu.fr (N. Malikova), pt@ccr.jussieu.fr (P. Turq).

0301-0104/$ - see front matter © 2005 Elsevier B.V. All rights reserved.
doi:10.1016/j.chemphys.2005.04.035

function of relative humidity) depends crucially on the charge of the clay layers (magnitude and localisation) and the nature of the compensating ion, in general, it occurs in three stages. Swelling begins in a step-wise manner (discrete layers of water formed in the interlayer, states referred to as monolayer/monohydrated, bilayer/bihydrated, etc.), becomes continuous thereafter and in the extreme a colloidal suspension of clay particles (<10 aligned layers) is formed [4–7]. Beyond the microscopic scale, aggregates of aligned clay layers form particles of the order of 10–1000 nm in size, with porosities on the meso- (8–60 nm) and macroscale (>60 nm) [8,5,7,6]. As will be shown, this type of multi-scale structure renders the analysis of dynamic data in clays rather complex. The problem has been addressed both by experimental and modelling techniques.

Microscopic models of clays include the atomic detail of the clay layers as well as the interlayer species, in the simplest case the charge-balancing ions (counterions) and water. Microscopic simulations of clays have been an active field of research since the late 1980s and began with simulations at ambient temperature and pressure, of clays with various cationic species [9–12]. More recently, several studies appeared dealing with non-ambient conditions (increased temperatures and pressures), which are primarily linked to the issue of storage of radioactive waste or bore-hole stability [13–15]. In addition, clay systems with small organic molecules have also been modelled, inspired by clays acting as retention sites or sites of catalytic activity [16]. Majority of simulation studies on clays concentrates on the static properties such as interlayer spacing as a function of relative humidity and distribution of interlayer species. Only in some cases has dynamical information been extracted and that in the form of diffusion coefficients only. Bearing in mind that various models of water have been used as well as differing location and abundance of charges on clay layers, the simulated diffusion coefficients ($D_{\mathrm{sim}}$) for montmorillonite clays can be summarised as follows (two-dimensional values quoted, see next section for further details): monovalent counterions ($\mathrm{Na}^+$, $\mathrm{Cs}^+$) in monohydrated systems, $D_{\mathrm{sim}}^{\mathrm{ions}} = 0.2\text{–}2.5 \times 10^{-10}\ \mathrm{m^2\,s^{-1}}$, $D_{\mathrm{sim}}^{\mathrm{water}} = 1.7\text{–}7.0 \times 10^{-10}\ \mathrm{m^2\,s^{-1}}$, in bihydrated systems, $D_{\mathrm{sim}}^{\mathrm{ions}} = 3.7\text{–}10 \times 10^{-10}\ \mathrm{m^2\,s^{-1}}$, $D_{\mathrm{sim}}^{\mathrm{water}} = 12\text{–}15 \times 10^{-10}\ \mathrm{m^2\,s^{-1}}$ [12,14,15,17,18].

Apart from microscopic simulations, the information into the dynamics of interlayer species in clays is at present available from inelastic neutron scattering studies. Whereas microscopic simulations give access to dynamics of both water and ionic species in the clay system, neutron scattering studies have been limited to the investigation of dynamics of water, relying on the dominating incoherent signal of its constituent hydrogen atoms. Attempts to exploit the coherent signal, in the neutron spin echo technique, and provide information on the dynamics of cations have been, for the moment, unsuccessful in our own trials and elsewhere [19]. Both microscopic simulation and neutron scattering study dynamics on the same scale of time and space (up to thousands of picoseconds, distances up to a few nanometres) and thus a direct comparison can be attempted. This is to be contrasted with abundant macroscopic diffusion studies of clays (tracer experiments) [20,21], the space- and time-scale of which (distances order of meters and time order of hours, days) places it aside the two techniques above and direct comparison with them is impossible.

The first studies into the dynamics of water in clay systems by neutron scattering, more specifically by the time-of-flight technique, date back into the early 1980s and consider both monovalent and bivalent counterions at low hydration states. The quasi-elastic broadening as a function of the wave-vector squared ($Q^2$) was usually seen to approach a plateau at high values of $Q^2$ and thus the data were analysed using a jump-diffusion model for the motion of water and diffusion coefficients, residence times and mean-squared jump lengths between sites were determined [22–24]. In these jump-diffusion models, a Gaussian distribution of jump-lengths has been used most widely. Evidence for jump diffusion (appearance of plateau) was seen when raw TOF data were analysed using two Lorentzians representing translational and rotational motion as well as using a more simplistic approach with a single Lorentzian for translational motion. Across the various studies, for montmorillonite systems with monovalent counterions, the measured diffusion coefficient of water varies between 0.5 and $4 \times 10^{-10}\ \mathrm{m^2\,s^{-1}}$ for samples at relative humidity (relative humidity is the ratio of the partial pressure of water and the water vapour pressure at a particular temperature) around 40% and reach up to $10 \times 10^{-10}\ \mathrm{m^2\,s^{-1}}$ at relative humidity around 80% (loosely corresponding to a monolayer and a bilayer, respectively). This range becomes larger when measurements on different types of clay and/or bivalent cations are included. However, overall these early studies do not feature, at ambient temperature and first two hydration states, values of diffusion coefficients higher than half of the bulk value for water ($D_{\mathrm{exp}}^{\mathrm{bulk\ water}} = 23 \times 10^{-10}\ \mathrm{m^2\,s^{-1}}$). This is true for three types of clay studied (hectorite, montmorillonite, vermiculite) and both mono and bivalent counterions [22–25].

In the recent years, a combination of the TOF and NSE technique has been employed to study water in clay systems [19,26]. As in the earlier studies, the time-of-flight technique suggested a jump diffusion. The NSE data were also interpreted using a jump-diffusion model, however, in this technique the evidence for a plateau is weaker due to a lack of points and significant error bars in the high-$Q$ region. We note that the diffusion coefficients arising from the data in [19,26] have been recently revised [27]. The corrected values are $26.4 \times 10^{-10}\ \mathrm{m^2\,s^{-1}}$ for the TOF technique and $1.7 \times 10^{-10}\ \mathrm{m^2\,s^{-1}}$ for NSE

[27]. These studies therefore show rather surprising results. Not only is there a difference of a factor of 15 between the diffusion coefficients determined by the two techniques now available (as the authors note themselves [19]), also the TOF data gives higher values than seen in the early studies, values approaching bulk water behaviour [27,28].

In summary therefore, comparing diffusion coefficients of water in montmorillonite clays with monovalent counterions, determined by microscopic simulation and neutron scattering, the observed ranges agree within a factor of 3 for the monohydrated systems ($D_{\mathrm{sim}}^{\mathrm{water}} = 1.7\text{–}7.0 \times 10^{-10}\ \mathrm{m^2\,s^{-1}}$, $D_{\mathrm{exp}}^{\mathrm{water}} = 0.5\text{–}4 \times 10^{-10}\ \mathrm{m^2\,s^{-1}}$) and a factor of 1.5 for the bihydrated systems ($D_{\mathrm{sim}}^{\mathrm{water}} = 12\text{–}15 \times 10^{-10}\ \mathrm{m^2\,s^{-1}}$, $D_{\mathrm{exp}}^{\mathrm{water}} = 10 \times 10^{-10}\ \mathrm{m^2\,s^{-1}}$). Only the recent measurements of TOF [26] on bihydrated vermiculite do not fall within the range specified above ($27 \times 10^{-10}\ \mathrm{m^2\,s^{-1}}$). The aim of this paper is to take further the dynamic information on water in clays obtained by simulation and experiment, beyond the comparison of diffusion coefficients, and hint at the reasons for discrepancies between simulation, TOF and NSE. For this purpose a montmorillonite clay with $\mathrm{Na^+}$ counterions in the bihydrated state is analysed.

## 2. Modelling techniques

The unit cell of the model montmorillonite clay used here was $\mathrm{Na_{0.75}[Si_8](Al_{3.25}Mg_{0.75})O_{20}(OH)_4}$ in the unhydrated state, closest possible to the real clay system studied. Rare isomorphic substitutions in the latter could not be accounted for by the model due to the finite size of the simulation box. In its final form, the simulation box consisted of two clay layers (area 20.72 Å × 17.94 Å, thickness 6.54 Å) each formed of 8 above unit cells and its charge being balanced by 6 cations in the interlayer (Fig. 1). The counterion considered was $\mathrm{Na^+}$, simulated in a bihydrated state corresponding to 12 water molecules per cation [12]. Periodic boundary conditions were applied in all three directions, resulting in a model clay system consisting of infinite parallel equally spaced clay layers with identical composition of mobile species in each interlayer.

The inter-atomic potentials between each pair of atoms in the simulations box were the Lennard-Jones and Coulombic potentials representing the Van der Waals/steric repulsion and electrostatic interactions, respectively. Atomic charges and Lennard-Jones parameters for each atom were taken from Smith [29] for the clay and Berendsen et al. [30] for the model of water (SPC/E model). Both the clay layers and individual water molecules were considered here as rigid. Further details of this common model of clay systems can be found in previous simulation studies [9,11,31,32].

Fig. 1. Simulation box for Monte Carlo and molecular dynamics, consisting of two half-layers (hs), central layer (cs) and two interlayer spacings (int) with numbers of ions and water molecules in a predetermined ratio, corresponding to a given hydration state.

Monte Carlo simulations were used to determine the equilibrium layer spacing for a given composition of the interlayer. Thereafter molecular dynamics simulations (NVE ensemble, $t_{\mathrm{step}} = 0.001$ ps) traced the motion of the interlayer cations and water, while the clay layers themselves were fixed at the equilibrated positions. Coordinates of all mobile atoms were recorded every 0.02 ps throughout simulations of 655 ps in total length. The final data from molecular dynamics simulations are thus, for each atom, in the form of trajectories or time-dependent position $\mathbf{R}(t)$. The information obtained in the atomic trajectories is vast; here we concentrated on the trajectories of the hydrogen atoms in the system and determined diffusion coefficients using the mean squared displacement (MSD) method. Due to anisotropy of the system each principal direction was analysed separately. The one-dimensional relationship for the MSD method is

$$\lim_{t\to\infty} \frac{\langle r^2(t)\rangle}{t} = 2D_{\mathrm{MSD}}, \tag{1}$$

where $r$ is displacement, $t$ is time and $D$ the diffusion coefficient. In practice, the diffusion coefficient is calculated from the gradient of the linear part of the plot of MSD, $\langle r^2(t)\rangle$, versus time. For simulated diffusion coefficients we have used throughout the paper the two-dimensional diffusion coefficient in the $xy$ plane, plane of clay layers (an average of the one-dimensional diffusion coefficients in the $x$ and $y$ directions). The diffusion coefficient along the $z$ axis determined by the MSD method was zero. In addition, the incoherent intermediate scattering function, $S_{\mathrm{inc}}(Q,t)$, and the elastic incoherent structural factor, $\mathrm{EISF}(Q)$, formally corresponding to $S_{\mathrm{inc}}(Q,t)$ in the limit of $t \to \infty$, were calculated on the basis of the motion of hydrogen atoms according to the formulae

$$S_{\mathrm{inc}}(Q,t) = \frac{1}{N_{\mathrm{H}}} \sum_{\forall \mathrm{H}} \overline{\langle \exp\left[-\mathrm{i}\mathbf{Q}\cdot\mathbf{R}_{\mathrm{H}}(0)\right] \exp\left[\mathrm{i}\mathbf{Q}\cdot\mathbf{R}_{\mathrm{H}}(t)\right]\rangle}^{Q}, \tag{2}$$

$$\mathrm{EISF}(Q) = \frac{1}{N_{\mathrm{H}}} \sum_{\forall \mathrm{H}} \overline{\left\langle \left|\exp\left[-\mathrm{i}\mathbf{Q}\cdot\mathbf{R}_{\mathrm{H}}\right]\right|^2 \right\rangle}^{Q}. \tag{3}$$

At every value of $Q$, for each H atom separately, the average of the correlation functions was carried out over $10Q$ vectors having the same modulus and being isotropically distributed in space (notation $\overline{\langle\cdot\rangle}^{Q}$).

## 3. Experimental techniques

Natural sodium montmorillonite was obtained by purification and homoionisation of commercial bentonite MX-80. Bentonite (40 g) dispersed in de-ionized water (1 $\mathrm{dm}^3$) was centrifuged (≈20,000$g$ for 30 min) and the top part of sediment re-dispersed in de-ionized water (pH = 5, 80 °C) by stirring (12 h, 2 times) to obtain a particular size fraction (<2 μm) of montmorillonite clay particles. This fraction was dispersed in 0.1 M NaCl solution by stirring (12 h), repeatedly washed (de-ionized water) until complete removal of $\mathrm{Cl}^-$ ions ($\mathrm{AgNO_3}$ test), dried (80 °C), crushed and resulting powder stored under dried atmosphere. As determined by Guillaume et al. [33], the resulting material is $\mathrm{Cat_{0.76}[Si_{7.96}Al_{0.04}](Al_{3.1}Mg_{0.56}Fe^{III}_{0.18}Fe^{II}_{0.16})O_{20}(OH)_4}$. Dried purified samples (at least three days under dry atmosphere) were then equilibrated (three weeks) at the desired relative humidity (85% or 95% – see Section 4) at 25 ± 2 °C. The water intake was monitored by mass measurements. The drying of the purified sample before equilibration at a given relative humidity is a crucial step in the sample preparation, due to observed hysteresis in the swelling of clays (causes the appearance of different hydration states at a given relative humidity depending on the initial state).

Neutron spin echo (NSE) [34,35] and time-of-flight (TOF) [36] experiments were carried out on the MUSES and MIBEMOL spectrometers in LLB, Saclay, France. NSE measurements were performed under ambient pressure on 2 mm thick samples (order of 0.5 mm equivalent water thickness). Sample cells were filled under controlled relative humidity and no water loss from the full sample cell was confirmed by weighing throughout the experiment. The montmorillonite samples was fully hydrogenated and thus, to a good approximation, the incoherent scattering signal from the H atoms in the sample was monitored. Polarisation of the scattered neutron beam was measured at carefully chosen $Q$ values, between 0.5 and 1.8 $\mathrm{\AA}^{-1}$, in zones of no coherent contribution from the clay structure. As mentioned previously, deuteration of the clay samples in order to exploit the stronger coherent signal [$P(Q) = C(Q) - (1/3)I(Q)$, where $P(Q)$, $C(Q)$ and $I(Q)$ are polarisation, coherent and incoherent signal, respectively], resulted in a dramatic decrease in the polarisation, most probably due to incomplete exchange of H atoms by D atoms, and deuterated samples were thus not analysed further. By combination of both the NSE and NRSE (neutron resonance spin echo) technique [37–39], measurements for correlation times up to 500 ps/1000 ps were achieved.

Time-of-flight measurements of the incoherent signal from the hydrogenated montmorillonite sample were carried out under reduced pressure (He 200 mbar) at incident neutron wavelength of 9 Å ($Q$ range: 0.21–1.28 $\mathrm{\AA}^{-1}$). These high resolution measurements at 9 Å allow analysis of the quasi-elastic zone in terms of translational motion without a rotational contribution due to both a very low intensity of the rotational signal (the intensity contributing to the elastic peak is significant at small $Q$, thus strongly diminishing the intensity of the quasi-elastic signal) and resolution considerations (the rotational contribution in form of a wide Lorentzian is seen as a flat background at high resolution).

## 4. Results and discussion

In this section, we shall initially follow the analysis of previous papers concerned with dynamics in clays and present an overview of diffusion coefficients determined from our simulation, NSE and TOF data. While discussing the problems encountered, we shall turn back to a more direct comparison between simulation and experiment on the level of the intermediate scattering function.

Departing from the approximation of the van Hove self correlation function [$G(R,t)$] being a Gaussian, the intermediate scattering function [$S(Q,t)$, measured by NSE] is an exponential and the scattering function [$S(Q,\omega)$, measured by TOF] is a Lorentzian [40]. The $S(Q,t)$ data both from simulation (Fig. 2) and from NSE measurements (Fig. 3) were fitted with stretched exponentials of the form

$$S(Q,t) = A\exp\left[-(t/\tau)^{\beta}\right] + B, \quad \text{with } 0 < \beta \leqslant 1, \tag{4}$$

$\beta < 1$ usually indicates a distribution of relaxation times and the average relaxation time at each $Q$ is then

$$\langle\tau\rangle = \frac{\tau}{\beta}\Gamma\left(\frac{1}{\beta}\right). \tag{5}$$

The quasi-elastic parts of the TOF spectra at 9 Å were fitted with

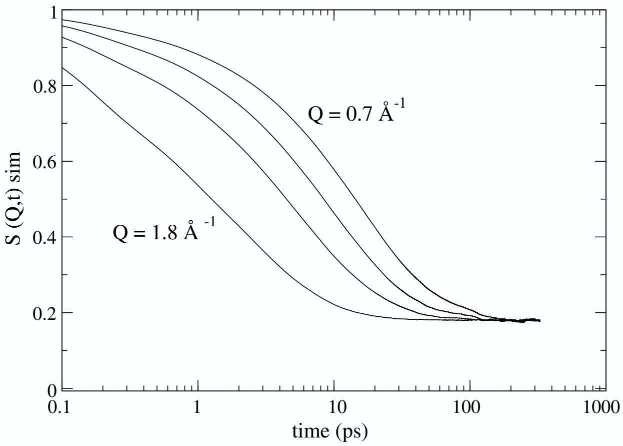

Fig. 2. Simulated $S(Q,t)$ of sodium montmorillonite in bihydrated state (12 $H_2O/Na^+$) for $Q = 0.7, 0.9, 1.2, 1.8$ Å$^{-1}$. $S(Q,t)$ was extracted from trajectories of 288 H atoms (144 water molecules), each trajectory was 655 ps in length with consecutive readings 0.02 ps apart.

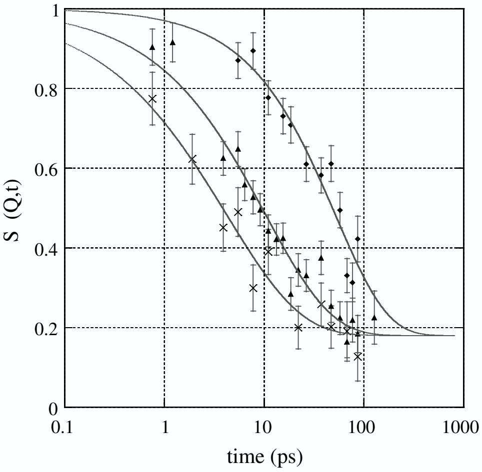

Fig. 3. Experimental $S(Q,t)$ from neutron spin echo measurements of sodium montmorillonite prepared under 85% relative humidity, three different $Q$s: 0.7 Å$^{-1}$ (♦), 1.2 Å$^{-1}$ (▲) and 1.8 Å$^{-1}$ (×).

$$S(Q,\omega) = A(Q)\delta(\omega) + [1 - A(Q)]\frac{1/\tau}{(1/\tau)^2 + (\omega)^2}, \qquad (6)$$

the delta function representing the elastic peak and the single Lorentzian modelling translational motion only. This analysis yields a relaxation time ($\tau$) for each $Q$ similarly to the case of NSE and simulation. The summary of relaxation times as a function of $Q^2$ determined by the three techniques is presented in Fig. 4.

Following the steps of previous studies and analysing the slopes of the three sets at small $Q$ (diffusion coefficient = slope at small values of $Q^2$), a fairly good agreement is found between the simulation and time-of-flight, yielding for both a diffusion coefficient of approximately $10 \times 10^{-10}$ m$^2$ s$^{-1}$, while the NSE data yield a value around $5 \times 10^{-10}$ m$^2$ s$^{-1}$. Thus, for this clay system we observe a maximal difference in the diffusion coefficients between the two experimental techniques of a factor of 2. (Samples at 95% relative humidity – all TOF and 0.5, 0.75 and 1.0 Å$^{-1}$ NSE measurements, samples at 85% relative humidity – the rest of NSE measurements. No significant differences in the relaxation times in the two samples were seen from the NSE measurements.)

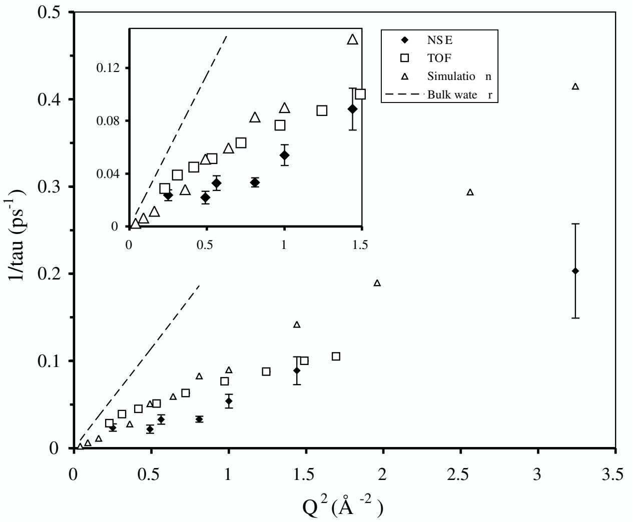

Fig. 4. $1/\langle\tau\rangle$ versus $Q^2$ from analysis of $S(Q,t)$ from simulation and NSE data and from $S(Q,\omega)$ from TOF data.

The TOF diffusion coefficient agrees with earlier studies on montmorillonite clays [22–24], whereas the present NSE value is higher than the only data published for this technique which deal with a vermiculite clay ($1.6–1.8 \times 10^{-10}$ m$^2$ s$^{-1}$) [19]. At this stage we note that this discrepancy is not surprising considering the higher charge on clay layers (1.29e and 0.76e per unit cell for vermiculite and montmorillonite used, respectively), the higher abundance of tetrahedral substitutions in case of vermiculite and its rather different structure on the mesoscale (larger clay particles). The value of the simulated diffusion coefficient extracted from Fig. 4 is very close to the simulated diffusion coefficient calculated with the MSD method ($D_{\mathrm{MSD}} = 11.35 \pm 1.75 \times 10^{-10}$ m$^2$ s$^{-1}$). Consistency is thus demonstrated between the various ways of extracting diffusion coefficients from simulated particle trajectories. The MSD method can be seen as a direct method, for which no analogue exists in the experimental analysis. In the indirect method, by fitting of the intermediate scattering functions, the simulation and NSE data undergo the same treatment.

The difficulty in extracting diffusion coefficients from the representation in Fig. 4 is clear due to a number of reasons. Primarily it is the lack of necessary points at small $Q$ values. Further, both the NSE and simulated $S(Q,t)$ data could not be fitted with a single exponential. The $\beta$ exponent descended with increasing $Q$ from 0.85 to 0.65 for the NSE data and from 0.7 to 0.55 for the simulated $S(Q,t)$. This, rather surprisingly, suggests that even in the model system there is a wide range of relaxation times and the significance of the calculated average relaxation time is difficult to assess. (The fitting procedure in the case of TOF data is of more complex a nature than for the other two techniques and in our case a variable $\beta$ exponent was not considered. A trial analysis of the same data with varying $\beta$ exponent resulted in $\beta < 1$, however very small difference was obtained in the value of the final diffusion coefficient.)

From Fig. 4 the only technique that suggests jump-diffusion is the TOF. No plateau is seen at high values of $Q^2$ in the simulation data, whereas the NSE data set lacks necessary values in this region. Zones of $Q$ values for which a contribution from coherent scattering appears (for this system $Q$ between 1.3 and 1.8 and lower than 0.5 Å$^{-1}$) have to be avoided in the NSE technique when incoherent signal is measured. Simulation data themselves are subject to increased uncertainty at small $Q$, where the finite length of the simulation comes into play (maximum simulation length considered was 655 ps), as well as at large $Q$, where care has to be taken with the time-step between the consecutive readings in the atomic trajectories ($t_{\text{dump}} = 0.02$ ps). A linear dependence without the appearance of a plateau has been reported in other modelling studies on neighbouring clays [41,42]. In addition, a similar disagreement in water dynamics between TOF and simulation has been seen elsewhere, such as in polymer solutions [43]. For bulk water itself, the situation is not entirely clarified. While a plateau at high $Q$ values has been observed for water in many quasi-elastic neutron scattering studies, especially for water under super-cooled [44,45] or confined [46,47] conditions, simulation data do not reproduce this behaviour [48,49]. At the same time, slightly different descriptions emerge regarding jump diffusion of water (surface water on zirconium oxide [50]), introducing fixed jump-lengths and thus a slight maximum in the inverse relaxation time versus $Q^2$ curve, before a plateau is reached. The difference in neutron experiments and simulation has been sometimes attributed to the incorrect comparison of relaxation times from a stretched exponentials (both $\tau$ and $\beta$ are $Q$ dependent) on one hand and a HWHM of a Lorentzian on the other [41,49]. This is unlikely to be the only reason; our own attempt at analyzing the TOF data using a Lorentzian with a variable $\beta$ exponent has produced almost no change to the overall shape of the curve. A revision of the zone of validity for the rotational/translational de-coupling is perhaps also necessary. It is indeed the high-$Q$ region that is the most affected if de-coupling does not apply.

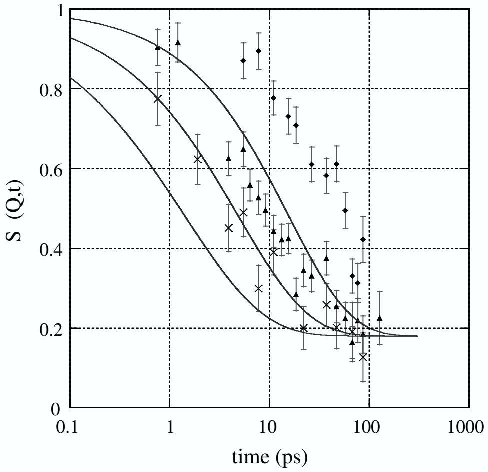

Fig. 5. Experimental $S(Q,t)$ from neutron spin echo measurements [point data: 0.7 Å$^{-1}$ (♦), 1.2 Å$^{-1}$ (▲) and 1.8 Å$^{-1}$ (×)] and simulated $S(Q,t)$ (—) of bihydrated sodium montmorillonite showing the same three $Q$s.

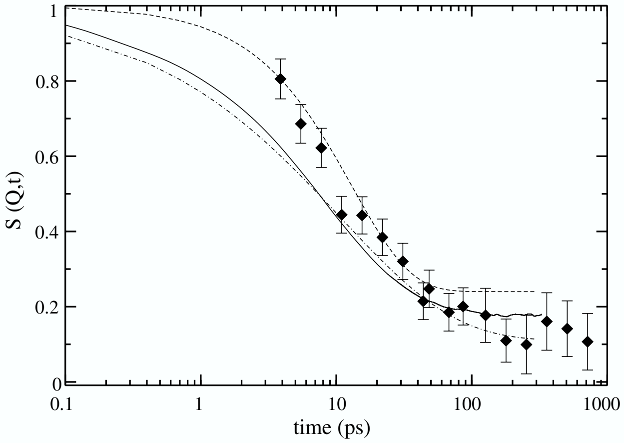

Fig. 6. Comparison of TOF, NSE and simulation data in the form of $S(Q,t)$ at $Q \simeq 1.0$ Å$^{-1}$. NSE (♦), simulation (—), TOF – Lorentzian with $\beta = 1$ (- - -), TOF – Lorentzian with $\beta < 1$ (- · -).

Going back a few steps in the analysis resulting in diffusion coefficients, Fig. 5 compares directly the simulated and experimental (NSE) intermediate scattering functions for three $Q$ values. The comparison of all three techniques is more difficult. We have attempted to represent this in the $(Q,t)$ domain for $Q \simeq 1.0$ Å$^{-1}$ on Fig. 6. The TOF data in this figure have been generated according to Eq. (4) using the parameters (i.e., $\tau$, $\beta$) of the Lorentzian or neighbouring function that models the quasi-elastic part of the $S(Q,\omega)$. Depending on the modelling function (e.g., Lorentzian with or without variable $\beta$ coefficient), the data in the $(Q,t)$ domain are rather different, even though they correspond to very similar average relaxation times. Using an apparently more appropriate model of isotropically averaged 2D diffusion [51,50], we have not been able to see a significant improvement in the fit of the quasi-elastic region of $S(Q,\omega)$ in comparison to the single Lorentzian for 3D diffusion presented here. The cases of 2D/3D diffusion have been discussed previously, the principal difference in the resulting signals occurring at zero energy transfer was pointed out [52]. In order to clearly demonstrate this, experimental data sets at constant $Q$ as a function of increasing resolution are necessary [52].

In summary of Figs. 5 and 6, the simulated $S(Q,t)$ curves show a systematic shift to lower relaxation times or faster dynamics, by a factor of up to 2 with respect to NSE data. Direct comparison to TOF is more difficult, depending on the function used to model the quasi-elastic part of $S(Q,\omega)$, the decay of TOF data in the domain $(Q,t)$ can approach closer NSE or simulation results. Further investigation into which model is the most appropriate for TOF data analysis is necessary.

From the experiment-simulation comparison, before being able to conclude that simulation simply does not reproduce the real dynamics in the system, due to incorrect inter-atomic potentials for example, the following points for the real system have to addressed. Firstly, are all interlayers at the same degree of hydration? Secondly, is the interlayer the only environment in which water molecules are found?

The degree of hydration or more specifically the interlayer spacing is experimentally followed by X-ray or neutron diffraction, where clear $00L$ reflections (probing periodicity in the direction perpendicular to clay layers) are observed for clay systems. The indications of an in-homogeneous interlayer spacing and of co-existence of different hydration states (interstratification) in a sample are the broadening of the $00L$ reflections as well as non-integer spacing between the higher-order reflections [53]. For the natural montmorillonite clay presented here, the 001 peak (as seen by neutron diffraction) was significantly broadened (HWHM 1 Å), pointing to the above phenomenon. The main causes for interstratification are linked to the in-homogeneous charge distribution on clay layers, an uncontrollable parameter in case of natural clay systems. Microscopic models of clays have been usually considered as satisfactory as long as they reproduce, for a given water content, the average interlayer spacing as taken from the 001 reflection. Here, the simulated water content (12 $H_2O/Na^+$), does indeed give rise to a spacing of $15.5 \pm 0.3$ Å observed experimentally for bihydrated Na-montmorillonite, however, this seems insufficient as forcing all interlayers into the same spacing renders the model too simplistic.

In addition to the problem of interstratification, the presence of water in other porosities of the clay system (mesopores) is not taken into account in the model. As described in the introduction, porosities on larger scales are omnipresent in macroscopic clay samples, especially for clays such as montmorillonite forming small particles. Also, with increasing relative humidity the proportion of water in larger porosities becomes more significant. Available estimates of mesoporous water (obtainable only indirectly from for example a combination of water vapour adsorption isotherms and BET nitrogen isotherms) in montmorillonite at 80% relative humidity give proportions of up to 20% of total water content [6,7,5].

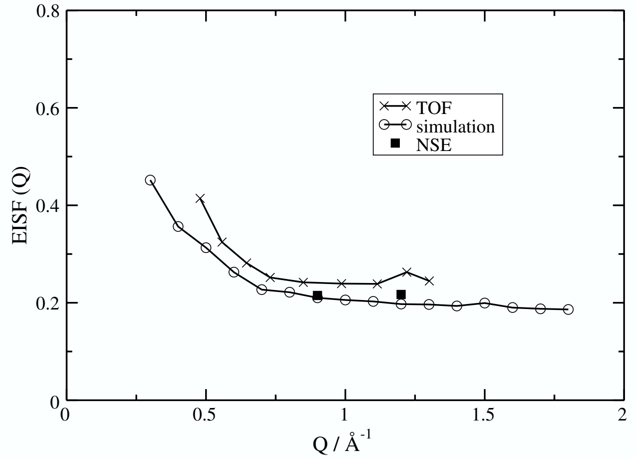

Fig. 7. The elastic incoherent structural factor, EISF($Q$), determined by TOF, NSE and simulation.

If not in the relaxation times, there is one aspect in which the experimental and simulated $S(Q,t)$ curves agree and that is the long-time plateau representing the proportion of immobile hydrogen atoms seen by the techniques. For sodium bihydrate (Fig. 5, data for sample prepared under 85% relative humidity) the value from the fit of the experimental $S(Q,t)$ curves (0.22) is to be compared with the value calculated from mass measurements before and after hydration of the sample (0.21) and with the value of the model bihydrated system simulated (0.18). Overall then, the total degree of hydration in the model and real systems is very close, but the repartition of the water present is very likely not the same, affecting the overall water dynamics. While various environments (monolayer, bilayer, mesopores) are possible for the real sample, the model accounts only for one type of interlayer water (bilayer).

Fig. 7 summarizes the EISF($Q$) information from all three techniques. The simulated data were determined from particle trajectories according to Eq. (3), the TOF data are the ratio of the elastic peak intensity to total intensity at each $Q$. NSE data are shown for two $Q$ values and represent the long-time plateau of the exponential fit.

As for the $S(Q,t)$ function, the family of immobile H atoms (clay OH groups) in the system gives rise to a constant background in the EISF($Q$). Looking at the high-$Q$ end, this background is 0.25, 0.22 and 0.18 for the TOF, NSE and simulation, respectively. In the discussion on immobile H atoms, we have to take into account the characteristic times of the different techniques. The TOF spectrometer in the set-up used is insensitive to motions with characteristic times greater than 70/100 ps, for NSE the cut-off is around 500 ps. Comparing the NSE and TOF EISF($Q$) values at high $Q$ with the percentage of immobile H atoms in the real sample (from mass measurements – 0.21), the NSE time-window then reaches sufficiently far into the long correlation times to see the relaxation of all the mobile H atoms in the sample, within error of the determined EISF($Q$). This is not the case for TOF. The value of the simulation corresponds exactly to the fraction of the immobile H atoms in the model system (0.18) and thus simulation achieves, at the high-$Q$ end, what NSE achieves for the real system.

Viewing the low-$Q$ part of Fig. 7, an increase in EISF($Q$) is seen by both TOF and simulation (no low-$Q$ data available for NSE technique due to coherent scattering as already mentioned). In confined systems this is usually seen as the signature of the confined motion. In this case, we hesitate with this interpretation. As the water molecules in the clay system are confined only in one dimension, no increase in the EISF($Q$) in the low-$Q$ region should occur as is explained below.

It has been shown analytically that for a geometry of two parallel plates separated by $L$ in the $z$ direction, the scattering function *along the z-axis* $S(Q_z, \omega)$ is of the form

$$S(Q_zL, \omega) = A_0(Q_zL)\delta(\omega) + \sum_{n=1}^{\infty} A_n(Q_zL)L_n(\omega)\left[D(n\pi/L)^2\right], \tag{7}$$

where $L_n(\omega)$ are Lorentzians of the shown HWHM, where $D$ is the diffusion coefficient. The analytical form of $A_0(Q_zL)$ is

$$A_0(Q_zL) = \frac{2}{(Q_zL)^2}(1 - \cos(Q_zL)), \tag{8}$$

where $Q_z$ is a wave vector perpendicular to the plates (along the direction of confinement) [54,55]. However, the overall scattering function $S(Q, \omega)$ for $Q$ along any direction in space (with components $Q_x$, $Q_y$, $Q_z$) is

$$S(Q, \omega) = \sum_{n=0}^{\infty} A_n(Q_zL)L_n(\omega)\left[D\left(Q_x^2 + Q_y^2 + \frac{n^2\pi^2}{L^2}\right)\right], \tag{9}$$

therefore a combination of Eq. (7) with Lorentzians of finite widths, representing unbounded diffusion in the $x$ and $y$ directions. Therefore, the function represented by $A_0(Q_zL)$ no longer modulates the intensity of the elastic peak in the 3D case, instead it modulates the intensity of the first Lorentzian of Eq. (9) [54]. The only contribution to the EISF($Q$) for the presented 3D system of clays is the constant background corresponding to the percentage of the immobile H atoms (clay OH groups). The increase in EISF($Q$) observed by TOF and simulation could then be treated as another piece of evidence for insufficiently long characteristic times for both of these techniques at low $Q$ values (maximum correlation time in simulation is 320 ps). This is more easily verified for simulation than for TOF, by increasing the simulation length, and it is envisaged.

## 5. Conclusion

In summary, from the analysis of diffusion coefficients of water in bihydrated Na-montmorillonite, both simulation and time-of-flight yield approximately $10 \times 10^{-10}\ \mathrm{m^2\ s^{-1}}$, while the NSE data gives approximately $5 \times 10^{-10}\ \mathrm{m^2\ s^{-1}}$. From the direct comparison of simulated and experimental $S(Q, t)$ and EISF($Q$), we conclude (1) that the simulated system represents well the proportion of mobile and immobile H atoms (clay OH groups) in the system as seen by NSE (and TOF) techniques, (2) the relaxation times for small $Q$ values might be underestimated by both TOF and simulation due to insufficiently large maximum correlation times probed, (3) the comparison of model and real montmorillonite system is difficult due to several water environments in the real sample not considered by the model.

Returning to the issue of characteristic times, which techniques should then be in closer agreement? The observed decay of the $S(Q, t)$ signal in NSE (especially the slowest decay at low-$Q$) is within the time-window of the simulation, but not of TOF. This would suggest better agreement between NSE and simulation, with TOF data showing faster dynamics. This is however only the case if simulation truthfully reproduces the real dynamics in the system. Following this argument, the observed closer agreement between simulation and TOF presented here could therefore be even treated as accidental (simulation perhaps grossly overestimating the real interlayer dynamics and coinciding with TOF measurements, which themselves are an overestimate due to the short characteristic times of the technique). Even if less significant for the overall relaxation times, the issue of the most appropriate function modelling the quasi-elastic part of $S(Q, \omega)$ is still unclear for this system. For the present experimental data, no clear differences in the quality of the fit are seen for the various models (2D/3D diffusion).

The discrepancies between simulated and experimental dynamics raise then the issue of interstratification and water in real samples being present in porosities not represented in the model. Let us consider the entire real clay system as a combination of clay particles with interlayer water (slow dynamics) and mesoporous water in-between them (bulk-like dynamics). With significant proportion of water in mesopores, small relaxation times seen by both of the experimental techniques would contrast with the long relaxation times from simulation. This is not observed here. At the same time, experimental information on the dynamics of water in mesopores of clays is far from clear at the moment and the above picture remains a hypothesis. Further the combined effect of interstratification and the presence of mesoporous water in the real montmorillonite samples are even more difficult to predict. To assess whether the model of the interlayer dynamics is correct or not is thus very difficult as we simply might not be comparing the same model and real systems.

To uncouple all the contributions in the real montmorillonite samples, a wider set of data from the three techniques, for montmorillonite systems with varying counterions and degrees of hydration, might be more instructive. As the water content in the interlayer and other porosities is highly dependent on the type of counterion and degree of hydration of the entire sample [5,7,6], the importance of each contribution could then be assessed.

At this stage, we also look towards other clay systems, in one aspect or another simplified versions of montmorillonite. In overcoming the problem of interstratification, a promising candidate is a synthetic hectorite clay, which is prepared under carefully controlled conditions resulting in a homogeneous charge distribution on the clay layers [56]. As already observed by neutron diffraction, the hectorite system exhibits a very sharp transition from monohydrated to bihydrated interlayers as relative humidity is increased (i.e., very narrow humidity range of co-existence) and very thin diffraction peaks at each stage indicating a much narrower distribution of interlayer spacings for each state. For the moment, water dynamics in this system has been analysed by the NSE technique and shows promising results.

Regarding presence of mesopores, montmorillonite forms particles of variable and rather small sizes in comparison to other clays (100–200 nm laterally), which in the macroscopic sample favours mesopore formation. Vermiculite clays, mentioned several times already, form particles on the scale of millimetres. These large clay particles have already been exploited to study anisotropy of diffusion in clays as preferential orientations of the clay particles are easily achieved [19,26]. However, the experimental analysis of dynamics in vermiculite has not been taken beyond the determination of overall diffusion coefficients and the simulated dynamic data for direct comparison is not available.

## Acknowledgment

N.M. gratefully acknowledges the support of ANDRA (Agence Nationale pour la Gestion des Déchets Radioactifs).

## References

[1] R.F. Giese, C.J. van Oss, Surfactant Science Series, vol. 105, Marcel Dekker, New York, 2002.
[2] ANDRA, Referentiel Materiaux, Tome 1: Contexte et objet, Rapport C.RP.AMAT.01.060, 2001.
[3] R.W.G. Wyckoff, Crystal Structures, Miscellaneous Inorganic Compounds, Silicates, and Basic Structural Information, vol. 4, John Wiley and Sons, New York, 1968.
[4] L.L. Schramm, J.C.T. Kwak, Clays Clay Miner. 30 (1982) 40–48.
[5] I. Bérend, J.M. Cases, M. Francois, J.P. Uriot, L.J. Michot, A. Masion, F. Thomas, Clays Clay Miner. 43 (1995) 324–336.
[6] J.M. Cases, I. Bérend, M. Francois, J.P. Uriot, F. Thomas, J.E. Poirier, Langmuir 8 (1992) 2730–2739.
[7] J.M. Cases, I. Bérend, M. Francois, J.P. Uriot, L.J. Michot, F. Thomas, Clays Clay Miner. 45 (1997) 8–22.
[8] ANDRA, Referentiel Materiaux, Tome 2: Les Materiaux argileux, Rapport C.RP.AMAT.01.060, 2001.
[9] A. Delville, Langmuir 8 (1992) 1796–1805.
[10] E.S. Boek, P.V. Coveney, N.T. Skipper, J. Am. Chem. Soc. 117 (1995) 12608–12617.
[11] F.C. Chang, N.T. Skipper, G. Sposito, Langmuir 13 (1997) 2074–2082.
[12] V. Marry, P. Turq, T. Cartailler, D. Levesque, J. Chem. Phys. 117 (2002) 3454–3463.
[13] A.V.C. de Siqueira, N.T. Skipper, P.V. Coveney, E.S. Boek, Mol. Phys. 92 (1997) 1–6.
[14] N. Malikova, V. Marry, J.-F. Dufréche, C. Simon, P. Turq, E. Giffaut, Mol. Phys. 102 (2004) 1965–1977.
[15] N. Malikova, V. Marry, J.-F. Dufréche, P. Turq, Curr. Opin. Colloid Interface Sci. 9 (2004) 124–127.
[16] J.O. Titiloye, N.T. Skipper, Mol. Phys. 99 (2001) 899–906.
[17] F.C. Chang, N.T. Skipper, G. Sposito, Langmuir 11 (1995) 2734–2741.
[18] R. Sutton, G. Sposito, J. Colloid Interface Sci. 237 (2001) 174–184.
[19] J. Swenson, R. Bergman, S. Longeville, J. Chem. Phys. 115 (2001) 11299–11305.
[20] M. Molera, T. Eriksen, Radio. Acta 90 (2004) 753–760.
[21] C. Daqing, T. Eriksen, Radio. Acta 82 (1998) 287–292.
[22] J.J. Tuck, P.L. Hall, M.H.B. Hayes, D.K. Ross, C. Poinsignon, J. Chem. Soc., Faraday Trans. 1 80 (1984) 309–324.
[23] J.J. Tuck, P.L. Hall, M.H.B. Hayes, D.K. Ross, J.B. Hayter, J. Chem. Soc., Faraday Trans. 1 81 (1985) 833–846.
[24] D.J. Cebula, R.K. Thomas, J.W. White, Clays Clay Miner. 29 (1981) 241–248.
[25] C. Poinsignon, J. Estrade-Szwarckopf, J. Conard, A.J. Dianoux, in: Proc. Int. Clay Conf., Denver 1985, 1987, pp. 284–291.
[26] J. Swenson, R. Bergman, W.S. Howells, J. Chem. Phys. 113 (2000) 2873–2879.
[27] E. Mamontov, J. Chem. Phys. 121 (2004) 9193–9194.
[28] J. Swenson, R. Bergman, W.S. Howells, S. Longeville, J. Chem. Phys. 121 (2004) 9195.
[29] D. Smith, Langmuir 14 (1998) 5959–5967.
[30] H.J.C. Berendsen, J.R. Grigera, T.P. Straatsma, J. Phys. Chem. 91 (1987) 6269–6271.
[31] E.S. Boek, P.V. Coveney, N.T. Skipper, Langmuir 11 (1995) 4629–4631.
[32] M. Chávez-Páez, L. dePablo, J.J. dePablo, J. Chem. Phys. 114 (24) (2001) 10948–10953.
[33] D. Guillaume, A. Neaman, M. Cathelineau, R. Mosser-Ruck, C. Peiffert, M. Abdelmoula, J. Dubessy, F. Villieras, A. Baronnet, N. Michau, Clay Miner. 38 (3) (2003) 281–302.
[34] F. Mezei, Z. Phys. 255 (1972) 146–160.

[35] F. Mezei, Lecture Notes in Physics, vol. 128, Springer Verlag, Berlin, 1980.

[36] M. Bée, Quasi-elastic Neutron Scattering; Principles and Applications in Solid State Chemistry, Biology and Material Science, Adam Hilger, Bristol, 1988.

[37] R. Golub, R. Gähler, Phys. Lett. A 123 (1987) 43–48.

[38] R. Gähler, R. Golub, Z. Phys. B – Condens. Matter 65 (1987) 269–273.

[39] R. Gähler, R. Golub, J. Phys. France 49 (1988) 1195–1202.

[40] J.P. Hansen, I.R. McDonald, Theory of Simple Liquids, Academic Press, Dordrecht, 1986.

[41] M. Arab, D. Bourgeard, K.S. Smirnov, Phys. Chem. Chem. Phys. 5 (2003) 4699–4707.

[42] M. Arab, D. Bourgeard, K.S. Smirnov, Phys. Chem. Chem. Phys. 6 (2004) 2446–2453.

[43] O. Borodin, F. Trouw, D. Bedrov, G.D. Smith, J. Phys. Chem. B 106 (20) (2002) 5184–5193.

[44] J. Teixeira, M.-C. Bellissent-Funel, S.-H. Chen, A.J. Dianoux, J. Phys. C 7 (1984) 65–71.

[45] M.-C. Bellissent-Funel, J. Teixeira, J. Mol. Struct. 250 (1991) 213–230.

[46] M.-C. Bellissent-Funel, K.F. Bradley, S.H. Chen, J. Lal, J. Teixeira, Physica A 201 (1993) 277–285.

[47] J. Teixeira, J.-M. Zanotti, M.-C. Bellissent-Funel, S.H. Chen, Physica B 234–236 (1997) 370–374.

[48] J.J. Ullo, Phys. Rev. A 36 (2) (1987) 816–826.

[49] S.-H. Chen, P. Gallo, F. Sciortino, P. Tartaglia, Phys. Rev. E 56 (4) (1997) 4231–4243.

[50] E. Mamontov, J. Chem. Phys. 121 (18) (2004) 9087–9097.

[51] A.J. Dianoux, F. Volino, H. Hervet, Mol. Phys. 30 (1975) 1181–1194.

[52] R.E. Lechner, Solid State Ionics 77 (1995) 280–286.

[53] C.E. Weaver, Am. Miner. 41 (1956) 202–221.

[54] P.L. Hall, D.K. Ross, Mol. Phys. 36 (1978) 1549–1554.

[55] P.L. Hall, D.K. Ross, Mol. Phys. 42 (1981) 673–682.

[56] J. Breu, W. Seidl, A. Stoll, Z. Anorg. Allg. Chem. 629 (2003) 503–515.

*Chem. Mater.* **2005,** *17,* 3499−3512

# New Insights on the Distribution of Interlayer Water in Bi-Hydrated Smectite from X-ray Diffraction Profile Modeling of 00*l* Reflections

Eric Ferrage,*,†,‡ Bruno Lanson,† Natalie Malikova,‡,§ Alain Plançon,||
Boris A. Sakharov,†,⊥ and Victor A. Drits†,

*Environmental Geochemistry Group, LGIT, Maison des Géosciences, Joseph Fourier University, CNRS, BP53, F-38041 Grenoble Cedex 9, France, ANDRA, Parc de la Croix Blanche, 1-7 rue Jean Monnet, F-92298 Châtenay-Malabry Cedex, France, Laboratory Liquides Ioniques & Interfaces Chargées, Paris 06 University, Case Courrier 51, 4 Pl. Jussieu, F-75252 Paris, France, Crystallography Laboratory, ISTO, University of Orléans, CNRS, F-45067 Orléans Cedex 2, France, and Geological Institute, Russian Academy of Sciences, 7 Pyzhevsky Street, 109017 Moscow, Russia*

*Received November 15, 2004. Revised Manuscript Received April 25, 2005*

The interlayer configuration proposed by Moore and Reynolds (*X-ray Diffraction and the Identification and Analysis of Clay Minerals*; Oxford University Press: New York, 1997) and commonly used to reproduce the 00*l* reflections of bi-hydrated smectite is shown to be inconsistent with experimental X-ray diffraction data. The alternative configuration of interlayer species with cations located in the mid-plane of the interlayer and one sheet of $H_2O$ molecules on each side of this plane is also shown to imperfectly describe the actual structure of bi-hydrated smectites. Specifically, the thermal fluctuation of atomic positions (Debye−Waller factor) used to describe the positional disorder of interlayer $H_2O$ molecules has to be increased to unrealistic values to satisfactorily reproduce experimental X-ray diffraction data when using this model. A new configuration is thus proposed for the interlayer structure of bi-hydrated smectite. Cations are located in the mid-plane of the interlayer, whereas $H_2O$ molecules are scattered about two main positions according to Gaussian-shaped distributions. This configuration allows reproduction of all 00*l* reflections with a high precision, with only one new variable parameter (width of the Gaussian function). The proposed configuration is consistent with those derived from Monte Carlo calculations and allows matching more closely the amount of interlayer water that can be determined independently from water vapor adsorption/desorption isotherm experiments. In addition, the proposed configuration of interlayer species appears valid for both dioctahedral and trioctahedral smectites exhibiting octahedral and tetrahedral substitutions, thus not allowing differentiation of these expandable 2:1 phyllosilicates from their respective interlayer configurations.

## Introduction

Smectite is a 2:1 phyllosilicate with a layer structure consisting of an octahedral sheet sandwiched between two siliceous tetrahedral sheets. Isomorphic substitutions in either tetrahedral or octahedral sites induce a permanent negative layer charge, which is compensated for by the presence of hydrated cations in the interlayer. The observation of 00*l* basal reflections on X-ray diffraction (XRD) patterns has shown that with increasing relative humidity smectite expands stepwise, with the different steps corresponding to the intercalation of 0, 1, 2, or 3 sheets of $H_2O$ molecules in the interlayer.[1−6] From these pioneering studies, it is now commonly accepted that the expandability of 2:1 phyllosilicates is controlled by factors such as the nature of interlayer cations, and the layer charge and its location (octahedral vs tetrahedral). These general observations have led to different models in which crystalline swelling is controlled by the balance between the repulsive forces between neighboring 2:1 layers and the attractive forces between hydrated interlayer cations and the negatively charged surface of siloxane sheets.[6−11]

The development of XRD modeling techniques allowed investigation of structures in which different hydration states coexist, thus improving these early observations.[12−17] Ferrage

---

* To whom correspondence should be addressed. E-mail: e.ferrage@nhm.ac.uk.
† Joseph Fourier University, CNRS.
‡ ANDRA.
§ Laboratory Liquides Ioniques & Interfaces Chargées, Paris 06 University.
|| University of Orléans, CNRS.
⊥ Russian Academy of Sciences.

(1) Moore, D. M.; Reynolds, R. C., Jr. *X-ray Diffraction and the Identification and Analysis of Clay Minerals*; Oxford University Press: Oxford and New York, 1997.
(2) Nagelschmidt, G. *Z. Kristallogr.* **1936**, *93*, 481−487.
(3) Bradley, W. F.; Grim, R. E.; Clark, G. F. *Z. Kristallogr.* **1937**, *97*, 260−270.
(4) Mooney, R. W.; Keenan, A. G.; Wood, L. A. *J. Am. Chem. Soc.* **1952**, *74*, 1371−1374.
(5) Walker, G. F. *Clays Clay Miner.* **1956**, *4*, 101−115.
(6) Norrish, K. *Discuss. Faraday Soc.* **1954**, *18*, 120−133.
(7) Van Olphen, H. *J. Colloid Sci.* **1965**, *20*, 822−837.
(8) Kittrick, J. A. *Soil Sci. Soc. Am. J.* **1969**, *33*, 217−222.
(9) Kittrick, J. A. *Soil Sci. Soc. Am. J.* **1969**, *33*, 222−225.
(10) Laird, D. A. *Clays Clay Miner.* **1996**, *44*, 553−559.
(11) Laird, D. A. *Clays Clay Miner.* **1999**, *47*, 630−636.
(12) Ben Brahim, J.; Besson, G.; Tchoubar, C. In *5th Meeting of the European Clay Groups*: Prague, 1983; pp 65−75.
(13) Ben Brahim, J.; Besson, G.; Tchoubar, C. *J. Appl. Crystallogr.* **1984**, *17*, 179−188.
(14) Bérend, I.; Cases, J. M.; François, M.; Uriot, J. P.; Michot, L. J.; Masion, A.; Thomas, F. *Clays Clay Miner.* **1995**, *43*, 324−336.
(15) Cases, J. M.; Bérend, I.; Besson, G.; François, M.; Uriot, J. P.; Thomas, F.; Poirier, J. P. *Langmuir* **1992**, *8*, 2730−2739.

10.1021/cm047995v CCC: $30.25

et al. used such a modeling approach to characterize the hydration of several montmorillonite and beidellite samples and observed that the nature of the interlayer cation, and in particular its affinity for water, influences the layer thickness of bi-hydrated and monohydrated layers.[18,19] They also confirmed that the relative proportions of the different layer types, which correspond to the different hydration states, depend on both the amount and the location of smectite layer charge. In addition, these authors showed that XRD peak profiles and positions can be satisfactorily reproduced, especially over the low-angle region (~5−12° $2\theta$ Cu Kα), only if hydration heterogeneity is taken into account. They were thus able to refine the structure of smectite and in particular to investigate atomic positions of interlayer species. In particular, they showed that the atomic positions reported by Moore and Reynolds for $H_2O$ molecules in bi-hydrated layers induce a dramatic misfit over the medium- to high-angle region (12−50° $2\theta$ Cu Kα) by strongly modifying the intensity ratio between the different 00*l* reflections.[1,18]

The present article thus aims at further refining the structure of interlayer $H_2O$ in bi-hydrated smectites from the fit of experimental XRD patterns. The proposed structure is compared with the positional distribution commonly derived from Monte Carlo simulations, whereas the adjusted amounts of interlayer water are compared with those determined experimentally from water vapor adsorption−desorption experiments.

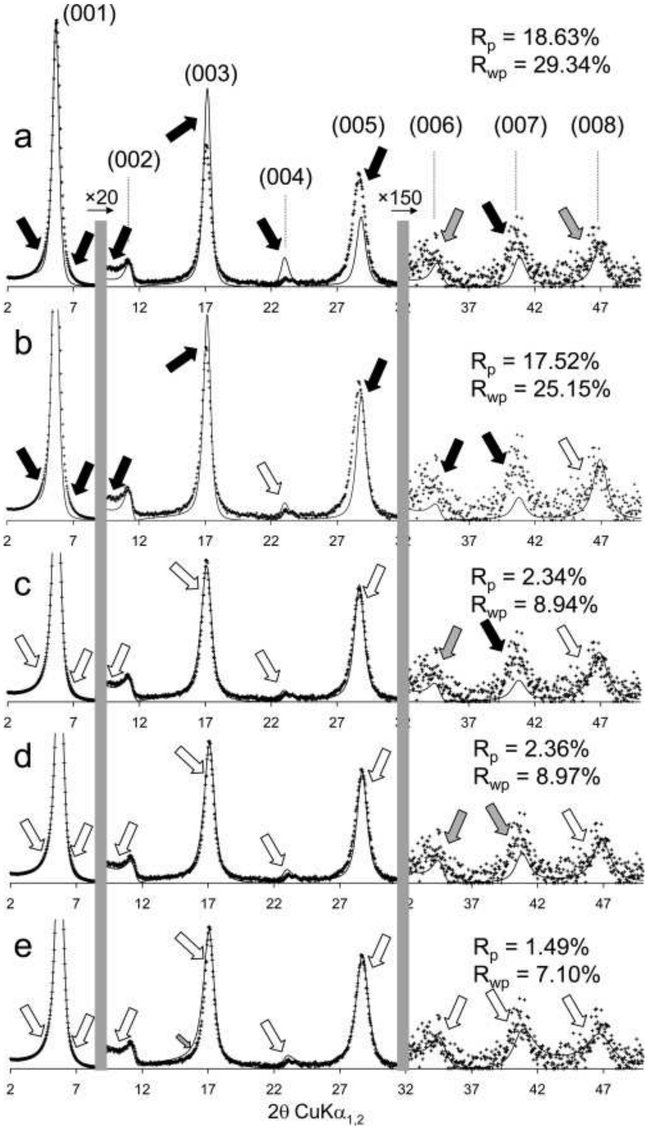

**Figure 1.** Comparison between experimental and calculated XRD patterns for the Ca-saturated SWy-1 montmorillonite sample recorded at 80% RH. Structural parameters used for the calculations are listed in Tables 1, 2, and 3. Experimental data are shown as crosses whereas calculated profiles are shown as solid lines. Solid arrows indicate a significant misfit between experimental and calculated patterns, whereas gray and open arrows indicate poor and good fits, respectively. 00*l* reflections are indexed in parentheses. (a) Calculation for a periodic bi-hydrated structure (layer thickness of 2W layers = 15.48 Å) assuming the usual configuration of $H_2O$ molecules (ref 1). (b) Calculation for a periodic bi-hydrated structure (layer thickness of 2W layers 15.48 Å) assuming a 2WS configuration (see text for details) with $B_{wat}$ = 2 Å$^2$ for $H_2O$ molecules (ref 18). (c) Calculation performed accounting for hydration heterogeneities and assuming a 2WS configuration with $B_{wat}$ = 2 Å$^2$ for $H_2O$ molecules (ref 18). Hydration heterogeneity was described by assuming the coexistence of a major MLS containing 2W and 1W layers (95:5 ratio) and of a second structure containing the three layer types (2W/1W/0W = 85:13:2) in a 61:39 ratio (Table 2). (d) Calculation performed accounting for hydration heterogeneities and assuming a 2WS configuration with $B_{wat}$ = 11 Å$^2$ for $H_2O$ molecules. (e) Calculation performed accounting for hydration heterogeneities and assuming a 2WG configuration (see text for details).

## Background

**Smectite Hydration Heterogeneity as seen by XRD Profile Modeling.** In agreement with the stepwise evolution of the $d_{001}$ basal spacing on XRD patterns, the hydration state of smectite has been described using three layer types exhibiting different layer thicknesses corresponding to the common hydration states reported for smectite in nonsaturated conditions. Dehydrated layers (0W, layer thickness ~9.6−10.1 Å), monohydrated layers (1W, layer thickness ~12.3−12.7 Å), and bi-hydrated layers (2W, layer thickness ~15.1−15.8 Å) have thus been defined. In the first two layer types, interlayer cations are located in the mid-plane of the interlayer, together with $H_2O$ molecules for 1W layers. For 2W layers, interlayer cations are also commonly assumed to be located in the mid-plane of the interlayer.[1] In addition, it is usually assumed that two planes of $H_2O$ molecules, each bearing 0.69 $H_2O$ per $O_{20}(OH)_4$, are located at 0.35 and 1.06 Å from the cation along the $c^*$ axis (Debye−Waller parameter $B_{wat}$ ~2 Å$^2$ for these two planes), whereas a third denser plane (1.20 $H_2O$ per $O_{20}(OH)_4$) is located further from the central interlayer cation at 1.20 Å along the $c^*$ axis ($B_{wat}$ = 11 Å$^2$).[1] The pattern calculated for the Ca-saturated reference SWy-1 montmorillonite (Ca−SWy-1) assuming a homogeneous 2W hydration state and the above configuration for interlayer species is compared in Figure 1a to the experimental pattern recorded at 80% RH. With these usual hypotheses, the calculated pattern fits most of the experimental pattern features but significant discrepancies can be observed over the medium- to high-angle region despite the low intensity diffracted. In particular, the position of the 005 reflection and the low-angle "tail" of the 002 reflection are not well reproduced (Figure 1a). Ferrage et al. challenged

---

(16) Cases, J. M.; Bérend, I.; François, M.; Uriot, J. P.; Michot, L. J.; Thomas, F. *Clays Clay Miner.* **1997**, *45*, 8−22.

(17) Cuadros, J. *Am. J. Sci.* **1997**, *297*, 829−841.

(18) Ferrage, E.; Lanson, B.; Sakharov, B. A.; Drits, V. A. *Am. Mineral.* **2005**, in press (MS 1776R).

(19) Ferrage, E.; Lanson, B.; Sakharov, B. A.; Geoffroy, N.; Jacquot, E.; Drits, V. A. *Am. Mineral.* **2005**, in preparation.

this usual configuration of interlayer species, and proposed an alternative configuration that includes a unique plane of $H_2O$ molecules located at 1.20 Å, along the $c^*$ axis, on either side of the central interlayer cation (2WS configuration).[18] The use of this 2WS configuration helps to reduce the discrepancies observed for the 003−005 reflections. In particular, this configuration allows decreasing the relative intensity of the 003 and 004 reflections, whereas the intensity of the 005 one is increased (Figure 1b). However, in the high-angle region the intensity ratio between the 007 and 008 reflections measured on the calculated pattern is inconsistent with that determined experimentally, although the intensity of the 008 reflection is correctly reproduced.

Ferrage et al. also demonstrated that the common hypothesis of a homogeneous hydration state for smectite is not consistent with the likely existence in smectite of structural heterogeneities affecting the layer charge distribution (from one interlayer to the other or within a given interlayer) and/or location (octahedral vs tetrahedral).[18] In turn these heterogeneities lead to the coexistence of different layer types in a single structure. Such hydration heterogeneity has been evidenced from the profile modeling of XRD patterns recorded on hydrated smectites.[12−17] Ferrage et al. have shown that this heterogeneity is systematically observed whatever the interlayer cation, the relative humidity (RH), and the amount and location of the layer charge deficit.[18,19] It is thus essential to account for the hydration heterogeneity to satisfactorily reproduce the experimental positions and profiles of reflections.

Ferrage et al. have shown indeed that accounting for smectite hydration heterogeneity allows better fitting of the profiles of all experimental 00*l* reflections.[18,19] In particular, heterogeneous samples were modeled by combining the contributions of several structures, each containing either one (periodic structure) or different layer types (mixed-layer structure, MLS) randomly interstratified ($R = 0$).[18−20] These different contributions should be seen as a simplified way to describe the actual hydration heterogeneity of the sample under investigation, with the different layer types not being distributed at random in the different crystallites. However, the coexistence of these contributions does not imply the actual presence of populations of particles in the sample, as their relative proportions may vary as a function of RH for example.[18] To account for the heterogeneous distribution of the different layer types within smectite crystallites, layers exhibiting the same hydration state that are present in the different MLSs must have identical properties as they may be accounted for in one or the other structure depending on the RH. In particular, for a given XRD pattern, each layer type must possess a constant crystal chemistry in the different MLSs. It was possible to reproduce the profile of all experimental 00*l* reflections of the experimental XRD pattern recorded on Ca−SWy-1 at 80% RH by considering two MLSs (Figure 1c) and the 2WS configuration for interlayer water.[18] Specifically, the position of the 005 reflection, the low-angle shoulder of the 002 reflection, and the “tails” of the 001 reflection are satisfactorily reproduced by taking hydration heterogeneity into account. Accounting for hydration heterogeneity also helps to reproduce the relative intensity of higher-angle reflections (002, 003, 004, and 005, for example) but significant discrepancies that could result from an incorrect structure model for interlayer water are still visible for high-angle reflections (Figure 1c). Specifically, the 006, 007, and 008 reflections are not satisfactorily reproduced, as, for example, the intensity ratio between the 007 and 008 reflections measured on experimental and calculated patterns are inconsistent. These discrepancies are reduced by increasing the Debye−Waller factor of $H_2O$ molecules ($B_{\mathrm{wat}}$) from 2 to 11 Å$^2$ for this 2WS configuration of interlayer $H_2O$ molecules (Figure 1d).[18] However, such high values of the Debye−Waller factor are not sufficient to conceal the disagreement for the intensity ratio between 007 and 008 reflections, and thermal atomic fluctuations most likely do not adequately describe the positional distribution of $H_2O$ molecules in 2W smectite layers, and additional hypotheses have to be sought.

**Interlayer Configuration of 2W Smectite Layers as seen by Monte Carlo Simulations.** In the above calculations, $H_2O$ molecules are distributed in discrete planes, and the positional distribution of $H_2O$ molecules results only from their thermal motion. However, this simplified description of the smectite interlayer structure does not allow fitting of the experimental XRD data (Figure 1c and d), most likely because the description of $H_2O$ molecule positional disorder is incomplete. A more complete (and perhaps realistic) description of the interlayer structure may be obtained from Monte Carlo (MC) simulations which allow taking into account all interactions among interlayer species, as well as those between these species and the 2:1 layer.[21] It is in particular possible to account for the hydration variability of interlayer cation which can form either inner-sphere or outer-sphere complexes with the 2:1 layer surface, leading to the existence or to the lack, respectively, of direct interactions with O atoms from the layer surface. In the latter case, these interactions are screened by $H_2O$ molecules from the cation hydration sphere. It has been shown that, as compared to other monovalent cations, $K^+$ cations tend to form inner-sphere complexes in montmorillonite interlayers and that these cations remain partially bound to the 2:1 clay surface even in the 2W state.[22,23] In contrast, $Li^+$ and $Na^+$ cations in 2W smectites are located in the mid-plane of the interlayer.[23−26] The location of the layer charge deficit has also been shown to influence the hydration of interlayer $Na^+$ cations, with the formation of inner-sphere complexes being favored by tetrahedral substitutions.[26] On the other hand, a majority of interlayer $Na^+$ cations are located in the mid-plane of the interlayer for octahedrally substituted 2W smectites.[23,24] A

---

(20) Ferrage, E.; Tournassat, C.; Rinnert, E.; Lanson, B. *Geochim. Cosmochim. Acta* **2005**, *69*, 2797−2812.

(21) Skipper, N. T.; Chang, F. R. C.; Sposito, G. *Clays Clay Miner.* **1995**, *43*, 285−293.

(22) Chang, F. R. C.; Skipper, N. T.; Sposito, G. *Langmuir* **1998**, *14*, 1201−1207.

(23) Boek, E. S.; Coveney, P. V.; Skipper, N. T. *J. Am. Chem. Soc.* **1995**, *117*, 12608−12617.

(24) Chang, F. R. C.; Skipper, N. T.; Sposito, G. *Langmuir* **1995**, *11*, 2734−2741.

(25) Chang, F. R. C.; Skipper, N. T.; Sposito, G. *Langmuir* **1997**, *13*, 2074−2082.

(26) Skipper, N. T.; Sposito, G.; Chang, F. R. C. *Clays Clay Miner.* **1995**, *43*, 294−303.

similar influence of the charge location was reported for K- and Li-saturated 2W smectites.[22,25] In contrast, whatever the charge location, $Mg^{2+}$ cations are systematically octahedrally coordinated in 2W smectites and located in the mid-plane of the interlayer.[27,28] In any case, MC simulations most often indicate that $H_2O$ molecules do not form a discrete plane but rather show that they are distributed about a "most probable" position. In addition, the mixed charge location common in smectite layers, and more especially in those of natural samples, can lead to the coexistence in a single smectite interlayer of different complexes, thus broadening the water distribution profile by perturbing the hydrogen bond network and the orientation of the water dipole.[29] Even though MC simulations do not commonly account for smectite hydration heterogeneity, which is best revealed by XRD analysis, such a description of $H_2O$ molecules positional disorder could be the missing link toward a better structure determination of $H_2O$ configuration in 2W smectite layers.

## Materials and Methods

**Experimental.** Samples investigated in the present work include two reference low-charge montmorillonites (SWy-1 and SWy-2) available from the Source Clays Repository (http://www.clays.org/sourceclays/SourceClays.html) and two synthetic saponite samples. The latter samples were selected because of their contrasting layer charges (0.8 and 1.4 per $O_{20}(OH)_4$).[30,31] The size fractionation of all samples, and their homoionic saturation were performed as described by Ferrage et al.[18] For all samples, oriented slides were prepared by drying at room temperature a clay slurry pipetted onto a glass slide. XRD patterns were then recorded using a Bruker D5000 diffractometer equipped with a Kevex Si(Li) solid-state detector, and an Ansyco rh-plus 2250 humidity control device coupled to an Anton Paar TTK450 chamber. Usual scanning parameters were 0.04° $2\theta$ as step size and 6 s as counting time per step over the 2−50° $2\theta$ Cu Kα angular range. The divergence slit, the two Soller slits, and the antiscatter and resolution slits were 0.5°, 2.3°, 2.3°, 0.5°, and 0.06°, respectively. Data collection conditions (60 and 80% RH for Sr-saturated samples, 40 and 80% RH for Ca-saturated samples, and 80 or 90% RH for Na-saturated samples) were selected because of the high amount of 2W layers (>90%) present in these conditions.[18]

**Simulation of X-ray Diffraction Data.** The algorithms developed initially by Drits and co-workers were used to fit experimental XRD profiles over the 2−50° $2\theta$ Cu Kα range using a trial-and-error approach.[32−34] Instrumental and experimental factors such as horizontal and vertical beam divergences, goniometer radius, and length and thickness of the oriented slides were measured and introduced without further adjustment. The mass absorption coefficient ($\mu^*$) was set to 45 $cm^2 g^{-1}$, as recommended by Moore and Reynolds,[1] whereas the parameter characterizing the preferred orientation of the particles in the sample ($\sigma^*$) was considered as a variable parameter. Additional variable parameters included the coherent scattering domain size (CSDS) along the $c^*$ axis which was characterized by a maximum CSDS value, set to 45 layers, and by a variable mean CSDS value ($N$).[35] In addition, because of the weak bonds between adjacent smectite layers, layer thickness was allowed to deviate from the average $d_{001}$ value. This cumulative deviation from periodicity, which is described as a "disorder of the second type",[36,37] is accounted for by introducing a variance parameter $\sigma_z$.[18] $z$-coordinates of all atoms building up the 2:1 layer framework, as well as those present in the interlayer of 0W and 1W layers, were set as proposed by Moore and Reynolds.[1] The interlayer structure of 2W layers has been refined to account for all features of experimental XRD patterns recorded on 2W-dominated samples. In particular, a double Gaussian distribution of $H_2O$ molecules along the $c^*$ axis (2WG) was assumed. This 2WG model accounts for both the presence of a unique plane of $H_2O$ molecules on either side of the mid-plane (Figure 1c and d) and the positional distribution of $H_2O$ molecules derived from MC simulations. The 2WG distributions considered in the present study are symmetrical relative to the interlayer mid-plane. They are characterized by the distance ($\Delta d$) between this mid-plane, where interlayer cations are supposed to be located, and the position of the maximum density of the Gaussian distribution. In addition, the total amount of interlayer $H_2O$ molecules was refined together with the full width at half-maximum intensity (fwhm) parameter of the Gaussian distribution. In the resulting structure model, $H_2O$ molecules were introduced using a 0.05-Å step along the $c^*$ axis, with a $B_{wat}$ factor equal to zero, as thermal motion is taken into account in MC calculations.

Two parameters were used to assess the overall goodness of fit. The unweighted $R_p$ parameter was considered because this parameter is mainly influenced by the most intense diffraction maxima such as the 001 reflection which contains essential information on the proportions of the different layer types and on their respective layer thickness values. The $R_{wp}$ parameter was also used to better account for the overall fit quality, especially in the high-angle regions.[38] Accessory quartz reflections were omitted for the calculation of these parameters. On their low-angle side, calculated XRD patterns are limited to ~5° $2\theta$ Cu Kα because significant discrepancies, possibly resulting from an incorrect description of crystalline defects not challenging the results described in the present study,[18] are observed over the low-angle region.[39]

**Monte Carlo Simulations.** Monte Carlo simulations in the NVT ensemble were used to obtain a detailed spatial distribution of the different species within smectite interlayers. The model montmorillonite-type smectite used in the simulations has a $Na_{0.75}(Si_8)(Al_{3.25}Mg_{0.75})O_{20}(OH)_4$ structural formula and exhibits substitutions only in the octahedral sheet. The simulation box includes two 2:1 layers, each consisting of 8 unit cells (total area 20.72 Å × 17.94 Å, thickness of the 2:1 layer 6.54 Å). The total negative charge of the 2:1 layers was thus compensated for by 6 $Na^+$ cations in the interlayer. The interlayer shift between adjacent 2:1 layers was set

---

(27) Skipper, N. T.; Refson, K.; McConnell, J. D. C. *J. Chem. Phys.* **1991**, *94*, 7434−7445.

(28) Greathouse, J.; Refson, K.; Sposito, G. *J. Am. Chem. Soc.* **2000**, *122*, 11459−11464.

(29) Sposito, G.; Skipper, N. T.; Sutton, R.; Park, S. H.; Soper, A. K.; Greathouse, J. A. *Proc. Nat. Acad. Sci. U.S.A.* **1999**, *96*, 3358−3364.

(30) Michot, L. J.; Villiéras, F. *Clay Miner.* **2002**, *37*, 39−57.

(31) Pelletier, M.; Michot, L. J.; Humbert, B.; Barres, O.; d'espinose de la Callerie, J. B.; Robert, J. L. *Am. Mineral.* **2003**, *88*, 1801−1808.

(32) Drits, V. A.; Sakharov, B. A. *X-ray Structure Analysis of Mixed-Layer Minerals*; Nauka: Moscow, 1976.

(33) Drits, V. A.; Lindgreen, H.; Sakharov, B. A.; Salyn, A. S. *Clay Miner.* **1997**, *33*, 351−371.

(34) Sakharov, B. A.; Lindgreen, H.; Salyn, A.; Drits, V. A. *Clays Clay Miner.* **1999**, *47*, 555−566.

(35) Drits, V. A.; Srodon, J.; Eberl, D. D. *Clays Clay Miner.* **1997**, *45*, 461−475.

(36) Guinier, A. *Théorie et Technique de la Radiocristallographie*; Dunod: Paris, 1964.

(37) Drits, V. A.; Tchoubar, C. *X-ray Diffraction by Disordered Lamellar Structures: Theory and Applications to Microdivided Silicates and Carbons*; Springer-Verlag: Berlin, 1990.

(38) Howard, S. A.; Preston, K. D. In *Modern Powder Diffraction*; Bish, D. L., Post, J. E., Eds.; Mineralogical Society of America: Washington, DC, 1989; Reviews in Mineralogy Vol. 20, pp 217−275.

(39) Plançon, A. *Am. Mineral.* **2002**, *87*, 1672−1677.

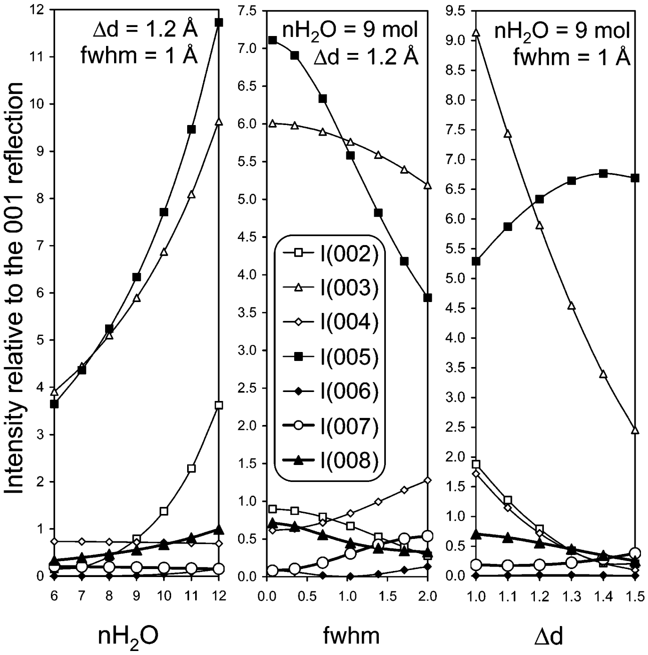

**Figure 2.** Relative intensities of 00*l* reflections, after normalization to the 001 reflection, as a function of structural parameters specific to the 2WG configuration (see text for details). The total amount of $H_2O$ molecules (n$H_2O$) is given per $O_{20}(OH)_4$, whereas the full width at half-maximum intensity (fwhm) of the distribution and the distance, in projection along the $c^*$ axis, from its maximum to the interlayer mid-plane (Δ*d*) are given in Å.

to different arbitrary values for the two interlayers considered and not allowed to vary during the calculation. For the typical layer thickness value (15.52 Å) determined for Na-montmorillonite by XRD profile modeling, the water content was estimated from the results of previous MC simulations performed with the NPT ensemble. The series of such simulations allows the determination of layer thickness as a function of water content, at constant pressure and temperature,[40] and the water content was found to be 9.5 $H_2O$ molecules per $O_{20}(OH)_4$. The resulting distributions of $H_2O$ molecules within 2W smectite interlayers were collected over 5 million MC steps, normalized, and made symmetric with respect to the mid-plane of the interlayer. The 2:1 layers were considered as rigid, and modeled with the rigid SPC/E model (O−H bond 1.0 Å, angle H−O−H 109.47°, charges $-0.848$ e$^-$ and $+0.424$ e$^-$ for oxygen and hydrogen atoms, respectively). Applied interaction potentials were the Lennard−Jones 6−12 and Coulombic potentials. Each atom in the simulation cell was thus characterized by two van der Waals parameters and by its charge. Additional details on the MC simulations can be found elsewhere.[25,41−43] Density profiles determined from MC calculations for interlayer sodium and $H_2O$ molecules were introduced in the XRD profile calculation using a 0.075-Å step.

## Results

**Influence of the Gaussian Distribution Profile on the Relative Intensity of 00*l* Reflections.** Figure 2 illustrates the influence of the different parameters used to describe the Gaussian distribution of $H_2O$ molecules, that is the total amount of $H_2O$ molecules (*n*$H_2O$), Δ*d*, and fwhm, on the relative intensity of 00*l* reflections. Calculations were performed assuming a periodic Ca−SWy-1 2W structure (layer thickness = 15.2 Å), and calculated intensities were systematically normalized to that of the 001 reflection. By increasing the total amount of $H_2O$ molecules the intensity of the 002, 003, 005 reflections greatly increases, that of the 008 reflection also increases but to a lower extent, whereas 004, 006, and 007 reflections are essentially unaffected (Figure 2). As its influence on 007 and 008 reflection intensity is limited, the *n*$H_2O$ parameter will not significantly affect the intensity ratio between these two reflections, which is a common and critical discrepancy between experimental and calculated profiles (Figure 1a−d). In contrast, the 008:007 intensity ratio is strongly affected by the fwhm of the Gaussian distribution, with this ratio being minimum for a Dirac distribution and increasing with the fwhm of the distribution. The 007 reflection is actually more intense than the 008 one for fwhm values larger than ~1.3 Å (Figure 2). In addition this parameter may be strongly constrained from its major influence on the intensity ratio between two intense reflections (003 and 005 reflections) which can be reversed by increasing the width of the Gaussian distribution of $H_2O$ molecules. However, the 003:005 ratio is also affected by the Δ*d* parameter which also affects the 008:007 intensity ratio, with both ratios increasing with increasing Δ*d* values. By increasing either the Δ*d* parameter or the fwhm, the intensity of the 002 reflection is systematically decreased, whereas that of the 004 reflection is increased or decreased, respectively. The intensity calculated for the 006 reflection is low regardless of the values used for these two parameters.

**Modeling of XRD Patterns.** For all XRD patterns recorded on smectite samples, calculations were performed using three different configurations of $H_2O$ molecules in the interlayers of 2W layers: (i) a 2WS configuration with two planes of $H_2O$ molecules characterized by a $B_{\mathrm{wat}}$ factor of 2 Å$^2$ and a Δ*d* parameter of 1.2 Å,[18] (ii) a similar 2WS configuration with a larger Debye−Waller factor ($B_{\mathrm{wat}}$ = 11 Å$^2$), and (iii) a configuration with $H_2O$ molecules distributed according to the 2WG configuration. Optimum parameters used to characterize smectite hydration heterogeneity, that is the relative proportions of the different MLSs coexisting in the sample and their compositions (relative proportions of 2W, 1W, and 0W layers), are reported in Table 1 together with the layer thickness values for the different layer types, *N*, $\sigma^*$, $\sigma_z$, and the water content in 1W layers. For 2W layers, the water content, the Δ*d* parameter, and the fwhm of the Gaussian distribution are reported in Table 2 for the different configurations of interlayer $H_2O$ molecules.

*Ca-Saturated Montmorillonite*. For sample Ca−SWy-1 at 80% RH, the calculations performed for 2WS configurations of $H_2O$ molecules (Δ*d* = 1.2 Å) and $B_{\mathrm{wat}}$ factors of 2 and 11 Å$^2$ have been described above (Figure 1c and d). The 2WS configuration provides a satisfactory fit to experimental patterns for 00*l* reflections with $l < 6$. However, this model does not allow concealing the discrepancy observed over the high-angle range, and more especially for the 008:007 intensity ratio, even if the Debye−Waller factor of $H_2O$

---

(40) Marry, V. Ph.D. Dissertation, Pierre et Marie Curie University, Paris, 2002.

(41) Marry, V.; Turq, P.; Cartailler, T.; Levesque, D. *J. Chem. Phys.* **2002**, *117*, 3454−3463.

(42) Delville, A. *Langmuir* **1992**, *8*, 1796−1805.

(43) Boek, E. S.; Coveney, P. V.; Skipper, N. T. *Langmuir* **1995**, *11*, 4629−4631.

**Table 1. Optimum Structural Parameters Used for the Simulation of Experimental XRD Profiles**

| | | | | | layer thickness[c] | | | | | | |
|---|---|---|---|---|---|---|---|---|---|---|---|
| sample | rel. ab. (%)[a] | 2W[b] | 1W[b] | 0W[b] | 2W | 1W | 0W | $n$H$_2$O 1W[d] | $N$[e] | $\sigma$*[f] | $\sigma_z$[g] |
| Ca−SWy-2 (40%RH)[h] | 87 | 100 | 0 | 0 | 15.18 | 12.60 | 10.00 | 3.2 | 8.7 | 6.5 | 0.35 |
| | 13 | 60 | 30 | 10 | | | | | | | |
| Ca−SWy-1 (80%RH)[i] | 61 | 95 | 5 | 0 | 15.51 | 12.85 | 10.00 | 3.3 | 6.0 | 6.5 | 0.27 |
| | 39 | 85 | 13 | 2 | | | | | | | |
| Sr−SWy-1 (60%RH)[i] | 82 | 100 | 0 | 0 | 15.53 | 12.58 | 10.00 | 3.5 | 7.5 | 5.5 | 0.35 |
| | 18 | 75 | 15 | 10 | | | | | | | |
| Sr−SWy-1 (80%RH)[i] | 84 | 100 | 0 | 0 | 15.73 | 12.70 | 10.00 | 5.5 | 7.5 | 5.5 | 0.35 |
| | 16 | 75 | 15 | 10 | | | | | | | |
| Na−SWy-2 (80%RH) | 90 | 96 | 2 | 2 | 15.52 | 12.55 | 9.60 | 3.2 | 8.2 | 11.0 | 0.25 |
| | 10 | 60 | 30 | 10 | | | | | | | |
| Na−Sap$_{0.8}$ (90%RH) | 44 | 100 | 0 | 0 | 15.40 | 13.20 | 9.80 | 5.7 | 13.0 | 2.0 | 0.19 |
| | 56 | 90 | 5 | 5 | | | | | | | |
| Na−Sap$_{1.4}$ (90%RH) | 91 | 100 | 0 | 0 | 15.00 | 12.90 | 9.80 | 5.0 | 12.0 | 11 | 0.12 |
| | 9 | 70 | 20 | 10 | | | | | | | |

[a] Relative proportion of the different contributions to the diffracted intensity. [b] Relative proportion of the different layer types in the different contributions to the diffracted intensity. 2W, 1W, and 0W stand for bi-hydrated, monohydrated and de-hydrated smectite layers, respectively. [c] Layer thickness of the different layer types. [d] Number of H$_2$O molecules in 1W layers (per O$_{20}$(OH)$_4$). [e] Mean thickness of the coherent scattering domain size along the c* axis (in layers). [f] $\sigma$* parameter characterizing the sample orientation (in deg, ref 1). [g] Standard deviation of the layer thickness parameter (in Å) (ref 18). [h] Data from Ferrage et al (ref 20). [i] Data from Ferrage et al (ref 18).

**Table 2. Structural Parameters of the Interlayer Space Determined from XRD Profile Modeling as a Function of the Assumed Water Configuration**

| | 2WS, $B_{\text{wat}} = 2$[a] | | 2WS, $B_{\text{wat}} = 11$[a] | | 2WG[b] | | |
|---|---|---|---|---|---|---|---|
| sample | $n$H$_2$O[c] | $\Delta d$[d] | $n$H$_2$O | $\Delta d$ | $n$H$_2$O | $\Delta d$ | fwhm[e] |
| Ca−SWy-2 (40%RH) | 6.2 | 1.20 | 6.6 | 1.30 | 7.8 | 1.34 | 1.4 |
| Ca−SWy-1 (80%RH) | 6.6 | 1.20 | 6.8 | 1.32 | 10.0 | 1.37 | 1.7 |
| Sr−SWy-1 (60%RH) | 6.0 | 1.20 | 6.8 | 1.32 | 8.5 | 1.40 | 1.2 |
| Sr−SWy-1 (80%RH) | 6.0 | 1.20 | 7.0 | 1.41 | 9.5 | 1.52 | 1.5 |
| Na−SWy-2 (80%RH) | 7.4 | 1.20 | 8.2 | 1.41 | 9.5 | 1.50 | 1.4 |
| Na−Sap$_{0.8}$ (90%RH) | 8.5 | 1.20 | 9.3 | 1.33 | 10.5 | 1.39 | 1.4 |
| Na−Sap$_{1.4}$ (90%RH) | 8.4 | 1.20 | 9.0 | 1.33 | 9.4 | 1.35 | 0.8 |

[a] 2WS corresponds to an interlayer configuration of H$_2$O molecules distributed as one plane on either side of the interlayer mid-plane. The Debye−Waller temperature factor for water ($B_{\text{wat}}$) is given in Å$^2$. [b] 2WG corresponds to an interlayer configuration of H$_2$O molecules distributed according to a Gaussian function on either side of the interlayer mid-plane. [c] The number of H$_2$O molecules is given per O$_{20}$(OH)$_4$. In this case, $B_{\text{wat}}$= 0 Å$^2$. [d] The distance, in projection along the $c$* axis, between the interlayer mid-plane and the maximum density of the distribution of H$_2$O molecules ($\Delta d$) is given in Å. [e] The width of the Gaussian distribution of interlayer H$_2$O molecules (fwhm) is given in Å.

molecules is maximized ($B_{\text{wat}}$ = 10−11 Å$^2$).[44] In this case, the water content and the $\Delta d$ parameter are increased from 6.6 to 6.8 H$_2$O per O$_{20}$(OH)$_4$ and from 1.20 to 1.32 Å, respectively, as compared to the 2WS configuration with $B_{\text{wat}}$ = 2 Å$^2$ (Table 2). A 008:007 intensity ratio consistent with that observed experimentally can be obtained by considering the 2WG configuration for interlayer H$_2$O molecules. In this case, broad Gaussian distributions were assumed (fwhm = 1.7 Å), and both the water content and the $\Delta d$ parameter were increased as compared to alternative interlayer configurations (Table 2). This 2WG configuration also allows better fitting of the profile of the 005 reflection, but that of the 003 one is slightly altered as a result of a low-angle tail broadening (Figure 1e).

The combination of two structures, a main periodic one with only 2W layers and a second one containing the three layer types (Table 1), accounts for the hydration heterogeneity of sample Ca−SWy-2 at 40% RH, and leads to the coexistence of 2W, 1W, and 0W layers (95%, 4%, and 1%, respectively).[18] The 2WS configuration allows describing most features of the experimental XRD patterns ($R_{\text{p}}$ = 1.31% and $R_{\text{wp}}$ = 8.13%, Figure 3a). However, the 008 reflection is significantly more intense than the 007 one. By increasing the Debye−Waller $B_{\text{wat}}$ factor from 2 to 11 Å$^2$, the 008:007 intensity ratio appears closer to the experimental one, although the two estimates of the fit quality are not affected (Figure 3b). This ratio is best reproduced by assuming a 2WG distribution with a fwhm of 1.4 Å (Figure 3c) although $R_{\text{p}}$ and $R_{\text{wp}}$ parameters are almost unaffected. As compared to the 2WS mode the total amount of H$_2$O molecules in such 2WG configuration is considerably increased from 6.2 (assuming a $B_{\text{wat}}$ factor of 2 Å$^2$) to 7.8 per O$_{20}$(OH)$_4$ (Table 2).

*Sr-Saturated Montmorillonite.* At both 60 and 80% RH, the hydration heterogeneity of sample Sr−SWy-1 is minimum as it contains an overwhelming proportion of 2W layers (95, and 96%, respectively; Table 1).[18] As for the Ca-saturated samples, the 2WS configuration for H$_2$O molecules leads to a satisfactory fit to the experimental XRD patterns, especially for 00$l$ reflections with $l$ < 6, and for the 008 reflection (Figures 4a and 5a). However, significant discrepancies between experimental and calculated patterns are visible for the 002 reflection and the 008:007 intensity ratio. These discrepancies are significantly reduced by increasing the Debye−Waller factor of H$_2$O molecules from 2 to 11 Å$^2$, but they do not vanish completely (Figures 4b and 5b). The optimum fit to the experimental XRD patterns was again obtained assuming a 2WG distribution of interlayer H$_2$O molecules with a large fwhm value (1.2, and 1.5 Å for Sr−SWy-1 samples recorded at 60 and 80% RH, respec-

---

(44) Lipson, H. In *International Tables for X-ray Crystallography*; Casper, J. S., Lonsdale, K., Eds.; International Union of Crystallography, 1967; Mathematical tables Vol. 2, pp 235−315.

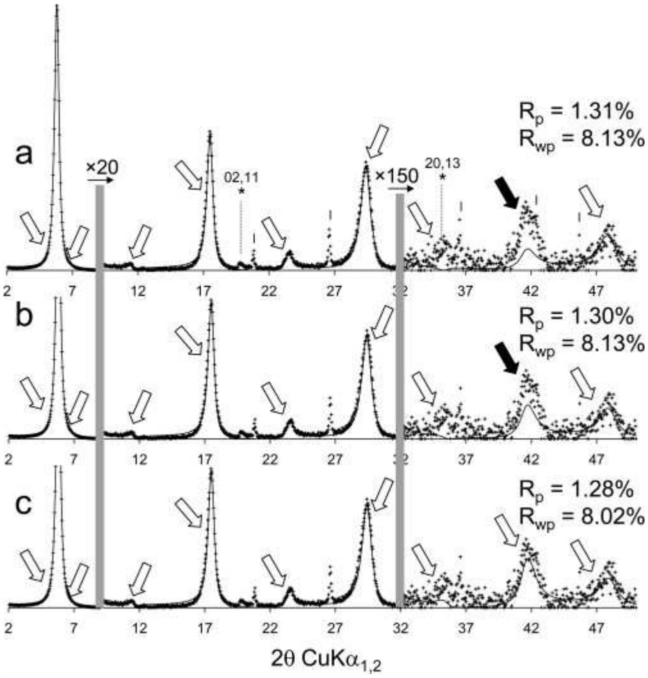

**Figure 3.** Comparison between experimental and calculated XRD patterns for the Ca-saturated SWy-2 montmorillonite sample recorded at 40% RH. Structural parameters used for the calculations are listed in Tables 1, 2, and 3. Patterns as for Figure 1. (*) indicates hk bands, whereas vertical ticks denote the presence of accessory quartz reflections. (a) Calculation performed assuming a 2WS configuration with $B_{wat} = 2$ Å$^2$ for $H_2O$ molecules (ref 18). (b) Calculation performed assuming a 2WS configuration with $B_{wat} = 11$ Å$^2$ for $H_2O$ molecules. (c) Calculation performed assuming a 2WG configuration.

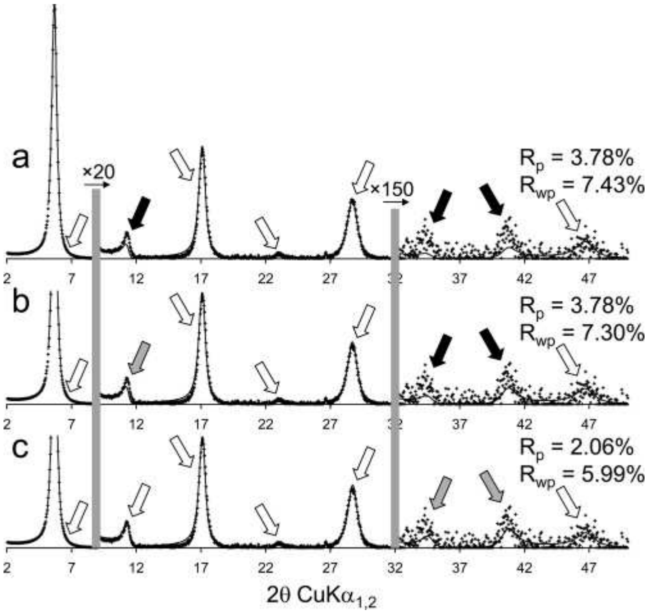

**Figure 4.** Comparison between experimental and calculated XRD patterns for the Sr-saturated SWy-1 montmorillonite sample recorded at 60% RH. Structural parameters used for the calculations are listed in Tables 1, 2, and 3. Patterns as for Figure 1. (a) Calculation performed assuming a 2WS configuration with $B_{wat} = 2$ Å$^2$ for $H_2O$ molecules (ref 18). (b) Calculation performed assuming a 2WS configuration with $B_{wat} = 11$ Å$^2$ for $H_2O$ molecules. (c) Calculation performed assuming a 2WG configuration.

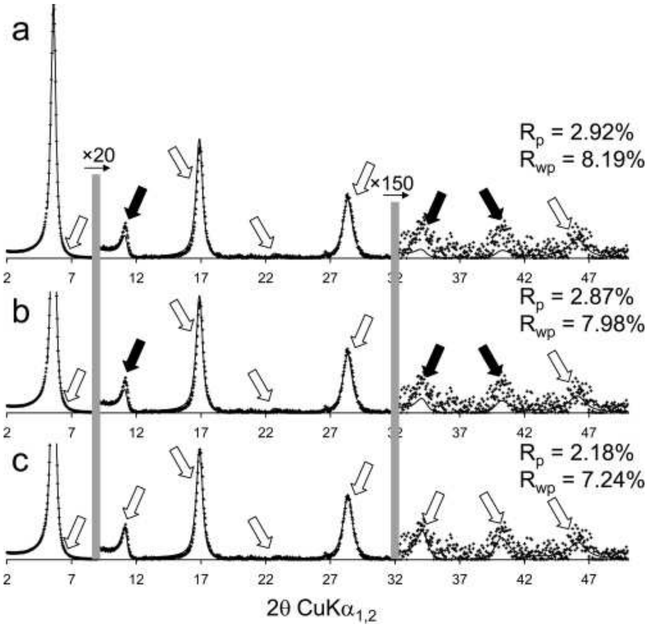

**Figure 5.** Comparison between experimental and calculated XRD patterns for the Sr-saturated SWy-1 montmorillonite sample recorded at 80% RH. Structural parameters used for the calculations are listed in Tables 1, 2, and 3. Patterns as for Figure 1. (a) Calculation performed assuming a 2WS configuration with $B_{wat} = 2$ Å$^2$ for $H_2O$ molecules (ref 18). (b) Calculation performed assuming a 2WS configuration with $B_{wat} = 11$ Å$^2$ for $H_2O$ molecules. (c) Calculation performed assuming a 2WG configuration.

tively; Table 2; Figures 4c and 5c). For the two samples, both $R_p$ and $R_{wp}$ are lower for the 2WG configuration of interlayer $H_2O$ molecules than for the 2WS ones.

*Na-Saturated Montmorillonite*. At 80% RH, the Na−SWy-2 sample exhibits a high proportion (92%) of 2W layers, whereas minor amounts of 1W and 0W layers (5%, and 3%, respectively) account for the hydration heterogeneity (Table 1). As for the previous sample, the 2WS configuration of $H_2O$ molecules leads to a satisfactory agreement between experimental and calculated data, especially for 00*l* reflections with $l < 6$, and for the 008 reflection (Figure 6a). However, by using a Debye−Waller factor of 2 Å$^2$ the intensities calculated for the 006 and 007 reflections are too low as compared to the experimental ones. Increasing the $B_{wat}$ factor up to 11 Å$^2$ significantly reduces these discrepancies, although the 008:007 intensity ratio remains imperfectly reproduced (Figure 6b). The optimum fit to the experimental data for this sample was again obtained assuming a 2WG distribution of $H_2O$ molecules (Figure 6c; $R_{wp} = 5.33\%$, $R_p = 2.59\%$). The $\Delta d$ and fwhm parameters of this 2WG distribution are 1.50 Å and 1.4 Å, respectively (Table 2). A similar fit to the experimental data (Figure 6d; $R_{wp} = 5.34\%$, $R_p = 2.57\%$) was obtained assuming the distribution of interlayer species shown in Figure 7, while all other parameters were kept constant (Table 1). This distribution was derived from the MC simulations performed using the NVT ensemble. MC calculated distributions exhibit a single peak for the oxygen atoms, and two for the hydrogen atoms, between the interlayer mid-plane and the surface of the 2:1 layer, and are characteristic of the presence of a single plane of $H_2O$ molecules on either side of the cation plane which is located in the center of the interlayer. The distance between the maximum of the oxygen distribution and the maximum of the hydrogen distribution closer to the 2:1 layer is ~1.0 Å which is the length of the O−H bond in the water molecule. This indicates a preferential orientation of the $H_2O$ molecules in the interlayer, with one of the O−H bonds almost perpendicular to the surface of the 2:1 layer. Similar configurations of $H_2O$ molecules in the interlayer of octa-

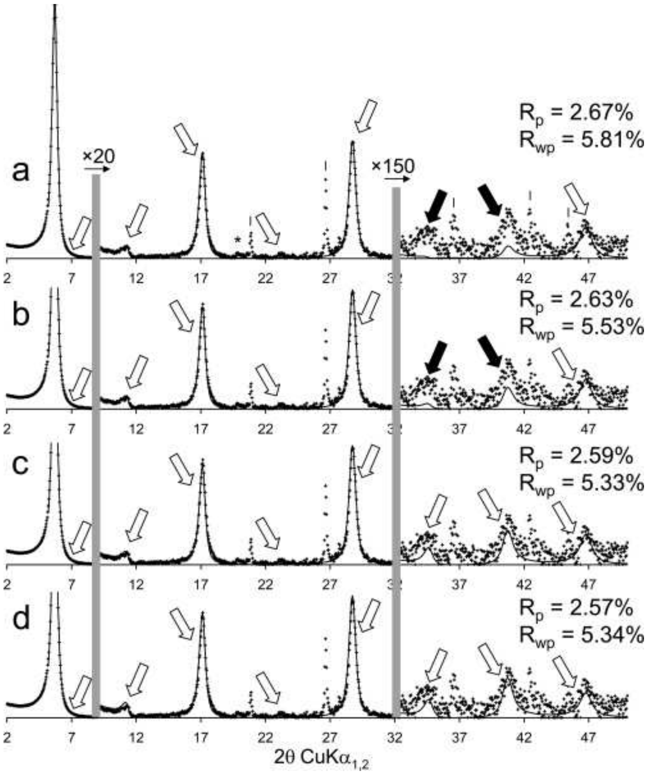

**Figure 6.** Comparison between experimental and calculated XRD patterns for the Na-saturated SWy-2 montmorillonite sample recorded at 80% RH. Structural parameters used for the calculations are listed in Tables 1, 2, and 3. Patterns as for Figures 1 and 3. (a) Calculation performed assuming a 2WS configuration with $B_{wat} = 2$ Å$^2$ for $H_2O$ molecules (ref 18). (b) Calculation performed assuming a 2WS configuration with $B_{wat} = 11$ Å$^2$ for $H_2O$ molecules. (c) Calculation performed assuming a 2WG configuration. (d) Calculation performed assuming the distribution of interlayer species derived from MC simulations using the NVT ensemble and shown in Figure 7.

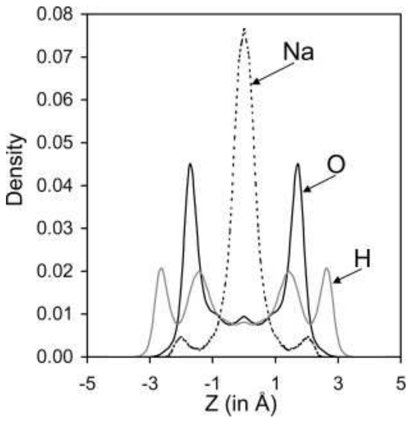

**Figure 7.** Density profiles of interlayer species along the $c^*$ axis derived from MC simulations performed using the NVT ensemble. $z$-coordinates are given in Å with the origin located in the interlayer mid-plane. Solid, dashed, and gray lines represent O, H, and $Na^+$ atoms, respectively.

hedrally substituted smectites have been previously reported from IR spectroscopy results[45] and from microscopic simulations.[24] As for all other samples, the amount of interlayer $H_2O$ molecules has to be increased, together with the $\Delta d$ parameter, as the positional distribution of these species increases (Table 2).

*Na-Saturated Synthetic Saponites*. At 90% RH, the hydration heterogeneity of both synthetic saponites is minimum as they exhibit an overwhelming proportion of 2W layers (94 and 97% for Na−$Sap_{0.8}$ and Na−$Sap_{1.4}$ samples, respectively; Table 1). As compared to the natural ones, these two synthetic samples present larger CSDS along the $c^*$ axis, as evidenced by the sharpening of the 00$l$ reflections (Table 1; Figures 8 and 9). Layer thickness of 2W layers decreases from 15.4 to 15.0 Å as the layer charge increases from 0.8 to 1.4 per $O_{20}(OH)_4$ (samples Na−$Sap_{0.8}$ and Na−$Sap_{1.4}$, respectively; Table 1). For both samples, the 2WS configuration of $H_2O$ molecules with $B_{wat} = 2$ Å$^2$ allows satisfactory fitting of 00$l$ reflections with $l < 6$ (Figures 8a and 9a). Increasing the Debye−Waller factor up to 11 Å$^2$ leads to a perfect fit to the experimental data for the high-charge sample (Na−$Sap_{1.4}$; Figure 9b), whereas significant discrepancies are still observed between experimental and calculated patterns for the low-charge sample (Na−$Sap_{0.8}$; Figure 8b). For this latter sample, the optimum fit to the experimental data was again obtained assuming a 2WG distribution of $H_2O$ molecules in the smectite interlayer with $\Delta d$ and fwhm parameters (1.39 and 1.4 Å, respectively) similar to those obtained for natural samples (Figure 8c and Table 2). For the Na−$Sap_{1.4}$ sample, a fit similar to the one obtained with a 2WS distribution of $H_2O$ molecules and a high $B_{wat}$ factor

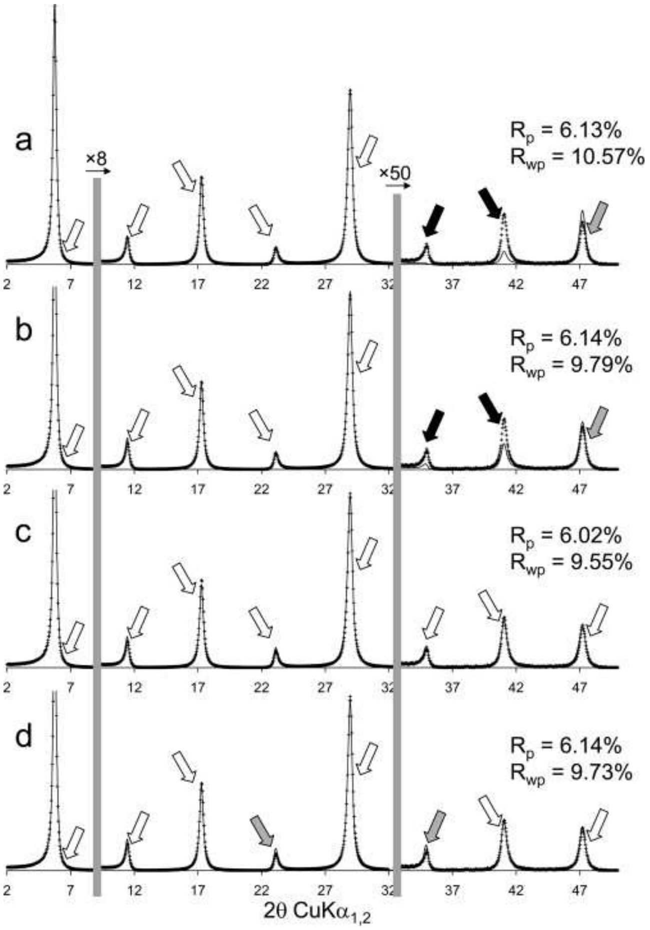

**Figure 8.** Comparison between experimental and calculated XRD patterns for the Na-saturated $Sap_{0.8}$ saponite sample recorded at 90% RH. Structural parameters used for the calculations are listed in Tables 1, 2, and 3. Patterns as for Figure 1. (a) Calculation performed assuming a 2WS configuration with $B_{wat} = 2$ Å$^2$ for $H_2O$ molecules (ref 18). (b) Calculation performed assuming a 2WS configuration with $B_{wat} = 11$ Å$^2$ for $H_2O$ molecules. (c) Calculation performed assuming a 2WG configuration. (d) Calculation performed assuming a 2WS configuration with $B_{wat} = 30$ Å$^2$ for $H_2O$ molecules, 10.5 $H_2O$ molecules per $O_{20}(OH)_4$) in 2W layers, and $\Delta d$ =1.38 Å.

---

(45) Sposito, G.; Prost, R. *Chem. Rev.* **1982**, *82*, 553−573.

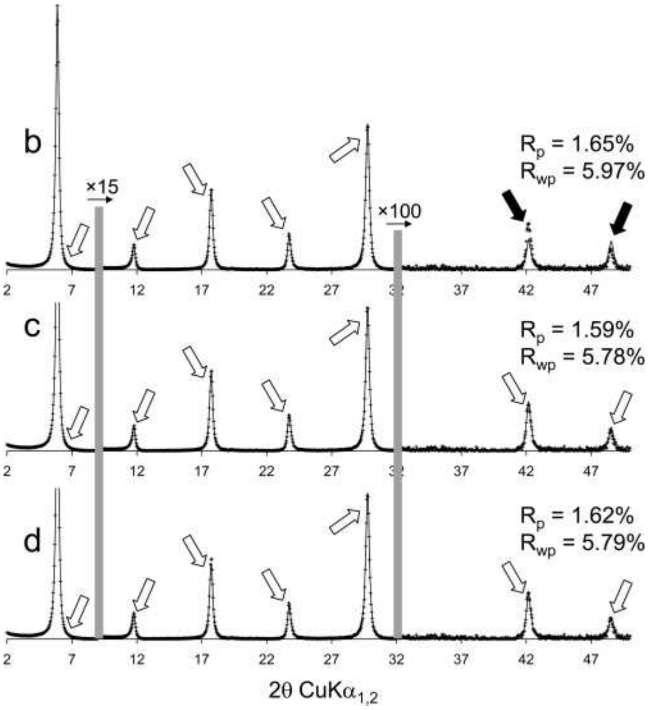

**Figure 9.** Comparison between experimental and calculated XRD patterns for the Na-saturated $Sap_{1.4}$ saponite sample recorded at 90% RH. Structural parameters used for the calculations are listed in Tables 1, 2, and 3. Patterns as for Figure 1. (a) Calculation performed assuming a 2WS configuration with $B_{wat}$ = 2 Å$^2$ for $H_2O$ molecules (ref 18). (b) Calculation performed assuming a 2WS configuration with $B_{wat}$ = 11 Å$^2$ for $H_2O$ molecules. (c) Calculation performed assuming a 2WG configuration.

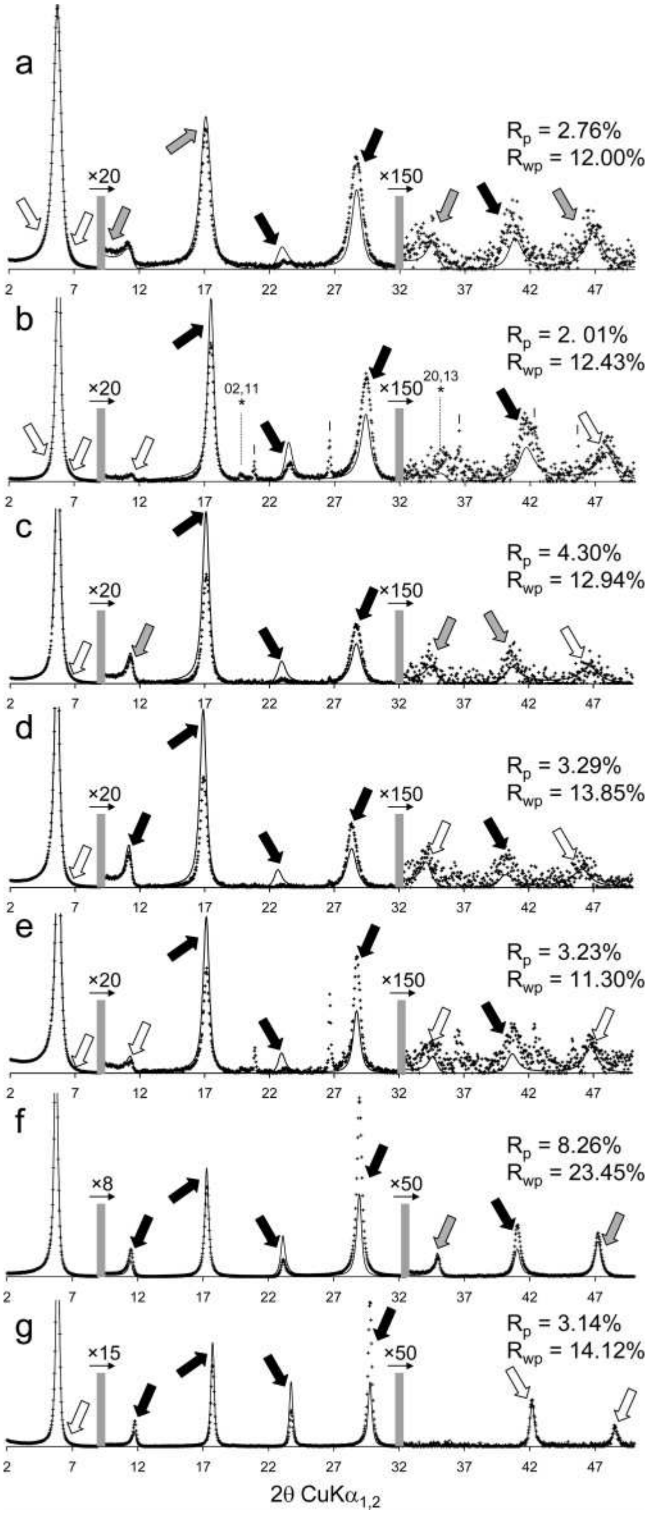

**Figure 10.** Comparison between experimental XRD patterns and those calculated assuming the usual configuration of $H_2O$ molecules (ref 1). Hydration heterogeneity has been taken into account for all calculations. Structural parameters used for the calculations are listed in Table 1. Patterns as for Figures 1 and 3. (a) Ca-saturated SWy-1 montmorillonite sample recorded at 80% RH. (b) Ca-saturated SWy-2 montmorillonite sample recorded at 40% RH. (c) Sr-saturated SWy-1 montmorillonite sample recorded at 60% RH. (d) Sr-saturated SWy-1 montmorillonite sample recorded at 80% RH. (e) Na-saturated SWy-2 montmorillonite sample recorded at 80% RH. (f) Na-saturated $Sap_{0.8}$ saponite sample recorded at 90% RH. (g) Na-saturated $Sap_{1.4}$ saponite sample recorded at 90% RH.

was obtained assuming a 2WG distribution of $H_2O$ molecules (Figure 9b and c). However, the fwhm parameter of this distribution is significantly lower (0.8 Å) than those typically obtained for natural samples (1.2−1.7 Å; Table 2).

## Discussion

**Shortcomings of the Usual Description of $H_2O$ Molecule Positional Disorder in 2W Smectite Interlayers.** By accounting for smectite hydration heterogeneity, it is possible to model experimental XRD patterns thus gaining additional insights into the structure of smectite interlayers. It should be noted first that the initial assumption of identical properties for all layers exhibiting the same hydration state and present in the different MLSs was verified for all samples, thus validating the proposed description of smectite hydration heterogeneity. In addition, the configuration of $H_2O$ molecules within 2W smectite layers commonly used for XRD pattern simulations can be discarded as it systematically leads to major discrepancies between experimental and calculated profiles (Figure 10).[18−20] Specifically, the use of this usual configuration systematically leads to poor fits to the experimental XRD patterns for low-angle high-intensity reflections such as 003, 004, and 005 reflections (Figure 10). By contrast, the distribution of $H_2O$ molecules within a single plane on either side of the mid-plane interlayer (2WS configuration) allows both fitting the profiles and reproducing the relative intensities of the 00*l* reflections with $l < 6$ (Figures 1c, 3a, 4a, 5a, 6a, 8a, 9a).[18] When assuming a Debye−Waller $B_{wat}$ factor of 2 Å$^2$, this model leads to significant discrepancies for high-order 00*l* reflections, which are partly resolved by increasing the positional disorder of $H_2O$ molecules ($B_{wat}$ = 11 Å$^2$; Figures 1d, 3b, 4b, 5b, 6b, 8b, 9b). However, except for sample Na−$Sap_{1.4}$, such an increased $B_{wat}$ factor does not allow satisfactory fitting of the high-order 00*l* reflections, which would

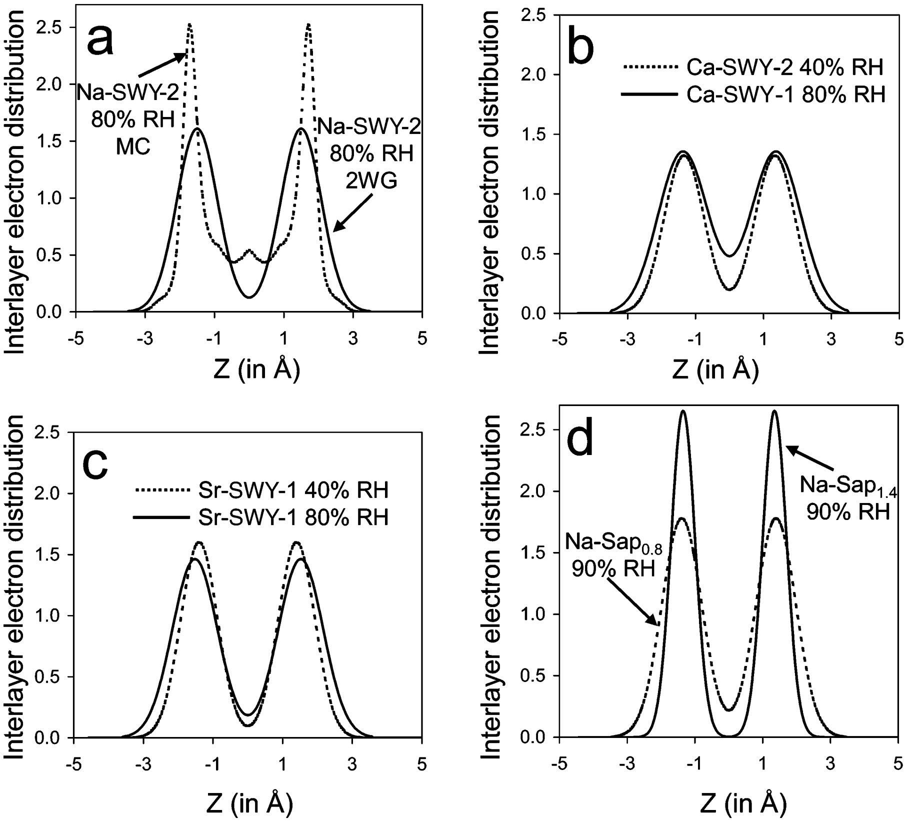

**Figure 11.** Density profiles along the $c^*$ axis of the electron distribution in the interlayer of bi-hydrated smectite layers. $z$-coordinates are given in Å with the origin located in the interlayer mid-plane. (a) Comparison between the electron distribution derived from the density profiles of interlayer species calculated using the NVT ensemble (Figure 7) and the one determined from XRD profile modeling for the Na−SWy-2 montmorillonite sample (80% RH). (b) Comparison between the electron distributions determined from XRD profile modeling for the two Ca-saturated montmorillonite samples under different RH conditions. (c) Comparison between the electron distributions determined from XRD profile modeling for the two Sr-saturated SWy-1 montmorillonite samples under different RH conditions. (d) Comparison between the electron distributions determined from XRD profile modeling for the two Na-saturated synthetic saponite samples with different amounts of layer charge.

**Table 3. Optimum Amounts of $H_2O$ Molecules Determined from XRD Profile Modeling for the Different Configurations of Interlayer Species, and from Water Vapor Adsorption/Desorption Isotherms**

| sample | type I configuration[a] | 2WS $B_{wat} = 2$[b] | 2WS $B_{wat} = 11$[b] | 2WG[c] | ads./des.[d] |
|---|---|---|---|---|---|
| Ca−SWy-2 (40%RH) | 7.25[e] | 8.32 | 8.58 | 10.11 | 8.62/10.17 |
| Ca−SWy-1 (80%RH) | 7.06 | 8.30 | 8.54 | 12.36 | 12.85/13.70 |
| Sr−SWy-1 (60%RH) | 7.06 | 7.60 | 8.85 | 10.72 | 7.87/9.29<br>(10.70/11.90) |
| Sr−SWy-1 (80%RH) | 7.14 | 7.69 | 8.95 | 12.09 | 9.83/10.45<br>(12.80/13.70) |
| Na−SWy-2 (80%RH) | 7.04 | 9.27 | 10.24 | 11.82 | 10.50/13.10 |
| Na−Sap$_{0.8}$ (90%RH) | 7.00 | 10.62 | 11.60 | 13.07 | 13.39/14.49[f] |
| Na−Sap$_{1.4}$ (90%RH) | 6.96 | 10.45 | 11.19 | 11.62 | 14.23/17.18[f] |

[a] Interlayer configuration of $H_2O$ molecules commonly used for the calculation XRD profiles including 2W layers (ref 1). [b] 2WS corresponds to an interlayer configuration of $H_2O$ molecules distributed as one plane on either side of the interlayer mid-plane. The Debye−Waller temperature factor for water ($B_{wat}$) is given in Å$^2$. [c] 2WG corresponds to an interlayer configuration of $H_2O$ molecules distributed according to a Gaussian function on either side of the interlayer mid-plane. In this case, $B_{wat} = 0$ Å$^2$. [d] Water amounts determined experimentally from water vapor adsorption/desorption isotherms. Data are taken from Cases et al. (ref 16), and from Bérend et al. (ref 14) for divalent and monovalent cations, respectively. [e] The water contents are given in mmol of water per g of clay. [f] Personal communication from Laurent Michot (LEM, Nancy, France).

require unrealistically high $B_{wat}$ factor values. In addition, the contrasting $B_{wat}$ factors adjusted for the two synthetic saponite samples recorded under similar RH and temperature conditions plead for a different origin to the actual positional disorder of $H_2O$ molecules in smectite interlayers.

**Distribution of $H_2O$ Molecules According to a Double Gaussian Function.** The 2WG model can be considered as an improved version of the 2WS model in which the actual positional disorder of $H_2O$ molecules is better accounted for (Figures 1e, 3c, 4c, 5c, 6c, 8c, 9c). In the 2WG model the interlayer cation is considered to lie in a fixed position located in the interlayer mid-plane and to have a Debye−Waller factor of 2 Å$^2$. This hypothesis does not imply that the interlayer cations are not distributed as $H_2O$ molecules are, but it was assumed as a first approximation that thermal motion would be sufficient to account for their positional disorder. In addition, the sensitivity to the positional disorder of these cations is much reduced as compared to $H_2O$ molecules, as the former species accounts for a minor part of the overall electronic density in smectite interlayers. For example, at 80% RH $Ca^{2+}$ cations account for only 6% of the interlayer electrons (Table 3).

When comparing the electronic density due to interlayer $H_2O$ molecules deduced from MC calculations with that obtained from XRD profile fitting (Figure 11a), it is possible to note that the overall profiles are globally alike despite significant differences. In particular, the two planes of $H_2O$ molecules on either side of the interlayer mid-plane are much narrower in the MC calculations (fwhm ~0.7 Å as compared to ~1.4 Å for XRD profile fitting) which indicate also a significantly higher electron density in the interlayer mid-plane. The narrower distribution obtained from the MC simulation can be due in part to the fixed interlayer displacement between adjacent layers considered for the calculations, although the influence of interlayer shift and/or layer rotation on the distribution of interlayer species derived from MC simulations is expected to be limited. The simplistic Gaussian functions used to model the distribution of $H_2O$ molecules are both shifted toward the interlayer mid-plane (by about 0.2 Å) and broadened as compared to MC calculations. Both the broadening and the shift of the Gaussian distributions are likely related to the specific profile of the MC distribution, and more especially to the high electron density in the interlayer mid-plane (Figure 7). However, the XRD profiles calculated assuming the two models are almost identical (Figure 6c and d) and plead for a limited sensitivity of calculated XRD patterns to these two parameters if the actual distribution profile is unknown.

*Validity of the 2WG Configuration Model.* Similar XRD patterns may be calculated with 2WG and 2WS models by increasing the $B_{\text{wat}}$ factor in the latter model (Figures 8c and d, and 9b and c). Because of the demonstrated sensitivity of calculated XRD patterns to the distribution of $H_2O$ molecules, this similarity can only result from similar contributions of $H_2O$ molecules to the structure factor in both models. Parameters affecting the structure factor include the scattering power, the position, and the amount of considered species. If the origin of the layer unit is set in the center of the layer octahedron, the contribution of $H_2O$ molecules to the structure factor of 00$l$ reflections for a periodic 2W smectite (2WS model) can be expressed as

$$F_{H_2O}(00l) = 2n_{H_2O} f_B\left(\frac{\sin\theta}{\lambda}\right)_{00l} \cos(2\pi l Z) \tag{1}$$

where $f_B((\sin\theta)/\lambda)_{00l}$ is the scattering power of $H_2O$ molecules taking into account their thermal motion ($B_{\text{wat}}$), $n_{H_2O}$ is the amount of $H_2O$ molecules at $Z = (1/2) - (\Delta d/h)$, $h$ being the layer thickness. $\Delta d$ is the distance between the interlayer mid-plane and the positions of the $H_2O$ molecules along the $c^*$ axis. With increasing values of $l$, the contribution of $H_2O$ molecules decreases together with $f_B(00l)$ as a result of the thermal motion of $H_2O$ molecules.

For the 2WG model, the contribution of interlayer $H_2O$ molecules to the structure factor of 00$l$ reflections for a periodic 2W smectite can be expressed as

$$F_{H_2O}(00l) = 4f\left(\frac{\sin\theta}{\lambda}\right)_{00l} \cos\left(2\pi l\left(\frac{1}{2} - \frac{\Delta d}{h}\right)\right) \sum_m n_m \cos\left(2\pi lm\frac{\Delta z}{h}\right) \tag{2}$$

where $f((\sin\theta)/\lambda)_{00l}$ is the scattering power of $H_2O$ molecules ($B_{\text{wat}} = 0$), and $\Delta d$ is the distance along the $c^*$ axis between the interlayer mid-plane and the position of the maximum density of the Gaussian distribution. $n_m$ is the amount of $H_2O$ molecules at a given distance ($m\Delta z$, $m$ being integer) from the maximum density of the Gaussian distribution. The sum $\sum_m n_m$ equals the total number of interlayer $H_2O$ molecules. For a given $l$ value, the positional distribution of $H_2O$ molecules disturbs their coherent scattering and thus decreases their absolute contribution to the structure factor. The decrease becomes more important as the $l$ indice increases. To quantify this decrease, eq 2 can be expressed as

$$F_{H_2O}(00l) = 2n^{eff}_{H_2O} f\left(\frac{\sin\theta}{\lambda}\right)_{00l} \cos\left(2\pi l\left((1/2) - \frac{\Delta d}{h}\right)\right) \sum_m n_m \cos\left(2\pi lm\frac{\Delta Z}{h}\right) \tag{3}$$

where $n^{eff}_{H_2O} = 2\sum_m n_m \cos(2\pi lm(\Delta Z/h))$ is the effective amount of interlayer $H_2O$ molecules contributing to the structure factor. Eqs 1 and 3 look similar but in the sum determining the $n^{eff}_{H_2O}$ value, the cosine term is lower than 1, and $n^{eff}_{H_2O}$ is thus lower than the total number of $H_2O$ molecules. In addition, the $n^{eff}_{H_2O}$ value decreases with increasing $l$ indices.

Thus, both 2WS and 2WG models are essentially different although in both cases the contribution of interlayer $H_2O$ molecules to the structure factor is strongly decreasing with increasing $l$ indices. In the first case, the thermal motion of these interlayer species is entirely responsible for the decrease, whereas in the latter model the decrease is related to the decreasing effective number of $H_2O$ molecules contributing to coherent diffraction effects. Note that both models may produce similar diffraction effects if appropriate values are used for the parameters describing the positional disorder of interlayer molecules. However, unrealistically large values were obtained for the $B_{\text{wat}}$ parameter when fitting Na−Sap$_{0.8}$ ($B_{\text{wat}}$ = 30 Å$^2$) as compared to Na−Sap$_{1.4}$ ($B_{\text{wat}}$ = 11 Å$^2$) although both XRD patterns were recorded under similar experimental conditions, and the 2WG configuration of $H_2O$ molecules appears as more realistic than the 2WS one. Additional support for the 2WG model arises from the close match between the number of interlayer $H_2O$ molecules determined using the 2WG model and that measured independently from water vapor isotherms.

*Water Content in Smectite Interlayer.* For a given sample, the total amount of interlayer $H_2O$ molecules can be approximated by weighing the water content hypothesized for each layer type by the relative abundance of this layer type and compared to that obtained from water vapor adsorption−desorption isotherm experiments (Table 3).[18] The water content determined by Ferrage et al. from XRD profile modeling assuming a 2WS model for the distribution of interlayer $H_2O$ molecules was reasonably consistent with that obtained from water vapor adsorption−desorption isotherm experiments.[14,16,18] However, the 2WG configuration provides the best agreement with the water contents determined experimentally from water vapor adsorption−desorption isotherm experiments, with the XRD values lying most often between the values obtained on either branches of the isotherm (Tables 2 and 3).

*fwhm of $H_2O$ Molecule Gaussian Distribution*. When using the 2WG model to describe the distribution of $H_2O$ molecules in 2W layers, the fwhm parameter represents the positional disorder of the species, which is characterized by the $B_{wat}$ factor in usual models. One may note that the diffraction effects resulting from the two configurations are similar and lead to a significant decrease of the coherent scattering of $H_2O$ molecules with increasing diffraction angle (see above). However, the $B_{wat}$ factor should be about constant for a given species whereas the fwhm parameter can be structurally interpreted. For example, when increasing the RH, the fwhm of the Gaussian distribution systematically increases for Ca- and Sr-saturated montmorillonites (Table 2, Figure 11b and c) most likely to accommodate the steady addition of $H_2O$ molecules weakly bound to the interlayer cation. On the contrary, with increasing layer charge, Na-saturated saponite samples hold more $H_2O$ molecules for a given RH value in a narrower distribution (Figure 11d and Table 2). A possible origin for such narrowing of $H_2O$ molecule distributions is the increased polarization of these interlayer species resulting from a stronger undersaturation of surface oxygen atoms.

*Relative Positions of Interlayer Cations and $H_2O$ Molecules*. The distance ($\Delta d$) between the interlayer cations, which are located in the interlayer mid-plane, and the maximum density of the interlayer $H_2O$ molecule distribution function was also varied from one model to the other, with the maximum $\Delta d$ values being obtained with the 2WG configuration of $H_2O$ molecules (Table 2). The $\Delta d$ values reported in the present study represent only indicative values that could be used for XRD profile modeling but a more complete study should be carried out to determine the key factors that influence this parameter.

**Consistency with Reported Interlayer Structures of Expandable 2:1 Phyllosilicates.** *Comparison with the Present Data*. Among expandable 2:1 phyllosilicates, vermiculite and smectite are differentiated from their contrasting layer charge, with vermiculite exhibiting a higher layer charge (1.2−1.8 per $O_{20}(OH)_4$) than smectite (0.4−1.2 per $O_{20}(OH)_4$).[46] This difference is usually revealed by the contrasting swelling behavior of the two minerals after magnesium saturation and glycerol solvation, vermiculite and smectite exhibiting basal spacings of ∼14 and ∼18 Å, respectively, after such treatment.[1,47,48] However, distinct hydration behavior has not been reported for these two mineral species, and the predominance of bi-hydrated layers has been documented for the two species as a function of relative humidity. As a consequence, these two expandable 2:1 phyllosilicates will be considered together in the following.

For modeling XRD results of clay minerals containing 2W layers, the interlayer water configuration usually assumed for bi-hydrated smectite is that used for the calculations showed in Figures 1a and 10 and already described (Type I, Figure 12).[1] This model does not allow the description of experimental XRD patterns (Figure 10) and may be rejected.

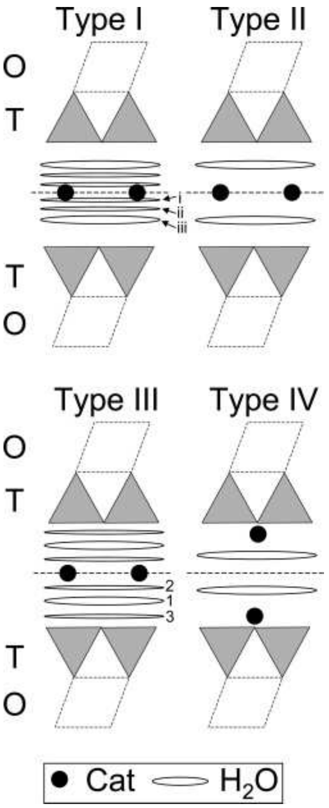

**Figure 12.** Schematic description of the different configurations proposed in the literature for interlayer species in 2W smectite layers. O and T refer to the octahedral and tetrahedral sheets of the 2:1 layer, respectively. Labels of the different sheets of $H_2O$ molecules are detailed in the text.

Most of the three-dimensional structural determinations of 2W interlayer configuration were actually performed on vermiculite as this mineral frequently exhibits ordered stacking sequences and because its higher content of interlayer cations allows for a more accurate refinement of cation positions as compared to smectite. In addition vermiculite, as illite, presents an ordered distribution of interlayer cations which eases the structural characterization of the interlayer configuration as compared to smectite.[49] The structural studies devoted to the configuration of interlayer species have led to different structure models that will be described below.

In bi-hydrated Mg-vermiculite, $Mg^{2+}$ cations are located in the mid-plane of the interlayer with one sheet of $H_2O$ molecules on each side of this plane (Type II, Figure 12).[5,50−53] According to this model, Mg is octahedrally coordinated by six $H_2O$ molecules, whereas additional $H_2O$ molecules, which are weakly bound to the cation, are located on the same plane as the six cation-bound $H_2O$ molecules.[54−57]

---

(46) Bailey, S. W. *Clay Miner.* **1980**, *15*, 85−93.

(47) de la Calle, C.; Suquet, H. In *Hydrous Phyllosilicates (exclusive of micas)*; Bailey, S. W., Ed.; Mineralogical Society of America: Washington, DC, 1988; Reviews in Mineralogy Vol. 19, pp 455−496.

(48) Walker, G. F. *Clay Miner. Bull.* **1958**, *3*, 302−313.

(49) Besson, G.; Misfud, A.; Tchoubar, C.; Méring, J. *Clays Clay Miner.* **1974**, *22*, 379−384.

(50) Mathieson, A. M.; Walker, G. F. *Am. Mineral.* **1954**, *39*, 231−255.

(51) Mathieson, A. M. *Am. Mineral.* **1958**, *43*, 216−227.

(52) Bradley, W. F.; Serratosa, J. M. In *Clays & Clay Minerals, Proceedings of the 7th Clay Conference*; Pergamon Press: 1960; pp 260−270.

(53) Shirozu, H.; Bailey, S. W. *Am. Mineral.* **1966**, *51*, 1124−1143.

(54) Alcover, J. F.; Gatineau, L.; Méring, J. *Clays Clay Miner.* **1973**, *21*, 131−136.

(55) Alcover, J. F.; Gatineau, L. *Clay Miner.* **1980**, *15*, 25−35.

(56) Alcover, J. F.; Gatineau, L. *Clay Miner.* **1980**, *15*, 239−248.

**Table 4. Structural Parameters of the Different Configurations Reported in the Literature for Interlayer Water in Bi-Hydrated Smectite Layers**

Type I Configuration[a]

| reference | sample | cation−$H_2O_{(iii)}$[b] | cation−$H_2O_{(ii)}$[b] | cation−$H_2O_{(i)}$[b] | $B_{wat}$[c,d] |
|---|---|---|---|---|---|
| Moore and Reynolds[1] | 2W−smectite | 1.20 | 1.06 | 0.35 | 11/2[§] |

Type II Configuration

| reference | sample | $O_{layer}$−$H_2O$[b] | cation−$H_2O$[b] | $d_{001}$[e] | $nH_2O/n$Cat[f] | $B_{wat}$[c] |
|---|---|---|---|---|---|---|
| Mathieson et al.[51] | Mg−vermiculite | 2.76 | 1.14 | 14.34 | | 5.4 |
| Shirozu et al.[53] | Mg−vermiculite | 2.67[g] | 1.17[g] | 14.33 | 7.44 | 6.1 |
| Alcover et al.[55] | Mg−vermiculite | 2.69 | 1.19 | 14.36 | | |
| Le Renard et al.[60] | altered Ca−phlogopite | 2.77 | 1.41 | 14.96 | 8.60 | |
| | altered Na−phlogopite | 2.71 | 1.43 | 14.87 | 10.70 | |
| | altered Li−phlogopite | 2.71 | 1.30 | 14.62 | 8.79 | |
| Beyer et al.[59] | Na−vermiculite | 2.70[g] | 1.44[g] | 14.85 | 4.00 | 3.9 |

Type III Configuration

| reference | sample | $O_{layer}$−$H_2O$[b,h] | cation−-$H_2O$[b,h] | $d_{001}$[e] | $nH_2O/n$Cat[f] | $B_{wat}$[c] |
|---|---|---|---|---|---|---|
| de la Calle et al.[61] | Ca−vermiculite | 2.78 | 1.45[f] | 14.92 | 7.34 | 5.5 |
| Slade et al.[58] | Ca−vermiculite | 2.82 | 1.41[f] | 14.89 | 8.02 | 2.5 |
| | Na−vermiculite | 2.66 | 1.42 | 14.85 | 5.58 | 3.9 |

Type IV Configuration

| reference | sample | $O_{layer}$−$H_2O$[b] | $O_{layer}$−Cation[b] | cation−$H_2O$[b] | $d_{001}$[e] | $nH_2O/n$Cat[f] | $B_{wat}$[c] |
|---|---|---|---|---|---|---|---|
| Ben Brahim et al.[13] | Na−Beidellite | 3.00 | 1.00 | 2.00 | 15.25 | 11.87 | 5 |

[a] Configurations of interlayer water in bi-hydrated smectite layers are schematized in Figure 12. [b] Distances are measured in projection along the $c^*$ axis and given in Å. $O_{layer}$, $H_2O$, and cation stand for the outermost plane of oxygen from the 2:1 layer, the $H_2O$ molecules, and the interlayer cations, respectively. [c] $B_{wat}$ is the Debye−Waller temperature factor reported for $H_2O$ molecules (in Å$^2$). [d] Debye−Waller factor is 11 Å$^2$ for plane iii and 2 Å$^2$ for planes i and ii, respectively. [e] Basal distance $d_{001}$ along the $c^*$ axis is given in Å. [f] $nH_2O/n$Cat represents the ratio between the number of interlayer $H_2O$ molecules and that of interlayer cations. [g] Average value for the different planes of $H_2O$ molecules. [h] Distances are given for the denser plane of $H_2O$ molecules.

A Type II configuration of $H_2O$ molecules was also proposed for Na-saturated vermiculite,[58,59] and for Na-, Ca-, and Li-rich altered phlogopites.[60]

A second configuration of interlayer species has been proposed for Ca-saturated vermiculites (Type III, Figure 12).[58,61,62] In this model, two distinct coordinations are reported for $Ca^{2+}$ cations, with two out of three $Ca^{2+}$ cations being octahedrally coordinated as in type II configuration, whereas remaining $Ca^{2+}$ cations exhibit a cubic coordination. This dual coordination induces the presence of two discrete planes of $H_2O$ molecules (planes 2 and 3, Figure 12) in addition to that observed in the type II configuration, which holds most $H_2O$ molecules (plane 1, Figure 12). The increased heterogeneity of $H_2O$ configuration in Ca-, Sr-, and Ba-saturated samples as compared to Mg-saturated ones was confirmed both from diffraction and IR results.[56,57] A Type III configuration of $H_2O$ molecules was also proposed for Na-saturated vermiculite.[58] Figure 13 compares the 2WG configuration of interlayer $H_2O$ molecules determined for Ca−SWy-2 (40% RH) in the present study with that reported in the literature for Ca-saturated vermiculite.[58,61] After normalization of the three distributions to the denser plane of $H_2O$ molecules, the three planes of $H_2O$ molecules appear closely related to the 2WG configuration proposed in the present study to describe the positional distribution of interlayer species.

To compare the $\Delta d$ values obtained in the present study with those reported in the literature (1.14−1.45 Å, Table 4), these values can be normalized to the thickness of the interlayer space to better account for the balance of the interactions with the interlayer cation on one hand and the 2:1 layer on the other hand (Table 5). Following such a normalization procedure, the $\Delta d$ values determined for the 2WG configuration of $H_2O$ molecules are consistent with those reported in the literature, whereas lower values are obtained when assuming a 2WS configuration.

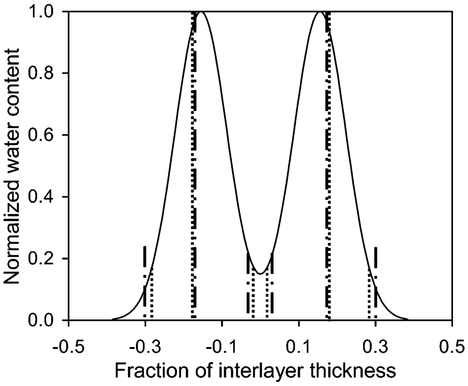

**Figure 13.** Comparison of the distributions of $H_2O$ molecules reported for bi-hydrated smectites. The distributions are normalized to the denser plane of $H_2O$ molecules, and $z$-coordinates are given in fraction of the interlayer with the origin located in the interlayer mid-plane thickness.The distribution determined from XRD profile modeling for the Ca-saturated SWy-2 montmorillonite sample (40% RH) is plotted as a solid line, whereas data from de la Calle et al. (ref 58) and from Slade et al. (ref 61) are shown as dashed and dotted-dashed lines, respectively.

---

(57) Fornés, V.; de la Calle, C.; Suquet, H.; Pezerat, H. *Clay Miner.* **1980**, *15*, 399−411.

(58) Slade, P. G.; Stone, P. A.; Radoslovitch, E. W. *Clays Clay Miner.* **1985**, *33*, 51−61.

(59) Beyer, J.; Graf von Reichenbach, H. *Clay Miner.* **2002**, *37*, 157−168.

(60) Le Renard, J.; Mamy, J. *Bull. Groupe Franç. Argiles* **1971**, *23*, 119−127.

(61) de la Calle, C.; Pezerat, H.; Gasperin, M. *J. Phys.* **1977**, *C7*, 128−133.

(62) de la Calle, C.; Suquet, H.; Dubernat, J.; Pezerat, H. *Clay Miner.* **1978**, *13*, 275−197.

**Table 5. Distances along the $c^*$ Axis between the Interlayer Mid-Plane and the Maximum Density of the $H_2O$ Molecule Distribution normalized to the Thickness of the Interlayer Space for the Different Configurations of Interlayer Species**

| | 2WS | 2WS | |
|---|---|---|---|
| sample | $B_{wat} = 2$[a] | $B_{wat} = 11$[a] | 2WG[b] |
| Ca−SWy-2 (40%RH) | 27.8%[c] | 30.1% | 31.0% |
| Ca−SWy-1 (80%RH) | 26.8% | 29.4% | 30.5% |
| Sr−SWy-1 (60%RH) | 26.7% | 29.4% | 31.1% |
| Sr−SWy-1 (80%RH) | 26.1% | 30.7% | 33.1% |
| Na−SWy-2 (80%RH) | 26.7% | 31.4% | 33.4% |
| Na−$Sap_{0.8}$ (90%RH) | 27.1% | 30.0% | 31.4% |
| Na−$Sap_{1.4}$ (90%RH) | 28.4% | 31.4% | 31.9% |
| mean value | 27.1% ± 0.7% | 30.3% ± 0.8% | 31.8% ± 1.0% |
| literature mean value[d] | | 32.7% ± 2.1% | |

[a] 2WS corresponds to an interlayer configuration of $H_2O$ molecules distributed as one plane on either side of the interlayer mid-plane. The Debye−Waller temperature factor for water ($B_{wat}$) is given in Å$^2$. [b] 2WG corresponds to an interlayer configuration of $H_2O$ molecules distributed according to a Gaussian function on either side of the interlayer mid-plane. [c] The distance along the $c^*$ axis between the interlayer mid-plane and the maximum density of the $H_2O$ molecule distribution ($\Delta d$) is normalized to the thickness of the interlayer (layer thickness minus the thickness of the 2:1 layer, 6.54 Å). [d] Average value calculated from the data reported for Type II and Type III configurations of interlayer species (refs 51, 53, 55, and 58−61).

In addition, $z$-coordinates along $c^*$ axis were recalculated together with typical distances between the 2:1 layer and the planes of $H_2O$ molecules, and between $H_2O$ molecules and interlayer cations (Table 4). For type II and III configurations the distance between the 2:1 layer and the densest plane of $H_2O$ molecules scatters between 2.36 and 2.82 Å and is consistent with the formation of H-bonds between interlayer $H_2O$ molecules and the clay framework. The distance between the densest plane of $H_2O$ molecules and the interlayer cation ranges from 1.14 to 1.45 Å.

*Specific Interlayer Structure Resulting from the Presence of Tetrahedral Substitutions*. A third configuration of water in 2W smectite has been envisaged for Na-beidellite samples, with $Na^+$ cations being partly engaged in the ditrigonal cavities of the 2:1 layers and the coordinated $H_2O$ molecules distributed on either side of the interlayer mid-plane which is devoid of atoms (Type IV, Figure 12).[12,13,63] Such a migration of the interlayer cation from the interlayer mid-plane toward the 2:1 clay framework is consistent with MC simulations and IR spectroscopy results which both support the formation of inner-sphere complexes for monovalent cations in tetrahedrally substituted 2:1 phyllosilicates.[21,24,26,31] In the present study, similar distributions of interlayer species have been determined whatever the location of the layer charge deficit in agreement with previous reports of Type II and Type III configurations of interlayer species in tetrahedrally substituted 2W vermiculites.[58−60] The central location of $Na^+$ cations was found to be consistent with experimental XRD data even when $Na^+$ cations account for a significant part of the interlayer electronic density (13% of the interlayer electrons for sample Na−$Sap_{1.4}$). Furthermore, if a Type IV configuration is assumed for the distribution of interlayer species, significant discrepancies arise between experimental and calculated patterns, especially for the 002 and 003 reflections which are extremely sensitive to the presence of interlayer species at the interlayer mid-plane position (Figure 14). In conclusion, the present data do not provide experimental evidence for the migration of monovalent cations toward the surface of tetrahedrally substituted 2:1 layers.

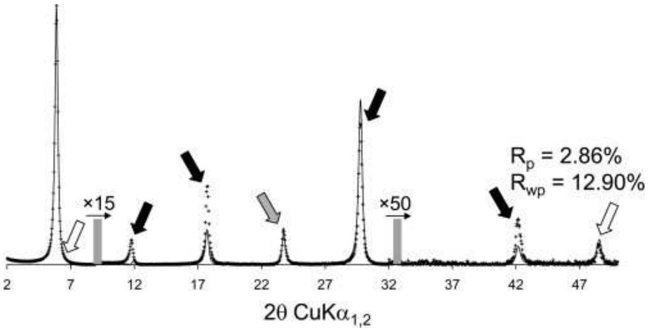

**Figure 14.** Comparison between experimental and calculated XRD patterns for the Na-saturated $Sap_{1.4}$ saponite sample recorded at 90% RH. Structural parameters used for the calculations are listed in Tables 1, 2, and 3. Patterns as for Figure 1. Calculation is performed assuming a Type IV configuration of interlayer species with a shift of the interlayer cation from the interlayer mid-plane toward the 2:1 clay framework (ref 13).

**Acknowledgment.** The results presented are a part of a Ph.D. thesis granted by Andra (French National Agency for Nuclear Waste Disposal). Andra is thanked for the permission to publish this manuscript and for financial support. B.L. acknowledges financial support from the CNRS/PICS709 program, and from the CNRS/SdU "postes rouges" fellowships granted to B.A.S. V.A.D. and B.A.S. are grateful to the Russian Science Foundation for partial financial support. Laurent Michot (LEM, Nancy, France) is thanked for the fruitful discussions about smectite hydration. Jean-Louis Robert (IST Orléans, France) kindly provided the synthetic saponite samples.

CM047995V

---

(63) Ben Brahim, J.; Armagan, N.; Besson, G.; Tchoubar, C. *J. Appl. Crystallogr.* **1983**, *16*, 264−269.

Abstract:

Montmorillonite clays in low hydration states, with $Na^+$ and $Cs^+$ compensating counterions, are investigated by a combination of microscopic simulation and quasi-elastic neutron scattering to obtain information on the local structure and dynamics of water and ions in the interlayer. At first predictions of simulation into the dynamics of water and ions at elevated temperatures are shown (0°C – 80 °C, pertinent for the radioactive waste disposal scenario). Marked difference is observed between the modes of diffusion of the $Na^+$ and $Cs^+$ counterions. In water dynamics, a significant step towards bulk water behaviour is seen on transition from the mono- to bilayer states. Secondly, a detailed comparison between simulation and quasi-elastic neutron scattering (Neutron Spin Echo and Time-of-Flight) regarding ambient temperature water dynamics is presented. Overall, the approaches are found to be in good agreement with each other and limitations of each of the methods are clearly shown.

Key words: clay, montmorillonite, microscopic simulation, neutron scattering, dynamics, water

Résumé:

La structure locale et la dynamique de l'eau et des cations dans l'espace interfoliaire des argiles montmorillonitiques, faiblement hydratées et avec des cations compensateurs $Na^+$ et $Cs^+$, sont étudiées par une combinaison de simulation microscopique et de diffusion quasi-élastique des neutrons. Les prédictions des simulations sur la dynamique de l'eau et des ions aux températures élevées (0°C–80°C, gamme pertinente pour le stockage des déchets radioactifs) sont présentées. Une différence marquée est observée entre les modes de diffusion des deux cations compensateurs. Pour la dynamique de l'eau, la transition entre les états mono- et bicouche est une étape marquante vers le comportement de l'eau bulk. Une comparaison détaillée entre simulations et diffusion quasi-élastique des neutrons (écho de spin et temps de vol) est présentée pour la dynamique de l'eau à température ambiante. Globalement, les approches sont en bon accord et les limitations de chacune sont clairement montrées.

Mots clefs: argile, montmorillonite, simulation microscopique, diffusion des neutrons, dynamique, l'eau